Systematic analysis of NO_2 long-range transport events in GOME-2 satellite data and MACC-II reanalysis model data

Dissertation zur Erlangung des Grades *Doktor der Naturwissenschaften*

Achim W. Zien*

Institut für Umweltphysik
Fachbereich 1
Universität Bremen

2015–09–06

*achim@zien.me

Abstract / Zusammenfassung

Abstract

Intercontinental long-range transport (LRT) events of NO_2 relocate the effects of air pollution from emission regions to remote, pristine regions. I detect transported plumes in tropospheric NO_2 columns measured by the GOME-2 / MetOp-A instrument with a specialized algorithm and trace the plumes to their sources using the HYSPLIT lagrangian transport model. With this algorithm I find 3808 LRT events over the ocean for the period 2007 to 2011. I perform an analogous study on data from MACC-II reanalysis and compare the results from both datasets. LRT events occur frequently in the mid-latitudes, emerging usually from coastal high-emission regions. In the free troposphere, plumes of NO_2 can travel for several days to the polar oceanic atmosphere or to other continents. They travel along characteristic routes and originate from both continuous anthropogenic emissions and emission events such as bush fires. Most NO_2 LRT events occur during autumn and winter months, when meteorological conditions and emissions are most favorable. The evaluation of meteorological data shows that the observed NO_2 LRT is often linked to cyclones passing over an emission region. The total transported NO_2 content is several permil of the total estimated emission. Results from GOME-2 and MACC-II agree on the Northern Hemisphere while MACC-II produces significantly less transport on the Southern Hemisphere.

Zusammenfassung

Der interkontinentale Langstreckentransport (long-range transport, LRT) von NO_2 bewirkt eine Verschiebung der Auswirkungen von Luftverschmutzung von Emissions- hin zu windabwärts gelegenen – auch unverschmutzten – Regionen. In dieser Arbeit erfasse ich im Transport befindliche Wolken von troposphärischem NO_2 in Daten des GOME-2/MetOp-A-Satelliteninstruments mithilfe eines darauf zugeschnittenen Algorithmus. Der Ursprung dieser Wolken wird mithilfe des Lagrangeschen Transportmodells HYSPLIT ermittelt. Dieser Algorithmus findet 3808 solcher Ereignisse im Beobachtungszeitraum 2007–2011. In gleicher Weise erfasse ich solche Ergeinisse in Modelldaten der MACC-II-Reanalyse und vergleiche die Ergebnisse. LRT-Ereignisse treten oft und regelmäßig in den mittleren Breiten auf und entspringen meist Küstenregionen mit hoher NO_2-Emission. In der freien Troposphäre können diese Wolken mehrere Tage vom Wind über den polaren Ozean oder bis zu anderen Kontinenten getragen werden. Dabei folgen sie charakteristischen Routen und können sowohl aufgrund durchgängiger, menschlicher Emission als auch aufgrund einzelner Großemissionen – wie Buschfeuer – enstehen. Die meisten LRT-Ereignisse finden in den Herbst- und Wintermonaten statt; zu dieser Zeit sind die meteorologischen Bedingungen günstig und die Emissionen besonders hoch.

Bei der Auswertung meteorologischer Bedingungen stellt sich heraus, dass Zyklone, die über ein Gebiet hinweg ziehen, eine wahrscheinliche Ursache sind. Die Gesamtmenge an solcherart transportiertem NO_2 beträgt mehrere Promille der geschätzten Gesamtemission. Während die Ergebnisse aus GOME-2- und MACC-II-Daten auf der Nordhemisphäre weitestgehend übereinstimmen, sind auf der Südhemisphäre wesentlich weniger und kleinere LRT-Ereignisse in MACC-II-Daten zu beobachten.

Contents

1 Introduction

Global and local environmental change is an important topic of our era. The vanishing of biodiversity, pollution of air, ground and water, as well as global climate change will affect our and our children's lives. The problem with these phenomena is, that they are part of a complex web of interactions of chemicals, radiation, dynamics, animals and humans. It is apparent that we face huge challenges. Challenges, that can only be overcome by the study of the processes that create them so that we can counteract or mitigate their undesired effects or prevent their occurrence in the first place.

One such problem is the pollution of our atmosphere. Acid rain from washed-out sulfates, urban ozone smog, global warming and the ozone hole, caused by formerly unknown side-effects of abundantly employed chlorofluorocarbons (CFCs), are the most prominent results of air pollution.

In three of these problems, nitrogen-oxides like NO and NO_2 are involved:

- NO_2 is the largest source of acid rain by now
- NO_2 fosters the creation of ozone in the atmospheric surface boundary layer
- NO_2 fosters ozone destruction in the stratosphere

At least, NO_2 itself is no greenhouse gas. However, it does still impact climate change via the creation of tropospheric ozone and by removing OH from the atmosphere, which in turn leads to a longer lifetime of methane (CH_4), one of the strongest common greenhouse gases.

NO_x – NO_2 and NO – is emitted in similar parts from human activity and natural processes, with an indication of larger amounts of anthropogenic emissions. Usually – due to its short atmospheric lifetime – it stays in its emission region, affecting only the environment that produced it.

However, as this study will show, NO_2 can also be transported over large distances towards other emission regions or towards otherwise pristine and sensitive regions like the Arctic. There, the relocated NO_2 may drastically impact atmospheric chemistry and cause smog, acid rain and respiratory diseases.

This phenomenon has not been analyzed in a systematic manner before my studies. As NO_2 is typically short-lived, it was not part of studies that dealt with long-range transport of long-lived species. Yet, transport events are clearly visible in raw satellite data. This study will use both satellite observations and model simulations to look for these events and retrieve information about their causes, properties, affected regions, typical routes and potential problems in their detection.

In Chapter 2, I will detail basic properties of the trace gas in question: NO_2. Chapter 3 will then explain the basics of long-range transport and summarize other studies that have analyzed this phenomenon before. Chapter 4 and Chapter 5 give descriptions

of the GOME-2 / MetOp-A satellite dataset and MACC-II reanalysis model dataset that I use in this study, respectively. Chapter 4 also details on the challenges on retrieving NO_2 data from satellite measurements and peculiar effects of its observational geometry. The algorithm that was used to derive the long-range transport dataset from both satellite and model data is described in Chapter 6. Finally, the plumes retrieved from GOME-2 / MetOp-A and MACC-II reanalysis are analyzed in Chapter 7 and Chapter 8, respectively. Chapter 8 also includes the comparison of results from both datasets. A short discussion of the results is provided in Chapter 9.

This thesis expands on my results from Zien et al. (2014).

Hopefully, this work will help understand the impact of NO_2 long-range transport and affect emission policies, if neccessary.

2 Nitrogen dioxide (NO_2)

Nitrogen dioxide (NO_2) is an unstable trace gas which occurs in the Earth's atmosphere. It is both anthropogenic and natural in origin (with the anthropogenic part dominating) and is a byproduct of all combustion processes. NO_2 is very toxic (EU classification) and causes respiratory symptoms in mammals (World Health Organization, 2003) under a long-term exposure of concentrations above $\approx 50\,\mu g/m^3$. It can also have significant impact on ozone (O_3) chemistry, which in turn affects health and crop yields. When washed out of the atmosphere, NO_2 can cause acid rain, affecting humans, animals, vegetation and buildings. It can also act as a fire accelerant. NO_2 is an orange gas with a sharp, biting odor.

2.1 Properties

NO_2 consists of a nitrogen atom bonded to two oxygen atoms at a distance of $\approx 120\,pm$, bent in an angle of $\approx 134°$. With its molecular mass of $\approx 46\,g/mol$ it is heavier than the main constituents of the Earth's atmosphere: molecular nitrogen N_2, molecular oxygen O_2 and atomic argon Ar. The abundance of its constituent atoms means that NO_2 will readily form as soon as it is energetically possible.

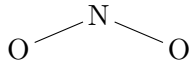

Nitrogen Dioxide

Its electronic ground state is a doublet state. NO_2 is a radical species; it is highly reactive due to its single free electron. Also, the bond to the second oxygen atom is relatively weak which makes NO_2 a strong oxidizer. It is thus an unstable trace gas and will usually decay within at most a few days after its synthesis.

A part of the absorption spectrum of NO_2 is plotted in Figure 2.1. While the strongest absorption features lie in the spectral range $\lessapprox 420\,nm$, the range of 425–497 nm possesses the most distinguished absorption features that are highly uncorrelated to any other absorption features of common atmospheric compounds in this spectral range. Thus, the error of attributing absorption to NO_2 when it originates from another species (and vice versa) is minimized and unambiguous detection and quantification by absorption spectroscopy is possible.

NO_2 is subject to photodissociation, which converts NO_2 to NO. In lower radiative flux, the NO will recombine with atmoic oxygen to form NO_2. This leads to a diurnal cycle between NO and NO_2. Due to the efficient interconversion, these two species are often treated as one, combined species: NO_x (NO and NO_2).

Almost all NO_2 in the atmosphere was originally emitted as NO and later converted into NO_2 until it forms an equilibrium state. This Leighton photostationary state is

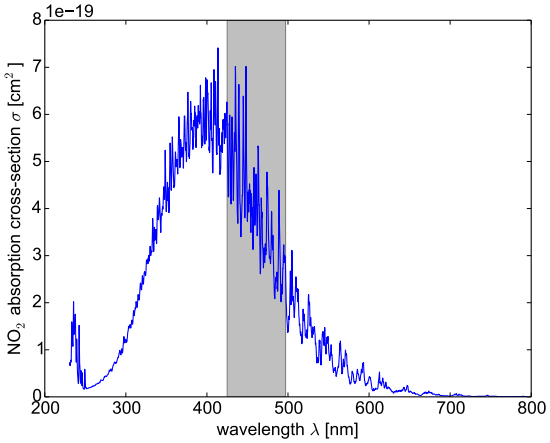

Figure 2.1: NO_2 laboratory absorption spectrum in the near-UV to near-IR range at 273 K. The grey shaded area indicates the fitting window used in the NO_2 retrieval in Chapter 4. Data: Burrows et al. (1998)

usually in the range of $NO/NO_x \approx 0.2$–0.8 – depending on altitude, temperature and illumination (Ehhalt et al., 1992). NO typically forms in combustion processes or lightning, when temperatures are elevated enough to aid in breaking up the ambient N_2 and O_2:

$$N_2 + O_2 \rightarrow 2NO \tag{2.1}$$

Then, NO and NO_2 are linked via the equilibrium equations:

$$NO + O_3 \rightarrow NO_2 + O_2, \tag{2.2}$$

$$NO_2 + h\nu \rightarrow NO + O, \tag{2.3}$$

with photon energies $h\nu = E = \frac{hc}{\lambda}$ and $280\,\text{nm} \lessapprox \lambda \lessapprox 420\,\text{nm}$.

These two reaction paths lead to an equilibrium between NO and NO_2 that is dependent mainly on O_3 concentrations and irradiation. It will thus vary with altitude, time of day and season.

Another path to convert NO to NO_2 is the reaction with the hydroperoxyl radical HO_2 (or, analogously, any other alkylperoxy radical RO_2):

$$NO + HO_2 \rightarrow OH + NO_2. \tag{2.4}$$

After being released in the reaction Equation 2.3, molecular oxygen O is highly reactive and is likely to combine with O_2 to form ozone:

$$O + O_2 \xrightarrow{M} O_3, \tag{2.5}$$

with another molecule M to satisfy conservation of momentum.

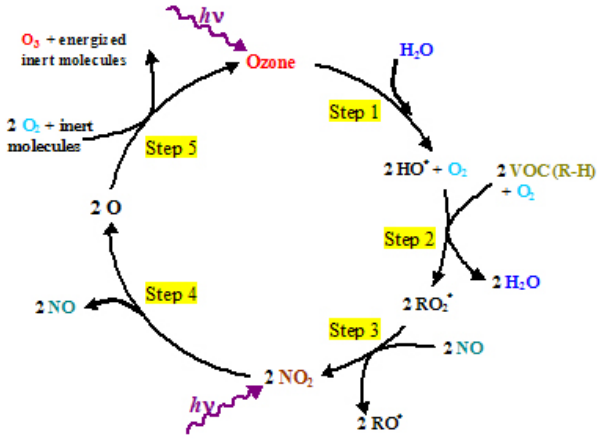

Figure 2.2: Illustration of the ozone production cycle. Figure: Casiday and Frey (2001)

However, it may also react with another atomic oxygen to form molecular oxygen or find even further reaction partners like the hydroxyl radical OH.

$$2O \rightarrow O_2 \tag{2.6}$$
$$O + OH \rightarrow HO_2 \tag{2.7}$$

Hydroxyl can be formed by photodissociation of O_3 into electronically excited $O(^1D)$, which in turn reacts with water vapor to form two hydroxyl radicals.

While both Equation 2.2 and Equation 2.5 will lead to the dissociation and synthesis of O_3, respectively, these two reactions do not occur at the same rate. In the troposphere, the common presence of volatile organic compounds (VOCs) in industrialized areas as well as the abundance of available water vapour will lead to a reaction cycle that will produce ozone from atomic oxygen in the presence of NO_x, see Figure 2.2.

$$O_3 + H_2O \xrightarrow{h\nu} 2OH + O_2 \tag{2.8}$$
$$2OH + O_2 + 2VOC(R-H) \rightarrow 2H_2O + 2RO_2 \tag{2.9}$$
$$2RO_2 + 2NO \rightarrow 2RO + 2NO_2 \tag{2.10}$$
$$2NO_2 + h\nu \rightarrow 2NO + 2O \tag{2.11}$$
$$2O + 2O_2 \xrightarrow{\text{impulse transfer}} 2O_3 \tag{2.12}$$

This cycle consumes molecular oxygen and forms ozone, thereby oxidizing VOCs. NO is only a catalyst in this reaction cycle: it enters in the third step and is released again in the fourth step in equal amounts. This means that as long as VOCs, oxygen and water vapour are present – typical conditions in the troposphere of high population density regions – NO_x will enable the production of O_3. This leads to the infamous photochemical ozone smog.

Finlayson-Pitts and Pitts Jr (1999, p. 242) note that, "the impact of added NO_x on the generation of O_3 depends on existing levels. At low NO levels, added NO leads to increased O_3 formation. However, at sufficiently high NO_x, OH reacts with NO_2 to form HNO_3, effectively removing NO_x from the system and terminating ozone production. The level at which this occurs in the upper troposphere is $\approx 300\,\text{ppt}\,\text{NO}$."

Regardless of production rates, NO_x does not have to be replenished and will not be removed from the atmosphere in this reaction. This makes O_3 production in the troposphere particularly sensitive to NO_x emission.

In the stratosphere, almost no VOCs are available to keep the ozone cycle as per Equation 2.8 and following running. Thus, NO reacts with O_3, destroying the ozone in the process. The strong UV irradiation in the stratosphere leads to an elevated concentration of atomic oxygen O from photolyzed O_3 which will in turn react with NO_2 to form molecular oxygen and NO:

$$\begin{aligned} \text{NO} + \text{O}_3 &\rightarrow \text{NO}_2 + \text{O}_2 && (2.13)\\ \text{O}_3 &\xrightarrow{h\nu} \text{O}_2 + \text{O} && (2.14)\\ \text{NO}_2 + \text{O} &\rightarrow \text{NO} + \text{O}_2 && (2.15)\\ & && (2.16) \end{aligned}$$

In this process, NO is recycled and two ozone molecules are destroyed and converted to three oxygen molecules.

In the presence of OH, NO_2 can further be converted into nitric acid HNO_3:

$$\text{NO}_2 + \text{OH} \rightarrow \text{HNO}_3 \tag{2.17}$$

HNO_3 can convert back to NO_2 via photodissociation or reaction with another hydroxyl radical:

$$\begin{aligned} \text{HNO}_3 &\xrightarrow{h\nu} \text{NO}_2 + \text{OH} && (2.18)\\ \text{HNO}_3 + \text{OH} &\rightarrow \text{H}_2\text{O}_2 + \text{NO}_2 && (2.19) \end{aligned}$$

However, these backreactions occur at slow rates, due to the relative stability of HNO_3 and the small concentrations of OH and HNO_3. HNO_3 is soluble and can easily be washed out by liquid water in the atmosphere. Thus, HNO_3 is one of the main sinks for NO_x in the atmosphere. With the introduction of widespread catalytic hydrodesulfurization, HNO_3 has become the strongest source of acid rain, as already indicated by Galloway and Likens (1981).

Two HNO_3 molecules may react with each other to form water and dinitrogen pentoxide N_2O_5, a highly unstable oxidizing agent, that can occur either as a salt or as a bipolar molecule:

$$2\text{HNO}_3 \rightarrow \text{H}_2\text{O} + \text{N}_2\text{O}_5. \tag{2.20}$$

During nighttime, NO_2 may react with O_3 to form NO_3:

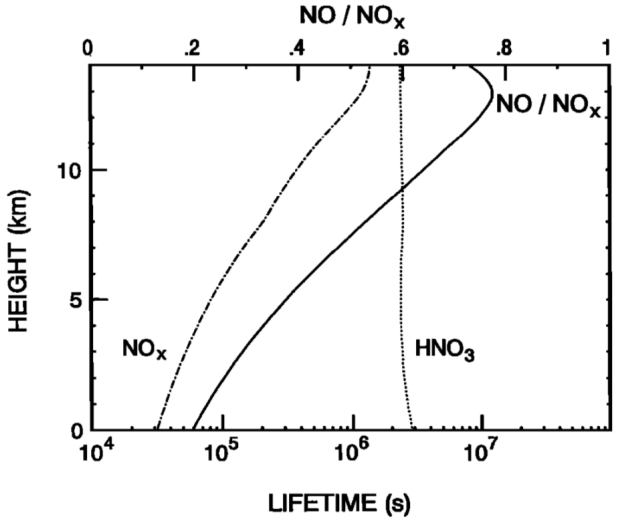

Figure 2.3: Estimated lifetime of NO_x and HNO_3 as well as NO / NO_x ratio, dependent on altitude. Note the logarithmic time-axis. Elevated NO_2 is significantly more stable than at the surface. Graph: Ehhalt et al. (1992)

$$NO_2 \ + \ O_3 \rightarrow NO_3 \ + \ O_2. \tag{2.21}$$

NO_3 is very sensitive to photodissociation. Thus, despite being a radical, it only plays a significant role in nighttime chemistry. It may convert to HNO_3. However, in global chemical models, this reaction path only contributes about 20 % of total HNO_3 production from NO_x. Thus, OH concentrations are the major factor determining NO_x sinks.

Except for NO and HNO_3, all of the aforementioned nitrogen compounds will eventually undergo dry deposition. While HNO_3 still has the highest deposition rates, NO_x will be removed from the atmosphere without it, eventually.

The lifetime of NO_x is dependent on environmental parameters, such as pressure and temperature, irradiation, and abundance of radical species. While radical species determine which paths of decay are possible, pressure and temperature determine the interaction rates and chances of recombination, e.g. after photodissociation. Radiative flux determines how readily NO_2 and its reaction products are dissociated.

Ehhalt et al. (1992) determined an approximate relationship between altitude and lifetime of NO_2 (Figure 2.3). This serves as a guideline and cannot be used to determine actual decay rates and extrapolate NO_2 content in long-range transport events, due to the unknown factors mentioned above. The figure also illustrates how the Leighton photostationary state between NO and NO_2 is dependent on altitude – an effect of the varying pressure and temperature. Again, these are only guidelines, not hard numbers to be implemented.

As seen in Figure 2.3, NO_x lifetime can range from a few hours in the planetary boundary layer (even less in exhaust plumes, where NO_x is mixed with reactive species)

to a few days in the free troposphere. This has also been observed by Beirle et al. (2011); Brasseur et al. (1999). This directly implies that observed long-range transport most likely takes place in the free troposphere, as the required lifetime is not attainable in the planetary boundary layer.

Peroxyacetyl nitrate (PAN, $CH_3C(O)OONO_2$) is a reservoir species that will form in the presence of NO_2 and hydrocarbons (Singh and Hanst, 1981a). This will be the case in the atmosphere of most polluted urban areas and also in transported exhaust. PAN will form up to an equilibrium described by the reaction with acetaldehyde and acetone:

$$CH_3C(O)OONO_2 \longleftrightarrow CH_3C(O)OO \ + \ NO_2 \tag{2.22}$$

It thus serves as a reservoir species for NO_2. If ambient NO_2 or hydrocarbon concentrations fall, PAN will decompose, releasing more NO_2. PAN is also temperature sensitive and the equilibrium of Equation 2.22 will rapidly shift away from PAN at high temperatures. Therefore, PAN concentrations are generally dependent on altitude, with typical concentrations of 17 pptv in the lower and 360 pptv in the upper troposphere, where most transport events will take place. This is an effect of the abundance of chemical agents and ambient temperature.

Depending on local chemistry, PAN reactions will either shorten or prolong the lifetime of NO_2. It appears most likely, that PAN will rapidly form in the beginning of a long-range transport event, leading to a shortened lifetime of NO_2, while it will release NO_2 when ambient NO_2 concentrations descrease later during the event, prolonging apparent NO_2 lifetime. In particular, PAN will decompose and release NO_2 when descending onto the shore of a continent, reaching higher ambient temperatures.

PAN may contain a significant fraction of reactive nitrogen in the local atmosphere. Depending on conditions, concentrations of PAN may be roughly the same as concentrations of NO_x. As PAN cannot be detected with current satellite instruments (Chapter 4), this may effectively double the amount of potential NO_x (of which only NO_2 can even be observed).

2.2 Sources

NO_2 usually resides in the planetary boundary layer, the free troposphere and the stratosphere. Concentrations of NO_2 in the stratosphere vary on a long timescale (besides diurnal variations due to solar irradiation) and usually form smooth spatial patterns. In contrast, concentrations in the planetary boundary layer vary on very short timescales – due to the short lifetime and fluctuating anthropogenic emission – and form strong, detailed spatial patterns, mostly following population density and industry.

NO_2 in the planetary boundary layer is usually created via oxidation of NO. For emission purposes, NO and NO_2 are treated jointly as NO_x. NO_x is emitted by anthropogenic and natural sources in roughly equal amounts. It is a byproduct of almost all combustion processes. This can only be mitigated by controlling oxygen concentrations in the combustion process. Martin et al. (2003) find a total yearly NO_x emission of 43 Tg N/a in 1996–1997.

Tropospheric emissions can originate from various processes (emission rates according to Bradshaw et al. (2000)):

- surface transportation, industry, aircraft, cement production: $16 \ldots 30\,\mathrm{Gg\,N/a}$
- anthropogenic and natural biomass burning: $4 \ldots 16\,\mathrm{Gg\,N/a}$
- microbial soil emissions: $3 \ldots 8\,\mathrm{Gg\,N/a}$
- lightning NO_x ($LiNO_x$): $1.2 \ldots 10\,\mathrm{Gg\,N/a}$

Except for $LiNO_x$ and emissions by aircraft, all of these processes emit NO_x in the planetary boundary layer. This means that the NO_2 directly impacts the environment, but decays rapidly. This has lead to the understanding that NO_x emissions are mostly localized and do not affect downwind regions. Due to the short lifetime of a few hours, NO_2 observations (on a fixed time of the day) can directly be used as estimate for the emission strength of regions. This holds true for most times, but occasionally, NO_2 long-range transport can lead to an export of significant amounts of NO_2 to downwind regions.

NO_x emissions – as measured by NO_2 observations from space – have risen in several parts of the world (especially in emerging economies) since satellite observations of NO_2 started in 1995 with the GOME / ERS-2 instrument (Burrows et al., 1999; Leue et al., 2001; Richter and Burrows, 2002; Martin et al., 2002). In industrialized countries, an opposing trend can be observed. Between 2002 and 2010, emission regulations and the installation of filters has led to rather steady NO_x emissions in Europe and slightly decreasing emissions in North America (Richter et al., 2005; Hilboll et al., 2013), followed by a clear decrease in emissions in both regions in the last years.

Regulations have a slow impact on emissions as it takes time to implement and enforce them. However, NO_x emission is in large fractions directly tied to a nation's production and transportation. Thus, economic crises and prosperity can be seen in the data (Vrekoussis et al., 2013; Lelieveld et al., 2015). This is especially striking in China. Here, Richter et al. (2005) find an exponential increase in NO_2 levels as the chinese economy prospers. In 2008, when the economic crisis struck, NO_x levels decreased slightly only to rise again in subsequent years.

Interestingly, the weekly cycle of NO_2 columns can also be used to determine weekend days for different regions, by locating days which show a significant decrease in NO_2 levels (Beirle et al., 2003). This also allows to estimate the anthropogenic fraction of total NO_x emissions and NO_2's lifetime in these conditions.

There are multiple inventories of NO_x emissions. One well known global inventory of NO_x emissions is EDGAR (Olivier et al., 1996; Janssens-Maenhout et al., 2012). It models seasonal emissions based on reported transportation, power plants, industry, population distribution, and average biomass burning observations. In this process, several assumptions are made to approximate actual emissions. The following questions have to be answered:

- What human activities are there (like transportation, production, heating, etc.)?
- What sort of technologies are in use to which proportions (old or new engines, filters, catalytic converters, etc.)?
- What are the specific emissions factors of the technology used (grams of NO_x emitted per used fuel)?

- How are emissions distributed temporally and spacially (concentrated on industrial district, roads, during rush hours, less during the night and on weekends)?

Strong discrepancies between the inventory and satellite observations can occasionally be found where government agencies do not report individual power plants or other major emitting facilities in their country or when the answers to one of the above questions change – better technologies may be used, more or less production may be taking place depending on the economy, etc. (Konovalov et al., 2008; Zhang et al., 2007). This may lead to a misrepresentation of the NO_x emissions which may also manifest in the analysis of NO_2 long-range transport in model data.

In early versions of the long-range transport plume verification process for this study, EDGAR data was used to model credible emission regions (see Subsection 6.2.4). This was later replaced by a simpler approach.

3 Long-range transport

Long-range transport of atmospheric trace gases over intercontinental distances is a major, concurrent research topic. It has become apparent that trace gas emissions can no longer be regarded as local concerns, but need to be dealt with globally. This is true not only for stable species – such as CO_2, CFCs and methane – but also for species with lifetimes of a few months or even just a few days.

For unstable species, this process of long-range transport has to be linked to meteoroloigcal phenomena which allow the trace gas to travel over large distances in a short time and which enhance their lifetime.

3.1 Atmospheric structure

The atmosphere is structured in layers. Most human activities take place in the planetary boundary layer, the layer where surface friction and obstacles strongly impact atmospheric movements. The planetary boundary layer can be subdivided into three layers.

Directly above the surface lies the viscous boundary layer, which is dominated by proximity to surface objects and does not couple to major atmospheric movements. This layer is only a few centimeters thick and does not impact our observations measurably.

The two layers above the viscous boundary layer (fluid-dynamically described as the Prandtl and Ekman layer) comprise the convective layer (Ekman, 1902). This is the layer where convective processes strongly couple atmospheric properties at different altitudes. It is affected by the diurnal cycle of heating and cooling of the surface: during day-time is can rise up to $1,000\,\mathrm{m}$ and shrink to as little as $20\,\mathrm{m}$ during night-times (Etling, 2008; Arya, 2001). The wind in this layer is only partially coupled to the geostrophic wind – the wind in the free troposphere above the planetary boundary layer – and shows much lower speeds, following roughly a logarithmic wind profile for indifferent stability. Most short-lived trace gases from human emissions are confined to the convective layer and only affect the local chemistry. Due to low wind speeds, these trace gases cannot be transported over long distances.

In the Prandtl layer, the middle sublayer of the planetary boundary layer, horizontal winds are dominated by surface friction and flow from high- to low-pressure regions.

The third and topmost of the sublayers of the planetary boundary layer is the Ekman-layer. This layer ranges from the top of the Prandtl-layer to the free troposphere. The boundary between the Ekman-layer and the free troposphere is defined as the altitude where local wind is indistinguishable from the geostrophic wind. In this layer, the wind rapidly changes its direction and speed with altitude, going from the Prandtl layer to the free troposphere. While at the lower end of the Ekman-layer, the wind speed and direction are still dominated by surface effects, it assimilates to the free geostrophic wind

in the free troposphere. Wind speeds may even exceed geostrophic wind speed due to overshooting in the coupled differential equations governing the wind profile.

The geostrophic wind is the wind vector that resembles a stationary equilibrium in which the force of a pressure gradient and the coriolis force of the moving air parcels negate each other. Therefore, the geostrophic wind is parallel to isobaric lines and is higher in regions of a steep pressure gradient. In the vicinity of the surface, wind gets slowed down due to friction. This friction adds another vector to the force diagram which is pointing opposite of the direction of movement and therefore orthogonal to the Coriolis force. Therefore, in the stationary state, the wind direction is not parallel to isobaric lines and instead shifted by a small angle in counter-clockwise and clockwise direction on the Northern and Southern Hemisphere, respectively.

Under stable meteorological conditions, there is no efficient exchange of gas from the planetary boundary layer to the free troposphere. It is, however, possible that events like a passing cold front or strong convection lead to a mixing of air from the planetary boundary layer into the free troposphere. A cold front consists of a rapidly moving body of cold air directly above the surface. When this body of air meets a stationary warm body of air, it will stay near the surface, causing the warm body of air to rapidly rise, taking any contained trace gas with it. In strong convective events, a heat source at or near the surface causes an unstable atmospheric state. The hot air will rapidly rise in a tube of convection while cold air descends around it. Strong convection can take place due to strong solar irradiation onto a highly absorbing surface, usually in thunderstorm clouds. Some of the strongest examples of deep convection are caused by massive biomass burning which can result in convective cells that elevate trace gases and soot up to the lower stratosphere (see Labonne et al., 2007).

The free troposphere is the atmospheric layer ranging from the top of the Ekman-layer to the tropopause, which is typically defined as the local altitude where the temperature gradient with descending altitude (the so-called lapse rate) sinks below 2 K/km (McCalla, 1981). The troposphere is relatively self-contained. There are rarely any processes which efficiently exchange gas between the troposphere and the stratosphere – the layer above the tropopause – and non-violent exchange processes are typically very slow. The free troposphere shows little diurnal effects in its dynamics, which are dominated by meso- and large-scale weather pheonomena such as low- and high-pressure regions. However, its chemistry is still impacted by the dirunal cycle and its varying amounts of solar irradiation. This especially affects gas species subject to photo-dissociation.

Above the tropopause begins the stratosphere, ranging from 8–15 km to about 50 km, depending on season and latitude, among other factors. Stratospheric chemistry is dominated by long-lived species and photochemistry. For the most part, stratospheric chemistry is decoupled from tropospheric chemistry by separation via the tropopause. Inside the stratosphere, temperature increases with altitude, leading to generally stable atmospheric conditions. This is due to the ozone layer that resides inside the stratosphere and absorbs large amounts of incoming ultraviolet (UV) radiation, thereby heating up.

Surface weather is mostly dominated by high- and low-pressure regions in the troposphere. These are formed by differences in atmospheric heating and atmospheric mechanics. High-pressure regions are typically relatively stable while low-pressure regions travel over the Earth's surface. The pressure gradient between high- and low-pressure regions leads to a net force that accelerates air from a high-pressure region towards

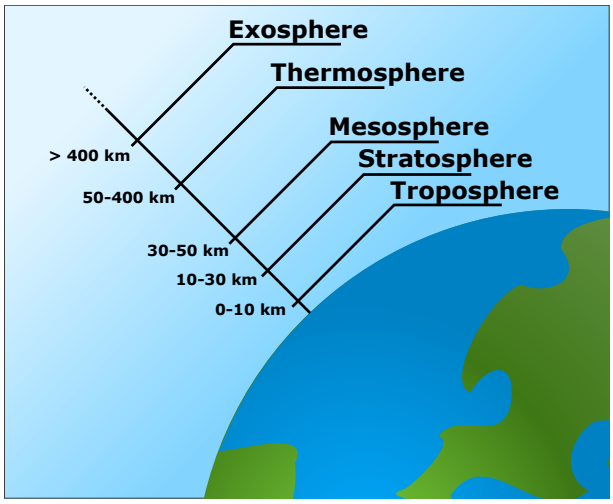

Figure 3.1: Illustration of the Earth's atmosheric layers (Bredk, 2007).

low pressure regions. As the Earth rotates, this motion is subject to the Coriolis-force which rotates the wind velocity vector until it is orthogonal to the pressure gradient and the opposing forces of Coriolis-force and pressure gradient force cancel each other. This means that – neglecting surface friction, as is appropriate in the free troposphere – winds follow isobaric lines and follow a circular motion around low-pressure regions. On the Northern Hemisphere, this motion will be counter-clockwise, and clockwise on the Southern Hemisphere. Moving low-pressure regions are also called cyclones, for this reason.

When a cyclone forms, there usually forms a sharply bounded section of cold air moving around it at high velocity. This is the so-called cold front. When a cold front enters a region of stable warm air, it will induce strong lifting as the dense, cold air moves below the thin, warm air and forces it upwards. As the warm, moist air rises and cools off, it is likely that it will reach a state above the dew point and clouds start to form which may lead to strong rain fall.

The warm air forms a band that leads upwards to the center of the cyclone. It enables transport from the planetary boundary layer to the free troposphere and is thus called a warm conveyor belt (WCB) (Browning, 1999).

Cyclones are also usually accompanied by a warm front preceeding the cold front. The warm front travels slower than the cold front and will eventually coalesce with it, leading to an occluded front where warm air resides above the cold air near the surface.

Global atmospheric convection can be described with three major circulation patterns on each Hemisphere. The radiative flux per surface area is largest near the equator, with the exact latitude changing seasonally. There, air near the surface heats up quickly and rises in deep convection to higher atmospheric layers, leading to clouds and heavy rain in the tropics. This air then moves away from the equator as new air follows in convection. Due to the Coriolis-force, this warm, elevated air follows a cruved motion towards the north-west and south-west on the Northern and Southern Hemisphere, respectively. The

air will cool down, until eventually it is dense enough to sink down. Upon sinking, the dry air will heat up, thereby taking up moisture from the surface. This leads to the agglomeration of deserts around $30°N/S$. The (relatively) cold, dense air near the surface then travels back towards the equator, on a trajectory bent towards the south-east and north-east on the Northern and Southern Hemisphere, respectively. This leads to typical easterly surface winds called Trade Winds. This tropical large-scale convection is called the Hadley cell.

Another, similar cell forms between the Arctic circles and the respective Poles. Between these cells, heat is exchanged by transport of cold and warm air masses in cyclones and anticyclones, respectively. The more prominent cyclones typically travel towards the north-east on the Northern Hemisphere (south-east on the Southern Hemisphere). At the interface of this third and the second cell, drastic temperature differences lead to a phenomenon called the polar jet stream. This is a narrow (a few hundred kilometers wide) area of strong easterly wind, at altitudes of 7–12 km. This jet stream is routinely used to accelerate air travel and can also accelerate plumes of polluted air in long-range transport events, if they arrive at these altitudes and latitudes. Another jet stream can be found between the Hadley cell and the second cell. This subtropical jet stream is much weaker than the polar jet stream.

All of these phenomena apply symmetrically to both the Northern and Southern Hemisphere.

3.2 Concept

Long-range transport (LRT) describes the process that trace gases emitted in one region are transported over long distances to remote regions. These transports can bridge distances of several thousand kilometers. They lead to an effective relocation of polluted air to pristine regions. Thus, for pollutants that are subject to long-range transport, air quality and air pollution have to be treated as gobal instead of local phenomena.

Most emissions of pollutants take place near the surface, in the planetary boundary layer. Long-range transport is not likely to occur there, due to low wind speeds. This means that – in order for long-range transport to happen – there needs to be an efficient mechanism to lift the trace gas from the planetary boundary layer into the free troposphere, where wind speeds are much higher. This is especially true for highly reactive or unstable species, which have a short lifetime. For the most short-lived species, anomalously high wind speeds are required to transport them over significant distances during their lifetime – these might occur in the context of a cyclone, for example – while stable or longer-lived species can also be long-range transported via slow diffusive processes.

Not only are wind speeds higher in the free troposphere; as detailed in Section 2.1, NO_2 lifetime is greatly increased above the boundary layer. This is a crucial factor to allow long-range transport of NO_2.

The convective processes neccessary for NO_2 long-range transport are also likely to lead to the formation of clouds as surface air rises almost adiabatically and, eventually, reaches its dew point. It is thus expected that such events are usually linked to cloud formation. Studies of transported NO_2 plumes will therefore have to take the effects of clouds on observations into account.

As cyclones are not locally bound but rather follow a – usually eastward – trajectory, they can efficiently relocate long-lived species which are lifted up upon the passing of the cold front and follow the cyclone on its course.

Effectively, long-range transport can transport atmospheric pollution from emission regions to remote regions, which drastically impacts otherwise pristine regions where little to no emissions take place. There, even small amounts of reactive or catalyzing species may alter atmospheric chemistry. As atmospheric chemistry is often non-linear this may lead to drastically different chemical compositions.

If NO_2 is transported to a region that emits large amounts of biogenic VOCs, this may potentially trigger ozone production and lead to a chain of other pollutants as byproducts. In this way, NO_2 may act as a catalyst.

Note that if NO_2 concentrations reach very high levels, this may halt O_3 production. Pollution hotspots with exceptionally high NO_2 concentrations will therefore not be so drastically affected by additional NO_2 that is long-range transported there.

NO_2 long-range transport events may release more NO_2 to their destinations' atmosphere than is apparent from observations of the NO_2 content of the plumes during transport – not only due to the NO content that is invisible to satellite observations. For example, PAN may decompose upon descending onto a long-range transport's downwind region, leading to a rapid increase in NO_2 concentrations. Other reservoir species might also reconvert to NO_2 if they reach an air mass with sufficient concentrations of radical species or are subject to increase of temperature and pressure (Singh and Hanst, 1981a; Schultz et al., 1998; Walker et al., 2010). This leads to an additional, effective relocation of NO_2 from emission to downwind regions.

This study will show that the distances covered by long-range transport can reach up to several thousand kilometers, bridging oceans, and the horizontal extent of long-range transport plumes can reach more than 1000 km. Due to this large horizontal extent, plumes are subject to shear inside the cyclones that usually trigger their emission, which often – but not always – will lead to typical arc-like structures and filamentation of long-range transport plumes.

3.3 Relevance

The interest in the study of atmospheric long-range transport is increasing in the last years. While it does not have the drastic worldwide impact of global warming, it can still affect individual, sensitive regions drastically. Local emission legislations are powerless against the impact of pollution from long-range transport on air quality and their local ecosystem. Therefore, not only the emission of stable species that affect the global climate is of global political concern, but also the emission of transported, short-lived pollutants that have an impact on the planetary boundary layer (or the surface, e.g. in the case of acid rain).

NO_2 is a toxic trace gas that can lead to respiratory diseases. In the planetary boundary layer, it enhances ozone production, leading to severe health problems and affecting the ecosystem, for example by reducing crop yield and leading to smog episodes. Besides that, NO_2 can be washed out of the atmosphere in the form of nitrous acid (HNO_3), solved in water droplets. This will lead to acid rain. Since sulfur filters were

introduced in European factories, nitrous acid is the major contributor to acid rain, ahead of sulfic acid (Galloway and Likens, 1981).

For NO_2, the dominant perception is that emissions stay localized – with a few exceptional long-range transport events – and are thus of no relevance to other regions, making NO_2 emission regulations a local concern, only. However, this is not the case and NO_2 is regularly relocated from major emission regions to pristine regions over the ocean and to other continents, as this work will show. While most long-range transport events dissolve due to chemical conversion, physical dispersion and filamentation before they reach another shore, they will relocate NO_2 to the oceanic atmosphere and some events will reach other continents due to the sheer number of plumes emitted over the course of a year.

Arctic Haze is a phenomenon that occurs for a few decades now (Shaw, 1995). This haze contains condensed particles and shows a significant amount of sulfates and nitrates (Quinn et al., 2007). It is most likely a phenomenon that is triggered by external pollution which activates chemistry in the sensitive Arctic atmosphere. Some fraction of Arctic Haze could be explained by transport of aerosols and reactive species such as NO_2 from Europe and Asia as NO_2 can easily react with ozone during Arctic Winter to form nitrate.

3.4 Previous studies

There are a number of satellite based case studies of individual events of NO_2 long-range transport. Wenig et al. (2003) report the first observation of such an event, a plume emitted from South Africa in May 1998. In their study, a high-pressure system favored a localized build-up of NO_2 concentrations which were then rapidly lifted to an altitude of 2–6 km above mean sea level (a.m.s.l.) by a passing low-pressure system. There, longer lifetime and higher wind speeds allowed the NO_2 to travel onto the open ocean.

Stohl et al. (2003) investigated an episode in which an explosively developing cyclone transported a significant plume of NO_2 over the Atlantic in about one day. The NO_2 was lifted upwards by a warm conveyor belt (WCB). In a climatological study, they find "intercontinental express highways" between North America and Europe which are much stronger in winter and can contribute about 2–3 pptv of European NO_2 concentrations during winter. This value is small compared to concentrations in emission hotspots which can reach up to $\approx 1\,\mathrm{ppbv}$. However, in unpolluted regions this may already contribute a significant fraction of total NO_2 concentrations.

Schaub et al. (2005) discuss an event during which NO_2 from the central German Ruhr area was lifted into the free troposphere (over the course of a day) and transported into the Alps where a significant increase in concentrations was measured in-situ on the Zugspitze and on multiple sites in Switzerland.

Studies by Spichtinger et al. (2001) and Riuttanen et al. (2013) illustrate further aspects of individual, observed transport events.

Unfortunately, there are – to my knowledge – no in-situ measurements of tropospheric NO_2 long-range transports by aircraft which would allow us to determine typical vertical concentration profiles and verify the results of this study with non-satellite observations.

Lin et al. (2010) have focussed on modeling NO_2 long-range transport with global

chemical transport models (GCTMs). They find that 8–15 % of NO_x emissions are transported over 1000 km from their source regions, using WRF-Chem (Weather Research and Forecasting model, chemistry, Michalakes et al., 2001) and CMAQ (Community Multi-scale Air Quality model, Byun et al., 1999) for rapid vertical transport and MOZART (Model for OZone And Related chemical Tracers, Emmons et al., 2010) as GCTM. They also note that in most GCTMs, rapid convection (such as in frontal passages) is not adequately represented, which biases the simulation of long-range transport events. The modeling of horizontal transport tends to dilute the plumes' boundaries, which are found to be rather sharp in observational data.

Heckel et al. (2005) found that there are elevated NO_2 levels in GOME and SCIAMACHY satellite measurements over the Atlantic Ocean, following the typical storm tracks between North America and Europe. These appear to be caused by long-range transport of NO_2 and occur at least weekly during winter and less frequent during the other seasons. This study suggested that long-range transport of NO_2 might be a common phenomenon and led to the study presented in this thesis.

So far there has – to my knowledge – not been a systematic study of NO_2 long-range transport events using global observational data. Such studies are necessary in order to judge the impact of NO_2 long-range transport on the atmospheric chemistry in pristine and sensitive environments such as the Arctic and to validate its impact as estimated from GCTMs.

4 GOME-2 satellite data

In-situ and local remote sensing observations are a valuable source of scientific data about our Earth's atmophere. They provide the most precise data for case studies and the study of local phenomena. However, to monitor the Earth's atmosphere globally and over long periods of time, satellite-borne remote sensing instruments are the only viable option. Observations from satellite are inevitably far less fine spatially resolved and less frequent than local measurements, but a single instrument can cover the entire globe in continuous operation for more than a decade. If the observation of the desired quantity is possible via satellite, this makes these instruments the first choice to study regional and global phenomena.

For this study, I have used remote sensing observations from the GOME-2 (Global Ozone Monitoring Experiment-2) instrument (Callies et al., 2000) aboard the MetOp-A (Meteorological Operational satellite programme[1], satellite *A*) meteorological satellite.

4.1 Differential optical absorption spectroscopy

Any information on global NO_2 concentration distributions in the atmosphere currently has to be obtained from remote sensing, as in-situ observations cannot cover sufficient fractions of the globe.

One remote-sensing technique used to obtain information on trace gas concentrations in the atmosphere is the so-called Differential Optical Absorption Spectroscopy (DOAS; Solomon et al., 1987; Platt and Stutz, 2007). In the DOAS technique, high-frequency variations in spectral absorption measurements are used to infer the optical depth of a trace gas of interest. Via the absorption cross-sections from laboratory measurements, it is possible to deduce the column density of the trace gas from its optical depth. This serves as a first indication of trace gas total amounts.

In the DOAS technique, two spectra of light intensity are recorded: the signal spectrum $I(\lambda)$ and the reference spectrum $I_0(\lambda)$. The signal spectrum contains the absorption signal of the trace gas of interest, determined by its absorption cross section σ and its slant column-density SCD, which indicates the total amount of this trace gas that could absorb radiation on path from its source to its observation. The reference spectrum is assumed to be the radiative spectrum without any absorption from trace gas in the Earth's atmosphere in the spectral region of interest. The DOAS equation is thus a special case of the Beer-Lambert law:

$$\ln \frac{I_0(\lambda)}{I(\lambda)} = \sum_{j=1}^{J} \sigma'_j(\lambda) \cdot \mathrm{SCD}_j + \sum_{p=0}^{P} a_p \cdot \lambda^p \tag{4.1}$$

[1] `http://www.esa.int/Our_Activities/Observing_the_Earth/The_Living_Planet_Programme/Meteorological_missions/MetOp/Overview14`

J denotes the set of chemical species j that affect the total absorption spectrum, with

$$\sigma'_j(\lambda) = \sigma_j(\lambda) - \sum_{p=0}^{P} b_{j,p} \cdot \lambda^p \tag{4.2}$$

as the high-variability part of the absorption cross-section for each chemical species, that quickly changes with photon wavelength. Here, $\sigma_j(\lambda)$ is the full spectrum of species j while $b_{j,p}$ are the coefficients of a polynomial function of wavelength, describing the low-variability part of j's spectrum.

In Equation 4.1, a_p then denote the fitted P^{th}-order polynomial of the low-variability part of the full absorption spectrum.

This approach removes all the low-variability-parts from both the observed absorption spectrum and the species' laboratory absorption spectra, leaving only characteristic high-variability features of each species. These can be fitted much more precise than the entirety of the spectrum in which atmospheric and surface scattering introduce low-variability features – not easily distinguishable from absorption – that are hard to model adequately.

In satellite observations, typically, the reference spectrum is a direct observation of the solar spectrum. The signal spectrum is an observation of a location of interest on the Earth's surface. It measures the earth-shine: the solar radiation that is backscattered from surface and atmosphere of the Earth. Thus, the signal spectrum will inherit the shape of the reference spectrum and show features from absorption, scatter and emission of atmospheric and surface constituents (Figure 4.1). Typically, the Earth shine is composed of light that was:

- scattered by the surface
- scattered by a single air molecule (single scattering)
- scattered by multiple air molecules and/or the surface once or multiple times (multiple scattering)

From these two spectra, a relative absorption spectrum $s(\lambda)$ can be obtained as

$$s(\lambda) = \frac{I(\lambda)}{I_0(\lambda)}. \tag{4.3}$$

This spectrum is the result of interactions of the reference spectrum with particles in the atmosphere, the ground, the ocean, vegetation and more.

With the absolute values of the NO_2 cross-section, we can then compute the slant column-density (SCD) of NO_2 using the Beer-Lambert law:

$$s(\lambda) = 1 - e^{-\int_{L(\lambda)} \sigma(\lambda) n(l) \mathrm{d}l}, \tag{4.4}$$

with the laboratory absorption cross-section $\sigma(\lambda)$, and the trace gas concentration $n(l)$ along the light path L. Assuming that absorption does not fully deplete the incoming radiation – we do not experience saturation effects and the term in the exponential function is small – we can approximate this as:

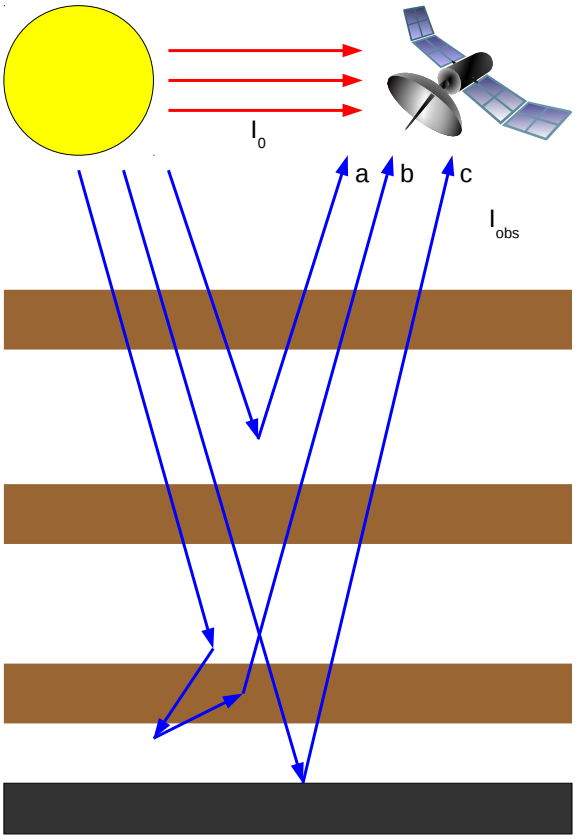

Figure 4.1: Typical observation geometry with a satellite instrument observing in nadir direction. It observes the Earth Shine (I_{obs}), the solar radiation scattered back towards the instrument by the Earth's surface and atmosphere. Typical light paths for consideration are (a) single-scattering, (b) multiple-scattering and (c) direct reflection off the surface. To determine the observed trace gases (indicated as brown clouds), the solar irradiation above the atmosphere is also measured (I_0).

$$s(L,\lambda) \approx \int_{L(\lambda)} \sigma(\lambda) n(l) \mathrm{d}l \tag{4.5}$$

$$= \sigma(\lambda) \int_{L(\lambda)} n(l) \mathrm{d}l. \tag{4.6}$$

From this equation we can determine the so-called slant-column density SCD, the trace gas concentration integrated along the light-path:

$$\mathrm{SCD}(L) = \int_L n(l) \mathrm{d}l \tag{4.7}$$

This slant-column density SCD forms the basis for all further analysis and gives an indication of the NO_2 concentrations at the point of observation, taking the local light-path for the wavelength of interest into account. The SCD can be set in relation to the Vertical Column Density (VCD) – the trace gas concentration integrated vertically from surface to space:

$$\mathrm{SCD}(\lambda) = \mathrm{VCD} \cdot \mathrm{AMF}(\lambda), \tag{4.8}$$

where AMF is the so-called air-mass factor, relating SCD and VCD. While the VCD describes the amount of trace gas that radiation passes on a straight path from surface to space, the SCD describes the amount of trace gas that radiation passes in an actual observational geometry. This quantity is dependent on wavelength, as the light-path will vary with wavelength. The AMF relates these two quantities and is also dependent on wavelength. Usually, the AMF is calculated from radiative transfer modeling.

The errors of assuming the same light path for all radiation in the selected spectral band is negligible, if a representative wavelength for light-path calculations and a sufficiently narrow wavelength window are used.

In principle, it would be possible to determine the trace gas column density along the light path by fitting its laboratory absorption spectrum to the full absorption spectrum $s(\lambda)$. This is limited, however, by the dependency of the light-path on the wavelength of the light. For nadir observations – where the light-path has to be modeled – light in different wavelengths can take drastically different paths from the sun to the satellite instrument which prohibits a retrieval of absorbing species in a broad window.

Therefore, we first select a fitting window $\lambda_{\min} \leq \lambda \leq \lambda_{\max}$ that encompasses the most prominent and discerning spectral features of the trace gas of interest with as little specral interference as possible from other species.

To remove the broad-band absorption or scattering features of the surface as well as the atmosphere and its constituents, we consider only the high-frequency absorption features by fitting the local spectrum with a low-order polynomial, typically of fourth to sixth order. In this study, we obtain the NO_2 fit using a sixth-order polynomial. This leaves us with a small segment of the absorption spectrum in which all slowly varying features are removed, leaving only localized absorption features (Figure 4.2 and Figure 4.3).

We now fit the spectrally localized absorption features of the trace gas of interest to the resulting fast-varying spectrum in the fitting window, along with species interfering

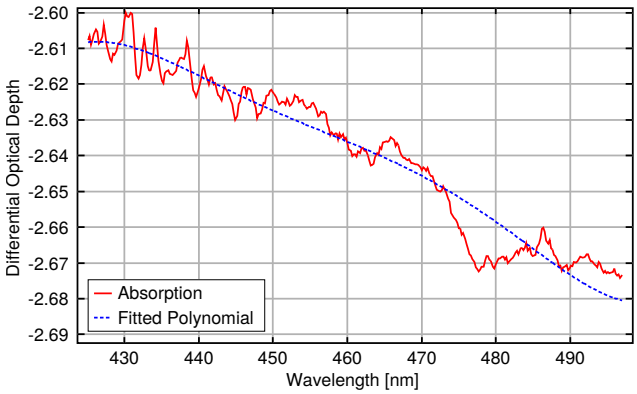

Figure 4.2: Polynomial fit for an observation on 2010-10-02T10:28:07 UTC over the North Sea during a long-range transport event. Broader absorption features that extend over about 10 nm are removed from the signal, while characteristic absorption features are retained.

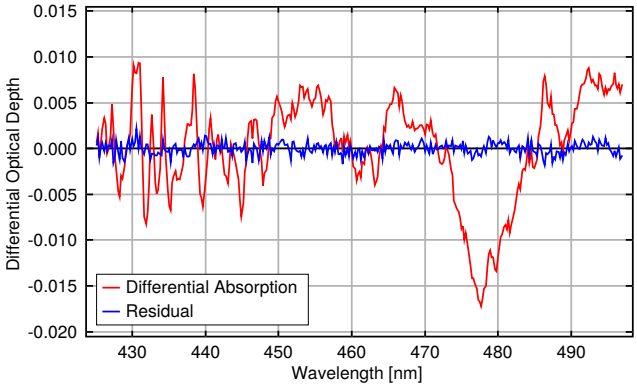

Figure 4.3: Differential absorption spectrum (red) for the scene from Figure 4.2, after the polynomial fit shown therein is subtracted. The blue line shows the residual spectrum that could not be attributed to a trace gas or atmospheric effect after all fits have been performed and can be attributed to noise in the signal, instrumental effects and uncertainties in the atmospheric composition.

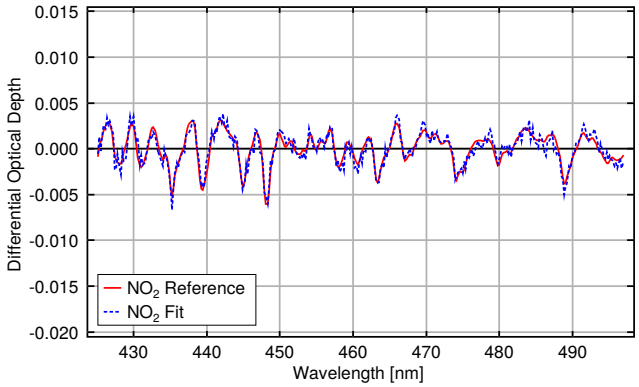

Figure 4.4: Sample NO_2 fit for the polynomial-removed scene from Figure 4.2. The NO_2 fit is composed of the scaled reference spectrum and the fit residual – the part of the asorption spectrum that could not be explained by other trace gases and known effects. The fit residual is small in comparison to the absorption signal of interest.

in that spectral range. For NO_2, we use a fitting window of $425\,\text{nm} < \lambda < 497\,\text{nm}$. The interfering species and other spectral contributions whose spectra are fitted alongside the NO_2 absorption spectrum are O_3, $O_2 \cdot O_2$, liquid water and water vapour. Additionally, the Ring spectrum (Grainger and Ring, 1962) – accounting for rotational Raman scattering – and an intensity offset – taking stray light inside the instrument into account – are fitted to the observed absorption spectrum. This fitting process yields the full absorption spectrum of NO_2 in direction of observation.

In Figure 4.4 a sample DOAS-fit for NO_2 in the used fitting window is shown. Fits for O_3 (Figure 4.5), $O_2 \cdot O_2$ (Figure 4.6) and the Ring spectrum (Figure 4.7) are also shown.

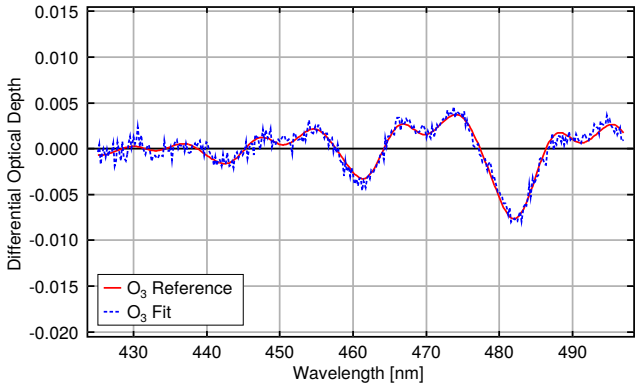

Figure 4.5: Spectral fit of O_3 analogous to Figure 4.4.

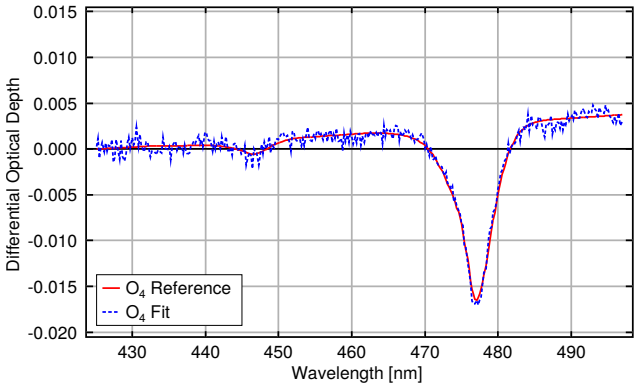

Figure 4.6: Spectral fit of $O_2 \cdot O_2$ analogous to Figure 4.4.

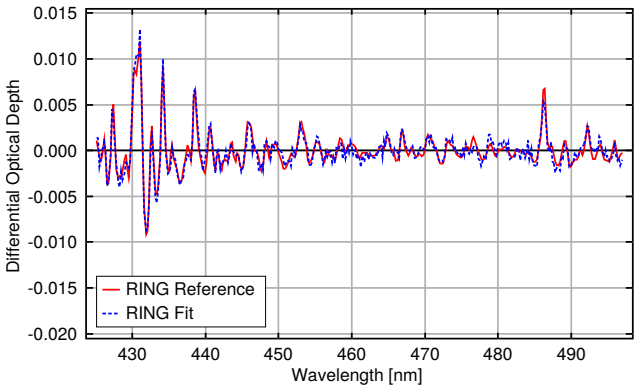

Figure 4.7: Spectral fit of the Ring spectrum analogous to Figure 4.4.

Figure 4.8: Illustration of MetOp-A in orbit. Picture: ESA - AOES Medialab.

4.2 GOME-2

This study uses data from the GOME-2 / MetOp-A (Global Ozone Monitoring Experiment 2 aboard MetOp-A) instrument as observational data. GOME-2 are a set of three satellite-borne instruments aboard the MetOp satellites, operated by EUMETSAT[2] (European Organisation for the Exploitation of Meteorological Satellites). For this study, I used data from the GOME-2 I instrument aboard MetOp-A (Callies et al., 2000). This is the first instrument of the series. MetOp-A was launched 19 October 2006. GOME-2 / MetOp-A started operation on 04 January 2007 and continues operation up to the point of this writing.

MetOp-A (Figure 4.8, Figure 4.9) is a meteorological satellite in a sun-synchonous orbit around the Earth at an altitude of 817 km a.m.s.l.. A sun-synchonous orbit is a near-polar orbit; the satellite crosses the Earth's surface roughly from North to South and vice versa, slightly missing the poles. If adjusted correctly, this allows the satellite to cross the Equator always at the same local time. This is ideal for spectroscopic observations and for observations focussed on atmospheric chemistry as it allows for well-illuminated and comparable observational scenes, respectively. The local time will vary slightly towards the mid-latitudes – with earlier local times on the Northern Hemisphere and later times on the Southern Hemisphere – and strongly towards the poles. There are two possible orbits that fulfill this criterion: one, where eventually the orbit changes from ascending node during night to descending node during the day near the North Pole and vice versa near the South Pole; and one orbit with ascending and descending node switched.

The orbital period of MetOP-A amounts to 101 minutes which results in a little more than 14 orbits each day. The same orbits repeat after a cycle of 412 orbits. Together with the swath width of 1920 km across-track the orbital period leads to a near-global

[2] `http://www.eumetsat.int/`

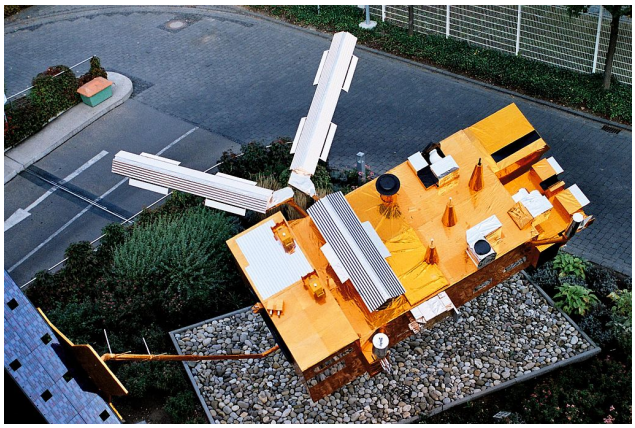

Figure 4.9: Model of MetOp in front of the EUMETSAT building in Darmstadt. Photo: Wikipedia user Ysangkok.

daily coverage. Only in the tropics, GOME-2 / MetOp-A data show small strips of data gaps between consecutive orbits. This leads to missing information in global maps of daily aggregated data. Due to lighting conditions, GOME-2 / MetOp-A cannot measure over the pole in local winter.

The GOME-2 / MetOp-A instrument uses a mirror to reflect sun- and Earth-shine into its spectrometers. The mirror is rotated to observe the Earth in nadir direction (pointing in the direction of the Earth's center) in a sweeping-broom pattern (tilting across-track) and to observe direct solar radiation as the reference spectrum. In the GOME-2 / MetOp-A instrument, four channels cover a spectral range of 240–790 nm with a spectral resolution of 0.44–0.53 nm in the spectral window for the detection of NO_2 (425–497 nm). In normal operation, GOME-2 / MetOp-A obtains 24 ground-pixels per swath in its forward scan (first part of the sweep), with only three pixels for the backscan (second part of the sweep). Backscan pixels are not used in this study. The surface extent of GOME-2 / MetOp-A pixels is $80 \times 40\,\mathrm{km}^2$. The integration time for forward scan pixels is 0.1875 s. See Table 4.1 for more details.

This daily near-global coverage and the continuous operation for many years gives a comprehensive and consistent data set for the study of global trace gas concentrations.

As becomes apparent from Table 4.1, the horizontal resolution of GOME-2 / MetOp-A is rather coarse. This does not present a problem to this study, as NO_2 long-range transport events can exhibit horizontally extended plumes of gas that can easily reach a longest diameter of 1,000 km or more, as this study will show. Thus, a medium-sized single plume may be covered by up to 200 individual measurements. Small-scale spatial features of long-range transport plumes cannot be observed with GOME-2 / MetOp-A, but the large-scale shape and its evolution are clearly visible at this resolution. The scale of long-range transport plumes is large enough that we will grid the satellite data to a regular $0.5° \times 0.5°$ grid in latitude-longitude direction. This will lead to verified plumes covering between 2 and about 2000 grid cells.

GOME-2 / MetOp-A receives a single spectrum for each section of the atmosphere it observes. While – due to the intricacies of radiative transfer – this spectrum does not

Table 4.1: Specifications of the GOME-2 / MetOp-A satellite instrument used for this study (from `http://www.esa.int/Our_Activities/Observing_the_Earth/The_Living_Planet_Programme/Meteorological_missions/MetOp/Performance10`).

Spectral range [nm]	240–790
Angular pixel size [°×°]	0.286° (across track) × 2.75° (along track)
Surface pixel size [km × km]	80 × 40
Pixels across track	24
Pointing accuracy [km]	2
Integration time [s]	0.1875
Orbital period [s]	6060
Ground track repeat cycle	29 days / 412 orbits
Mean altitude [km]	817
Orbital eccentricity	≈ 0

directly relate to the amount of trace gas within the viewing direction of the instrument, it is apparent that this data can only determine the location of a trace gas in horizontal coordinates. After the DOAS-fit (Section 4.1), the data have become 2-dimensional maps of NO_2 slant-column densities.

There are efforts made (Richter et al., 2014; Hilboll et al., 2014) to extract some information on the vertical distribution of the trace gas from the spectrum. To this end, NO_2 slant-column densities at different wavelengths are compared. This provides some information on the vertical distribution of the NO_2. However, this is still a work-in-progress and not yet implemented for the used data set. I thus base my study on 2-dimensional data without any information on the vertical distribution of NO_2.

4.3 Radiative transfer

For DOAS measurements, we use the solar spectrum above the Earth's atmosphere as a reference spectrum. The solar spectrum can be approximated as a Planck-spectrum with a black-body temperature of $T_\odot \approx 5780\,\mathrm{K}$ with absorption lines – the so-called Fraunhofer lines (Fraunhofer, 1817) – from gas in the outer gas layers and the solar corona.

When this radiation enters the Earth's atmosphere, it is subject to a variety of radiative processes. Ultimately, a fraction of the incoming light will be scattered back into space where a satellite can measure it in a spectrometer. This so-called Earth-shine is composed of the reference spectrum and the effects of radiative processes in the atmosphere, such as absorption, scattering and emission. This process is called radiative transfer – the evolution of an incoming spectrum to an outgoing spectrum when passing through a volume.

In the observation of Earth-shine in the UV/visible part of the electromagnetic spectrum, for most purposes it is enough to consider the effects of atmospheric gases, the surface albedo[3] and clouds (if present). Depending on the observational scenario, it can

[3]More precisely: the spectral surface reflectance. In this study, I will use the term albedo for simplicity,

be neccessary to take radiative transfer in the ocean, effects of vegetation, aerosols in the atmosphere and spectral absorption or full radiative transfer in the surface into account. For the global analysis in this study, I will only take the basic effects into account: gases, albedo and clouds.

When solar radiation enters the Earth's atmosphere, it is subject to a wide range of effects, depending on its constituents. The radiation is Rayleigh-scattered by the gas in the atmosphere. For scattering on gas, the Rayleigh approximation is sufficient as scattering particles are of much smaller diamater $d \lessapprox \lambda/10$ than the scattered radiation. In our case ($\lambda > 400\,\mathrm{nm}$) this translates to a particle size below 40 nm. The strength of Rayleigh-scattering is strongly dependent on the wavelength λ of the scattered light and the particle diameter d, with the Rayleigh scattering cross-section:

$$\sigma_s \propto \frac{d^6}{\lambda^4} \tag{4.9}$$

In a typical atmospheric scenario, radiation in the visible spectral range will be scattered once or only be reflected off the surface. However, especially in the dense atmosphere near the surface, a photon may be scattered multiple times before being finally absorbed or emitted back to space. Elastic scattering, especially multiple scattering, leads to a loss of directional information of the radiation while preserving the wavelength.

Gas in the atmosphere does not only scatter but also absorb radiation. The absoprtion is strongly dependent on the present gas species, their concentration and their absorption spectra. The typical strength of absorption in the visible range will be below 10 % except for highly polluted regions, which usually also feature high aerosol densities. Absorbed photons are typically removed entirely from the spectral range of interest – their energy is re-emitted at higher wavelengths. As the constituents of the atmosphere have typical absorption spectra, each present species will imprint its characteristic absorption onto the solar spectrum before it is measured.

Larger particles – aerosols and water droplets – cannot be treated via Rayleigh-scattering any more. Here, we have to employ Mie-scattering (Mie, 1908) which treats scattering (and absorption) of light on particles that are of a size larger than the wavelength of interest. Mie-theory is a complex field of study. In our calculations, we use predetermined scattering functions from a database, parameterized in Legendre polynomials.

Another key component in modeling radiative transfer is the surface with its absorption and scattering properties. In this study, we have used a lambertian reflector with an isotropic albedo as model for the surface. This means that the intensity of the radiation scattered into a direction of angle ϑ when irradiated from an angle ϕ, $I(\vartheta, \phi)$ from the surface's normal vector will be equal to

$$I(\vartheta, \phi) = I_{\mathrm{irradiation}} a \cos\vartheta \cos\phi, \tag{4.10}$$

regardless of the azimuth. Here, $I_{\mathrm{irradiation}}$ is the intensity downwelling towards the surface. $I_{\mathrm{normal}} = I_{\mathrm{irradiation}} \cos\phi$ is the irradiation emitted in direction of the surface normal vector. In satellite observations, the observation angle ϑ is usually close to 0 °

which actually refers to the spectral surface reflectance averaged over all wavelengths.

(nadir direction), which effectively removes this term from Equation 4.10, leaving only the incidence angle ϕ as geometrical variable.

$$I_{\text{nadir}}(\phi) \approx I_{\text{irradiation}} a \cos\phi, \tag{4.11}$$

The total amount of radiation scattered back by the surface is determined by the surface's albedo a with

$$I_{\text{scatter}} = a I_{\text{irradiation}} = a I_{\text{extinction}}. \tag{4.12}$$

Here, $I_{\text{extinction}}$ is the total amount of radiation which interacts with the surface via scatter or absorption. As the surface is fully opaque and does not transmit any radiation, this is equal to $I_{\text{extinction}}$.

Water droplets in clouds can have a dominating impact on radiative transfer. Opaque clouds have a high albedo and only very little radiation passes through them to lower atmospheric layers; even less is then transmitted back towards space, where the satellite can observe it. This means that clouds have a strong shielding effect – they effectively block trace gases in lower atmospheric layers from absorbing light in the observed spectrum and thus inhibit their detection. The high albedo of clouds will also lead to a strong impact of trace gas directly above the cloud on the observed spectrum, due to enhanced multiple scattering. Inside the clouds, light paths can be significantly elongated and photons are likely to be scattered tens, hundereds of times or more (Wagner et al., 1998).

To model the radiative transfer – the propagation of a spectrum of light from the sun entering the Earth's atmosphere and being observed from satellite – all of these factors are integrated into a radiative transfer model. For this study, we use SCIATRAN 3.1, a sophisticated model that can model a wide variety of scenarios of radiative transfer (Rozanov et al., 2014). SCIATRAN 3.1 uses a numerical approach to solve the radiative steady state problem and calculate absorption and scattering on atmospheric levels.

SCIATRAN 3.1 takes into account the effects of Rayleigh-scattering, multiple trace gases, clouds, surface properties, incoming solar spectra, aerosols, oceanic interaction and more. It can operate in planar, spherical and pseudo-spherical mode. In pseudo-spherical mode, the atmosphere is treated as spherical for the initial downwelling radiation. All scattering and re-emission towards space is modeled in a planar geometry. For our analysis, we have only used the modeling of Rayleigh-scattering, multiple-trace gases, surface albedo and elevation, and clouds in a pseudo-spherical mode using a scalar discrete ordinate method.

In radiative transfer simulations, we take the trace gases O_3, NO_2 and $O_2 \cdot O_2$ into account.

The altitude grid used for this study is denser near the surface, where tropospheric NO_2 is located and (multiple) scattering is strongest. In case of clouds, there is an additional fine subgrid within the cloud to capture the intense interactions of radiation with abundant water droplets.

Clouds of interest in this study will most likely be water clouds and we employ a scattering function that is based on water droplets of diameter 16 μm. Inside the cloud, the vertical grid is highly refined, with 100 layers instead of less than ten in abscence of the cloud. The optical thickness is distributed evenly over the entire cloud with the

exception of its boundaries, where the optical thickness per altitude decreases exponentially to allow for a smoother transition between the cloudy and cloudfree domain of radiative transfer. We use an optical thickness of $\tau = 50$ for this study as we are mostly interested in thick but not entirely opaque clouds.

We use two kinds of radiative transfer simulations in this study: calculations of a scene's reflectivity at 437.5 nm wavelength and calculations of a scene's NO_2 air-mass factor (AMF). The effect of misjudging the optical thickness of clouds, by setting it to a constant value of 50, will partly be mitigated by the fact that both the cloud fraction – the fraction of a satellite instrument pixel affected by clouds – and the NO_2 air-mass factor are determined for an optically thick cloud.

When calculating reflectivities, SCIATRAN 3.1 calculates the fraction of radiation of a particular wavelength λ that is reflected back into space $I_\uparrow(\lambda)$ to the total amount of irradiation of the scene $I_\downarrow(\lambda)$.

$$R(\lambda) = \frac{I_\uparrow(\lambda)}{I_\downarrow(\lambda)} \tag{4.13}$$

The air-mass factor relates the observed slant-column density to the vertical column density (VCD), which is easier to interpret. In Equation 4.7 we obtained the local slant-column density from GOME-2 / MetOp-A spectral observations via a DOAS analysis. This is the total amount of trace gas that is neccessary to explain the absorption features in the measured spectrum. It can be approximated as the product of absorption coefficient σ and the trace gas concentration ρ integrated along the light path.

This light path, however, is not a single line, but an integral of of light paths for infinitesimal fractions of the total observed intensity. Thus, it is hard to interpret this value on its own; we have to consider the radiative transfer that led to this absorption. Then, we can convert the slant-column density to the vertical column density, which is far easier to interpret: it is the total column density of the trace gas from the surface to the top of atmosphere (ToA).

$$\mathrm{VCD} = \int_{\mathrm{surface}}^{\mathrm{ToA}} \rho(h)\mathrm{d}h \tag{4.14}$$

The air-mass factor is then simply a scale factor that relates slant-column density and vertical column density:

$$\mathrm{AMF}(\lambda) = \frac{\mathrm{SCD}(\lambda)}{\mathrm{VCD}} \tag{4.15}$$

The air-mass factor can be pictured as the average light path elongation in the atmosphere, weighted by the local trace gas mixing ratio. When observing the surface in nadir direction and neglecting scattering in the atmosphere, the air-mass factor in a plane-parallel scenario will amount to:

$$\mathrm{AMF} = 1 + \frac{1}{\cos\ \mathrm{sza}}, \tag{4.16}$$

where sza is the solar zenith angle, the angle between the surface's normal vector and the direction of solar irradiation. When the sun is at the zenith (in the back of the

satellite), the air-mass factor will amount to 2 – each trace gas molecule is passed twice, once before and once after reflecting on the surface.

The air-mass factor is dependent on various atmospheric parameters. Especially, it depends on the vertical distribution or vertical profile of the trace gas of interest. Neglecting saturation – which is a valid approximation under all but the most polluted scenes – it is possible to simplify the dependency on the trace gas profile and derive an altitude-dependent air-mass factor, the so-called Block Air-Mass Factor (BAMF).

This block air-mass factor denotes the sensitivity of the observational scenario to a trace gas at a given altitude. By integration, the block air-mass factor can be related back to the air-mass factor for a trace gas g:

$$\mathrm{AMF}_g(\lambda,\, \mathrm{sza}) \approx \int_{\mathrm{surface}}^{\mathrm{ToA}} n(h)\mathrm{BAMF}_g(\lambda, h,\, \mathrm{sza})\mathrm{d}h \tag{4.17}$$

This approximation is valid for non-saturated absorption. In the case of saturation, radiation might not reach lower atmospheric layers or additional absorption might reach the non-linear regime. Fortunately, it is easy to check the valitidity of the assumption by computing the air-mass factor and vertical column density for a given scenario and converting it to an optical depth S:

$$S(\lambda) = \mathrm{AMF}(\lambda)\mathrm{VCD}\sigma(\lambda) \tag{4.18}$$

For an optical depth $S \ll 1$, this approximation is valid.

Both the air-mass factor and block air-mass factor are a function of the wavelength λ of observation and might vary drastically depending on the presence of absorbing species, trace gases, and presence of water droplets or aerosols.

In operational data, I use look-up tables (LUT) to retrieve the reflectivities and air-mass factors for a satellite scene. In these LUTs, I have computed the reflectivity and air-mass factor for a broad spectrum of scenes of varying solar zenith angle sza, viewing angle va, relative azimuth of viewing and solar zenith angle azi, surface albedo a and surface elevation (see Table 4.2). I will then linearly interpolate between the 2^5 points of this regular grid to retrieve the value of the reflectivity or air-mass factor for the observation geometry for each individual pixel in GOME-2 / MetOp-A obervations.

Using sensitivity studies, I have assured that the relative changes between one grid point and its neighbor are never larger than 1 %. Linear interpolation should reduce the errors in retrieved values to less than 0.1 % which gives this method no noticeable impact on the results, compared to uncertainties in the vertical trace gas profile, cloud properties and surface albedo.

4.4 Vertical column densities

To determine the NO_2 vertical column densities, we have to make assumptions about the vertical NO_2 profile. Usually, a global climatology is used to determine the local mean vertical profile. Then, look-up tables are used to retrieve the air-mass factor for every pixel in the satellite data. This assumes that the NO_2 distribution is fairly regular and does not vary strongly in time or space. It is a good approximation for time-averages, such as monthly, seasonal or yearly means.

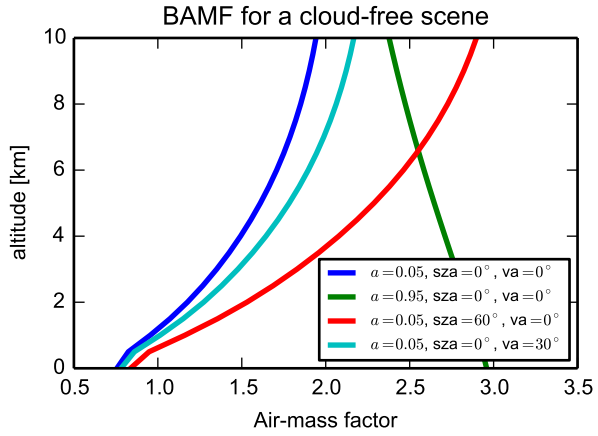

Figure 4.10: Sample block air-mass factors at $\lambda = 437.5\,\text{nm}$ for a cloud-free scene. The decrease in block air-mass factor near the (dark) surface is similar under all viewing geometries. Variances in viewing geometry roughly reflect the range of values encountered in GOME-2 / MetOp-A observations. An albedo of $a = 0.05$ is typical for observations over the ocean, although lower and also higher values (sunglint) are possible. The increase of block air-mass factor over a bright surface is due to enhanced multiple scattering near the surface.

When studying NO_2 long-range transport events, however, we are interested in NO_2 observations under unstable conditions, with rapidly varying NO_2 distributions that are subject to sudden uplift and strong winds. It is evident that the vertical NO_2 profile in these cases will not adhere to climatological simulations. Instead we have to devise an air-mass factor LUT that is specifically intended for these purposes.

GOME-2 / MetOp-A data do not yield information on the altitude of the absorbing trace gas. Thus, I cannot model the vertical profile from observations. Instead, I have to make assumptions on the typical vertical profile of a NO_2 long-range transport event.

For all further analysis, I will assume the NO_2 to be contained inside a boxcar profile of an altitude range of 3–5 km.

In the abscence of clouds, the block air-mass factor of NO_2 over a mostly dark surface shows no strong structures. It is steady over large parts of the atmosphere, declining in the vicinity of the surface. Figure 4.10 shows sample block air-mass factors for cloud-free scenes. A variance in height between 0–10 km may double the block air-mass factor or more, depending on sza. Fortunately, long-range transported NO_2 is likely to be vertically extended, which will counteract the strong trend.

4.5 Observation under cloudy conditions

As noted in Section 3.2, NO_2 long-range transport events are likely to be linked to the passage of a cold front which is able to elevate the NO_2 into altitudes where wind speeds are higher and its lifetime is longer. However, frontal systems usually have cloud

formation associated to them. As both are formed by lifting of boundary layer air parcels to higher altitudes – where the dew point is lower and humidity condensates into water droplets – it is likely that both will travel along similar routes. This means that a significant amount of NO_2 in plumes from long-range transport events will be affected by clouds in its observation.

Most products of trace gas observations from satellite in the UV / visible range use a cloud filter to exclude pixels affected by clouds from the data. Clouds have a strong impact on radiative transfer. They have a large optical depth – compared to gaseous optical depths – and impact the air-mass factor by three mechanisms:

1. albedo effect
2. multiple scattering (light path elongation)
3. shielding

The cloud top is a bright surface, with an albedo in the range of $a \approx 0.7$–0.9 (Kokhanovsky et al., 2005; Kokhanovsky and Nauss, 2006). This leads to enhanced multiple scattering directly above the cloud which makes the instrument more sensitive to trace gas in this region, increasing the local block air-mass factor. A high albedo will also lead to a larger fraction of observed photons that have passed through the lowest layers of the atmosphere, whereas a small albedo leads to the observed spectrum being dominated by single- and multiple-scattering processes in elevated parts of the atmosphere as light reaching the surface is mostly absorbed.

Inside the cloud, the optically dense medium fosters frequent multiple scattering. The mean free path of a photon is very short, but it might scatter tens, hundreds or more times within the cloud before escaping towards space or finally being absorbed. This means that the light path inside the cloud is strongly elongated. Another effect is that the deeper down inside the cloud the photons are, the less likely it is that they will eventually reach the instrument in space. This means that the block air-mass factor will be enhanced in the top layers, while it will decrease towards the bottom of the cloud.

Only little radiation will be transmitted through the cloud and into the parts of the atmosphere between cloud and surface. Even less radiation will be transmitted back into space. This means that the sensitivity of a satellite instrument to trace gas below the cloud is very low – the trace gas there is practically invisible to the instrument – reflected in a small local block air-mass factor.

All of these effects depend in their strength on the optical properties of the cloud – scattering function and optical depth – and the viewing geometry and surface properties. These effects are illustrated in Figure 4.11.

In actual observations, we never deal with a single, homogeneous cloud that covers the entire observation scene. We will not even have a single, homogeneous cloud that perfectly covers the entirety of an instrument pixel. However, the effect of radiative transfer in other pixels onto a pixel of interest is negligible in practical scenarios. Thus, the radiative transfer in each pixel is usually treated independently. This is the so-called independent pixel approximation.

In this case, I also assume that this approximation holds true on the sub-pixel scale for GOME-2 / MetOp-A observations. Thus, each pixel can be treated as a linear

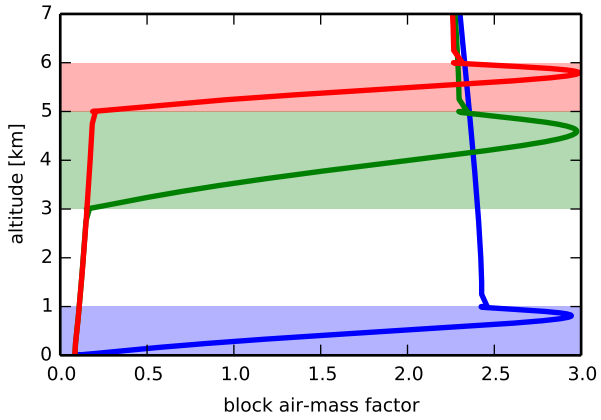

Figure 4.11: Three exemplary block air-mass factors ($\lambda = 437.5$ nm) for scenes with clouds of optical thickness 20 at the respective shaded altitudes. Solar zenith angle and viewing angle are set to 0°, the surface albedo is set to $a = 0.1$. The absolute altitudes of trace gas and cloud only have a small impact on sensitivity – the dominant effect stems from the relation of their respective altitudes.

combination of sub-pixels with different radiative transfer. In practical considerations, this will be a combination of one sub-pixel with a standardized cloud and one cloud-free sub-pixel. The relative amount of an actual instrument pixel that is covered by the cloudy sub-pixel is called the cloud fraction (CF) and is a value between zero (cloud-free) and one (pixel fully affected by clouds). Thus, there will be one (potentially vanishing) part of the pixel that is not affected by the above effects and one part that will be affected by all three of these effects.

The impact of these three effects on the block air-mass factor is illustrated in Figure 4.11. It is evident that it is crucial to know the vertical relation between NO_2 and cloud to determine the correct air-mass factor for observations in cloudy scenes. Especially, it is important to know if the NO_2 is above, below or mixed with the cloud – and if it is mixed, where inside the cloud it resides. If the NO_2 is above or below the cloud, the precise altitude does not impact the air-mass factor substantially. The strongest block air-mass factor gradients take place around the cloud; it dominates the radiative transfer.

As illustrated in Figure 4.12, I have to consider observations of cloudy scenes to systematically analyze NO_2 long-range transport. Otherwise, this study would be limited to long-range transport under cloud-free conditions – a small fraction of all transport taking place. This means that I cannot rely on the data set used for most observations. Instead, I have to prepare a special data set especially tailored to the purpose of detecting and assessing NO_2 long-range transport events. For this, I have to make assumptions about the typical cloud properties and the vertical distribution of the transported NO_2.

From a simple consideration, it makes sense that NO_2 and cloud should exhibit a strong vertical and horizontal overlap. NO_2 from the surface is lifted up with the sur-

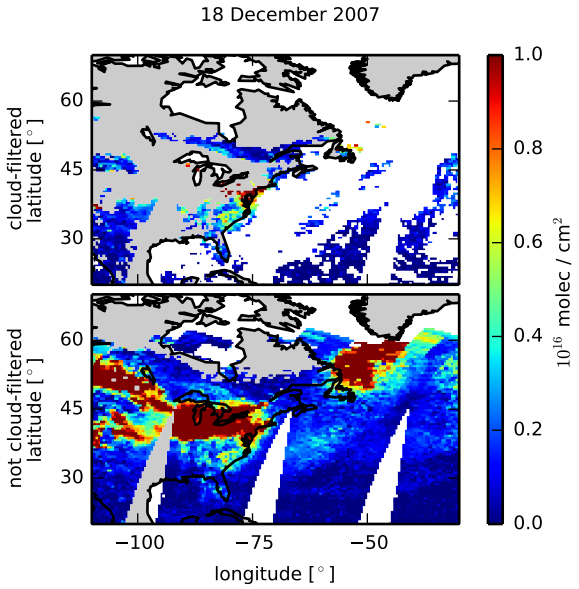

Figure 4.12: Illustration of the effect cloud filtering has on the possibility to detect NO_2 long-range transport in satellite data. The selected scene shows one of the most prominent plumes in the analyzed data set (2007–2011). In the cloud filtered data (top), the plume cannot be detected, while it is fully visible in the non-filtered data (bottom).

rounding air. Either the convection will stop before any water droplets form; then the scene will simply be cloud-free. Or the convection will stop only after the air parcel has reached its dew point. Then clouds will form all the way up to the top of convection. However, NO_2 follows this motion and will then be mixed within the cloud.

Crawford et al. (2003) have performed in-situ observations of a long-range transport event over the Pacific. It was caused by a frontal system transporting emissions from Asia. They do not measure NO_2 – unfortunately, there are no airborne in-situ measurements of long-range transported NO_2 available, to my knowledge – but CO, which is a relatively stable trace gas. The CO in their long-range transport event was emitted in biomass burning, in the same process that also emits NO_x. Chemical processing will convert some or all of the NO_2 emitted from the fire to HNO_3, H_2NO_5 and other species. However, the same convective processes are responsible for elevating both species.

In their measurements they find that CO is well mixed within the cloud. The vertical bondaries of the CO plume are rather sharp and extend roughly from $2,000\,\mathrm{m}$ to $5,500\,\mathrm{m}$ over roughly $3,500\,\mathrm{m}$.

As there are no in-situ measurements of long-range transported NO_2 available, we will use these CO measurements as a model for the vertical NO_2 profile. I have verified this result using data from MACC-II (Monitoring Atmospheric Composition and Climate – Interim Implementation) reanalysis which also exhibits long-range transport events. In this rich dataset, I have analyzed the relation of liquid and frozen water content to NO_2 concentrations for selected points of a long-range transport event over the North Sea and Atlantic in October 2010 (see Subsection 7.1.4 and Subsection 8.1.3 for the case study of this event as seen in GOME-2 / MetOp-A and MACC-II reanalysis, respectively). In this prominent long-range transport event, clouds and NO_2 are horizontally colocated in both observations and model data. I have analyzed the profiles at three locations inside the plume that should correspond to different plume ages, as the strongly elongated plume was emitted over a longer timespan.

In this study, the vertical profiles of liquid and frozen water content and NO_2 concentrations overlap very strongly, justifying the approximation of a coinciding boxcar profile for our analysis (Figure 4.13 and Figure 4.14). Findings of Barth et al. (2007) indicate, that mixing of NO_2 and cloud in an observation of deep convection is a good approximation. The simplification should not lead to significantly less precise air-mass factors. However, this is only a small study; we have not found a way to systematically analyze a large amount of vertical profiles in NO_2 long-range transport plumes for their vertical water and NO_2 profiles in relation to one another. Also, NO_2 uplift and clouds in this – or any – model are parameterized and may exhibit artifacts of this parameterization. They may or may not be representative of the actual profiles.

As a sensitivity study (Figure 4.15) shows the change in air-mass factor when NO_2 and cloud are not perfectly aligned is rather small as long as it stays below the cloud. Larger changes in air-mass factor may occur in scenes with a low sun (large solar zenith angle) when a significant amount of NO_2 resides above the cloud. However, there is no evidence of such situations and they appear unlikely under consideration of the mechanics of long-range transport.

For my analysis, I therefore assume that all plumes from NO_2 long-range transport will reside at a single altitude and all NO_2 will be mixed within the cloud, if any cloud is present. Both cloud and NO_2 will be represented by a single boxcar vertical profile,

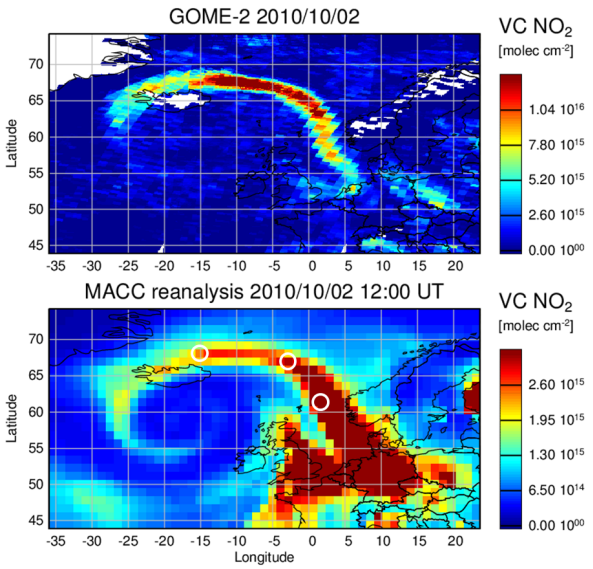

Figure 4.13: NO_2 long-range transport plume near Europe on 2010-10-02. Shown are the NO_2 vertical column densities for both GOME-2 / MetOp-A and MACC-II reanalysis data. Note the difference in color scale, with MACC-II reanalysis data showing significantly lower vertical column densities, yet clearly exhibiting a similar export pattern. White circles in the MACC-II reanalysis data indicate the location at which the vertical cloud and NO_2 profiles were sampled.

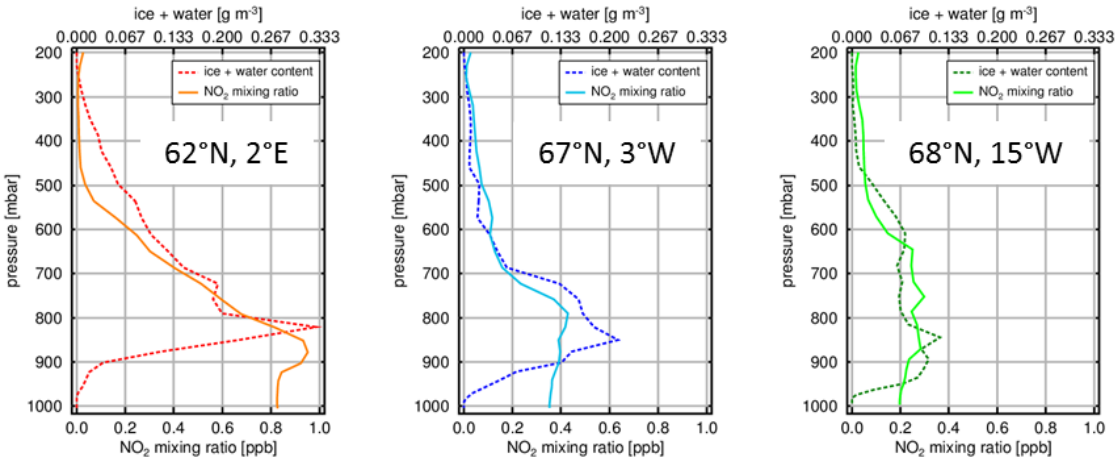

Figure 4.14: Vertical profiles of both liquid and frozen water content (dashed) and NO_2 mixing ratios (solid) for the three observations indicated in Figure 4.13. The three locations should show increasing plume age from left to right. In all three scenes, the vertical profiles show a strong overlap, indicating that the assumption of NO_2 and cloud coinciding vertically during long-range transportevents is justified. The high mixing ratios of NO_2 near the surface might be an artifact of the parameteization of the convection process, as NO_2 is unlikely to persist at such low altitudes during long-range transport events.

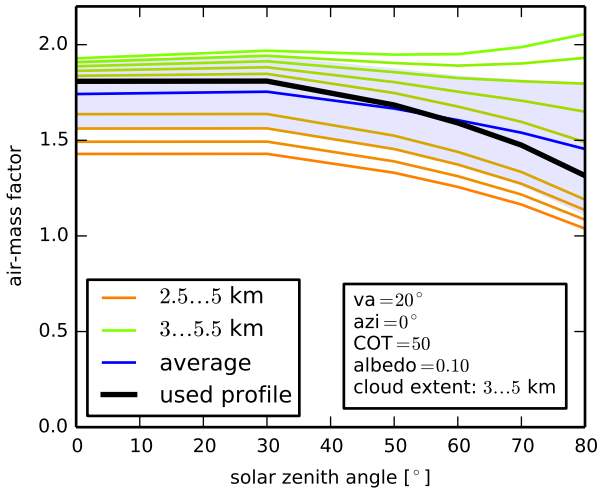

Figure 4.15: Dependency of the air-mass factor at $\lambda = 437.5\,\text{nm}$ on the solar zenith angle for varying NO_2 vertical profiles. For this sensitivity study, the cloud always extends from 3–5 km vertically with an optical thickness COT = 50 (same parameters as used for later analyses). Further, I set the albedo $a = 0.1$, viewing angle va = 20° and relative azimuth angle azi = 0° (opposing sun). The black line shows the profile used for further analyses, the blue line and the shaded area indicate the average of the AMFs computed for the different NO_2 profiles and their standard deviation, respectively. The results show that – while there is some variance – the air-mass factor from our simplification should be accurate enough as long as not a major part of the NO_2 resides above the cloud.

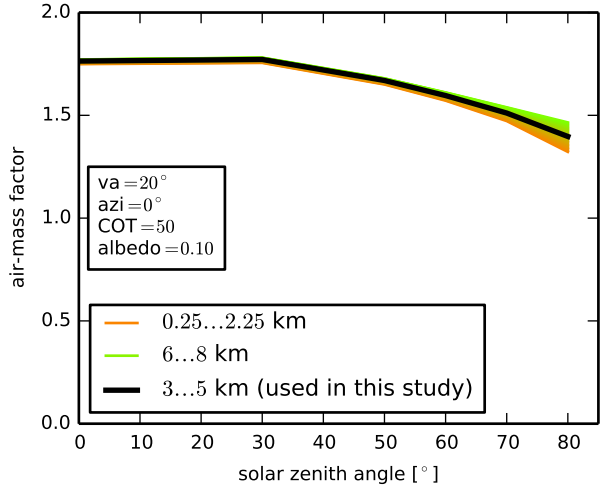

Figure 4.16: Dependency of the air-mass factor at $\lambda = 437.5\,\text{nm}$ on the solar zenith angle for a varying altitude of perfectly aligned NO_2 and cloud. For this sensitivity study, the boxcar profiles of NO_2 and cloud are always 2 km in vertical extend. Again, we set the cloud optical thickness $\text{COT} = 50$ (same parameters as used for later analyses). Further, we set the albedo $a = 0.1$, viewing angle $\text{va} = 20°$ and relative azimuth angle $\text{azi} = 0°$ (opposing sun). The black line shows the profile used for further analyses. The results show that – as long as the vertical profiles of cloud and NO_2 are aligned – there is almost no variance in the air-mass factor and our simplification should not significantly impact the results of further analyses.

with smoothed edges for the cloud to mitigate discontinuities on the boundary between cloudy and non-cloudy parts of the atmosphere.

Another sensitivity study (Figure 4.16) shows that the impact of the precise altitude of the NO_2 content and the cloud do not impact the air-mass factor significantly. The error of placing both NO_2 and cloud at a wrong altitude range is on the order of less than 5 %.

Further considerations such as multi-layered clouds or NO_2 are beyond the scope of this study. These scenarios should be rare and there is no way to account for them with the given measurement techniques and processing. Sea-spray aerosols over the ocean will either reside below the cloud and impact the air-mass factor only marginally or mitigate the decline of the NO_2 block air-mass factor near the surface, stabilizing our simplification.

For the cloud optial thickness (COT), I use a value of $\tau = 50$. This represents a moderately thick cloud as found in the passage of frontal systems, but not very optically thick clouds as found in thunderstorms (with a COT up to $\tau = 300$). Clouds in long-range transport may be optically thicker or thinner than assumed. A thicker cloud will lead to stronger shielding, higher albedo effect and a more steep slope of the block air-mass factor over the altitude of the cloud. However, a mismatch in COT will be partially

Parameter	value(s)	step size
Wavelength	437.5 nm	
Cloud optical thickness	50	
Cloud altitude (above surface)	3–5 km	
NO_2 altitude	3–5 km	
Surface altitude	0–9 km	0.25 km
Surface albedo	0–0.1, 0.1–0.3, 0.3–1	0.005, 0.02, 0.05
Solar zenith angle	0–85°	5°
Viewing angle	0–60°	5°
Azimuth angle	0–180°	10°

Table 4.2: Parameters and parameter ranges used in SCIATRAN 3.1 for determining the reflectivity and air-mass factor look-up tables for retrieval of the NO_2 vertical column densities.

compensated by the implementation of the cloud detection which assumes a COT of 50.

An overview of the parameters used for the calculation of reflectivities and air-mass factors with SCIATRAN 3.1 is given in Table 4.2.

To correct for the impact of clouds on the observations, we have to know how much clouds affect each pixel. In this study, this impact is represented by the cloud fraction (CF). It follows the simple approach, that a single pixel of the observation can be adequately represented by artificially dividing it into a section with no cloud influence and a section with homogeneous cloud influence. Thus, for each pixel we only determine a single set of observational parameters and determine the air-mass factor in both presence and abscence of a cloud. This neglects interactions between the cloudy and the cloud-free parts of the pixel and can misrepresent scenes with fragmented cloud cover. Considering the pixel size of GOME-2 / MetOp-A, this approach is reasonable for most observational conditions and boundary effects should not play a significant role.

After determining the cloud fraction and calculating the air-mass factor for the cloudy and cloud-free observation, we determine the resulting air-mass factor by weighting the cloudy and cloud-free air-mass factor with the respective fraction of the radiation reaching the instrument from each.

For GOME-2 / MetOp-A observations it is common to use the FRESCO+ cloud product Wang et al. (2008). FRESCO+ retrieves the effective cloud fraction and the cloud pressure from the O_2-A band around 760 nm. It uses the reflectivity of the scene, compared to the reflectivity of the surface with its specific albedo and a cloud as a lambertian reflector with albedo $a = 0.8$ to determine the effective cloud fraction and the strength of absorption in the O_2-A band as an indicator of the cloud's altitude. In FRESCO+ (as opposed to FRESCO), single Rayleigh scattering has been added to refine results.

This approach is sufficient for most purposes, where the cloud fraction is used to flag and mask out cloudy pixels in the data. In this study, however, I do not mask out cloudy pixels and need to take the radiative effects of clouds explicitly into account. For this reason, I use a similar cloud detection algorithm that operates directly on the

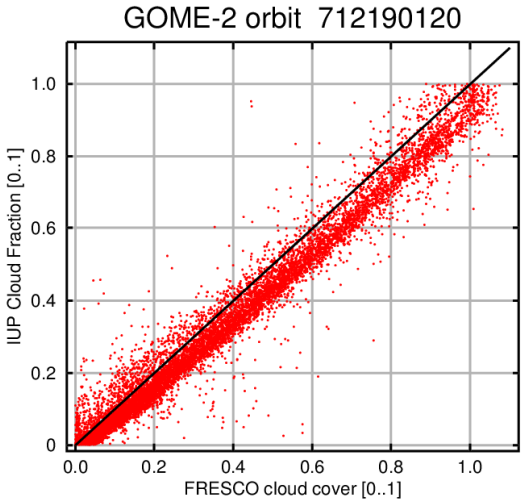

Figure 4.17: Scatter of effective geometric cloud fraction for both FRESCO+ and the customized method used in this study for each pixel in a GOME-2 orbit on 17 December 2007. In a few cases, there are strong differences in the retrieved cloud cover. For the vast majority of pixels, there is a strong correlation between values from both retrievals. Our custom cloud fraction tends to produce slightly lower cloud fractions.

wavelength range used in this study and takes the full radiative transfer into account.

The algorithm retrieves the reflectivity (again, at $\lambda = 437.5\,\mathrm{nm}$, the wavelength with the most prominent NO_2 absorption features) for the cloudy and the cloud-free scene, taking the viewing geometry as well as surface elevation and albedo into account. It then models the observed reflectivity by linear superposition of the cloudy and cloud-free reflectivity, thus yielding the geometric cloud fraction $\mathrm{CF}_{\mathrm{geom}}$.

$$R_{\mathrm{obs}} = \mathrm{CF}_{\mathrm{geom}} R_{\mathrm{cloudy}} + (1 - \mathrm{CF}_{\mathrm{geom}}) R_{\mathrm{cloud\text{-}free}} \tag{4.19}$$

Note that we have a single cloud scenario that we use for all scenes. See Table 4.2. We can transform this to

$$\mathrm{CF}_{\mathrm{geom}} = \frac{R_{\mathrm{obs}} - R_{\mathrm{cloud\text{-}free}}}{R_{\mathrm{cloudy}} - R_{\mathrm{cloud\text{-}free}}} \tag{4.20}$$

A comparison of cloud fractions determined by FRESCO+ and our specialized cloud retrieval can be seen in Figure 4.17.

In the next step, the algorithm takes into account that the air-mass factor of the observation is determined by radiative intensity. Observations over high-albedo surfaces contribute stronger to the overall air-mass factor than observations over dark surfaces. The algorithm therefore weighs the air-mass factor contributions from the cloudy and cloud-free scenes with the radiative cloud fraction $\mathrm{CF}_{\mathrm{rad}}$, the fraction of radiative intensity impacted by the presence of the cloud:

$$\mathrm{CF_{rad}} = \frac{R_{\mathrm{cloudy}}\mathrm{CF_{geom}}}{R_{\mathrm{cloudy}}\mathrm{CF_{geom}} + R_{\text{cloud-free}}(1 - \mathrm{CF_{geom}})} \tag{4.21}$$

Then, the total resulting air-mass factor for the scene is computed as

$$\mathrm{AMF} = \mathrm{CF_{rad}}\mathrm{AMF_{cloudy}} + (1 - \mathrm{CF_{rad}})\mathrm{AMF_{cloud\text{-}free}} \tag{4.22}$$

This algorithm then yields an air-mass factor for clear, partially cloudy and fully cloud-covered scenes which is tailored to the purposes of analyzing NO_2 in elevated plumes over the ocean. This air-mass factor is then used to determine the time series of NO_2 vertical column density maps. For the study of NO_2 long-range transport presented in this work, I use only this dataset.

4.6 Clouds over bright surfaces

The shielding and albedo effect of clouds can lead to unexpected effects over bright surfaces. For most observations, the surface albedo is low, which means that almost no light from the surface contributes to the observations, due to the clouds' small transmittance. This is the regular shielding effect.

However, bright surfaces – such as snow and ice – absorb only little radiation. Assuming a perfectly white surface that re-emits all radiation, all radiation that gets transmitted from the sun through the cloud to the surface will be reflected back to the cloud (neglecting absorption in the atmosphere). A small fraction of this radiation will be transmitted trough the cloud towards space. Due to the high albedo of a cloud, however, most of the radiation will be reflected from the cloud and traverse the atmosphere between surface and cloud once more in both downwards and upwards direction. This continues, with the amount of radiation below the cloud exponentially decreasing with the number of reflections. This is illustrated in Figure 4.18.

This will lead to very long light-paths in the atmospheric part between surface and cloud, which in turn leads to comparatively strong absorption by the same amount of NO_2 (Zien et al., 2010a). This can be seen in the block air-mass factors for this part of the atmosphere (Figure 4.19). Only small amounts of radiation reach the atmosphere below the cloud, but this radiation will carry a strong absorption signal back to the instrument. The absorption may be strong enough to lead to saturation effects. It might be possible to detect these as characteristic features in the shape of the absorption line in the observed spectrum.

If we assume the cloud to be a mirror of reflectivity r and transmittance $t = 1 - r$ at an altitude Δh above the surface, and the surface has albedo a, then – considering only vertical radiation – the average vertical light path between surface and cloud can be written as:

$$\bar{l}(r, a) = \sum_{i=0}^{\infty} i\, 2\Delta h\, (1 - r)^2\, r^{i-1}\, a^i = 2\Delta h\, \frac{a(1 - r)^2}{(1 - r\, a)^2} \tag{4.23}$$

In this simple representation, the maximum of this function is $\bar{l}(r, a) = 2\Delta h$, for $a = 1$ (perfect reflection) with an analytical air-mass factor $\mathrm{AMF} = \bar{l}/\Delta h = 2$. This means

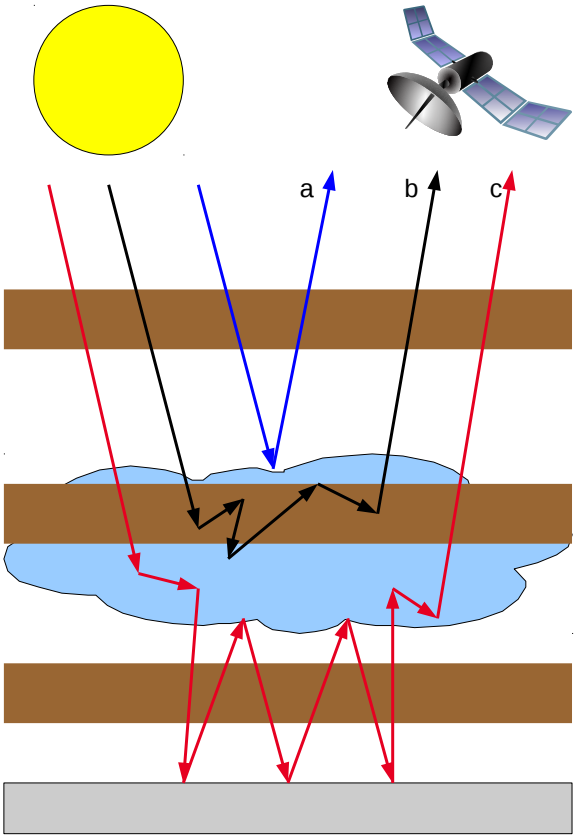

Figure 4.18: Illustration of the possible types of light paths in a scene with clouds over a bright surface. Brown clouds indicate a trace gas, the blue cloud is a water / ice cloud. The high albedo of the cloud will lead to a shielding effect, as most of the irradiation is reflected at the cloud top (a). Radiation entering the cloud will undergo strong multiple scattering, elongating the light path inside the cloud through any trace gas present before being emitted back to space (b). Radiation traversing the cloud towards the surface is likely to be reflected mulltiple times between surface and cloud bottom before being emitted back to space, which again leads to a vast increase in effective light path (c). Except for the third effect, these are exactly the effects present over a dark surface.

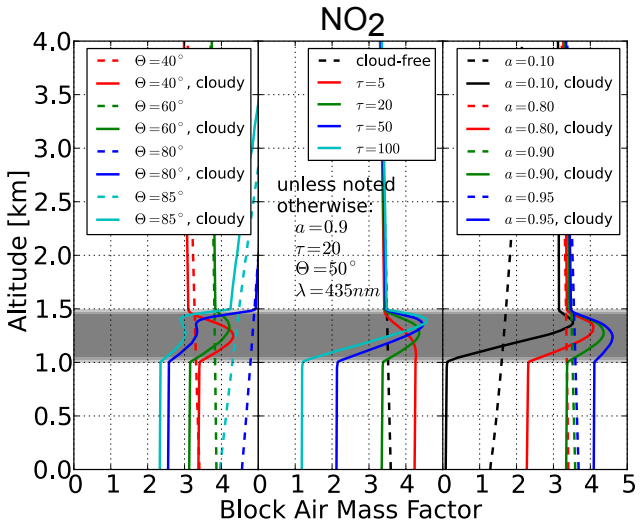

Figure 4.19: Block air-mass factor for NO_2 in cloudy scenes with (left) varying solar zenith angle, (middle) varying cloud optical thickness and (right) varying surface albedo. Default parameters are an albedo $a = 0.9$, cloud optical thickness 20 and sza $= 50°$. The location of the cloud is indicated with a grey shading. Over bright surfaces, there is always a peak in sensitivity (block air-mass factor) inside the cloud. A high albedo significantly mitigates the shielding effect of a cloud, yielding block air-mass factors in the same order of magnitude as without the cloud. This means that trace gas between a cloud and a bright surface can still be detected from satellite – in rare cases it could even be amplified. These results for $\lambda = 435\,\text{nm}$ are practically identical to the results for $\lambda = 437.5\,\text{nm}$ used in this study.

that in this approximation, the cloud-bright-surface effect can only mitigate shielding by clouds, never lead to an increase over the light-path in the abscence of a cloud.

However, this considers only the vertical light path. If we assume the cloud to be a perfect diffusor, removing all directional information from the incoming radiation, each iteration of the light path will be elongated, so that

$$\Delta h'(\alpha) = \frac{\Delta h}{\cos \alpha}, \tag{4.24}$$

where α is the angle from the normal vector. We cannot compute the average, as this function diverges for $\alpha = 90°$, when the light is emitted parallel to the surface. It is however easy to compute that – approaching $\alpha = 90°$ – the average light path can increase by a factor of 5 or more. This is still a strong simplification, but it serves to make the results from radiative transfer simulations plausible and understandable.

In significantly more complex radiative transfer simulations with SCIATRAN 3.1 as well, I found that in scenes with an overhead sun and albedo above $a > 0.8$, block air-mass factor values below the cloud can easily exceed those above the cloud.

When the sun irradiates the scene at a higher sza (a lower inclination), the block air-mass factor below the cloud is relatively invariant. This is due to the fact that the optically thick cloud immediately removes all directional information from the radiative field once it comes into contact with the cloud. This means that at a higher sza only the block air-mass factor above the cloud is affected substantially, increasing roughly by the geometric factor of BAMF $\propto 1/\cos \mathrm{sza}$ with some modulation from increased multiple scattering above the cloud. Thus, while this cloud-bright-surface albedo effect occurs under all viewing geometries, its relative impact is largest when the sun is near the zenith. Then, the cloud can effectively become transparent concerning the observation of trace gas below it.

Observational scenes are more complicated and even radiative transfer simulations can only simulate part of the effects. Due to high reflectivities, small errors in the radiative transfer simulation may lead to large errors in the calculation of radiances and thus the air-mass factor.

One factor that is especially uncertain is the spatial extent of this scene. For this effect to occur in observational data, the scene has to be very homogeneous and probably needs to extend beyond a single pixel – invalidating the independent pixel approximation. Gaps in cloud cover or patches of dark surface may easily interrupt the back-and-forth scatter between surface and cloud bottom, thus mitigating the effect.

This effect – enhanced or invariant block air-mass factor below a cloud over a bright surface – can be found in observational data, although a clear example as presented in radiative transfer calculations is hard to find. This is due to the fact that snow and ice – the brightest surfaces on earth – are usually only found in local winter (or on mountain-tops which bring their own problems with their distinct vertical structure). In local winter, however, the sun does not rise above sza $\approx 50°$ in regions with full snow cover. Under this angle, the cloud-surface albedo effect can only mitigate shielding by clouds, not wholly compensate it.

For this study, the dimer $O_2 \cdot O_2$ is especially interesting, due to two aspects:

- it has a very stable vertical distribution that can be calculated analytically from

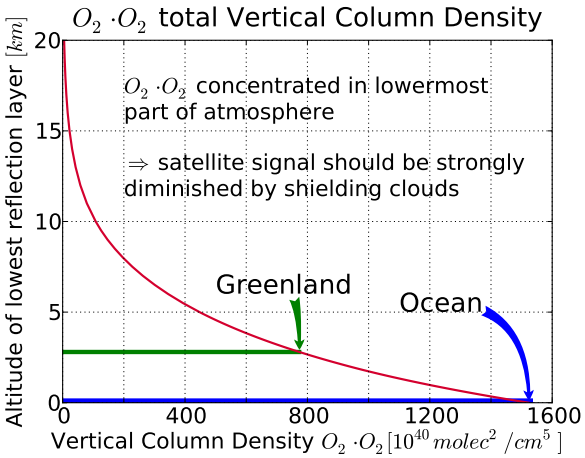

Figure 4.20: Vertical profile of $O_2 \cdot O_2$. The average altitude of the ocean and Greenland are indicated to show the expected vertical column for $O_2 \cdot O_2$ over these regions, which are used in further studies.

the pressure and temperature profile

- as it is a dimer of O_2, it depends on the square of the O_2 concentration, which results in a strong concentration peak near the surface (see Figure 4.20)

When looking at maps of $O_2 \cdot O_2$ pseudo-vertical column densities near and over Antarctica, clouds could be expected to be hardly visible due to this effect. As $O_2 \cdot O_2$ is mostly concentrated near the surface, its absorption should depend mostly on the block air-mass factor between a cloud and the surface. As we cannot model the cloud explicitly, we use an air-mass factor that was determined for a cloud-free scenario and apply it to all slant-column densities, regardless of cloud cover. In this approach, clouds should not be visible in $O_2 \cdot O_2$ vertical column density maps if the block air-mass factor is invariant under cloud presence.

However, this is not observed in operational data. GOME-2 / MetOp-A can measure $O_2 \cdot O_2$ via differential optical absorption spectroscopy, using a fit window centered on $\lambda \approx 476\,\mathrm{nm}$. Maps of $O_2 \cdot O_2$ vertical column densities with naive air-mass factors – i.e. neglecting cloud presence – show a significant decline over sea-ice and continental ice in Antarctica, albeit significantly smaller than over the open ocean, when clouds are present. The horizontal shape of the clouds is still easily discernible from $O_2 \cdot O_2$ observations (Figure 4.21).

This is to be expected, as observations near the poles always take place at high solar zenith angles (low sun). As shown in Figure 4.19, this means that the block air-mass factor below the cloud can never reach the amplified values above the cloud. Thus, the impact of the cloud will still be visible in a mitigated form.

Figure 4.22 shows the measured $O_2 \cdot O_2$ vertical column density – as determined via a naive air-mass factor – during the course of a year for a stretch of ocean in the North Atlantic Ocean and Greenland (Zien et al., 2010b). Both patches are at the same

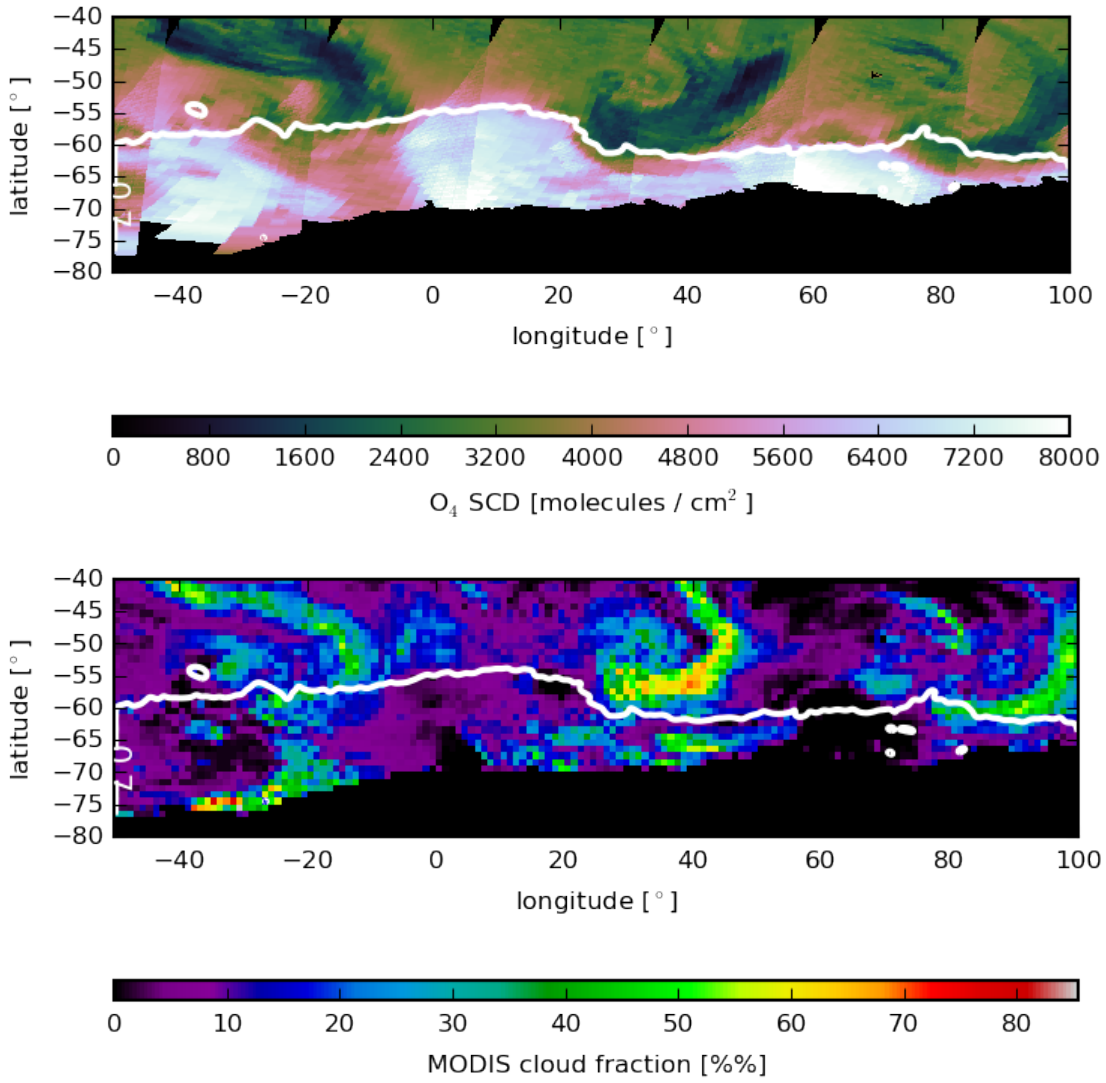

Figure 4.21: (Top) GOME-2 / MetOp-A slant-column densities of $O_2 \cdot O_2$ and (bottom) MODIS cloud fractions on 12 September 2007 near Antarctica. Black areas indicate continents or no measurement. The white line marks the 70 % sea ice cover contour, as observed by AMSR-E. Clouds are highly visible in $O_2 \cdot O_2$ concentrations over the open ocean. Their impact is strongly mitigated over sea ice with its high albedo.

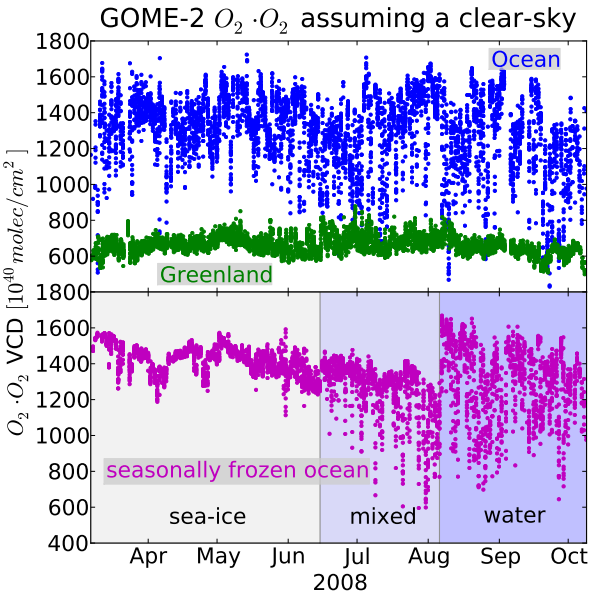

Figure 4.22: Naive $O_2 \cdot O_2$ vertical column density as retrieved from GOME-2 / MetOp-A by differential optical absorption spectroscopy. Data between March 2008 and October 2008 over the open ocean (blue), over seasonally frozen ocean (purple) and over Greenland (green) is shown. Air-mass factors were calculated without a cloud present. Albedo for Greenland and frozen ocean ist set to $a = 0.9$, for open ocean $a = 0.15$ and for mixed frozen/open ocean $a = 0.5$. While data over Greenland is very narrowly scattered – indicating a stable air-mass factor – observations over the ocean indicate a high variance in air-mass factor. Over the seasonally frozen ocean, both effects can be seen in the same geolocation, with a transitory phase in between.

latitude and different longitude. It is appararent, that the vertical column density over Greenland is very narrow; it shows much less scatter – both in absolute and relative terms – than the $O_2 \cdot O_2$ vertical column density over the ocean. However, this is only partially true after the ocean has frozen in this region. Then, the scatter narrows down almost in the same fashion as is the case over Greenland. This small scatter indicates that the air-mass factor over sea-ice is almost invariant to the presence of clouds – in this prolonged period there are bound to be many observations under cloudy conditions.

This effect will be important when studying Arctic and Antarctic trace gas concentrations near the surface from satellite. In favorable conditions, it may be possible to observe trace gases even under cloudy conditions without losing sensitivity, while usualy data from cloudy pixels are discarded (e.g. Vasilkov et al., 2010; Sihler et al., 2012).

In this study, however, this effect will not impact the data. GOME-2 / MetOp-A observes only very few plumes over sea-ice and in these cases the solar zenith angle is too large to bear particular impact on the air-mass factor. Mainly, however, most NO_2 is located mixed within the cloud. The block air-mass factor within the cloud is relatively

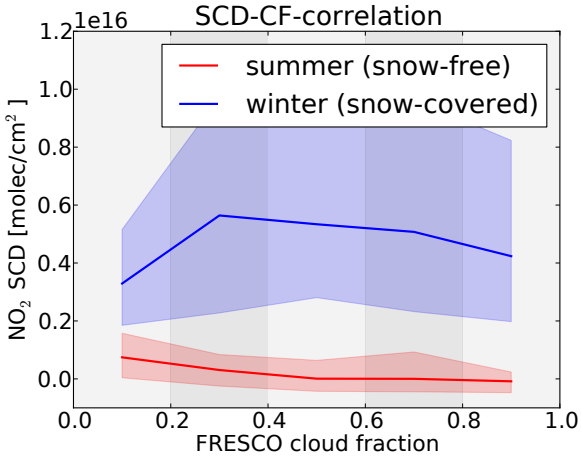

Figure 4.23: Average NO_2 vertical column density in the Edmonton, Canada area without any cloud-filtering or cloud modeling in radiative transfer binned by FRESCO+ cloud fractions. Shown are in blue the NO_2 vertical column density during periods of full snow cover and in red during periods without any snow (periods of partial snow cover are not shown). The solid line gives the median value during each period while the shaded area indicates the spread from first to third quartile (encompassing 50% of points). Snow-free periods show both lower absolute values and descending values towards high cloud cover. In contrast, periods of snow cover show higher values and an increase in observed NO_2 vertical column density from no cloud to thin cloud and only a moderate relative decrease afterwards.

invariant under changes of surface albedo. For these two reasons, the cloud-surface albedo effect will not impact the analysis of NO_2 long-range transport.

I have analyzed NO_2 vertical column densities in the Edmonton, Canada (53° N, 113° W) area to investigate the effect of cloud-ice interference on NO_2 observations (Zien et al., 2011a). The Edmonton area hosts a large petro-chemical and gas industry. It is responsible for vast NO_2 emissions throughout the year, with a strong increase during winter when the surface lies below continuous snow cover. In GOME-2 / MetOp-A maps of NO_2, Edmonton is easily discernible as a point-like source in Canada (McLinden et al., 2014).

I have studied NO_2 vertical column densities observed by SCIAMACHY (SCanning Imaging Absorption SpectroMeter for Atmospheric CHartographY, Bovensmann et al., 1999) in the area 52–54° N and 114–112° W. SCIAMACHY is a satellite spectrometer performing similar measurements to GOME-2 / MetOp-A at lower spacial resolution, with a more extensive waveband and at additional observational geometries. For these observations, I utilized a clear-sky tropospheric air-mass factor to convert slant-column densities to vertical column densities, ignoring any cloud impacts. I divided the data into categories of full, partial and zero snow cover, ignoring all data of partial cover. For

this, I used historic data from *The Cryosphere Today*[4] by the University of Illinois. In each of these categories, I then binned the NO_2 vertical column densities by FRESCO+ cloud cover (in bins of width 0.2), with 1082 datasets for zero and 1241 datasets for full snow cover. The results of this analysis are shown in Figure 4.23.

This shows that not only are NO_2 vertical column densities higher during periods of snow cover – due to longer life-time and more emissions during winter – but they also increase when moving from zero to light cloud cover and only slowly decrease when moving to stronger cloud cover. Obviously, these observations have a large spread. However, the quantiles all show the same trend and the monotonous decline of observed NO_2 during snow-free periods (correlation coefficient: $r = -0.289$) is not observed for periods of full snow cover ($r = -0.003$).

These are only statistical analyses, but they indicate that cloud cover will not make satellite instruments insensitive to trace gas below it as long as a bright surface will mitigate the shielding effect by light-path enhancement. These data may well be considered for analysis.

4.7 Stratospheric correction

After the satellite observations and the DOAS retrieval, the data product contains the combined tropospheric and stratospheric NO_2 slant-column density. The stratosphere contains a layer of elevated NO_2 concentrations (on the order of up to 10 ppb) in the altitude range of 30–40 km (Figure 4.24). This will dominate the absorption signal in all but highly polluted scenes – with a stratospheric vertical column density of about $(0.5 \ldots 5) \times 10^{15}$ molecules/cm^2, depending on latitude and season. It is therefore crucial to reliably remove any stratospheric contribution to the NO_2 signal before analyzing the data.

There are essentially two ways to remove the stratospheric contribution: from inference of measured data or from stratospheric modeling.

The typical approach for the first method is the so-called reference sector approach. Here, for each latitude, a sector is selected which is supposed to contain only stratospheric NO_2. Typically, this sector is a strip over the Pacific from North Pole to South Pole between 180° W and 160° W. There are no major emitters of NO_2 in this region and the ocean acts as a sink for NO_2 which is washed out. Thus, it is assumed that all NO_2 observed over this region is located in the stratosphere.

Then, it is assumed that the stratosheric NO_2 contribution is zonally invariant. This is an acceptable approximation for instruments in sun-synchronous orbits, as stratospheric chemistry is to a large degree driven by photochemistry. An average stratospheric contribution is computed from the reference sector for each latitude and subtracted from each measurement on the respective latitude. This way, the correction is based on actual observations, taking instrument effects into account, negelecting zonal variability in the distribution.

The other approach is to model stratospheric chemistry and determine stratospheric NO_2 concentrations. This requires a knowledge of the photochemistry of the stratosphere and a model that is initialized long enough and validated to resemble the intial conditions

[4] `http://arctic.atmos.uiuc.edu/cryosphere/`

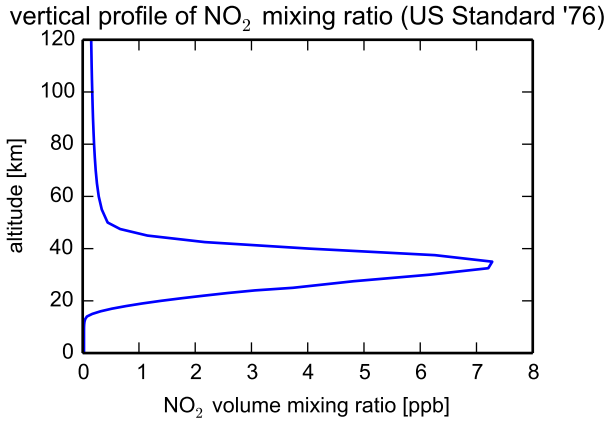

Figure 4.24: Typical vertical profile of NO_2 as determined in (National Oceanic and Atmospheric Administration et al., 1976) with a strong peak in mixing ratios in the stratosphere. This will be a significant contribution to the total vertical column density even though the absolute concentrations are fairly low due to low pressure in the stratosphere. Tropospheric mixing ratios can reach similar levels in polluted areas.

that determine the distribution of NO_2 and other species relevant to its chemistry, like OH, HNO_3, O_3, VOCs, and others. Such a model can simulate the distribution patterns of NO_2 in the stratosphere, where there is little short-term forcing from anthropogenic emissions, reasonably well.

In this study, I use a joint approach: the B3dCTM model (Aschmann et al., 2009; Hilboll et al., 2013) – a global 3-D chemical transport model (CTM) – is used to determine the horizontal distribution of the NO_2 in the stratosphere while the reference sector is used to offset the model zonally to match the observations. This yields a reliable stratospheric NO_2 vertical column density of matching amplitude and a modeled horizontal distribution, that is more representative than the zonal homogeneity used for the reference sector method.

In practice, the stratospheric contribution is removed directly from the slant-column densities before the tropospheric air-mass factor is applied to the observations. For this, a stratospheric air-mass factor is calculated similarly to the tropospheric air-mass factor and applied to the modeled stratospheric NO_2 vertical column density to yield the stratospheric NO_2 slant-column density. This stratospheric slant-column density is then subtracted from the total slant-column density. The tropospheric NO_2 vertical column density is subsequently computed by applying the troposperic air-mass factor.

This whole process yields a time series of maps of tropospheric NO_2 vertical column densities, optimized for observations of elevated plumes of NO_2, mixed with potential clouds in the scene.

4.8 Limitations

The GOME-2 / MetOp-A data set used in this study is optimized towards detecting NO_2 long-range transport events. However, there are some limitations when using this data.

4.8.1 Differential optical absorption spectroscopy fits

The DOAS technique has several parameters which determine its accuracy. The quality of the DOAS fit is determined mainly by the quality of the observed spectra (measurement and reference) and the laboratory absorption spectra of the relevant species. It is, however, also dependent on the chosen fitting window, the species included in the fitting process, the polynomial used for the low-frequency variation part of the absorption spectrum and other corrections.

A larger fitting window will include more spectral features of the trace gas in question – thus making the fit per se more reliable – while also including more spectral features of interfering species which may in turn lead to a less accurate estimate of the slant-column density of the trace gas of interest. The fitting window from 425 nm to 497 nm is the standard fitting window for the GOME-2 / MetOp-A NO_2 product at the Institute for Environmental Physics in Bremen and has proven to yield reliable results over many years.

The fit includes the species NO_2, O_3, $O_2 \cdot O_2$, liquid water and water vapour.

The polynomial used to remove the slowly varying part of the absorption spectrum is a regular third-order polynomial (Richter et al., 2011). Increasing or decreasing the order of this polynomial will lead to slightly different results. A third-order polynomial has – so far – yielded the most reliable results for most purposes.

Richter et al. (2011) report an uncertainty of the NO_2 slant-column density retrieval on the order of $5 \cdot 10^{14}$ molecules/cm^2, resulting from atmospheric uncertainties, interference of other species, intrument artifacts like stray light, cosmic rays and variances in spectral sensitivity, and many more factors.

4.8.2 GOME-2 / MetOp-A

GOME-2 / MetOp-A is a satellite-borne instrument. Unfortunately, this does not mean that it is immune to environmental impact. GOME-2 / MetOp-A degradation from its launch in 2007 to 2012 has recently been analyzed (Dikty and Richter, 2012). This study shows that degradation is strongest in the UV regime, while visible wavelengths are less impacted. The impact on the retrieval of NO_2 is relatively small and mostly manifests itself in a larger residual. Retrieved slant-column densities are not significantly impacted by degradation. However, the observed intensity is slowly diminishing – differently for the observation of Earth-shine and solar irradiation. This may lead to an increase in apparent cloud fractions which are retrieved from relative intensity. Fortunately, this study is not particularly sensitive to cloud fractions (see Section 4.5) and the greatest effect will occur for small cloud fractions. The impact on this study is small, as it is mostly interested in scenes with cloud fractions CF $\gtrapprox 0.1$ that are not strongly affected.

Besides that, the GOME-2 / MetOp-A detector is always subject to statistical and electronic noise which cannot be avoided.

Occasionally, GOME-2 / MetOp-A measurements will be contaminated by misconfigurations, high-energetic cosmic rays and particles and other effects. We have a blacklist of these events but this list might be incomplete. These defect measurements should be filtered out in the long-range transport detection algorithm presented in Chapter 6, but I cannot exclude that some artifacts enter the analysis.

4.8.3 Air-mass factor determination

The part of the trace gas retrieval with the most uncertainties is the determination of the air-mass factor for any given observation. In order to study NO_2 long-range transport events in GOME-2 / MetOp-A data, I have to make several assumptions on the vertical distribution of the NO_2 and on cloud properties. I have already detailed the impact of a misalignment between cloud and NO_2 and the impact of a wrong altitude above ground level for cloud and NO_2 in Section 4.5.

Surface albedo impacts the air-mass factor. As this study scrutinizes NO_2 plumes over the ocean, only the oceanic albedo will impact the observations. However, oceanic albedo depends on the observation geometry. Our data product uses a seasonal albedo determined from GOME observations which incorporates oceanic albedo variability with the varying typical observation scenarios.

However, sunglint cannot be considered in such a database. Sunglint is the strong reflection of light on a smooth water surface. When the incident angle of sun light onto the ocean is identical to the observation angle of the satellite instrument (specular reflection), the ocean surface can act as a mirror with a highly increased effective albedo of up to $a \gtrapprox 0.2$. As surface waves on the ocean lead to not a single but a distribution of surface normal vectors, this sun glint is broadened and can be observed at angles around the nominal sun glint angle. Roughening of the ocean surface can strongly wash out this effect. However, this effect cannot be predicted by geometry alone. The surface roughness does not only depend on synoptic wind speeds and oceanic flow, but also on more local effects like atmospheric gravity waves. Also, under cloudy conditions, there will be no sunglint as clouds remove all directional information from the incoming sunshine. Fortunately, it also affects only a small area of observation. Areas of sunglint will lead to a higher visibility of NO_2 in the troposphere, leading to higher retrieved vertical column densities. In the absence of transported pollution, this should hardly be visible in the data and would be filtered out by the methods described in Chapter 6. If sunglint coincides with long-range transport plumes in the absence of clouds, this will lead to an overestimation of NO_2 in the plume.

This study also neglects a common factor entering air-mass factor calculations: aerosols. Aerosols are solid or liquid particles dissolved in the air, like sand, sea-spray, soot and other combustion byproducts. The typical diameter of aerosols ($\gtrapprox 1\,\mu$m) is larger than the wavelength of observation, which means that scattering on these particles has to be modeled using Mie-theory.

In this study, aerosols do not play a significant role. I am interested only in observations over the open ocean. Due to subsidence, aerosols from continental areas – like sand and all major contributions of anthropogenic aerosols – do not usually play a significant

role over the ocean. The only aerosol present in significant amounts over the open ocean is sea-spray: water droplets and salt particles of different chemical composition. However, sea-spray is mostly located at low altitudes near the surface ($\lessapprox 100\,\mathrm{m}$) if no frontal system lifts it up. There, it has little impact on the observations. As the optical properties of clouds and sea-spray are similar, the cloud treatment in this data product will at least partially mitigate the impact of possible sea-spray in the observational scene.

As last and least factor, the calculation of the air-mass factors is a numerical process that is subject to the accuracy of the implementation in SCIATRAN 3.1 and to the numerical accuracy of the computing system. These inaccuracies are negligible in comparison to the physical and observational inaccuracies.

4.8.4 Stratospheric contribution

Another factor impacting the accuracy of tropospheric NO_2 vertical column densities in this data product is the stratospheric correction. For this study, I use a combined reference sector and model method. In most cases this approach will be more robust than any of those methods individually. However, it is still prone to errors in the individual methods.

While the reference sector is based on observations and is therefore intrinsically coherent to the used data, it neglects variability in the zonal distribution. It is possible – even in the combined method – that the observations in the reference sector are abnormally high or low and will thus introduce errors towards lower and higher values, respectively. As long as these errors do not occur on short time scales, they should not impact the detection of long-range transport events, while they could impact the amount of NO_2 observed in these plumes.

The B3dCTM model data include the full horizontal structure of the stratospheric NO_2 distribution, gridded in cells of $2.5\,^\circ \times 3.75\,^\circ$. However, this distribution is based on model calculations only, and not verified with observational data. Therefore, I use the refence sector to adjust the stratospheric NO_2 vertical column density by an offset such that they agree with the data in the reference sector. This makes the data product robust, but it is still prone to introducing errors towards higher or lower values in the case of a malshaped modeled distribution.

These errors towards higher and lower values should, however, be longer-lasting and should not be strongly correlated to short-term tropospheric wind fields. Longer-lasting anomalies could be detected in the initial stages of the presented algorithm, but they should be removed from the dataset in the verification stages, where only plumes that can be traced back to emission regions will be verified as long-range transport events.

While I cannot exclude false positive NO_2 long-range transport plumes from errors in the stratospheric correction in the set of retrieved plumes, the used algorithm should mitigate their impact and filter most errors out.

4.8.5 Lightning NO_x

There is another source of NO_2 over the ocean: lightning (Beirle et al., 2004, 2009). Schumann and Huntrieser (2007) report that approximately 5 ± 3 TgN/a may originate from NO_x emitted by lightning ($LiNO_x$). Ott et al. (2010) show that NO_x concentrations

in thunderstorm clouds may be higher than 10 ppbv. They also show that only a small fraction of this $LiNO_x$ is located in the cloud top, where the sensitivity of satellite observations is high. Instead, most of it is located in the lower parts of the cloud or below the cloud, where the sensitivity of satellite observations is low.

For this study we tried to locate major plumes of $LiNO_x$ found in MOZAIC data (Sauvage et al., 2011). Only a very small fraction of these events was found in corresponding data of SCIAMACHY NO_2. For this purpose, SCIAMACHY data was processed in the same way as the GOME-2 data in this study.

Additionally, the verification using backtrajectories makes it unlikely that $LiNO_x$ plumes are classified as long-range transport events in this study. Wenig et al. (2003) report that in their NO_2 long-range transport study, $LiNO_x$ is likely to contribute to the total NO_2 content, but is most likely not the only or dominant source.

However, low-pressure regions – which turn out to foster long-range transport – are often linked to thunderstorms which will produce $LiNO_x$, thereby creating a higher probability of lightning NO_2 contamination of our data. As there is no way to unambiguously distinguish NO_2 from lightning and transport over the ocean in satellite data, this is an additional source of uncertainty in our estimates.

5 MACC-II reanalysis model data

For the second part of my study, I have used results from the MACC-II (Monitoring Atmospheric Composition and Climate – Interim Implementation) reanalysis data set[1] (Inness et al., 2013). MACC-II reanalysis is a four-dimensional global chemical transport model (GCTM) which provides historic 3-D modeled concentrations of O_3, water vapor, NO_2 and many other species. The purpose of MACC-II reanalysis is to provide predictions and analyses of air quality, climate forcing and the stratospheric ozone layer – mainly for research applications but also for environmental policies.

While forecasts are driven by near real-time (NRT) observational data, all available observational data including data that was not available in near-realtime is used in the reanalysis.

5.1 Overview

A global chemical transport model includes both eulerian transport of chemical species in the atmosphere and significant chemical and photochemical reactions of these species. In contrast to a lagrangian model – where individual parcels of particles are traced – eulerian models are concerned only with the concentration of a certain type of particle in a defined volume (the model cells) and how these evolve over time. This makes large-scale simulations with abundant species much more feasible. Any information about the origin of amounts of a given species or individual parcels of particles is lost in this type of model.

MACC-II reanalysis models reactive gases, greenhouse gases and aerosols. The model is run with a variety of data assimilation systems for each of these components, mostly driven by remote sensing observations. Anthropogenic emissions are modeled through data from the EDGAR inventory (Janssens-Maenhout et al., 2012). See also Section 2.2. The meteorological prediction from the ECMWF IFS (Barros et al., 1995) is used in conjunction with the MOZART GCTM. While IFS data determines the trajectory of air parcels, the humidity and other basic meteorological parameters, MOZART will govern the chemical reactions, dry and wet deposition, photolysis, etc. These calculations are performed in a horizontal resolution of $1.125° \times 1.125°$, corresponding to roughly 125 km in latitudinal direction and 85 km in longitudinal direction in mid-latitudes, where most long-range transport events are observed. Instantaneous three-dimensional grids are exported for every 3-hour step since June 2003. There are 60 model levels, which provide a detailed vertical profile.

NO_2 emissions are modeled from an assembled emission inventory which consists of multiple regional inventories. For Europe, for example, these inventories are gridded

[1] `https://www.gmes-atmosphere.eu/about/project/details/`

latitudinal grid	−90°–90° in steps of 1.125°
longitudinal grid	−180°–180° in steps of 1.125°
model levels	60 levels in the range n–m km
temporal resolution	3-hourly
archive length	2003-06-01 – 2012-12-31

Table 5.1: Fundamental parameters of the NO_2 concentration data from MACC-II reanalysis (Engelen, 2014).

with a roughly 7 km × 7 km cell size. The European inventory – TNO-MACC-II (Nederlandse Organisatie voor Toegepast Natuurwetenschappelijk Onderzoek, Netherlands Organisation for Applied Scientific Research) – consists of a downscaling from officially reported emissions to the EMEP[2] (European Monitoring and Evaluation Programme McInnes, 1996) emission inventory. For further details, see Kuenen et al. (2014). Fire emissions are modeled from the Global Fire Emissions Database (GFED van der Werf et al., 2010).

For a detailed model description, see Stein et al. (2012).

Table 5.1 shows the most important parameters of the used MACC-II reanalysis data. For more details on the delivered data, see Engelen (2014).

Reanalysis data can be accessed directly via a webservice[3].

5.2 Data preparation

In order to apply the algorithm I developed for GOME-2 / MetOp-A tropospheric NO_2 vertical column densities (see Chapter 4) to data from MACC-II reanalysis, I need to transform three-dimensional grids of NO_2 concentrations in 3-hour timesteps into daily maps of tropospheric NO_2 vertical column densities.

To this end, the concentrations of NO_2 are simply integrated vertically over the entire troposphere. The tropospheric and stratospheric contribution are separated by finding the altitude of the tropopause, as defined by the World Meteorological Organization (WMO McCalla, 1981): the lowest altitude level for which the thermal lapse rate falls below the value of 2 K/m in the 2 km above the level of interest. This can easily be determined from MACC-II reanalysis data so that these data are consistent.

The model data have to be projected onto the Earth's surface by integrating their NO_2 concentrations vertically. This vertical integration is not subject to peculiarities seen for GOME-2 / MetOp-A data – such as determining the air-mass factor, illumination intensities and other complications of full radiative transfer. Thus, there will be no impact of clouds (Section 4.5), the vertical distribution of NO_2 (Section 4.3) or other phenomena described in Chapter 4.

In GOME-2 / MetOp-A data, there is only (approximately) a single observation of NO_2 at any given location on the Earth's surface each day. However, MACC-II reanalysis provides eight values for each day. For reasons of comparison, the concentrations at

[2] `http://www.ceip.at/ms/ceip_home1/ceip_home/ceip_topnavi/home_emep/`
[3] `http://apps.ecmwf.int/datasets/data/macc-reanalysis/`

9:30 a.m. local time are interpolated from this data set and exported into a single, two-dimensional map of tropospheric NO_2 vertical column densities for each day.

This makes the data in their basic properties comparable – they are both two-dimensional maps of tropospheric NO_2 vertical column densities at the same local time – however, they are subject to different effects. For example, model data have a significantly lower signal-to-noise ratio than satellite observations; they include several parameterizations that form only an approximation of the processes taking place in the atmosphere; they are limited to NO_2 emitted from sources in their emission inventories and the quality of tropospheric NO_2 vertical column densities will depend on these inventories being up-to-date; they are gridded differently using $1.125\,^\circ \times 1.125\,^\circ$ for MACC-II reanalysis and $0.5\,^\circ \times 0.5\,^\circ$ for GOME-2 / MetOp-A data.

Finding similar phenomena of long-range transport in both data sets will indicate that the results are not emerging from the limitations of a single data source (model or satellite) or special way to prepare the data. Instead, this will be a strong indication that what we find are observations of a phenomenon occuring in our atmosphere.

5.3 Limitations

At the given resolution, MACC-II reanalysis cannot explicitly model processes at a small horizontal or vertical scale. As other GCTMs, it uses prameterizations to deal with these small-scale processes. These parameterizations concern:

- chemical and photochemical reactions (MOZART)
- convective processes (IFS)
- mixing, eddies and filamentation (IFS)

These parameterizations will undoubtedly affect the appearance and prevalence of long-range transport events in MACC-II reanalysis data. This has to be taken into account when analyzing two quantities that are both subject to parameterization, as different parameterizations may lead to inconsistent results.

NO_2 emissions in MACC-II reanalysis do not include individual sources, only spacially averaged emission inventory data, albeit at high resolutions. This means that individual events or anomalies in the emissions are not properly modeled in MACC-II reanalysis data. For individual long-range transport events, this might pose a problem; these might not appear in MACC-II reanalysis data at all. However, most such events appear to have their origin in large-scale anthropogenic emissions from densely populated areas. Emissions in these regions are very predictable, so that the majority of long-range transport events should not be affected by the static emission inventory.

Besides that, GCTMs are always subject to computational uncertainty, potential leaks of trace gases or energy, physical approximations and other sources of uncertainty. These should, however, not pose a major problem for the use of MACC-II reanalysis in this study.

6 Long-range transport detection algorithm

In order to study the phenomenon of NO_2 long-range transport in a systematic way, I have developed an algorithm which automatically detects, assesses and verifies these events in timeseries of 2-D data. The algorithm is designed to work with both satellite (see Chapter 4) and model data (see Chapter 5) to allow a comparable study of both.

6.1 Concept

Long-range transport events are characterized by a plume of trace gas which is transported by rapid winds over long distances. Depending on the data used, these plumes have different characteristics. In data that feature a single observation each day, these plumes suddenly appear over a region without sources. Due to high wind speeds, observations of a long-range transport plume on consecutive days usually do not overlap. Such a positive anomaly in the data indicates that a long-range transport might be in progress.

A positive anomaly could, however, also originate from artifacts in the data. To exclude this possibility, the algorithm computes backtrajectories for all found anomalies, This way, it verifies that the plume originates within an emission region in the last few days. Also, anomalies below a certain threshold NO_2 content are discarded.

If a plume satisfies both conditions – a positive anomaly away from sources and a verified backtrajectory to an emission region – I assume that it actually belongs to a long-range transport event. Then, I can assess properties of this plume to perform further analyses on both the individual plumes and the entire data set.

6.2 Implementation

I implemented the algorithm in the Python programming language (Van Rossum and Drake, 2003), to allow for rapid design and iterative processing. For numerical computations, I used the powerful NumPy library (Ascher et al., 2001) supplemented with sophisticated elements from SciPy (Jones et al., 2001). The algorithm is based on the PyDOAS software suite (co-maintained by Andreas Hilboll), used by the Institute for Environmental Physics of the University of Bremen. The implementation in Python also allows the analysis of results to tie in directly to the detection algorithm.

Further, the algorithm utilizes two pieces of auxiliary software during its operation: SCIATRAN 3.1 and HYSPLIT_v4.

The algorithm takes a timeseries of daily tropospheric NO_2 vertical column density maps, global 3-D meteorological data and maps of the seasonal average of tropospheric NO_2 vertical column densities as input and returns a set of verified NO_2 long-range

transport events with their NO_2 content, age, altitude at observation, and a full back-trajectory for each cell on the coordinate grid belonging to it.

It operates in multiple steps:

1. Prepare the input data and create a set of sliding mean maps and sliding standard deviation maps from tropospheric NO_2 vertical column density maps in the input timeseries.

2. Iterate over all maps in the input timeseries, one date at a time:
   a) Subtract the sliding mean map for the corresponding date from the input data to obtain the daily anomaly.
   b) Divide the anomaly by the standard deviation map for that day to obtain a map of σ-levels.
   c) Select all cells with a σ-level above a certain threshold as seeds.
   d) Group seeds in close distance from each other into clusters.
   e) Discard seeds without a near neighbor.
   f) For all clusters, add all adjacent cells with a σ-level above a certain lower threshold and iterate until no further cells are added. Merge clusters if necessary.
   g) For all cells in the cluster, record the corresponding NO_2 vertical column density anomaly.
   h) These clusters form NO_2 anomaly plumes. They represent potential long-range transport events.

3. Iterate over all potential long-range transport events:
   a) Initialize a HYSPLIT_v4 backtrajectory simulation for the plume.
   b) Insert the coordinates of all cells in the plume into the simulation as starting points. Do this at different altitude levels in steps of 500 m from 1000 m to 6000 m.
   c) Calculate all the backtrajectories for 5 days backwards.
   d) Record horizontal and vertical coordinates for all cells at all timesteps from all initial altitudes.
   e) For each timestep and each initial altitude, determine the number of cells within the planetary boundary layer as its score.
   f) Select the timestep and initial altitude with the highest score as the most likely starting point of the plume's backtrajectory.
   g) Determine the seasonal average tropospheric NO_2 vertical column density for each cell in the plume at its starting location as its source pollution.
   h) If the source pollution averaged over all cells in the plume is above a certain threshold, accept the potential long-range transport as a verified long-range transport event.

i) Determine further properties of the plume from its cells, their respective NO_2 anomaly, and its most likely backtrajectory.

This outlines the conceptual working of the developed algorithm.

Potential double or multiple detections of a single plume in different (sequential) observations are treated as separate long-range transport events in this algorithm due to the complications of identifying these automatically.

Preparation of input data

The first step of the algorithm – illustrated in Figure 6.1 – only prepares the input data for further processing. In this step, the algorithm receives a timeseries of tropospheric NO_2 vertical column density maps[1]. Note that the algorithm has no indication about how this timeseries was obtained. It can thus be easily used to analyze data from both satellite observations and models in the same manner.

For each date of interest in the timeseries, the algorithm assembles a set of the n_{days} days preceeding and following the date of interest. Then, it computes global maps of the mean and standard deviation of this set and stores them as reference for the day of interest.

The day of interest is not included in this set, to avoid the impact of long-range transport plumes in the data on the mean and standard deviation maps corresponding to the date of their occurrence in the data. The mean and standard deviation of each point are thus based on up to $2n_{\mathrm{days}}$ data points. If no data is available for a coordinate cell in the input data in one or more maps of the set, the mean and standard deviation are computed on the remaining data points. For high latitudes, cells will regularly contain no observations or only a single observation in local winter. For the corresponding dates, these cells are masked out in later steps of the algorithm.

From visual inspection of the GOME-2 dataset, I have found that plumes from long-range transport events tend to move quickly and do not overlap spatially in observations of consecutive days. It is thus enough to exclude the day of interest and include the days immediately preceeding and following it without introducing any self-reference of long-range transport plumes that could hamper their detection.

To avoid any biases at the beginning and end of the timeseries, I do not compute any mean and standard deviation maps for both the first and last n_{days} in the timeseries, where the input data set availability is highly asymmetric.

6.2.1 Detection

After the global mean and standard deviation maps of tropospheric NO_2 vertical column density are created for the timeseries, the algorithm processes each day in the timeseries individually and isolated from the rest of the timeseries. Especially, the algorithm does not use knowledge about long-range transport plumes on preceeding or following days to find or interpret long-range transport events on the day of interest. This makes the detections less biased and gives a stronger confidence in events where the NO_2 plume

[1] In principle, the algorithm can also be used for other data and is not restricted to tropospheric data or the particular trace gas NO_2, although it was optimized for it.

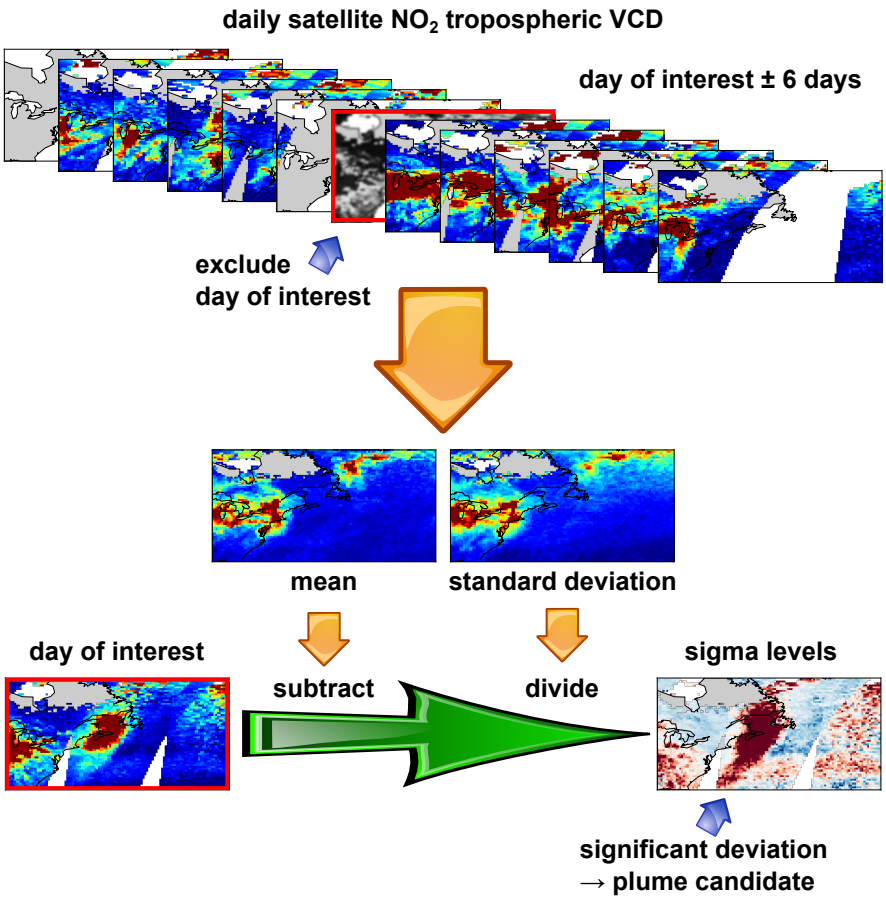

Figure 6.1: Schematics of how GOME-2 satellite data is prepared in order to detect NO_2 long-range transport events. The observational data are compared to a sliding mean and standard deviation of the n_{days} (in this study: six) days preceeding and following the day of observation. Strong positive anomalies in NO_2 vertical column densities are selected as candidates for long-range transport plumes.

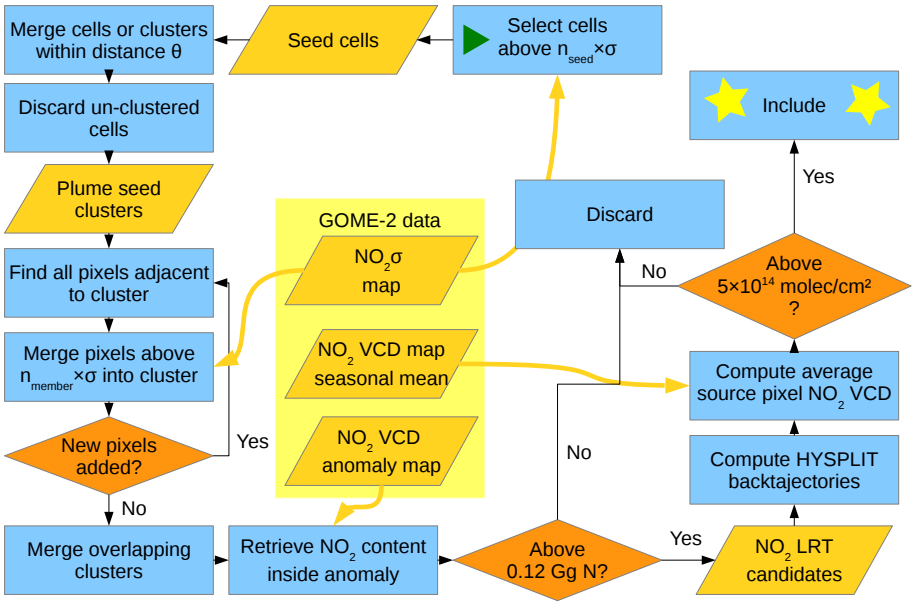

Figure 6.2: Schematics of how long-range transport plumes are detected using my algorithm, starting from the prepared GOME-2 data as shown in Figure 6.1. The algorithm starts at the green triangle ("play") and ends at the yellow stars.

was observed on multiple, consecutive days. Later, I manually link long-range transport plume observations from multiple days into a single long-range transport event in selected case studies in Section 7.1.

In the following, the algorithm finds cells in the input data, which exhibit a strongly elevated tropospheric NO_2 vertical column density, based on the input data and the corresponding sliding mean and standard deviation. Find schematics of these and further steps in Figure 6.2.

The algorithm takes the input NO_2 map for the day of interest and subtracts the corresponding sliding mean map – reflecting the current NO_2 background – to retrieve the tropospheric NO_2 vertical column density anomaly. This anomaly already exhibits positive and negative deviations from the background, resulting from source variability, natural variability, and short- or long-range transport of NO_2. In observational data, random fluctuations from the measurement process may show in the anomaly while model data should show no artifacts (if the model is well done).

This anomaly is then divided by the corresponding sliding standard deviation map. This results in a σ-level map for the day, representing the strength of observed deviations compared to intrinsic variability of the tropospheric NO_2 vertical column density at this date and in this cell. This allows the algorithm to only select cells with significant anomalies as potential members of long-range transport plumes. As the anomaly is determined from a deviation from the days before and after, this method is sensitive only to very rapidly moving or quickly appearing and disappearing masses of NO_2.

Now, the algorithm selects all cells in the σ-level map that are above a certain threshold

n_{seed} as potential long-range transport plume member cells. This means that only cells are selected that lie at least n_{seed} standard deviations above the current sliding mean value for the tropospheric NO_2 vertical column density. These cells are called seeds, as they form the initial core of the plumes during the detection process.

The seeds are now grouped together into clusters. Two seeds 1 and 2 that are separated by a distance of $\theta_{1,2} \leq \theta_{\text{sep}}$ are grouped together to form a cluster. The separation $\theta_{1,2}$ between the two seeds is measured by the great circle distance (with $\theta_{\text{sep}} = 1^\circ \hat{=} 111\,\text{km}$) of the centers of the seeds and is thus invariant of the latitude of the seeds in question.

Each seed s that is located within $\theta_{\text{s,c}} \leq \theta_{\text{sep}}$ of any member of an existing cluster c is added to the cluster. If a cluster *c1* has at least one member that is within a distance $\theta_{\text{c1,c2}} \leq \theta_{\text{sep}}$ of any member of another cluster *c2*, the two clusters are merged and form a new cluster that consists of all seeds of each of the initial two clusters *c1* and *c2* (compare Figure 6.2).

All seeds that do not have a nearest neighbor seed within a distance θ_{sep} are discarded at the end of this process. These seeds are likely to be statistical outliers and are expected to occur in noisy data. In fact, in GOME-2 / MetOp-A data, around half of all plumes are discarded in this way; in MACC-II reanalysis data, only around 10 % are discarded.

After this process is done, all seeds are either a member of a cluster of two or more seeds or have been discarded. All resulting clusters have a minimum separation of their individual seeds of more than θ_{sep} – they would have been merged otherwise.

Now, these clusters are grown by the algorihtm to include all surrounding cells that lie at or above a σ-level threshold of n_{member}. For each seed in the cluster, the algorithm looks at all cells within radius θ_{sep} of the seed. If any of these cells are not yet part of the cluster and exhibit a σ-level of at least n_{member}, they are added to the cluster and the same procedure is repeated for the newly added cell. This process ends when no cells with a σ-level of at least n_{member} are within a distance θ_{sep} of cells belonging to the cluster.

This two-step process of forming the cluster – first with σ-levels above n_{seed}, then above n_{member} – helps to filter out false positives in the data. Starting directly with all cells with a σ-level above n_{member} will yield a lot of clusters that are caused by artifacts in the input data. However, including only cells above n_{seed} will omit significant fractions of the NO_2 plumes. In the vicinity of a strong anomaly, it is very likely that cells above n_{member} are indeed a part of the plume.

When this process is finished, the algorithm has assembled a set of potential NO_2 long-range transport plumes: clusters consisting of a set of cells from the input data with a positive anomaly of at least $n_{\text{member}}\sigma$ above the current sliding mean.

Still, false positive results – plumes being detected where no transport occurs – and false negatives – the algorithm missing a long-range transport event in the data – are bound to occur. When tuning the parameters for this algorithm, I have to weigh off the amount of false positives and false negatives that the algorithm will produce. This is the case in any form of pattern matching and machine learning.

6.2.2 Assessment

Now, we have a set of potential NO_2 long-range transport plumes with their respective member cells.

For each cell in the plume, the tropospheric NO_2 vertical column density anomaly is recorded, as well as its coordinates and the surface area encompassed by the cell. The anomaly – current observation minus sliding mean – represents the contribution to the tropospheric NO_2 vertical column density from NO_2 in the plume.

The algorithm now calculates the total amount of NO_2 contained in the plume by adding up the product of the tropospheric NO_2 vertical column density anomaly and the area encompassed for each cell. This gives the total number of NO_2 molecules contained in the anomalous plume.

I implemented a limit on the minimum size a plume must have for further analysis. All plumes with an NO_2 content of $n_{\mathrm{molec,min}}$ or higher are considered for further analysis. All plumes that fail this requirement are discarded and not used in the further process.

This lower limit on the NO_2 content is implemented both to further filter out false positives and for computational purposes. The most massive NO_2 plumes are most interesting; the plethora of small plumes does not add much further insight and exhausts computational capacities.

6.2.3 Backtrajectories

By now, the algorithm has assembled a set of potential NO_2 long-range transport plumes above a minimum size and determined a few basic properties. In the next step, it will calculate backtrajectories for all cells in every plume at various altitude levels. This will allow us to determine the most likely origin of the plume, its altitude in the input data and its age. Also, it will allow us to verify it as a real NO_2 long-range transport plume.

The backtrajectories are calculated individually for each plume using the HYSPLIT_v4 lagrangian transport model (Draxler and Hess, 1997, 1998; Draxler, 1999). HYSPLIT_v4 computes trajectories of given individual air parcels forwards or backwards in time. In our case, it uses GDAS (Global Data Assimilation System, National Climatic Data Center, NESDIS, NOAA, U.S. Department of Commerce) meteorological data[2] to compute wind speeds. These data have a horizontal resolution of $1\,^\circ \times 1\,^\circ$ on 23 model levels from $1000 \ldots 20\,\mathrm{hPa}$. HYSPLIT_v4 operates using an adaptive internal integration time step and returns the current horizontal and vertical positions of the initial point set for every hour. It only operates on points (or point-like trace gas parcels), not volumes. So, no shear is applied to the individual cells and only their centers are traced. However, shear will be present when tracing multiple adjacent cells, as I do for this study. Also, HYSPLIT_v4 does not take any chemistry into account and thus cannot estimate the evolution of the plume's NO_2 content.

Since MACC-II reanalysis uses ECMWF meteorological data while I feed HYSPLIT_v4 with GDAS data, even a perfect detection of a plume in MACC-II reanalysis data might not lead to a perfect backtrajectory, barring all issues of spatial and temporal resolution.

The input data for the algorithm – a timeseries of global tropospheric NO_2 vertical column density maps – do not contain any information on the vertical profile of the observed NO_2 column. It is thus impossible to determine the altitude of the NO_2 plume directly from the input data. To calculate a backtrajectory, the algorithm needs full horizontal and vertical coordinates of the cell in question. To circumvent this problem,

[2] `https://ready.arl.noaa.gov/gdas1.php`

the algorithm computes multiple backtrajectories for each cell in the plume and later determines which best to use.

In practice, the algorithm runs multiple HYSPLIT_v4 simulations at different altitude levels for the observed plume cells. For each altitude level, the center of each cell is given as horizontal starting coordinates with the altitude level giving the vertical coordinate. The simulation is then run backwards for a simulated timespan of Δt_{back}. There needs to be a temporal truncation in the backtrajectories for the following reasons:

- NO_2 has a finite lifetime in the order of days (even in the free troposphere, see Section 2.1).
- Atmospheric turbulence will disperse any large scale plume over the course of multiple days.
- Practically, any plume of NO_2 can be traced back to a strong source *eventually* – especially, when probing multiple altitude levels.

The 3-dimensional coordinates of each cell center are recorded at each timestep in the simulation for each altitude level.

The algorithm uses altitude levels from 1,000 m to 6,000 m in steps of 500 m, resulting in a total of 11 levels. Altitudes below 1,000 m are not considered as altitudes upon observation (though these values are allowed in the backtrajectories), because there, the liefetime of NO_2 is too short to facilitate long-range transport. Furthermore, the plume can be expected to be vertically extended which prohibits 0 m a.m.s.l. as a valid center of the plume. Trajectories that lead to an observation at this altitude are thus not credible, although they might otherwise be favored in the following selection process. The simulation uses a lower boundary of 0 m and an upper boundary of 10,000 m. Trajectories that cross the upper boundary are discarded for all earlier times. These trajectories are not likely to be part of tropospheric long-range transport.

The algorithm now has to select a most likely starting altitude. I assume that the plume can be adequately described using only a single altitude for all member cells. This is a simplification to handle otherwise unfeasible amounts of possible plume shapes. However, observations in satellite data show that plumes stay compact and well-defined over an extended period of time. This means, that no strong shear winds – neither horizontal nor vertical (which would in turn lead to strong horizontal shear) – disperse the plumes which makes the single-altitude assumption a viable simplification.

To select the starting altitude, the algorithm computes a score for each timestep in the backtrajectories for each modeled altitude. This score is computed by counting the number of cells that reside within an altitude range of 0–1,000 m above the continental surface at this particular timestep. Cells over the ocean never contribute to the score, as there are no NO_2 sources which are concentrated enough to emit long-range transport plumes. The algorithm then selects the altitude and timestep with the highest score as the most likely starting point of the plume's backtrajectory.

I have implemented and tested other scoring mechanisms, which directly took the NO_2 pollution of of the grid cell, the dispersion of the cells or the duration of the backtrajectory into account. A study of the resulting backtrajectories for long-range transport events found by visual inspection showed, that this added complexity does

not lead to more plausible backtrajectories. I thus used the most simple scoring system in the final implementation of the algorithm.

From the selected temporal starting point of the backtrajectory, the algorithm can now derive the age of the plume at the time of observation, its altitude, its trajectory, altitude evolution, traveling speed, etc. The trajectories for all other altitudes are discarded. Also, trajectories for timesteps further back in time than the age of the plume (trajectories before the starting point) are discarded and not used in further analysis.

This method has some peculiarities. First, it will tend to find a young and low most likely backtrajectory for plumes in the vicinity of continents. This is, because the trajectories will quickly enter the lowest 1,000 m and quickly enter the continent, before the trajectories disperse and stray. A compact trajectory coming from the continent will always have a higher score than a more dispersed one, where individual cells will be above the 1,000 m limit or over the ocean. However, these trajectories are also more plausible in the vicinity of a continent. False attributions are possible, for example, when a plume from the continent travels over an island just off the coast. Then, trajectories are prone to ending over the island instead of the continent.

Second, for plumes that are far away from continents, high altitudes are more likely to be selected. This is due to the high wind speeds which allow the plume to travel there from the continent within the time frame configured for the HYSPLIT_v4 simulation. This may in some cases lead to a false estimate of altitude and age for a remote plume, although lower ages are more plausible considering the lifetime of NO_2.

6.2.4 Verification

The algorithm now has a set of potential NO_2 long-range transport plumes with their most likely backtrajectories, NO_2 content and more. In the last step of the algorithm, these plumes are divided into verified and non-verified long-range transports. This step uses the backtrajectories, seasonally-averaged tropospheric NO_2 vertical column densities and the number of cells in the plume.

By now, the algorithm has established the various properties of the plumes and their most likely backtrajectory *if* they are indeed part of a long-range transport event. The next step is to verify these transports.

For this, I have prepared seasonal[3] average maps of the cloud-free GOME-2 / MetOp-A tropospheric NO_2 vertical column density. These maps indicate the average pollutedness of the regions. As NO_2 in the planetary boundary layer has a very short lifetime, this yields a reasonable representation of the local NO_2 emission strength. The algorithm will use these data as a measure of NO_2 source strength.

The algorithm computes the average tropospheric NO_2 vertical column density at the starting points of the backtrajectories over all cells in the plume that were within 1,000 m from the surface at emission time. This gives the average pollutedness of the plume's most likely origin. A plume is only accepted as verified if this value is greater than a threshold of $\overline{VCD}_{\text{source}}$. All plumes that do not satisfy this criterion are discarded as non-verified.

[3] DJF: December, January, February; MAM: March, April, May; JJA: June, July, August; SON: September, October, November.

This threshold $\overline{VCD}_{\text{source}}$ is fine-tuned by visual inspection to include obvious examples of NO_2 long-range transport and reject obvious artifacts in GOME-2 satellite data. It is based on the assumption that emission regions below a certain pollutedness are not capable of spawning NO_2 long-range transport events. Thus, any plume that most likely originates in such a region is assumed not to be part of a long-range transport event.

After all of these steps, the algorithm has produced a set of verified NO_2 long-range transport events, with detailed information on their location, NO_2 content, horizontal extent, age, altitude and backtrajectory from a timeseries of input tropospheric NO_2 vertical column density maps, GDAS meteorological data and seasonal cloud-free average tropospheric NO_2 vertical column density maps. With this set, it is now possible to perform detailed studies on individual long-range transport plumes or statistical evaluations over all or some subset of the detected events.

6.3 Application

The described algorithm has a lot of freely definable parameters. These allow for fine-tuning of the algorithm's results.

In practice, I have applied the algorithm to a subset of the GOME-2 data that were later used in this study to tune its variables. I changed one or more of the variables and then visually inspected the results. I had previously identified multi-day NO_2 long-range transport events in the satellite data that should be detected and correctly attributed to their apparent sources by the algorithm. I also checked the algorithm's results for obvious artifacts in the data that were verified as long-range transport event and tried to minimize those.

This fine-tuning of algorithm parameters is a heuristic approach – the selected parameters are not grounded in physical equations, but dependent on the input dataset and the experimentor's judgement. However, it turned out that there is a range of parameter sets for which the results of the algorithm were relatively stable and where most obvious long-range transport events are correctly identified as such and only few artifacts are falsely identified as belonging to a long-range transport event.

In this study, the parameter sets for GOME-2 data and MACC-II reanalysis model data are almost identical. This is possible as both data were processed to contain the same information. The single exception is that due to the coarser horizontal resolution of the model data, the maximum merging distance for seeds and plumes θ_{sep} – the minimum great-circle angular separation between two clusters – had to be increased above the grid resolution (on the equator).

The parameter values used in this study can be found in Table 6.1.

Note, that it is practically inevitable in such an event detection and classification algorithm to retain from the data both false positives – artifacts or random fluctuations in the data that are classified as long-range transport events – and false negatives – factual long-range transport events that are either not identified or discarded as non-verified. The chosen set of parameters appeared to me as the optimum balance between false positive and false negative results and computational considerations.

Table 6.1: Parameters used to apply the algorithm to GOME-2 satellite data and MACC-II reanalysis model data. The parameters are identical, except for θ_{sep} which had to be increased for the coarse resolution of global chemical transport models. Required average source VCDs are low in comparison to observations of polluted areas to account for stray pixels in the backtrajectories.

	GOME-2	MACC-II reanalysis
$n_{\text{NO}_2,\text{min}}$	$5 \cdot 10^{30}$molec	$5 \cdot 10^{30}$molec
n_{seed}	5	5
n_{member}	3	3
θ_{sep}	1.0°	1.5°
$\overline{VCD}_{\text{source}}$	$2 \cdot 10^{14}$ molecules/cm^2	$2 \cdot 10^{14}$ molecules/cm^2
Δt_{back}	120 h	120 h
n_{days}	±6	±6

6.4 Limitations

There are some limitations that apply to this method of detecting NO_2 long-range transport events in timeseries of tropospheric NO_2 vertical column density maps.

6.4.1 Detection

The algorithm is designed to operate only over the ocean. NO_2 vertical column densities over continental areas are not considered as candidates for long-range transport plumes. There are multiple problems with detections over land masses:

- All emissions significant to NO_2 long-range transport are situated on the continents. This means that there is a lot of intrinsic variability in tropospheric NO_2 vertical column densities and it will be hard to adjust n_{seed} and n_{member} to reliably yield plumes from long-range transport events but only rarely from intrinsic variability. The number of false positives will inevitably rise. Also, the number of false negatives – long-range transport events that are not detected – will rise as plumes get covered up by high intrinsic variability from source emissions which will reflect in a high sliding standard deviation.
- Over the ocean, it is safe to assume that a plume will either have traveled there or be an artifact of the data. Over the continent, the plume's NO_2 could also have been emitted in place.
- Tracing the plumes back to their sources is highly error-prone. Over the ocean it is reasonable to assume that the NO_2 originates from the first emission region that the backtrajectories reach. Over the continent, plumes might be traced back to one emission region while they were actually emitted from another one that was reached by the same backtrajectory at earlier times (further in the backtrajectory) or an entirely different backtrajectory.
- Over continental areas, the assumption that all NO_2 will reside in a single, well-defined layer is not valid. This means that the air-mass factor calculations of

Chapter 4 are not valid there. Ths algorithm cannot estimate the plume's NO_2 content over the continent.

These reasons make it difficult to apply this algorithm to continental long-range transport.

The oceans with their low NO_x sources allow us to see plumes clearly, whereas we might easily miss them over the continents or interpret varying emissions or effects of meteorological conditions on NO_2 observations as long-range transport events. Plumes over the ocean can only result from transport processes, from artifacts in the observations or retrieval or from individual events such as large thunderstorms or uncontrolled fires on oil platforms. NO_x emissions from lightning are rarely detected in satellite data, due to both small vertical column densities and unfavorable viewing conditions (Beirle et al., 2009). However, in some cases they can interfere with our retrieval as discussed in section Subsection 4.8.5. Emissions from both ships and aircraft are too regular and too small in absolute concentrations to appear as anomalous plumes in the data.

Satellite measurements always have noise in their signal. Because of this intrinsic variability, the σ-levels of satellite data will be lower than the σ-levels for smooth model data. This means that anomalies have to be stronger (in absolute values) in satellite data to be considered as potential long-range transport plumes. This balances with the fact that model data tend to diffuse the plume shape stronger and thus lead to smaller anomalies.

Close to emission regions, where regular outflow of tropospheric NO_2 takes place, the algorithm is unlikely to discern a long-range transport plume from variability in the regular outflow. It will thus detect only few long-range transport plumes in the vicinity of high emission-regions. This can be seen in the age distribution of detected plumes in Subsection 7.2.2.

Artifacts that are traced back to a strong source region will also be accepted by the plume and lead to false positives. However, the verification process still mitigates the impact of false positives.

The algorithm has no means to link observations of the same plume on consecutive observations. I have done this manually for a set of case studies (as presented in Section 7.1). In principle, this could be implemented using the HYSPLIT_v4 backtrajectories, but it would also need to take the coarseness of the backtrajectories into account that may – again – lead to false positive and false negative links of long-range transports.

Also, the algorithm is dependent on a strong signal to noise ratio in the input data. Noisy data will lead to a reduction in the number of detected plumes, especially in the lower part of the mass spectrum.

6.4.2 Backtrajectories

As described in Subsection 6.2.3, the part of the algorithm concerning backtrajectories is prone to a few tendencies:

- It favors young plume ages and low plume altitudes in the vicinity of continents.

- It favors old plume ages and high plume altitudes at great distance from the nearest continent.
- Convoluted coast lines (like the European North Sea) are likely to produce more verified plumes, as emission regions are located in a broad range of wind directions which leads to many matches in the backtrajectories.

The first two tendencies describe a reasonable expectation, that plumes near their sources are still at low altitudes and have traveled there in a short amount of time, and remote plumes must have traveled there over a long time, probably at elevated altitudes where wind speeds are high. Therefore, these tendencies actually foster the correct assessment of plume properties and are in accordance with atmospheric physics.

In the backtrajectories, there are always stray trajectories – trajectories that deviate strongly from the bulk of the trajectories. These stray backtrajectories often originate from the boundary of the plume. They are caused by the low resolution of the input NO_2 data and deviations of the input altitude from the actual altitude of the NO_2 in the plume. In the chaotic meteorological system, these small deviations are exponentially amplified with backtracing time. The verification process takes this possibility into account and was designed to mitigate this problem by requiring only a relatively low source concentration averaged over all trajectories.

The altitudes were limited to steps of 500 m due to computational considerations. Also, measurements by Crawford et al. (2003) show that long-range transport plumes are vertically extended and 500 m should be a sufficient resolution to discern the different paths that plumes at different altitudes would take.

The algorithm is dependent on the fine-tuning of its parameters. For most of these parameters, there is no pure physical reasoning that could be used to set them to a proper value. Instead, the parameters are mostly set heuristically with some considerations of properties of the input data.

For the selection of the backtrajectories, it can happen that trajectories of multiple ages and altitudes yield a similar score. It might be that the trajectories with lower scores are actually more plausible. However, it is not feasible to check all potential long-range transport plumes by hand and this problem is thus inevitable in a large-scale study. This may lead not only to a wrong age and altitude of the plume but also to appropriating the long-range transport plume to the wrong source region. For trajectories with exactly the same score, the lowest, youngest trajectory is selected – considering that NO_2 has a short lifetime and is emitted mostly in the planetary boundary layer.

In sensitivity studies, more complex scoring systems for potential backtrajectories have not shown any further improvement and do not justify the amount of added complexity.

7 NO_2 long-range transport in GOME-2 data

7.1 Case studies

Before analyzing a full 5-year data set of detected long-range transport events, it is illustrative to scrutinize a few hand-selected events from the data that serve to exemplify the different types of transports and their nature. These events can easily be spotted in GOME-2 / MetOp-A data without any special treatment, except for disabling the cloud filter.

To gain understanding of these events, I use NCEP DOE AMIP-II Reanalysis (National Climatic Data Center, NESDIS, NOAA, U.S. Department of Commerce) data to correlate the event to meteorological data. A detailed listing of the retrieved properties of the following events can be found in Table 7.1.

7.1.1 North Atlantic, 17–19 December 2007

Figure 7.1 shows a very distinct and NO_2-laden example of a long-range transport event.

The NO_2 plume is first observed over the North Atlantic near the East Coast of the USA on 17 December 2007. On the subsequent day, it has moved towards the North-East, and can be found between Newfoundland and Greenland. On the next and last day of observation, It has moved to the North Atlantic, directly south of Greenland. The plume covers the pixels directly at the edge of the observations. From the shape and NO_2 vertical column densities, is apparent that the plume extends farther north beyond the field of observation of GOME-2 / MetOp-A. Parts of it might have already been transported over Greenland.

Unfortunately, the plume's separation from the shore cannot be observed in the data. This is due to a special mode in which GOME-2 / MetOp-A is rarely but regularly operated: the narrow swath mode. In this mode, the swath of GOME-2 / MetOp-A observations is reduced to about a sixth of its usual width, allowing the instrument to operate at higher resolution. This was the case on 16 December 2007, when – both seen in the timeseries and backtrajectories – the plume separated from its emission region on the northern East Coast of the USA. This leaves a gap in the data exactly over the region of interest.

From the NCEP DOE AMIP-II Reanalysis data and the HYSPLIT_v4 backtrajectories it is evident that the core of the plume originates from the major industrial regions near the north-eastern coast of the United States: New York, Chicago, Detroit, Boston. NCEP DOE AMIP-II Reanalysis meteorological data for this region show a small low-pressure region over the central United States that quickly evolves into a cyclone. This cyclone follows the typical storm tracks (Chang and Fu, 2002) from North America

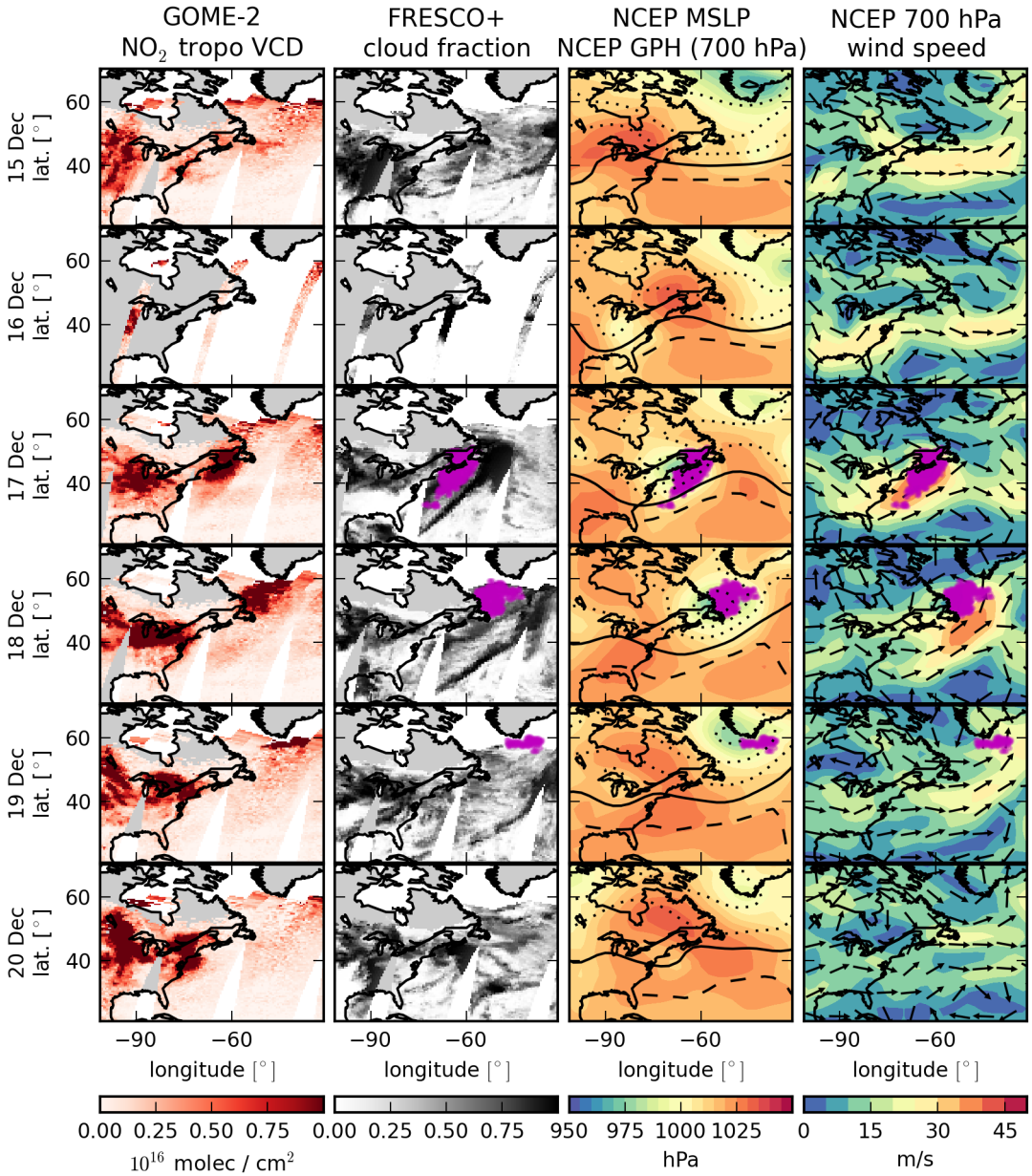

Figure 7.1: Timeseries of the days preceding and during a long-range transport event over the North Atlantic on 17 to 19 December 2007. The locations of satellite pixels identified as belonging to the long-range transport plume are indicated by purple circles in the meteorological data. Shown are (left) the GOME-2 NO_2 tropospheric vertical column density, (center-left) FRESCO+ cloud fractions, (right-center, colors) the NCEP DOE AMIP-II Reanalysis mean sea-level pressure and (right-center, contours) geopotential height at 700 hPa and (right) horizontal wind velocities at 700 hPa (speed and direction). For geopotential height, the solid line denotes 3 km, dashed / dotted lines indicate higher / lower geopotential height in steps of 125 m. In the time series, a small low pressure system is quickly evolving into a cyclone. It lifts an NO_2 plume over the industrial regions of the north-eastern USA into the free troposphere, which can be seen in the backtrajectories. Subsequently, it transports the plume towards Greenland where the plume disappears into the Arctic night, where GOME-2 / MetOp-A can no longer observe it.

Table 7.1: Properties of NO_2 plumes observed during long-range transport case studies as derivded from processing GOME-2 / MetOp-A data through the algorithm described in Chapter 6. All plume observations were processed independently of their previous or follow-up observations.

Date	Plume Center		Altitude [km]	Age [h]	NO_2 content [Gg N]	Area [10^3 km^2]
North Atlantic						
2007-12-17	$45°N$	$63°W$	1.0	46	2.31	1093
2007-12-18	$55°N$	$52°W$	1.5	83	1.98	698
2007-12-19	$58°N$	$42°W$	2.0	95	0.65	207
South Africa						
2008-07-08	$40°S$	$41°E$	1.0	35	0.27	166
2008-07-09	$42°S$	$53°E$	2.0	45	1.58	642
2008-07-10	$41°S$	$78°E$	1.5	87	1.74	1293
2008-07-11	$35°S$	$93°E$	6.0	91	1.40	1898
2008-07-12	$30°S$	$103°E$	4.5	115	0.39	881
Australia						
2008-04-27	$46°S$	$159°E$	4.0	85	1.83	1256
2008-04-28	$60°S$	$175°W$	1.0	59	0.89	311
2008-04-29	$52°S$	$152°W$	1.5	61	0.45	288
2008-04-30	$43°S$	$141°W$	3.0	118	0.16	319
Central Europe						
2010-10-01	$60°N$	$0°W$	1.0	21	0.38	372
2010-10-02	$64°N$	$11°W$	1.0	36	0.75	778

towards the North Atlantic and Arctic Ocean.

A cold front sweeps the East Coast of the United States on 16 December 2007. The NO_2 has built up in the region, under stable, relatively calm conditions. In the GOME-2 / MetOp-A data, the NO_2 is not observed as it resides in a high-pressure system near the surface under a stable cloud cover. In the backtrajectories (Figure 7.2) the bulk of the plume cells is lifted up on 16 December 2007. The cells already elevated and the cells lifted up later in the course of the transport are most likely stray pixels, an artifact from the transport modeling. The trajectories do not fully agree. Especially the trajectories for 18 December 2007 appear to be problematic; this is also the backtrajectory which estimates an earlier emission of the plume than the other backtrajectories. The trajectories of both 17 and 19 December 2008 agree on the initial uplift from the boundary layer during the course of 16 December 2007.

The altitude distribution of trajectories is neccessarily broad, as I use strongly simplified assumptions to calculate them: coarse resolution and a single layer plume. This will result in vastly different trajectories, especially for cells near the fringe of the plume.

The plume retains its compact form with relatively sharp boundaries. This indicates that the plume does not quickly disperse and closely follows the core of the cyclone. Only small distortions can be seen over the next two days. Tropospheric NO_2 vertical column densities stay highly elevated and the plume is clearly visible until it leaves the observable

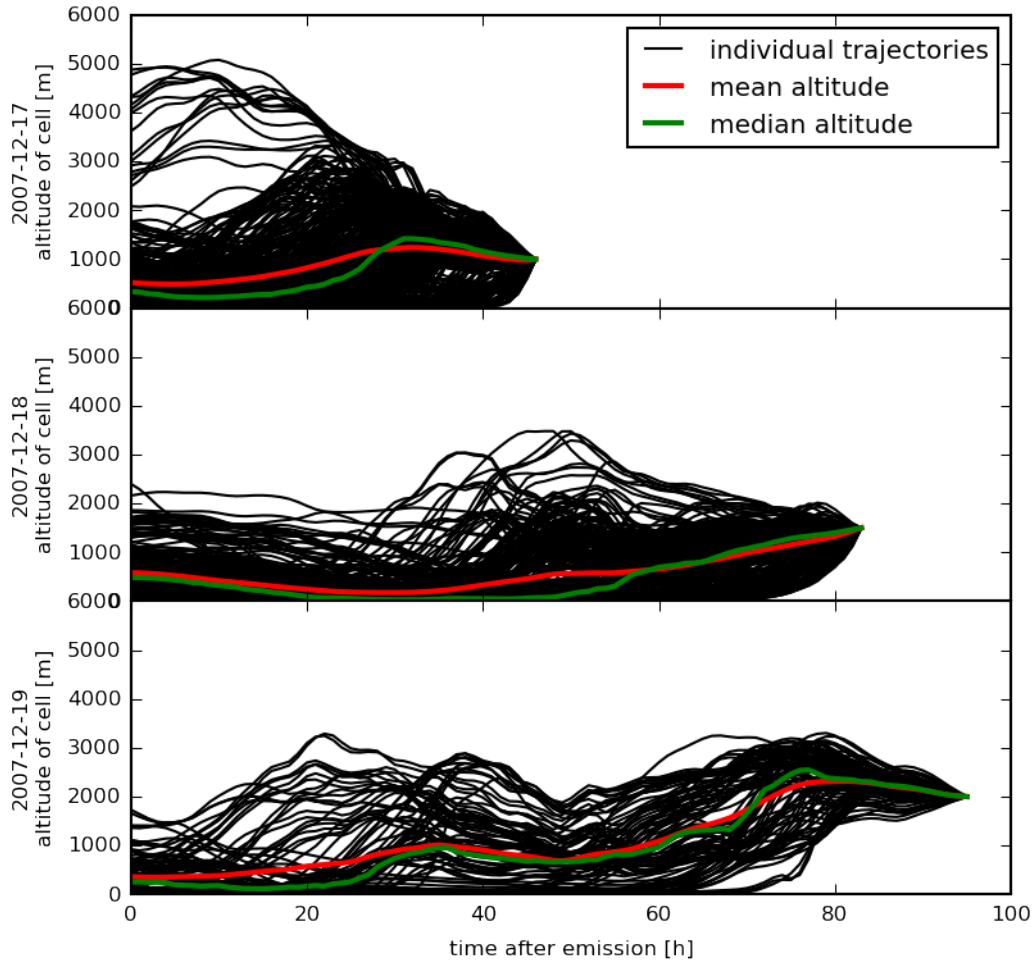

Figure 7.2: Altitudes of the backtrajectories for the long-range transport event over the North Atlantic on 17 to 19 December 2007. Black lines indicate the backtrajectories of individual cells. The red line indicates the mean altitude of the bulk of cells. The green line indicates the median altitude. The plots have been adjusted to start at the estimated emission of the plume. The altitude distribution gets broad rather quickly, but most trajectories return to the lower troposphere near the estimated emission time. Stray trajectories are clearly visible, especially on 17 December 2007.

region. This indicates that the plume must be elevated to the free troposphere, where NO_2 lifetime is increased to multiple days in contrast to a few hours in the planetary boundary layer. The high visibility of the plume combined with the observed cloudiness in FRESCO+ – which is very reliable over the ocean – also indicates that the NO_2 has to be mixed within or situated above the clouds.

On 19 December 2007 the plume starts to leave the area observable by GOME-2 / MetOp-A and enters Arctic Night. As GOME-2 / MetOp-A measures sunlight reflected by the Earth, it cannot observe under these conditions. Looking at the backtrajectories, however, it is apparent that a significant fraction (about one third to half) of the plume lies beyond our observations.

On 20 December 2007, the plume has disappeared from our field of view entirely. It is likely that it has traveled over the Arctic Ocean.

The track of the cyclone and the NO_2 plume are typical for this region, and follow the dominant storm track for the northern hemisphere (Whittaker and Horn, 1984).

From the combined backtrajectories of all three observations of the plume, the plume is estimated to be 50 hours old when it is first observed. The estimate is based on the best fitting consistent ages for the observations, forcing the age difference between consecutive observations to be 24 hours with corrections for zonal motion. This yields the time since it most likely detached from the planetary boundary layer by being lifted up (as described in Section 3.2). Consecutive observations are less than 24 hours apart as the plume moves towards the East. The plume is last observed at an age of 95 hours, just before it enters into Arctic Night.

The area covered by the plume is shrinking over consecutive observations, roughly proportional to the decrease in NO_2 content. The shape of the plume stays compact with sharp boundaries and little mixing on the fringes. This, together with the age, exemplifies that NO_2 long-range transports can span more than four days, with a compact plume that keeps its shape over a long time period. In the last observation, parts of the plume are being cut off by Arctic Night, leading to a drastic decrease in both size and NO_2 content that does not reflect the actual evolution of the plume ans serves as a lower limit to its extent.

Unfortunately, there are only two complete observations of the plume. From these observations – assuming exponential decay of the NO_2 content – the lifetime of NO_2 is estimated to be 149 hours. While this is only a rough estimate, it already indicates that NO_2 in long-range transports has much longer lifetimes than NO_2 in a typical planetary boundary layer emission scenario, which enables effective long-range transport. The initial size of the plume upon emission can then be estimated to be 3.22 Gg N.

Looking at the plume center of mass, it is possible to derive the minimum ground speed of the plume between two observations. Usually, the trajectories will follow a curved motion as the plume follows the cyclone's path. Also, the plume will likely rotate around the center of the cyclone. Thus, the ground speed derived by the difference in observation times and the great circle distance between the plume's center of mass on two consecutive observations, will only be a lower bound for the actual ground speed.

Between 17 and 18 December 2007, the minimum average ground speed amounts to 59 km/h or 16 m/s, which are not commonly achieved in the planetary boundary layer. Between 18 and 19 December 2007, I can only derive a lower limit on the lower limit, as parts of the more distant plume are cut off. This lower lower limit amounts to 32 km/h.

Over the course of the transport, the plume is slowly lifted from about 1,000 m to 2,000 m during the two days of observation. This is in accordance with the bulk of the backtrajectories of the last observation of the plume (Figure 7.2). This is ĺower than my assumption of a homogeneous distribution between 3,000 m and 5,000 m, but as shown in Section 4.4 and Section 4.5 this should have little impact on the air-mass factors used in satellite data retrieval.

Figure 7.3 illustrates how the backtrajectory of the last observation of the plume relates to the observations at earlier times, by indicating the positions of the plume cells at the respective points in time in the plots. A few things are striking about this depiction.

First, the bulk of the backtrajectories of the last observation of the plume follow the apparent trajectory of the plume in the observations. There is little room for doubt that these observations actually show the same plume at different times, which directly indicates that this has to be NO_2 transported by a long-range transport event. Figure 7.4 shows the same plume with the backtrajectories indicated as lines.

Second, there are stray trajectories. These separate from the bulk of the trajectories both in horizontal and vertical direction. These stray trajectories illustrate the limitations of the backtrajectory approach. Due to limited horizontal, vertical and temporal resolution of both meteorological and observational data and due to the assumptions about the vertical NO_2 distribution, cells do not accurately represent the NO_2 in the plume. This is especially true on the fringes of the plume. Due to the dynamic and chaotic nature of meteorological systems, this misrepresentation will grow exponentially – as parameterized by Lyapunov exponents (Lyapunov, 1992) – in both temporal forward and backward direction. This is a fundamental limitation of this kind of processes.

Third, the trajectories only cover a fraction of the observed plume at earlier times. A significant segment is not represented via this approach. This is a strong indicator that there is NO_2 beyond the satellite field of observation on 19 December 2007. This part of the plume would then represent the missing segment at earlier times.

This last observation also implies that the plume still contains a large fraction of the initial NO_2 which is likely to be transported for another day or two until the plume dissolves with the dissolving cyclone. This NO_2 is likely to be transported into the Arctic, where it can drastically impact the sensitive atmospheric chemistry of this pristine region.

A similar case of NO_2 long-range transport has been analyzed in a case study by Stohl et al. (2003). Unlike that study, here the NO_2 is centered on the cyclone as seen in NCEP DOE AMIP-II Reanalysis mean sea level pressure data. When we inspect further prominent long-range transport events emitted from the North American East Coast, we find that the NO_2 plumes typically follow a rapidly forming cyclone.

Only few NO_2 long-range transport events are as massive and prominent in GOME-2 / MetOp-A data as this one. There are two factors that combine to make the observation of such events less likely:

- NO_2 long-range transport events typically form in local winter when emission rates are at their maximum, cyclones are frequent and the lifetime of NO_2 is especially long.

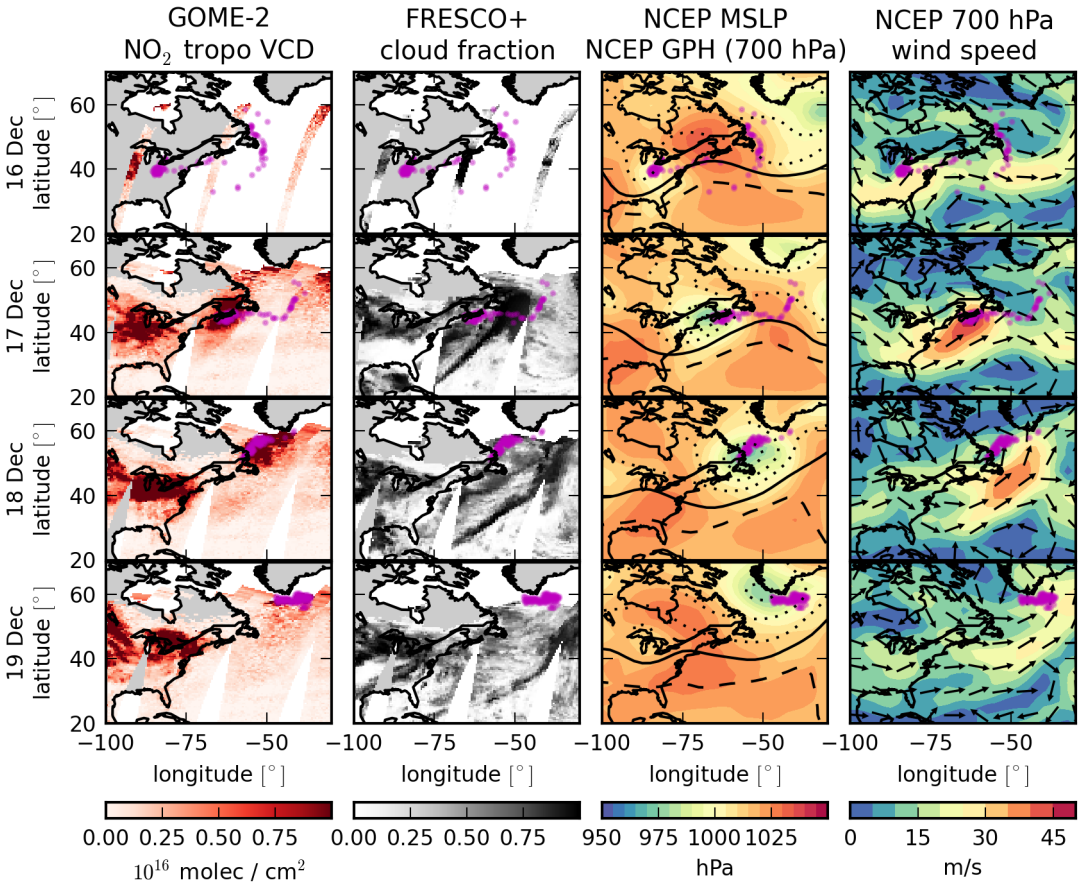

Figure 7.3: Illustration of the backtrajectory of the last observation of this long-range transport event (19 December 2007). Data as in Figure 7.1, but purple circles indicate the locations of the backtrajectories of the plume from 19 December 2007 at the respective dates. The plume detected on 19 December 2007 is only partially visible due to polar night. This becomes evident when comparing the backtrajectories on earlier dates with the observed NO_2 vertical column densities.

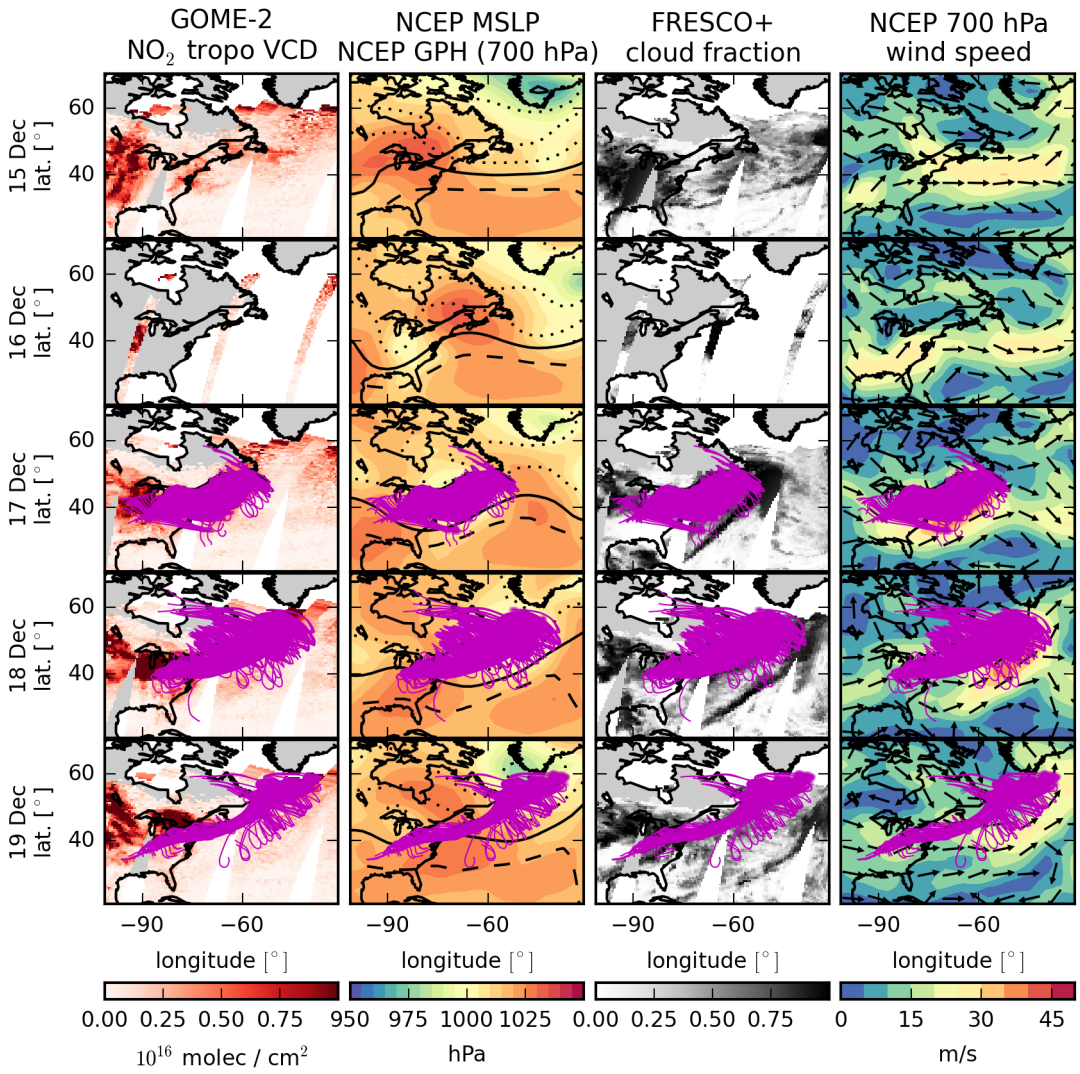

Figure 7.4: Illustration of the backtrajectories of all three observations of this long-range transport event. As in Figure 7.1, but with the trajectories of the plume cells indicated as lines.

- Most long-range transport events are driven polewards by typical wind patterns where GOME-2 / MetOp-A cannot observe during winter.

7.1.2 South Africa, 9–12 July 2008

Figure 7.5 shows a typical NO_2 long-range transport event emitted from the South African Highveld plateau area. This event can be observed for four consecutive days due to the favorable conditions in the Southern Hemisphere.

When the plume is first observed on 08 July 2008, it is estimated to have traveled for 29 hours since separating from its source, based on five consecutive observations. This is in accordance with the estimation from the initial observation alone (35 hours). In this observation, the plume is not fully visible, leading to imprecise estimations on especially plume size and mass, but also on its backtrajectory. Indications of the plume can already be seen in earlier observations on 07 July 2008, but are not detected by the algorithm.

The plume roughly follows isobaric lines at around $-40°$N in a curved trajectory; in the first two observations it appears to be following a weak cyclone, that is heading towards the Antarctic, before their trajectories diverge. The plume can easily be seen in satellite data until 11 July 2008. A hint of the plume can be seen near the West Coast of Australia on 12 July 2008, where this anomaly is still detected by the algorithm. On 13 July 2008, the plume can no longer be seen in the data – neither over the ocean nor continental Australia – and is not detected by the algorithm. It appears likely that the plume has either dispersed in the shear winds apparent on 12 July 2008 or has moved to Australia where the NO_2 either decomposed when entering lower atmospheric layers or is hidden from detection.

Both the satellite data and the backtrajectories show the plume originating from the Highveld plateau. The Highveld plateau features an agglomeration of industry and power plants near Johannesburg on an elevated stretch of land near the West Coast of South Africa. This emission region is located at $1,500\,\mathrm{m}$ a.m.s.l. which lowers the effort of injection into the free troposphere. Occasionally, NO_2 might be injected directly into the free troposphere from high smokestacks. This – together with the isolated location – makes South Africa one of the prime emitters of NO_2 long-range transport.

The isolated loaction of the Highveld plateau near the open ocean and remote from any other major emitters make South African plumes so highly visible in GOME-2 / MetOp-A data.

However, during this period, there were also some bush fires on the West Coast of South Africa. While the trajectories point to the Highveld plateau, it is possible that some of the NO_2 in the plume was emitted in biomass burning. Strong convection in the smoke plumes and the passing cyclone could have lifted the NO_2 to higher altitudes (where lifetime is increased) and transported it over the Highveld plateau where more, anthropogenic NO_2 joined the transport.

The plume starts very compact; this is another indication of the compact nature of its emission region. On 09 July 2008, not the entire plume can be observed (due to the relatively low latitudes, where there are gaps between individual orbits). The plume is estimated to contain (at least) $1.58\,\mathrm{Gg\,N}$, while on the following day – when the plume is fully isible in the satellite data – the NO_2 content is estimated to be $1.74\,\mathrm{Gg\,N}$. In

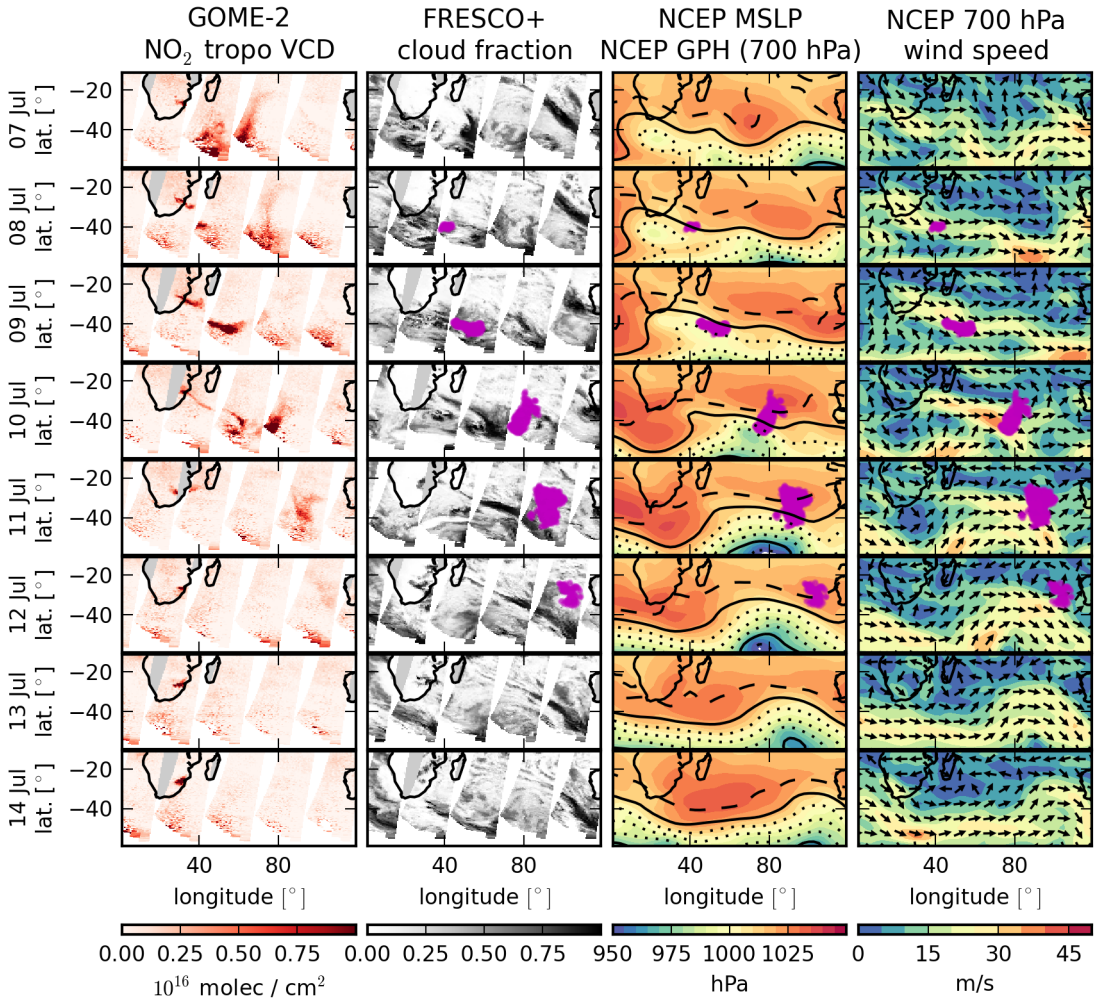

Figure 7.5: As for Figure 7.1, but showing a long-range transport event emitted from South Africa in July 2008. The NO_2 plume is transported from South Africa to the West Coast of Australia.

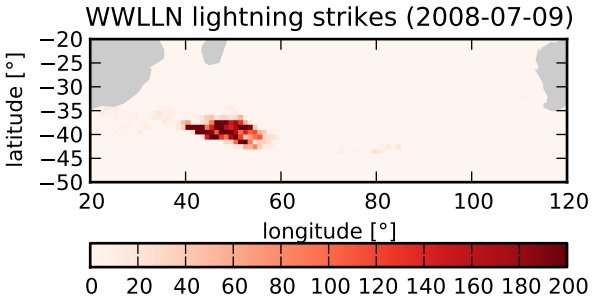

Figure 7.6: Number of lightning strikes on 10 July 2008 observed with WWLLN over the ocean near South Africa. The lightning strikes are colocated with the observed position of the NO_2 plume (Figure 7.5). Likely, this thunderstorm replenished the NO_2 content of the plume. On the following days, the thunderstorm produces significantly less lightning strikes and is no longer colocated with the transported plume.

the following days, the plume shrinks in plume content, while broadening a little from 10 to 11 July 2008. The step to the last observation is especially drastic and it is likely from satellite observations that, again, parts of the plume could not be observed. Still, there is also a drastic decrease in tropospheric NO_2 vertical column densities which indicates that rapid decay, wash-out or dispersion of NO_2 has set in, as the NO_2 enters the continental atmosphere with its altered chemistry. There are no clouds obscuring the observation on that day.

The decay of NO_2 between 10 and 11 July 2008 amounts to an NO_2 lifetime in the plume of approximately 110 hours; this is consistent with the observations in Section 2.1.

The World Wide Lightning Location Network (WWLLN) finds a significant amount of lightning strikes in the area where the plume is observed on 09 and 10 July 2008 (Figure 7.6). On the following days, the – then weaker – thunderstorm and the NO_2 plume are no longer co-located and further impact on the NO_2 plume can be excluded. With the detection algorithm, NO_2 from anthropogenic sources and $LiNO_x$ cannot be distinguished other than by location and trajectory. I cannot tell if this observation actually shows a long-range transport event or $LiNO_x$ or both. It is possible though unlikely, that the observed plume is not anthropogenic in origin, but rather originates in the strong thunderstorm and is then transported further downwind. In that case, it is not clear, why the NO_2 plume and the thunderstorm would separate. It appears more likely that the strong thunderstorm will replenish the NO_2 content of the plume, thereby enhancing its observed lifetime.

It is plausible that long-range transport events will occasionally be accompanied by thunderstorms. These may in turn lead to an enlarged NO_2 content or to an apparent longer lifetime of NO_2 inside the plume. From our efforts to observe $LiNO_x$ in reported strong thunderstorms and long-range transport plumes' distinguished seasonal and geographical distribution (see Subsection 7.2.3), however, it appears that thunderstorms will not be the single cause for most of the observed plumes.

The plume rises to 2,000 m until the first observation. On the following two days, the altitude varies strongly and independently estimated plume ages are inconsistent, while ages estimated (and to a reasonable degree: trajectories) from the first and final observation of the plume are consistent. This indicates that there were problems with finding the correct backtrajectory on 10 and 11 July 2008. This affects only plume age and altitude evolution, as can be seen in Figure 7.7. The backtrajectories on these last two observations show significantly higher elevated backtrajectories than the ones for the first two observations and also indicate a descent of the plume after about 3 days after emission.

I determined the minimum ground speed (see Subsection 7.1.1) between consecutive observations to be 97 km/h or 27 m/s between 09 and 10 December 2008 (when the plume is still following the cyclone's track), with 59 km/h and 51 km/h for the following days, after separating from the cyclone. Due to incomplete observation of the plume, the first and last value should be larger (the western part of the plume was cut off on the first, and the eastern part on the last observation). The obtained ground speeds neglect the track's curvature and the plume's rotation. These values indicate that the plume resides in the free troposphere and is linked to a strom.

This plume bears similarities to the one analyzed by Wenig et al. (2003). The plume they observed crosses the ocean and arrives in Australia within five days which is consistent with the four consecutive observations in our data. They find thunderstorms with lightning coinciding with the plume on two observations, but the $LiNO_x$ alone cannot explain the observed NO_2 vertical column densities in the plume. It might, however, replenish the plume and thereby increase its apparent lifetime.

Simulations with FLEXPART (Stohl et al., 2005), a more sophisticated lagrangian transport model, show the plume in their analysis to be traveling at altitudes from 2–6 km a.m.s.l. after it separated from the emission region in the Highveld plateau, which is mostly consistent with our assumptions and observations.

7.1.3 Australia, 27–30 April 2008

On 27 to 30 April 2008 a rare NO_2 long-range transport from Australia into the Pacific took place. Figure 7.8 shows the four consecutive observations of the associated NO_2 plume.

On 27 April 2008 the plume is first visible in the satellite data. This is the only complete observation of the plume. On the following days the plume is always located on the border of the satellite swath. Even on 30 April 2008 – when the tail of the plume ends where two consecutive orbits meet – parts of the plume may be obscured, as consecutive orbits are roughly 100 minutes apart. With regards to the obtained ground speed of the plume, it may have traveled on the order of 100 km during this time which is a significant fraction of the swath width.

On 28 April 2008, the plume travels around New Zealand to its southernmost location near Antarctic Night and crosses the date line. On the following days it follows the dominant wind pattern around the polar vortex over the Pacific. There is no trace of the plume in the satellite data after 30 April 2008.

The plume roughly follows isobaric lines between two relatively stable low-pressure systems (over the Antarctic Ocean) and one high-pressure system east of New Zealand.

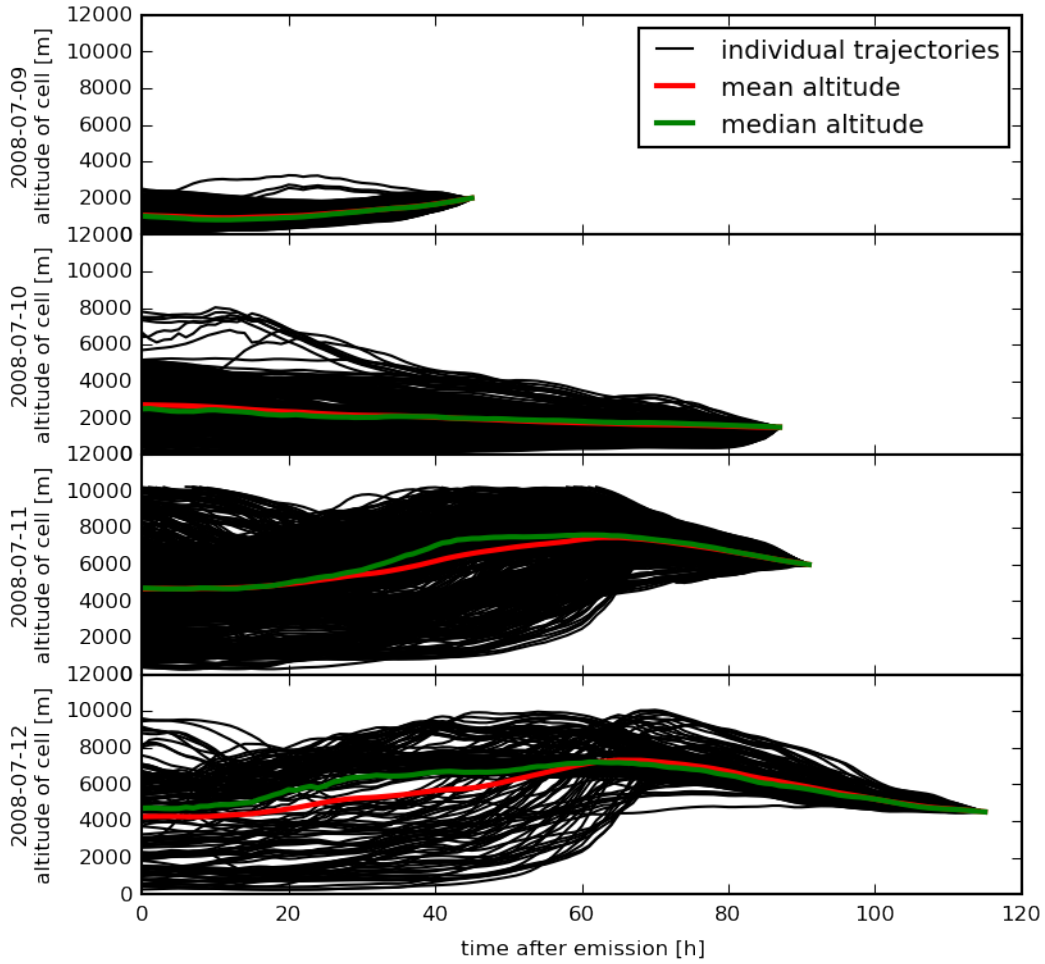

Figure 7.7: As in Figure 7.2, but for the long-range transport event emitted from South Africa that was observed from 09-12 July 2008. For the first two observations, backtrajectories indicate a rather low transport without any major uplift. In contrast, backtrajectories for the last two observations indicate a higher starting point, an uplift event for parts of the trajectories around 40...60 hours after emission and a descent starting after about 70 hours.

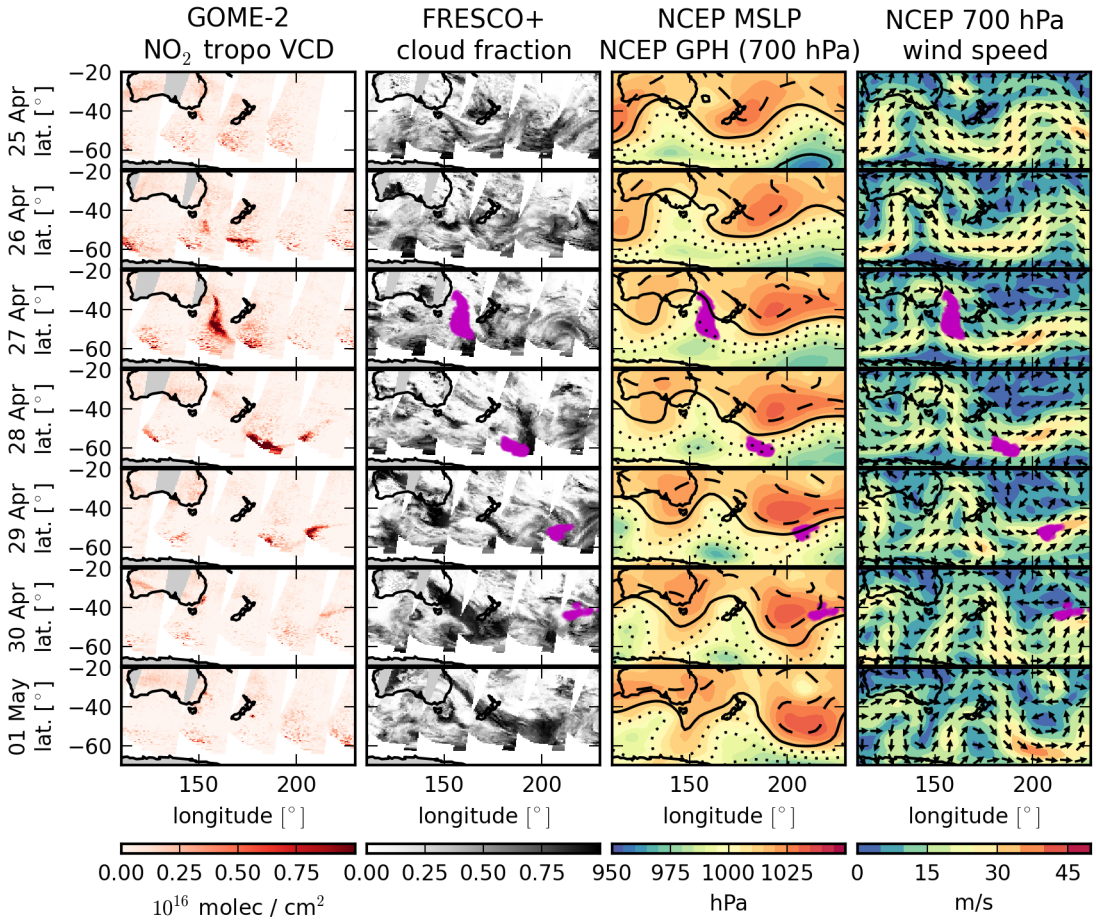

Figure 7.8: As for Figure 7.1, but showing a long-range transport event emitted from Australia over the Pacific, probably caused by bush fires in south-western Australia. Note, that this transport is not accompanied by a cyclone.

It travels in a channel of high wind speeds (as modeled on the 700 hPa level).

It is striking that there is no heavily polluted area visible in the satellite data in Australia – neither in the days preceeding the event nor in seasonal averages. Also, there are not many NO_2 long-range transport events starting from Australia in the 5-year dataset. This indicates that not continuous emission but rather an emission event caused this long-range transport event.

The backtrajectories point at an emission in south-western Ausralia. MODIS data show bush fires in this region. The most intense bush fires in Australia are found in the northern part. However, the meteorological conditions for long-range transport of NO_2 and for a long NO_2 lifetime are not given in this part of Australia. NO_2 is most likely transported towards the North and short lifetimes in this tropical region will lead to quick dispersion of the plume. It is thus expected that no long-range transport from the strong northern bush fires are found in GOME-2 / MetOp-A data.

NO_2 and glyoxal (CHOCHO) from large bush fires such as the Black Saturday fires are routinely observed in satellite data. GOME-2 / MetOp-A data show increased NO_2 vertical column densities over southwestern Australia on 25 and 26 April 2008, with tropospheric NO_2 vertical column densities on the order of $3 \cdot 10^{15}$ molecules/cm^2, a factor two higher than background levels. However, it is likely that our data product underestimates NO_2 levels in fire plumes. This is an effect of the massive aerosol load emitted in bush fires, especially the black carbon (Martin et al., 2003; Leitão et al., 2010; Giles et al., 2012). Due to its strong absorption, the aerosol will lead to a significantly lowered local air-mass factor for NO_2 in the plume. As the plume rises and ages, its constituents will subsidize slowly; the black carbon sinks below the trace gases and reveals the NO_2 to the satellite instrument. Under this consideration, the small but elevated levels might indicate the origin of the massive plume in the studied long-range transport event. An origin in bush fires would also explain the neccessary lifting of the NO_2 from the planetary boundary layer into the free troposphere in the abscence of a frontal system (see Labonne et al., 2007).

There is a storm that accompanies the NO_2 plume as it enters the oceanic atmosphere. There is a small thunderstorm off the east coast of Australia on 27 and 28 April 2008, as can be seen in Lightning Imaging Sensor (LIS, Christian et al., 1999; Christian, 1999) data. This thunderstorm coincides with the plume on 27 April, but not on the following day. Apparently, thunderstorm and NO_2 long-range transport are not linked to each other. However, from 28 April 2008 on, the plume is located outside the observable latitude range of LIS, so that further observations are not possible.

For this plume, the algorithm selecting a proper backtrajectory shows its limitations. The first estimation might be fairly reasonable; it might take two or three days to transport the plume from the southeast of Australia to the Pacific. The age estimations for the two following days are too low, with 59 hours and 61 hours. This is an artifact of the backtrajectory selection which in this case prefers trajectories ending over New Zealand instead of the more distant Australia. This also leads to significantly lower altitudes. The algorithm prefers a young, low-altitude plume because its trajectories will not have dispersed so much during the short time of transport. The bulk of trajectories will stay close together; this results in more trajectories residing in the continental planetary boundary layer – the applied selection criterion. On the last day of observation, the trajectory again traces the plume back to Australia, leading to a more reasonable

age estimation. From the regression of ages on different observations, I estimate the plume to be 47 hours old on the first observation which makes its origin in bush fires plausible.

This long-range transport event shows a strong exponential decay of NO_2 content, which is roughly cut in half every day. This is a significantly stronger decay than in the previous case studies (Subsection 7.1.1 and Subsection 7.1.2). I fit the observed NO_2 content to an exponential decay of shape

$$m(t) = m_0 \exp^{-\frac{t}{\tau}}, \tag{7.1}$$

with m_0 being the initial NO_2 content and τ being the lifetime of NO_2 in the plume (assumed to be invariant over time). This yields a lifetime of $\tau \approx 28$ hours and an initial NO_2 content of $m_0 = 11\,\mathrm{Gg\,N}$ when extrapolating backwards to the time of emission.

Calculating ground speeds, the plume appears to be slowing down over the course of the event. It starts with a minimum ground speed of 105 km/h or 29 m/s from the first to the second day of observation, slowing down to 74 km/h and 56 km/h on the following days. This might be an effect of the plume detaching from the low-pressure system over the Antarctic Ocean.

This event shows that not only major anthropogenic emission regions may cause long-range transport, but also single emission events if they are tied to favoring conditions. There is no low-pressure system moving over Australia in the preceeding days; no cold front could lift the NO_2 up from the planetary boundary layer into the free troposphere. This – together with the backtrajectories and the lack of strong anthropogenic sources in Australia – is a strong indication that this event was driven by NO_2 created in and lifted up by large bush fires. It is likely that most or all of the NO_2 long-range transport events originating from Australia are caused by biomass burning.

7.1.4 Europe, 1–2 October 2010

On 1 to 2 October 2010, GOME-2 / MetOp-A observed an NO_2 long-range transport event emitted from Europe over the North Sea towards the Arctic, as shown in Figure 7.9. This event appears to be part of a series of long-range transport events stemming from a large outflow out of the BeNeLux and Ruhr areas. The evolution of synoptic weather separates this outflow into multiple fragments that follow individual paths. Here, I analyze only the plume observed on 1 to 2 October 2010. This plume was also used to analyze the vertical relation of vertical profiles of liquid and frozen water content in clouds and NO_2 in long-range transport (Figure 4.14, Section 4.5).

The fragment preceeding the selected plume is detached from the outflow by diverging winds. After separating, it quickly disappears into Arctic Night, following south-westerly winds. Only an elongated tail of the preceeding fragment can be seen on 1 October 2010. The plume selected for this study marks the end of this outflow event and no further long-range transport is found near Europe in the following days.

The selected plume can be seen still integrated into the major outflow pattern of 1 October 2010; yet, its structure is already visible in the outflow. In principle, this structure could be a result of clouds obscuring the view of GOME-2 / MetOp-A. On the following day, the plume is fully separated from the outflow and has evolved into

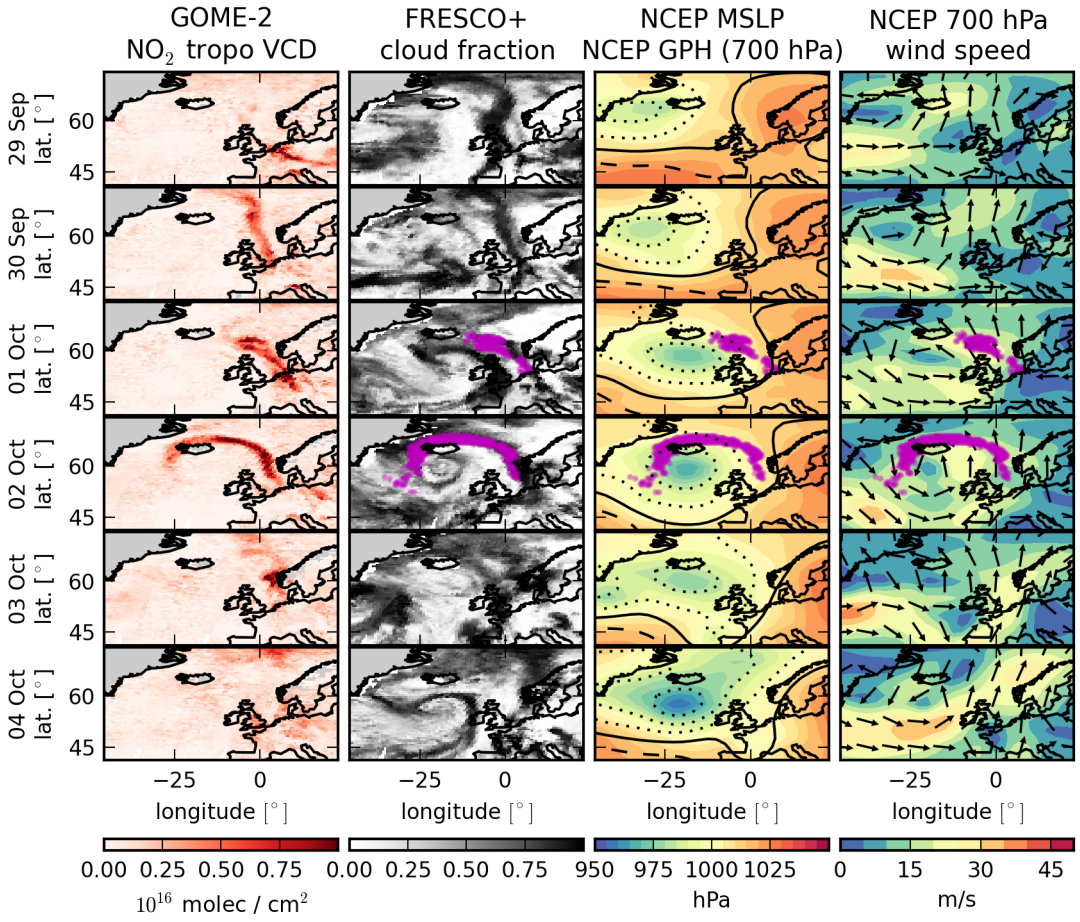

Figure 7.9: As for Figure 7.1, but showing a long-range transport event emitted from Europe over the North Sea. The plume is subject to strong shear winds as it is transported on the fringes of a cyclone and is dispersed after two days. This plume is part of a longer outflow that is fragmented after leaving Central Europe towards the North. The direction of transport – opposing major wind patterns – is typical for the European region.

a strong, arc-like shape as it is subject to the wind shear on the outer regions of the incoming cyclone.

In contrast to the previous case studies, the plume moves in opposite direction of the cyclone's movement. This is the reason for the strong filamentation of the plume's shape. The plume arcs around Iceland on 2 October 2010.

The NO_2 content of the plume appears to increase between consecutive observations. This may be an effect of the plume not having separated from the outflow on the first observation (which means that more cells can join the plume) and of self-similarity effects in this region. The algorithm obtains a sliding mean from the days around the observation and subtracts it from the tropospheric NO_2 vertical column densities. If there is a persistent outflow over multiple days, this will increase both the mean and the standard deviation, leading to less cells added and less NO_2 in each cell compared to an isolated event of the same observation. On 2 October 2010, the plume has separated enough to remove all of these self-similarity influences.

An apparent increase in NO_2 content can also be caused by a change in observational conditions, leading to a higher actual air-mass factor. This will result in a higher retrieved vertical column density. This may be the case if the surface albedo changes, the cloud starts to dissolve or the NO_2 rises above the cloud.

On 3 October 2010, the plume is not visible any more. Most of the NO_2 appears to have been dispersed in the violent shear of the cyclone. Upon visual inspection of the tropospheric NO_2 vertical column density map, increased levels can be found between Greenland and Svalbard and south of Iceland. The region between Greenland and Svalbard (not shown) is very close to Arctic Night and not included in the analysis. Here, fluctuations of observed tropospheric NO_2 vertical column densities are very large and inhibit a reliable detection of plumes, let alone NO_2 content. South of Iceland, a small upwards anomaly can be seen that is no longer detected by the algorithm. It might be a result of the enhanced dispersion in strong shear winds. It is also possible, that both are fragments of this plume, after it has been disrupted in the diverging wind field. However, it is not certain if any of these are remnants of the transport.

Due to strong shear and due to moving opposite to the cyclone's movement, the plume's ground speed is only 31 km/h during the time of observation. However, it is obvious that parts of the plume must have traveled at far greater velocities to create the strong arc visible on 2 October 2010. The strong shear also leads to a separation of this plume into a large plume and two smaller ones which were also detected – one of which travels to Greenland.

The estimated ages indicate that the plume is 16 hours old when it is first observed, making this one of the younger plumes in the data set, where we can actually observe the separation from the emission region. The plume is found to be at a low altitude of 1,000 m on both observations which may explain its quick decay after the second observation on 2 October 2010.

Europe is a special case concerning long-range transport: Due to its special geography, with emission hotspots situated around the North Sea bay, there are very frequent detections of newly emitted long-range transport events. As storm tracks frequently cross Europe to the south of the major emission regions, there is a prominent route transorting long-range transports towards the north-west.

7.2 Statistical analysis

The previous section illustrated the phenomenon of NO_2 long-range transport using a few hand-picked, striking examples from GOME-2 / MetOp-A data. While this gives insight on the types and properties of long-range transport events, it does not harness the full potential of a comprehensive satellite data set.

Therefore, in this section, I will perform a statistical analysis of NO_2 long-range transport in GOME-2 / MetOp-A data, using the results of the algorithm mentioned in Chapter 6. This analysis yielded a total of 3808 verified plumes of more than $5 \cdot 10^{30}$ molecules NO_2 in the global data from 2007–2011. 4818 plumes have been discarded in the verification process. This comprehensive data set allows a representative study of the typical properties of NO_2 long-range transport events and their seasonal and regional distribution.

7.2.1 Seasonal distribution

Figure 7.10 shows the seasonal NO_2 long-range transport plume count for the Northern and Southern Hemisphere.

There is a strong seasonality visible in the distribution of these events. Most plumes are emitted in local winter; to illustrate this seasonality, I analyze the Northern and Southern Hemisphere separately. In the Southern Hemisphere (SH), spring and autmun show equal counts, while in the Northern Hemisphere (NH) more plumes are found in autumn than in spring. In both cases, local summer shows the least long-range transport plumes, when emissions are low, few cyclones occur and NO_2 lifetime is short. Note that this only takes the number of found plumes into account, which will also increase with a higher lifetime of the plumes, but does not cover plume size.

Also, it is apparent that the Northern Hemisphere emits the majority of long-range transport events. This is a feature of geography, as the Northern Hemisphere features more land masses in the mid- to high latitudes. Especially, the Northern Hemisphere has more high-emission regions at latitudes suitable for long-range transport.

7.2.2 Plume properties

In the next step, I have analyzed the distribution of individual plume properties.

Figure 7.11 shows the NO_2 content distribution of long-range transport plumes, divided by season. Here, only plumes on the Northern Hemisphere are considered to avoid effects of counteracting seasonality from the Southern Hemisphere. The frequency of occuring plumes resembles an exponentially decreasing function of the form:

$$\mathrm{d}p(m) = \exp\left(-\frac{m}{m'}\right)\mathrm{d}m, \tag{7.2}$$

where $p(m)$ is the probability to find a plume of NO_2 content less than m and m' is the scale mass of the distribution. The scale mass indicates the size of a typical plume.

For the four seasons, the scale mass varies slightly. While winter (on the Northern Hemisphere: December to February, DJF) and autumn (September to November, SON) show a similar scale mass of 0.25 Gg N and 0.24 Gg N, respectively, spring (March to

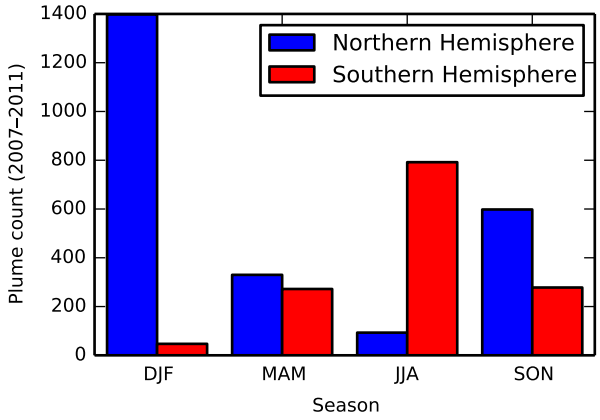

Figure 7.10: Number of verified long-range transport plumes found by the detection algorithm in 2007–2011. There is a strong seasonality in both hemispheres, with a strong peak in local winter.

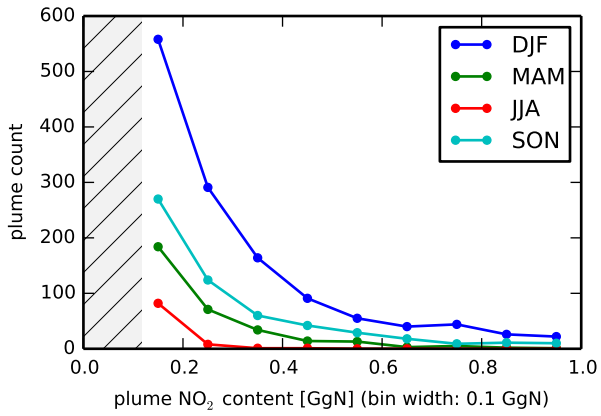

Figure 7.11: NO_2 content of long-range transport events in the Northern Hemisphere, for different seasons. Note the lower mass limit of 5×10^{30}molecules (hatched area, corresponding to 0.12 Gg N).

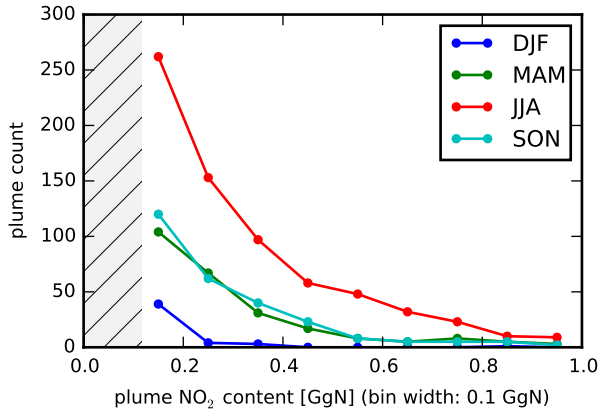

Figure 7.12: As in Figure 7.11, but for the Southern Hemisphere.

May, MAM) shows a significantly lower scale mass of only 0.16 Gg N. Plumes in spring are not only less frequent but also smaller than in autumn and winter. For the summer months (June to August, JJA), too few plumes were observed to compute the scale mass.

On the Southern Hemisphere (Figure 7.12), we find that again most emissions are observed in local winter (JJA). This will mostly include plumes from South Africa. Compared to results from the Northern Hemisphere, characteristic plume sizes for all seasons are significantly closer: 0.23 Gg N in MAM, 0.24 Gg N in JJA and 0.20 Gg N in SON.

I have analyzed the mass distribution for each individual year in the 2007–2011 period for the Northern Hemisphere. I employed the Mann-Whitney U test (Mann and Whitney, 1947) to find a difference in the seasonal distributions of NO_2 content between different years. However, the distributions show no significant difference and it appears that the sizes of plumes are not subject to a long-term trend visible on the 4-year scale.

This resulting distribution is a result of the distribution of NO_2 emitted into individual long-range transport plumes and the distribution of age at the time of observation. There is no filter removing multiple observations of the same plume on consecutive days – which gives the plot features of a cumulative distribution function. Also, plume age is not accounted for in the mass estimation, which biases the distribution towards lower NO_2 content.

Likewise, Figure 7.13 shows the seasonal distribution of plume ages at the time of observation. This distribution has three distinctive features, over all seasons:

- There are few plumes with ages below 24 h. This is an effect of major outflow regions. Here, long-range transport plumes cannot be discerned from regular outflow in the planetary boundary layer by the algorithm. Plumes are only detected when they have separated from the ouflow region, which will result in the plumes being identified only in the second satellite overpass, about 24 h later.

- After about 24 h to about 96 h the number of plumes observed is decreasing with

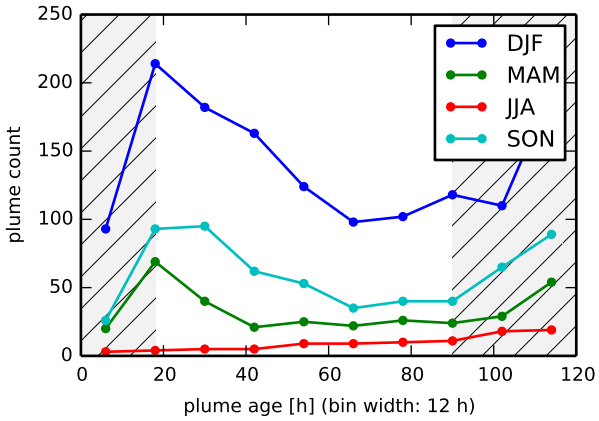

Figure 7.13: Plume age at the time of observation for long-range transport events observed in the Northern Hemisphere between 2007–2011, divided by season. The distribution illustrates the decrease of long-range transport detections with age in the range 24–96 h. Interference from outflow regions lowers the amount of plumes detected below 24 h (hatched). Increasing plume counts above 96 h (hatched) are an artifact of the method used to determine the most likely backtrajectory and are likely to feature an increased amount of false positive detections. See Subsection 6.2.4 for details.

increasing age. This is an effect of the decay of NO_2 in the plumes which will eventually lead to the plume being excluded from the dataset. Note, that there are duplicates in the data – plumes that were observed at both young and old ages. Taking this effect into account, the distribution will be flatter.

- After about 96 h the plume count increases again. This is a relict of the trajectory selection method. For remote plumes, long backtrajectories are more likely to enter the continental planetary boundary layer, despite dispersion. Plumes in this range are more likely to be false positives. However, they do not contribute much to the total NO_2 content and are left in the dataset, due to a lack of efficient identification of false positives.

When fitting an exponential decay function to the data outside the hatched area, the characteristic scale of the plume number distribution amounts to 97 hours during winter, 84 hours during spring and 70 hours during autumn. Unsurprisingly, this scale is close to the observed and expected lifetime of NO_2 during such events.

In the Southern Hemisphere (Figure 7.14), only the effects for small and large ages can be seen. Inbetween, the number of observations is essentially independent of the determined plume age. This might be attributable to easier observation conditions: once the plumes have separated from South Africa, they are over open and mostly clean (with regards to NO_2 contamination) ocean. This fortunate signal-to-noise ratio and large distance to the next shore allows this method to more easily observe older plumes.

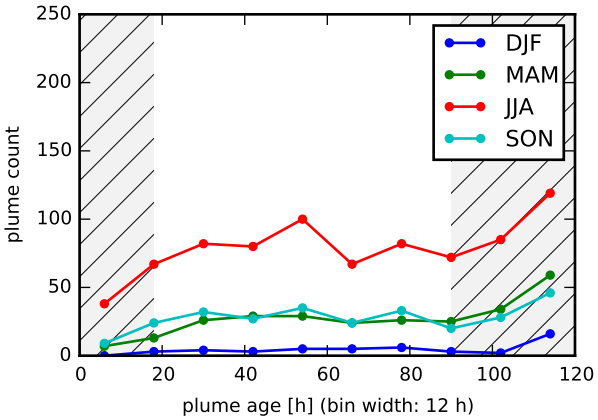

Figure 7.14: Plume age at the time of observation for long-range transport events observed in the Southern Hemisphere between 2007–2011, separated by season. Data as in Figure 7.13.

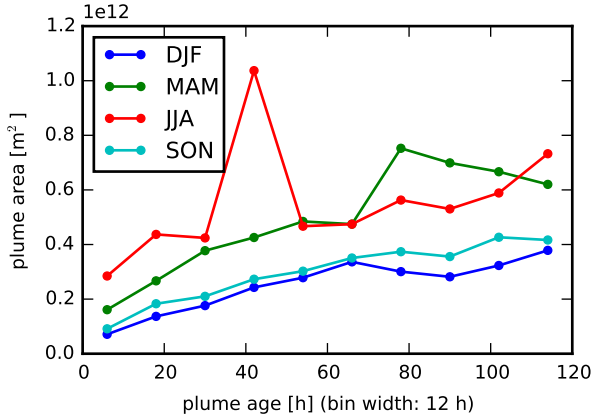

Figure 7.15: Average plume area at the time of observation for long-range transport events observed in the Northern Hemisphere between 2007–2011, divided by season. Note that very small numbers of observed plumes lead to unreliable results for JJA. Overall, plume areas increase with the age of the plume as expected. Plumes detected in winter are more compact than plumes detected during summer.

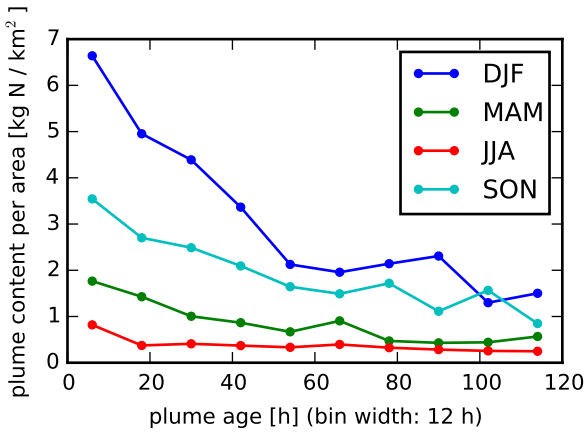

Figure 7.16: Average projected plume density on the Northern Hemisphere: NO_2 content per square kilometer. Plumes during winter are more compact. In all seasons, plumes quickly dilute.

In Figure 7.15, the average encompassed area of plumes in the Northern Hemisphere at different determined ages can be seen. For all seasons, the encompassed area will on average increase over time. This indicates that plumes are usually emitted with high tropospheric NO_2 vertical column densities and sharp boundaries. During transport they are subject to eddies and other forms of wind shear which blur their boundaries and disrupt the plume shape. This leads to an increase in plume area. This increase is limited by decay of NO_2 and too strong dilution of the NO_2 to still be detected in the plume. As the contrast between plume and background wanes, their size decreases.

Interestingly, the plumes appear to be more compact at all times during the main emission seasons (SON and DJF). This also holds on the Southern Hemisphere (MAM and JJA), where plume numbers are significantly lower and the determined mean area varies drastically. It is not clear if plumes are actually more compact during winter (despite typically stronger wind shear) or if the algorithm only detects a smaller plume area due to the lower signal-to-noise ratio.

A look into the observed NO_2 content per area (Figure 7.16 and Figure 7.17 for Northern and Southern Hemisphere, respectively) shows that indeed, the projected plume density is significantly higher during winter. On the Northern Hemisphere, the projected density quickly decreases with plume age (approximately exponentially), while it stays constant on the Southern Hemisphere. It appears most likely that this is tied to the observational circumstances and not a fundamentally different chemistry or diffusion process. However, stronger storms in the Northern Hemisphere might contribute to this effect with their shear.

Figure 7.18 shows the temporal evolution of plume altitudes. Most young plumes (younger than 24 h) reside at low altitudes – at 1–2 km – with a strong decline in frequency to higher altitudes. This distribution smoothens out as plumes get older, although there still remains a maximum at low altitudes. For the oldest plumes, there

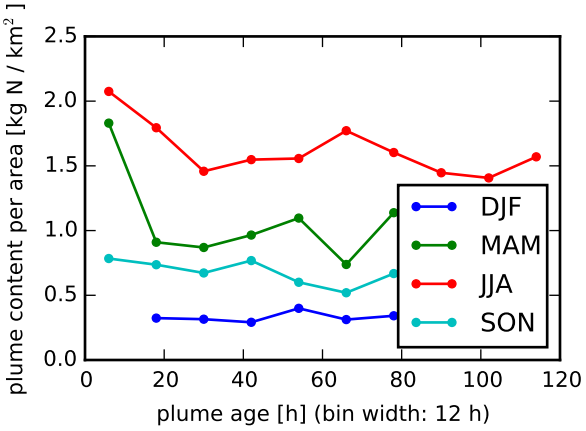

Figure 7.17: Average projected plume density on the Southern Hemisphere: NO_2 content per square kilometer. Plumes during winter are more compact. In contrast to the Northern Hemisphere (Figure 7.16), the plumes' density stays constant over time.

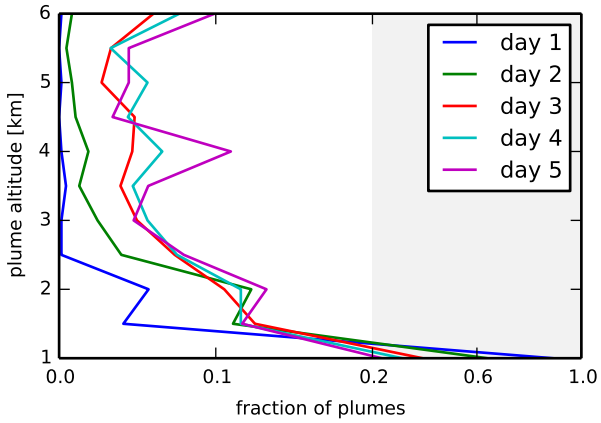

Figure 7.18: Altitude distribution of NO_2 long-range transport plumes over the 11 altitude levels sampled in the HYSPLIT backtrajectories. Shown are the graphs for plumes younger than one day, between one and two days of age, etc. While most young plumes reside on the lowest level, they tend to distribute more equally in altitude over the following days. Note the compressed axis for fractions higher than 20 %.

is a second peak in the altitude distribution at about 4 km. It is not clear if this is an artifact of the retrieval process – plume age and plume altitude are determined in the same process and thus depend on each other – or a preferred altitude at which plumes last the longest.

The altitude distribution of plumes suggests that I should adapt my assumptions from Section 4.5 for further studies. From the altitude distribution, it it can be seen that the center of the altitude distribution suggests to rather use 2–4 km than 3–5 km for the vertical plume extent. It can be seen that the altitude distribution is also strongly dependent on plume. A retrospective correction of tropospheric NO_2 vertical column densities in obtained plumes, depending on their estimated altitude might be possible, but is still subject to large errors in the altitude estimation and unfeasibile. As discussed in Section 4.5, the systematic error of a wrongly assumed altitude of the plume (and the cloud, if applicable) is marginal.

7.2.3 Routes

The comprehensive dataset allows to find any patterns in the typical routes of NO_2 long-range transport and to determine the most common sources.

To find the typical routes – without assumptions from the determined backtrajectories – I employ the following method:

- Iterate over all verified plumes and project the tropospheric NO_2 vertical column density of each member cell onto a global grid.
- Add the projections of all plumes.
- Count the number of days of valid observation for each cell and create a global map.
- Divide the a total tropospheric NO_2 vertical column density map by the number of observations map.

So, the mean tropospheric NO_2 vertical column density in long-range transport events $\overline{\mathrm{VCD}_{\mathrm{LRT}}}$ can be defined as:

$$\overline{\mathrm{VCD}_{\mathrm{LRT}}}(\mathrm{lat}, \mathrm{lon}) = \frac{\sum_{\mathrm{plumes}} \mathrm{VCD}_{\mathrm{plume}}(\mathrm{lat}, \mathrm{lon})}{N_{\mathrm{observations}}(\mathrm{lat}, \mathrm{lon})} \tag{7.3}$$

This gives an estimate of the typical NO_2 long-range transport routes; it is an estimator for the mean tropospheric NO_2 vertical column density observed in long-range transport events. As long-range transport events are frequent, the resulting map is smooth and gives an indication of the average flow of NO_2 in long-range transports. Multiple observations of individual long-range transports on different days are included in the data and lead to routes of longer lasting plumes to be adequately represented.

The resulting maps for individual seasons can be found in Figure 7.19. They show clear regional and seasonal differences in typical long-range transport routes with most of the long-range transport being observed in the mid-latitudes.

In the Northern Hemisphere, there are strong routes from the East Coast of the USA towards the North Atlantic, Greenland and the Arctic. There is also a route from

the East Coast towards Northern Canada in a giant arc as well as a less pronounced trajectory (due to short lifetimes) towards the tropics. Europe appears to emit long-range transports in all northern directions, with an especially pronounced route towards Greenland. Due to the convoluted coast-line, there is still significant NO_2 from long-range transport visible in spring, located over the Baltic Sea and the North Sea. China exhibits routes in winter and autumn that lead to Taiwan and Japan, with a dominant arc leading back to Eastern Russia over the Sea of Okhotsk. There is also a very fragmented route leading from the Beijing area over the Pacific towards the West Coast of North America. In spring, most of these routes can still be seen, though at a strongly attenuated level. During summer, there is almost no long-range transport visible, due to the short lifetime of NO_2 and missing frontal systems.

In the Southern Hemisphere, the only major emitter of NO_2 long-range transport is South Africa. There is a very distinct band of high average NO_2 long-range transport vertical column densities originating on the South African shore and dominantly leading out towards the Antarctic Circle (as far as GOME-2 / MetOp-A can observe it) and Australia. Further long-range transports are found near the shores of Argentina, but at a much lower frequency than for the four major emission regions. As most of these events also take place in winter, they appear to be linked to anthropogenic emission as well. Near Australia, however, long-range transport events appear to be far more rare and irregular than near the aforementioned emission regions. Most events are found in autumn (MAM), the main bush fire season. These two facts may indicate an origin in bush fires or other irregular emission events.

The arc-like routes – transporting NO_2 back to their origin or adjacent regions – are common in the Northern Hemisphere and caused by circular winds around the cyclones lifting the NO_2 from the planetary boundary layer to the free troposphere.

Plotting this map for all seasons combined but divided by plume age shows the typical plume movement (Figure 7.20). Young plumes are only located near the shores and starting in a rather narrow export band. Older plumes can (also) be found further off the shore and show higher scatter across the oceans. The oldest plumes can hardly be attributed to specific emission regions without backtrajectory calculations.

7.2.4 Sources

In the second step, I create an analogous map, in which the NO_2 content of each cell is relocated to the determined source of the cell – the coordinates at which the backtrajectory of the cell ends. Note, that all backtrajectories have the same temporal length: the estimated plume age.

This map then gives an estimator of the mean tropospheric NO_2 vertical column density that is emitted into long-range transport from this location. It serves as an indicator of the impact the region has on NO_2 long-range transport: The higher the values, the stronger the impact.

As seen in Figure 7.21, there are four hot spots of long-range transport sources. These are the same regions that were identified earlier in Subsection 7.2.3: China, Central Europe, the East Coast of North America and South Africa. There are some fuzzy souces: Western Argentina and Uruguay appear to be a weak but rather regular emission region – centered on Buenos Aires and Montevideo – while Australia appears to be very

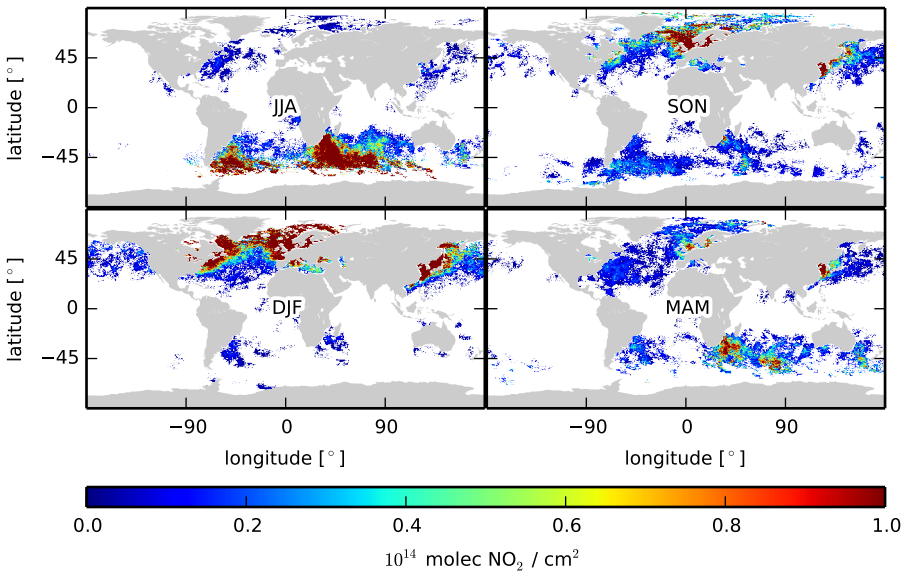

Figure 7.19: Seasonal maps of the mean vertical column density of NO_2 observed in plumes associated to long-range transport events. Note that columns near Europe are always higher than columns near North America – at least partially due to its special geography. There is a clear seasonality, favoring long-range transport events during winter. There is more NO_2 in transports on the Northern Hemisphere, where most of the emissions take place.

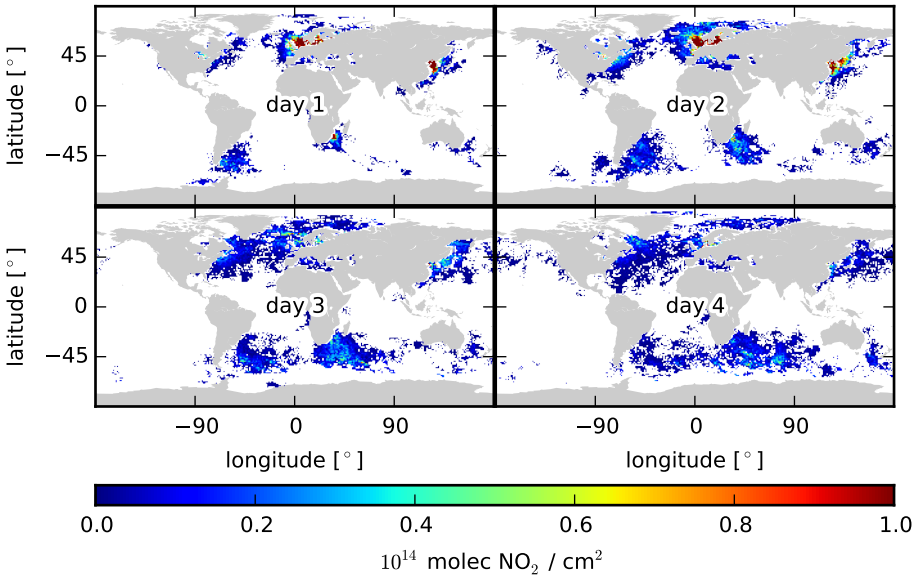

Figure 7.20: Route map as in Figure 7.19 but divided by plume age instead of season. *Day 1* refers to plumes with an estimated age of 0–23 hours. Young plumes are typically located closer to shores while older plumes are distributed more evenly and do not show maxima very close to emission regions.

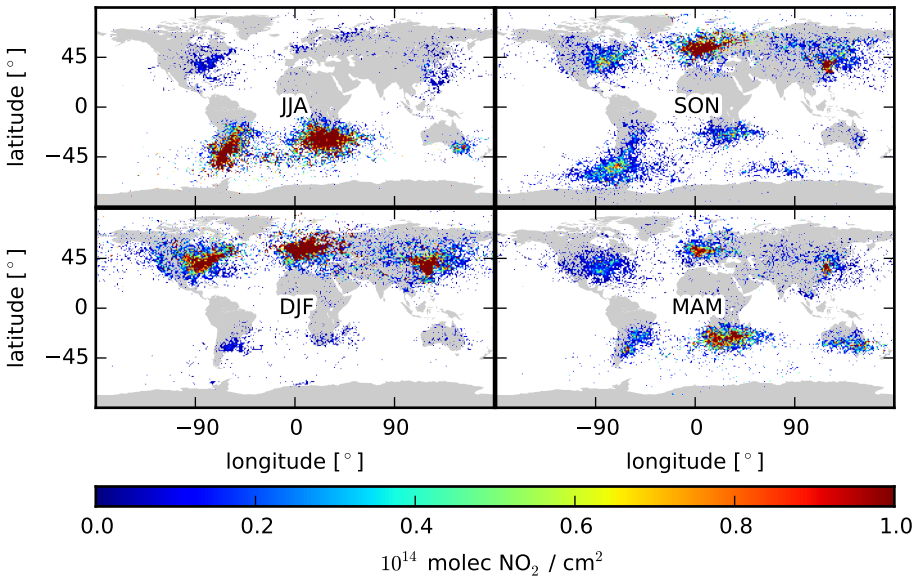

Figure 7.21: Seasonal maps of the mean tropospheric NO_2 vertical column density observed in plumes associated to long-range transport events, projected back to their sources as retrieved from the most likely backtrajectory.

irregular.

Most of the estimated source regions are a result of massive anthropogenic emissions due to industry and transportation. The lesser sources of long-range transported NO_2 – Australia and Argentina – could be caused by irregular emission events such as biomass burning. Especially Australia shows most long-range transport during autumn (MAM) – the prime season for biomass burning.

There is a strong scatter of points around these sources. This is a result of the limited resolution of both input data and the meteorological input data used for the HYSPLIT_v4 computations of backtrajectories (compare Subsection 6.4.2). This scatter is inevitable and increases roughly exponentially with increasing duration of the backtrajectory – given by the plume age. Taking this scatter into account, it is surprising that the resulting sources are determined to be rather sharp. This is also an indication that false positive detections do not dominate over the impact of correct detections.

For the South African emission region, there is a bias in the determined emission region towards the East of the Highveld plateau. This might be due to the elevated topography and dominant downwinds when air from the plateau is moving towards the East. These would cause the backtrajectory selection procedure to prefer a younger plume whose trajectories are still better correlated. In principle this selection bais will always tend to select an origin slightly downwind of the actual origin, but it is most prominent in this particular topography.

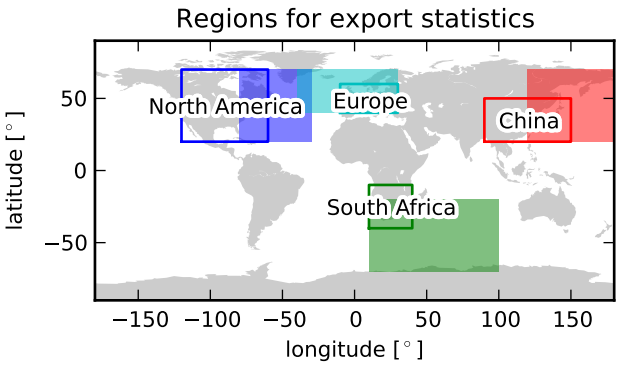

Figure 7.22: The regions used for the statistical study. Only plumes are considered that were observed over the ocean in the filled rectangle and were found over land-masses in the open rectangle 24 hours earlier.

7.2.5 Regions

Figure 7.21 allows to identify a number of prominent sources of NO_2 plumes subject to long-range transport. A study of the properties of these regions can yield further insight into the relevance of this phenomenon and possibly the mechanisms behind it.

For the following study, I identified the major emission regions of NO_2 long-range transport as Central East China, Central Europe, the East Coast of North America, and the Highveld plateau in South Africa. The emission and observation regions of are shown in Figure 7.22.

To identify unique plumes that were emitted in the source region, I filter the list of detected long-range transport plumes. From all the plumes whose center is situated inside the affected region, I select only the plumes that had their center of mass located over the continental part of the emission region 24 hours prior to their original observation in the satellite data. This way, multiple observations of the same plume are removed (in most cases). Due to this strict selection criterion, the obtained set of long-range transport plumes represents a lower boundary of the amount of NO_2 that was emitted from the source region onto the ocean. In other words: the impact of NO_2 long-range transport from these regions is at least as severe as indicated in the following study.

Figure 7.23 shows the amount of NO_2 exported from each region per year. The East China area emits the most NO_2 in long-range transport events, followed by Europe and North America. For all regions most NO_2 is emitted during winter, some fraction during autumn and almost none during spring. During local summer there are no observed events at all.

There are significant differences in the typical sizes of the observed plumes from different regions. Figure 7.24 shows the size distribution function. Typically, Europe's plumes are the largest (probably owing to concentrated emissions and its bay-like shape), followed by China. North America and South Africa have similar size distributions, which is most likely coincidental.

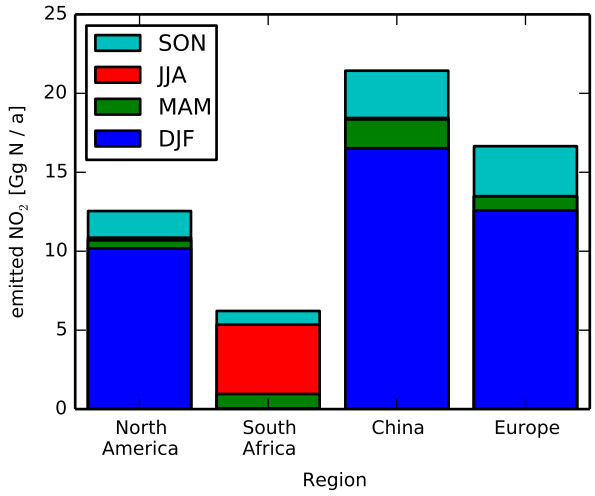

Figure 7.23: Total yearly NO_2 content in long-range transport plumes observed in GOME-2 data. The data is divided by the region in which the plumes were emitted (compare Figure 7.22) and highlighted for different seasons (cumulative histogram).

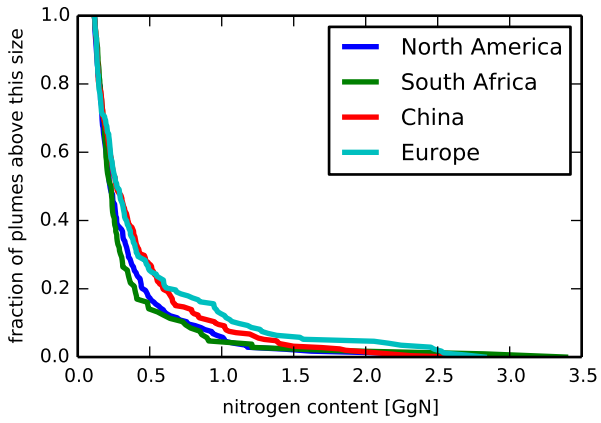

Figure 7.24: NO_2 content distribution of long-range transport events observed in the respective regions. South Africa has the smallest plumes, while Europe emits a large fraction of NO_2-rich plumes. The diagram shows, what fraction of a region's long-range transport population has an NO_2 content above the given value.

7.2.6 Meteorological conditions

The last part of the study of NO_2 long-range transport plumes in satellite data focusses on the meteorological conditions that accompany the emission of such a plume and might yield insights into the processes causing or supporting long-range transport.

For this study, I once again make use of the source regions and their associated plumes as defined in Subsection 7.2.5 and Figure 7.22.

Using NCEP DOE AMIP-II Reanalysis and GOME-2 / MetOp-A data, I then obtain composites of the following quantities:

- mean sea level pressure (MSLP)
- geopotential height at 700 hPa
- surface temperature
- FRESCO+ cloud fraction
- tropospheric NO_2 vertical column density as observed in this GOME-2 / MetOp-A data product

Due to the directional nature of wind velocities, it is not possible to create a meaningful composite that would allow the analysis of the dominant wind patterns.

Composite analysis of meteorological events has been performed in various studies, e.g. in order to analyze polar lows in the North Atlantic and Arctic Ocean (Blechschmidt et al., 2009) or transport of NO_x within South Africa (Abiodun et al., 2014).

GOME-2 / MetOp-A data are given once per day, NCEP DOE AMIP-II Reanalysis-data every 6 hours. I iterate over all plumes from the given region and retrieve their date and time of emission. From the full set of satellite or meteorological observations I then select the timestep closest to the date of emission and add it to the correlated (or signal) composite. All timesteps from the data that were not added to the correlated composite are then added to the uncorrelated (or meteorological background) composite. This procedure yields two distinct sets of meteorological observations: the signal composite contains only meteorological conditions associated to a long-range transport event, the background composite contains only meteorological conditions that are not associated to long-range transport.

To avoid the impact of seasonal meteorological variation, I select data only from the regional winter months: DJF for the Northern Hemisphere and JJA for the Southern Hemisphere. Otherwise, the difference between the composites would be dominated by seasonal differences: plumes occur mostly in winter and autumn, which means that data from winter would be overrepresented in the signal composite; likewise data from summer and spring would be underrepresented in the signal composite. Thus, the meteorological difference between summer and winter half would be strongly visible in the composites and dominate the effects leading to emission of long-range transport events.

I repeat the same procedure in steps of 24 h forwards and backwards, creating composites for "24 hours before/after plume emission" and similar.

I then compare the composite average of the signal and the background composite. Also, I employ the Mann-Whitney U test (Mann and Whitney, 1947) to analyze in

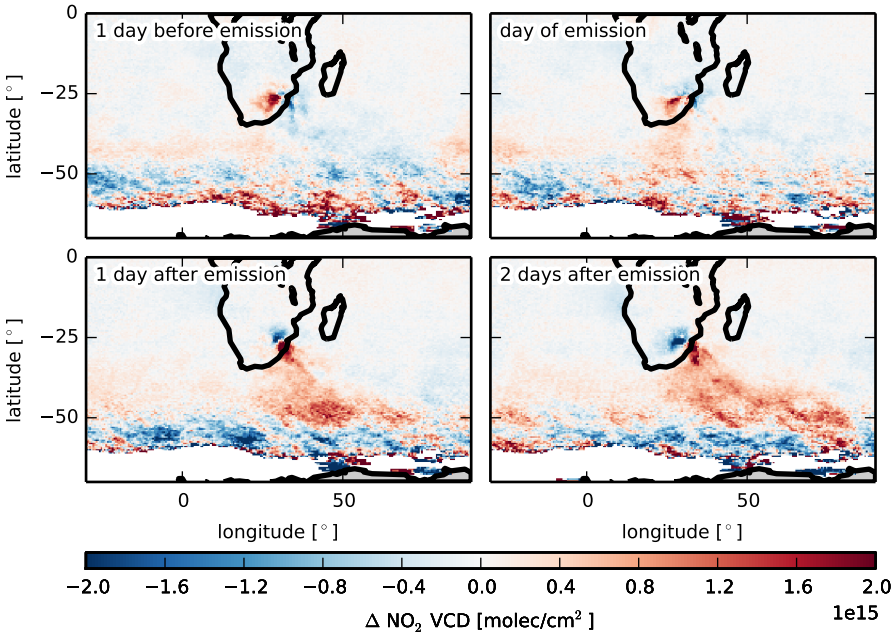

Figure 7.25: GOME-2 tropospheric NO_2 vertical column density for the days of plume emission in the South African region. Only events in JJA (2007–2011) are shown, to mitigate biases from meteorological seasonality. There is an anomaly towards high values over the Highveld region before plume emission. After emission, the NO_2 vertical column densities over the Highveld region are on average lower, while an upwards anomaly can be seen southeast of South Africa. High fluctuations in the GOME-2 data and few observations result in visible noise in the anomalies near polar night.

which regions the distributions in the signal and background composite follow compatible or significantly different distributions. The test computes a statistic that serves as a measure of the difference between two distributions of data and can be used to estimate the probability that both data sets follow the same underlying distribution. In the composite analysis, the probability of an identical distribution is computed for each grid cell individually, highlighting areas of significant difference between the two composites. Only spacially extended anomalies with probabilities of less than 1 % of resulting from statistical variance of identical distributions (i.e. that show significant results in the Mann-Whitney U test), are reported in this study.

In the analysis, a few striking features can be seen in the composites of mean sea-level pressure, surface temperature and FRESCO+ cloud fraction. There are also significant features appearing in the tropospheric NO_2 vertical column density composites, as should be expected from the underlying selection process. No analysis of composites of wind speed has been performed as the vectorial nature of these forbids superimposing them in a simple manner.

Figure 7.25 shows the deviations of signal and background composite of NO_2 in the

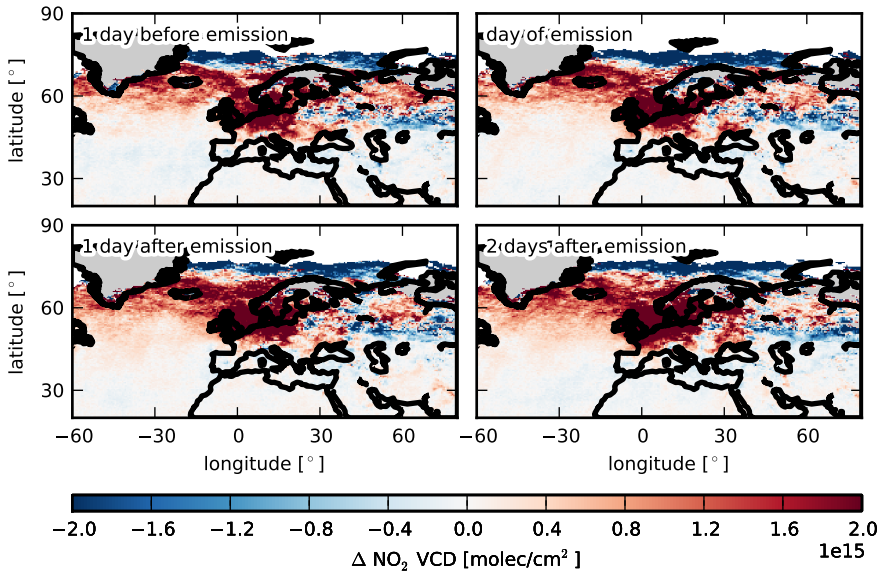

Figure 7.26: As in Figure 7.25, but for Europe and the North Sea. Only events in DJF (2007–2011) are shown. The data show significantly elevated levels of NO_2 vertical column density over Europe and the North Sea in the days before and during a long-range transport event.

days preceeding and following the emission of long-range transport events during winter in South Africa. An outflow of NO_2 is visible one and two days after emission of a long-range transport event, directed towards the polar circle in eastward direction. This serves as an indication of the effectiveness of this analysis.

On the day before emission, a strong, isolated peak in tropospheric NO_2 vertical column density is located exactly above the Highveld plateau. This indicates that there is a build-up of NO_2 preceeding a long-range transport transport event and favorable meteorological conditions alone may not be sufficient for a NO_2 long-range transport event.

Similar features can be seen during summer in the Northern Hemisphere in Europe (Figure 7.26) and China (not shown). There are still significant elevations of tropospheric NO_2 vertical column densities in the emission region, but they extend over a longer timespan and are not as locally confiend as in South Africa. Also, the outflow is far less pronounced and extends over a longer timespan. This indicates that it is a lot easier to correctly identify and trace back long-range transport events near the isolated emission region South Africa than near convoluted emission regions and shores as in Europe and China.

The evolution of the composite mean sea-level pressure for long-range transports near South Africa is shown in Figure 7.27. There is a low-pressure anomaly building up to the West on the day before and the days of emission, moving towards the southern tip of South Africa, together with surrounding high-pressure anomalies moving towards

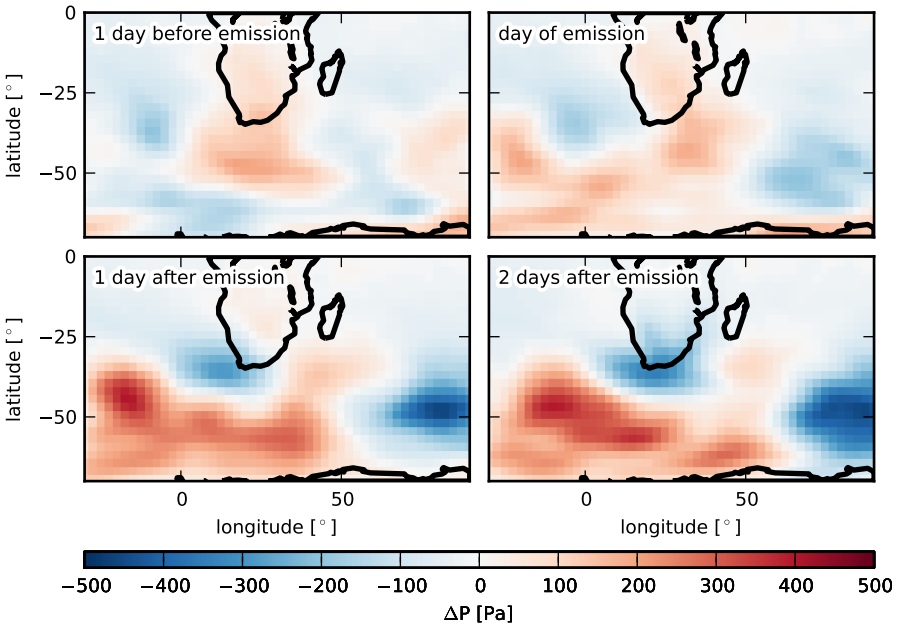

Figure 7.27: NCEP DOE AMIP-II Reanalysis mean sea-level pressure anomaly (given in Pa) for the days of plume emission in the South African region. Only events in JJA (2007–2011) are shown, to mitigate biases from meteorologic seasonality. The image shows significant high and low pressure patterns in the southern midlatitudes, moving from West to East.

the East. This low pressure anomaly is likely to be the result of cyclones causing the transport.

In Europe (Figure 7.28), again, this is much less dynamic. There is an anomaly on the order of $\Delta P \approx -5\,\mathrm{hPa}$ towards a reduced mean sea-level pressure over Western Europe, while there is an upwards anomaly on the same order over Western Russia and the Arctic. Central Europe lies right between these two anomalies. If these anomalies results from highs and lows, there will be a channel of high wind speeds right over a major emission region that will propel NO_2 offshore, in the direction that most European long-range transports travel.

For China, this result is much less clear, showing only a vague low-pressure anomaly moving from the Pacific towards the West onto the Asian continent.

The analysis of FRESCO+ cloud fractions only yields significant results for the China region where patterns of elevated cloud fraction can be seen offshore of Beijing on the days after emission. It is quite likely that a passing storm and elevation of boundary layer air will lead to cloud formation. As cloud formation is a complex process, I did not expect any significant results from this analysis and it may be coincidental.

There were no clear results of any anomaly in composite meteorological studies of the North American emission region. This may be an effect of the very elongated emission region, covering the entire East Coast of the North American continent. Also, several

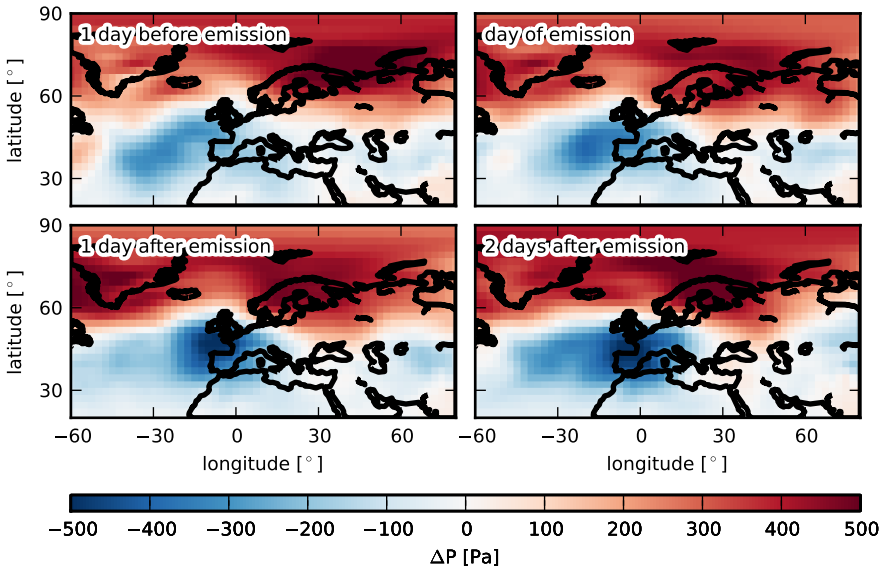

Figure 7.28: As in Figure 7.27, but for the Central European region. Only events in DJF (2007–2011) are shown. The data show a low-pressure anomaly over Western Europe over the course of the transport. Contrasting this, there is a high-pressure anomaly over the Arctic and Northern Russia.

storm tracks cross North America, moving into different directions. While all may lead to the emission of a NO_2 long-range transport, they may be acoompanied by various different meteorological conditions.

Keeping in mind that the emission times of long-range transports are only a vague estimation, the results of this analysis nonetheless yield significant insight into the emission mechanism of long-range transport events and further consolidate the underlying theory.

7.2.7 Correlation to the North Atlantic Oscillation (NAO)

Eckhardt et al. (2003) have shown in simulations that the North Atlantic Oscillation (NAO) may be responsible for transport of pollutants to the Arctic, modeling trace gases with lifetimes of 5 days. Christoudias et al. (2012) find similar patterns of pollution export as shown in Figure 7.19 to stem from zonal wind flow, resulting from the NAO. The results in Figure 7.28 indicate a possible negative correlation to the NAO, with emissions of plumes being linked to a negative NAO index – showing a high-pressure anomaly over Iceland and a low-pressure anomaly over the Azores. The high-pressure anomaly over Iceland is, however, spatially extended, making these results ambiguous.

A correlation of the frequency of plumes emitted from Europe with monthly NAO indices from the NCEP Climate Prediction Center[1] over all months (Figure 7.29) shows

[1] http://www.cpc.ncep.noaa.gov/products/precip/CWlink/

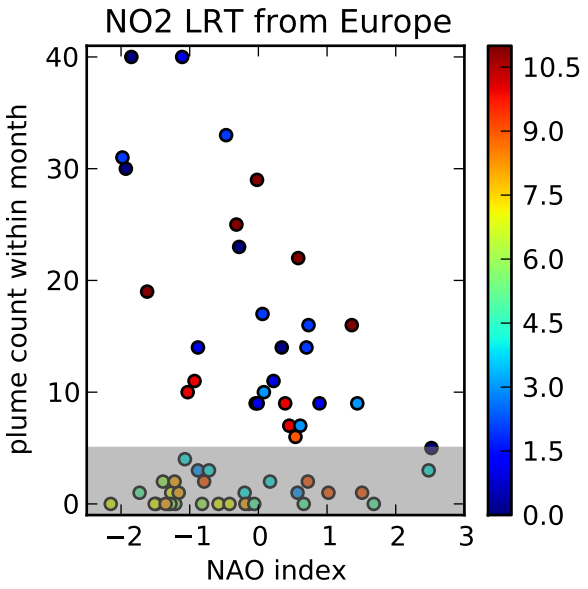

Figure 7.29: Correlation of plume frequency from Europe in a given month with the NAO index as determined by the NCEP Climate Prediction Center. Colors denote the calendaric month (with 0 being December). Values in the shaded area were not considered for the correlation analysis. There are two superimposed features: no correlation during spring to late summer and a strong negative correlation during autumn and winter.

no significant correlation (probability of a random distribution generating such data: 32 %). However, these two quantities exhibit two features: an uncorrelated part when few plumes are emitted and a highly correlated part when multiple plumes are emitted. When we remove all points with less than 5 plumes in the given month, the probability of a random distribution leading to these results is only 0.05 %, making this result highly significant. Plume emission rates significantly increase with a lower NAO index. This confirms results from the composite analysis. Negative NAO indices with low plume frequency are almost entirely spring to late summer, which are unfavorable for NO_2 long-range transport due to radiation budget.

This concludes the analysis of long-range transport in the GOME-2 / MetOp-A data set.

8 NO_2 long-range transport in MACC-II reanalysis data and comparison to results from GOME-2 / MetOp-A

The analysis of NO_2 long-range transport as observed in MACC-II reanalysis data to a large extent follows the methods described in Chapter 7. Only deviations from the preceeding analysis method for GOME-2 / MetOp-A data will be stated explicitly.

8.1 Case studies

First, I have looked into the case studies performed on satellite data (Section 7.1) to verify if selected, very distinguished events have been found in MACC-II reanalysis data as well. All events driven by anthropogenic emissions (Subsection 7.1.1, Subsection 7.1.2, and Subsection 7.1.4) have been found in the data.

In contrast to this, the event in Australia on 27 April 2008 which most likely originates from bush fires (Subsection 7.1.3) could not be found in MACC-II reanalysis data. Bush fires are emission events with very strong local convection driven by the heat of the fires, lifting their emissions to high altitudes. This small scale and non-continuous emission makes it hard to adequately model transport originating from bush fires. This is probably the reason why this event cannot be found in MACC-II reanalysis data.

Table 8.1 lists the properties of the individual plume observations in MACC-II reanalysis, comparable to Table 7.1.

8.1.1 North Atlantic, 16–19 December 2007

Figure 8.1 shows the long-range transport event analyzed in GOME-2 / MetOp-A data in Subsection 7.1.1. The visual first impression shows that the shape and course of the plume in both data sets are nearly identical and they are mostly observed on the same dates.

This plume is first classified as belonging to a long-range transport event on 16 December 2007, when two pixels over the Great Lakes are detected as anomalies and classified as transport event. In the tropospheric NO_2 vertical column density map the plume is evident and much more spatially extended than found by the algorithm. This illustrates a drawback of the employed automatic detection method. Unless noted otherwise, further analysis will exclude this very incomplete observation.

The plume stays relatively compact on 17 December 2007 (first observation in GOME-2 / MetOp-A data), with its perceived center just south-east of Newfoundland. On 18 December, the plume is located between North America and Greenland and has experienced wind shear, which elongates it into an arc-like structure.

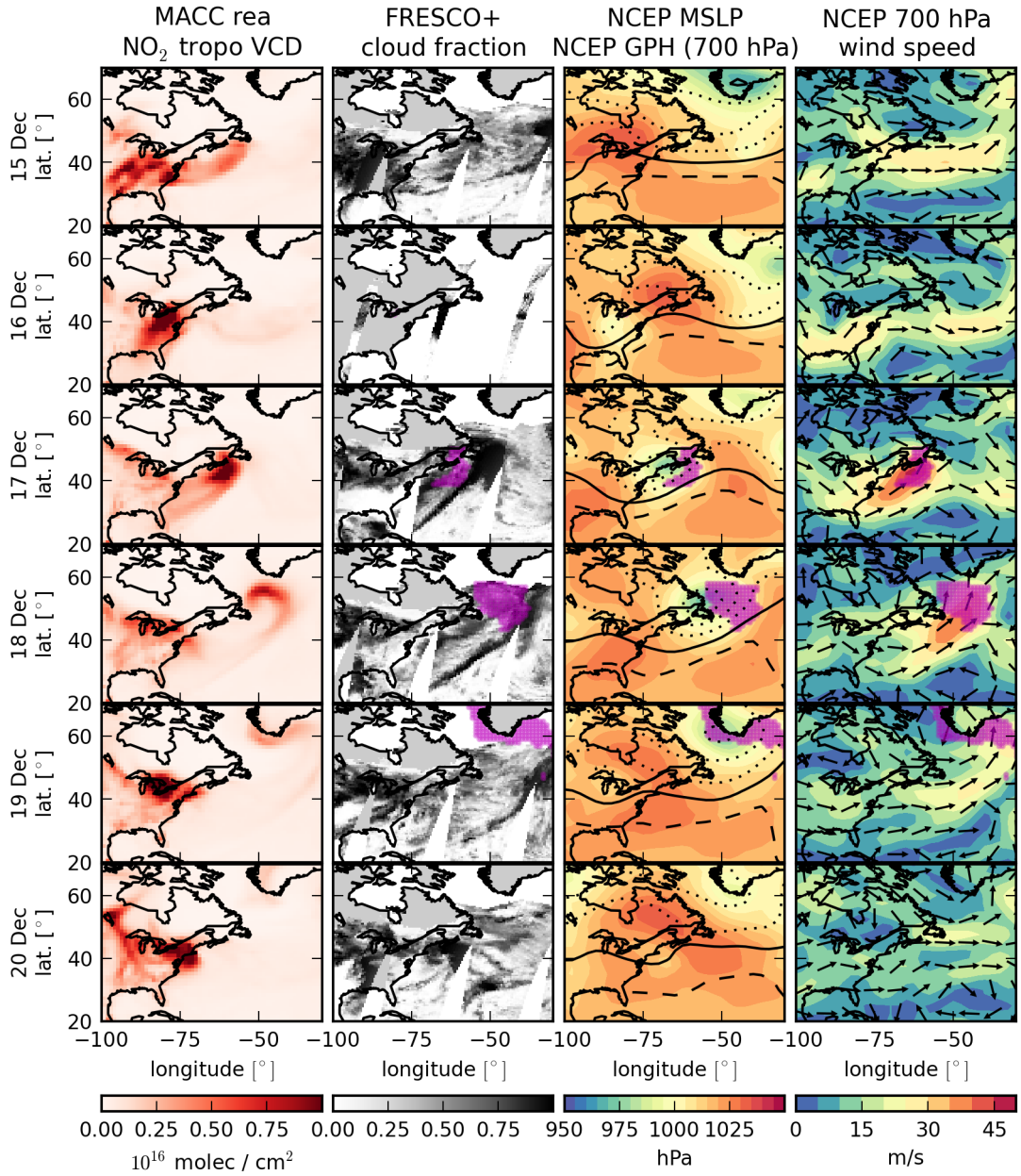

Figure 8.1: As for Figure 7.1 but showing MACC-II reanalysis data and plume cells as attributed during analysis of MACC-II reanalysis data. Two cells of the plume are found over the North American Great Lakes on 16 December 2007, the first full detection in MACC-II reanalysis data is made on 17 December 2007. The plume arrives over Greenland on 19 December 2007; Greenland's distinct coast line is visible in the plume, indicating that part of the NO_2 decomposes upon reaching shore.

Table 8.1: Properties of NO_2 plumes observed during long-range transport case studies as derived from processing MACC-II reanalysis data (analogous to Table 7.1).

Date	Plume Center		Altitude [km]	Age [h]	NO_2 content [Gg N]	Area [10^3 km^2]
North Atlantic						
2007-12-16	$43°N$	$80°W$	2.0	5	0.23	35
2007-12-17	$43°N$	$61°W$	1.0	49	1.31	824
2007-12-18	$53°N$	$46°W$	1.0	69	1.11	1747
2007-12-19	$60°N$	$40°W$	1.0	98	0.51	1715
South Africa						
2008-07-08	$34°S$	$34°E$	2.0	36	0.15	938
2008-07-09	$35°S$	$41°E$	2.0	47	0.19	1646
2008-07-10	$38°S$	$56°E$	3.0	117	0.19	3768
2008-07-11	$42°S$	$76°E$	4.5	110	0.13	5986
Central Europe						
2010-10-01	$60°N$	$11°W$	1.0	15	0.22	575
2010-10-02	$65°N$	$21°W$	1.0	37	0.26	975
2010-10-03	$65°N$	$1°E$	1.5	65	0.42	655

On 19 December, the plume forms an arc around the southern tip of Greenland. This could be a coincidence and be caused only by the wind and wind shear patterns of the cyclone. However, it appears more likely that upon arrival on the shore of Greenland, the NO_2 decomposes, probably due to higher irradiation over a high-albedo surface. Also, Greenlands elevated topology could block the NO_2 from moving there, as the plume resides at a low altitude. Due to the low air and surface temperatures in Greenland during winter, it is not expected that PAN from the plume decomposes into NO_2, which would lead to an increase in tropospheric NO_2 vertical column densities.

On 20 December, only faint remnants of the plume are found near the southern coast of Greenland. They are no longer classified as long-range transport event by the algorithm and vanish on 21 December 2007.

On 17 December, the plume is estimated to be 49 hours old since its emission which is in good agreement with the estimated 46 hours in GOME-2 / MetOp-A data. The following two observations are estimated to have an age of 69 and 98 hours, respectively, which is roughly consistent. The backtrajectories of the observations all point at a passing cold front as the on-shore origin of this long-range transport event, in accordance to results from GOME-2 / MetOp-A observations.

All backtrajectories find the plume at the lowermost altitude level of 1,000 m. This is not in agreement with the results from satellite data, which find increasing altitudes. This is most likely an effect of an incomplete observation on 19 December in satellite data, which leads to a backtrajectory that is not appropriatly representative for the entire plume.

The modeled NO_2 plumes are much less massive than the observed ones. In the model data, the plume is estimated to consist of 1.1 Gg N on 17 and 18 December, where

GOME-2 / MetOp-A observes roughly twice as much NO_2 in the plume. This decreases to 0.51 Gg N on 19 December, where even the incomplete observation in GOME-2 / MetOp-A yields a total of 0.65 Gg N. There are several factors in the model which could explain this discrepancy.

- Convection is difficult to parameterize. An insufficient parameterization could lead to less efficient convection which does not include all NO_2 in the transport. However, this does not appear to be the case as the remaining NO_2 over the source region is significantly diminished and indicates an efficient convection during the frontal passage.
- The model might miss a build-up of tropospheric NO_2 over the source region which will lead to increased NO_2 columns upon emission of the plume. In turn, this would lead to a higher NO_2 content in the transported plume.
- Emissions on the Southern Hemisphere could be systematically too low in the used emission inventories.
- The elevation of NO_2 from the planetary boundary layer into the free troposphere may not occur fast enough in MACC-II reanalysis so that NO_2 decays more rapidly (see Figure 2.3). Chemical loss of NO_2 could be overestimated.

It is also possible that the radiative transfer calculations for GOME-2 / MetOp-A data underestimate the air-mass factor inside the plume which would in turn lead to a overstimated tropospheric NO_2 vertical column density. This would be the case if the majority of NO_2 in the plume resides above clouds. My analysis assumes that, if clouds are present, the NO_2 is mixed within the cloud.

In horizontal extent, however, the plume shows differences to the observations in GOME-2 / MetOp-A data. The initial detection shows the plume to be a bit smaller than in satellite data ($824 \cdot 10^3\,\mathrm{km}^2$) on 17 December. It then increases in size to $1.7 \cdot 10^6\,\mathrm{km}^2$ which it keeps on the following day, while sizes in GOME-2 / MetOp-A data decrease in later observations.

In GOME-2 / MetOp-A data, strong dispersion of the plume will dilute concentrations enough to make them indistinguishable from noise in the data. These outer cells of the plume are then no longer detected by the algorithm and the plume apparently shrinks in horizontal extent. While conceptually this means that parts of the plumes will be missed in satellite data, this behavior may be desirable for practical purposes as the definition of a plume loses its meaning in the outer rim.

Estimating the decay time of NO_2 in the plume, I neglect the first observation which only consists of two data points and is highly misrepresentative of the long-range transport event. Observations of this sort should be removed from the data set in future iterations of the algorithm. Alternatively, analysis of NO_2 long-range transport over both ocean and continents would render such a filter obsolete.

When considering the observations from 17 to 19 December 2007, an exponential regression yields an initial plume content of $m_0 = 2.69\,\mathrm{Gg\,N}$ and a NO_2 lifetime of $\tau = 58\,\mathrm{h}$. This is only about half the lifetime that was found for this plume when observed with GOME-2 / MetOp-A. This discrepancy might stem from various reasons:

a suboptimal parameterization of chemistry in MACC-II reanalysis, from problems with the relatively low signal-to-noise-ratio in satellite observations in comparison to model data, from an incorrect altitude of the plume in MACC-II reanalysis (or other problems in modeling its transport out of the planetary boundary layer) or a problem in the GOME-2 / MetOp-A data retrieval. The estimated initial masses of the plume from both data sets are of similar order and agree within the coarse approximations made.

The minimum average ground speed of the plume amounts to 67 km/h from 17 to 18 December 2007 and to 36 km/h on the following days. As evident from comparing Figure 7.1 and Figure 8.1, these travel velocities are in accordance with satellite observations, even when the plume is only partly observed in GOME-2 / MetOp-A data on 19 December 2007.

In Figure 8.2 you see MACC-II reanalysis, FRESCO+ and NCEP DOE AMIP-II Reanalysis data, overlaid with the plume cells from the penultimate observation at their positions at the corresponding time in the backtrajectory, as determined by HYSPLIT_v4. In comparison with the analogous Figure 7.3 for the observation of the same plume in GOME-2 / MetOp-A data, these backtrajectories are very similar with a bulk of cells following the plume along and a similar amount going astray. When looking at the last observation of this event, the plume cells are quickly dispersed in the backtrajectory, probably owing to the incomplete observation and complex wind patterns upon arrival at the shore.

Figure 8.3 shows the corresponding altitude evolution of the backtrajectories for all observations of this event. For the first observation, a clear uplift of the plume can be seen about 24 hours after its emission. This uplift is still visible at this point in time for the second observation, although it is diluted by a significant proportion of backtrajectories staying at lower altitudes. These are likely to be stray trajectories. For the last observation, the uplift event can be seen at a later time, diluted by even more stray trajectories. Only few of the backtrajectories from this observation trace back to the likely emission region. This is most likely simply an effect of the dynamic nature of meteorology and the plume's old age.

From the analysis of this event, it is evident that this plume transported NO_2 from North America to Greenland's pristine climate.

8.1.2 South Africa, 8–11 July 2008

The long-range transport event emerging from South Africa in July 2008 that was analyzed in Subsection 7.1.2 can also be found in MACC-II reanalysis data. The individual observations of this event as well as accompanying meteorological conditions are shown in Figure 8.4.

The trajectory of the event in MACC-II reanalysis data shows significant deviations from the trajectory in satellite data. It is also apparent that tropospheric NO_2 vertical column densities in MACC-II reanalysis data are significantly lower than estimated from GOME-2 / MetOp-A data, showing little more than 10 % of the estimated NO_2 content in the plume. This is symptomatic of the Southern Hemisphere, as will be shown in Subsection 8.2.1. While the plume is hardly visible in visual inspection (Figure 8.4), it is still detected in the algorithm – due to low noise in the model data over the remote Indian Ocean.

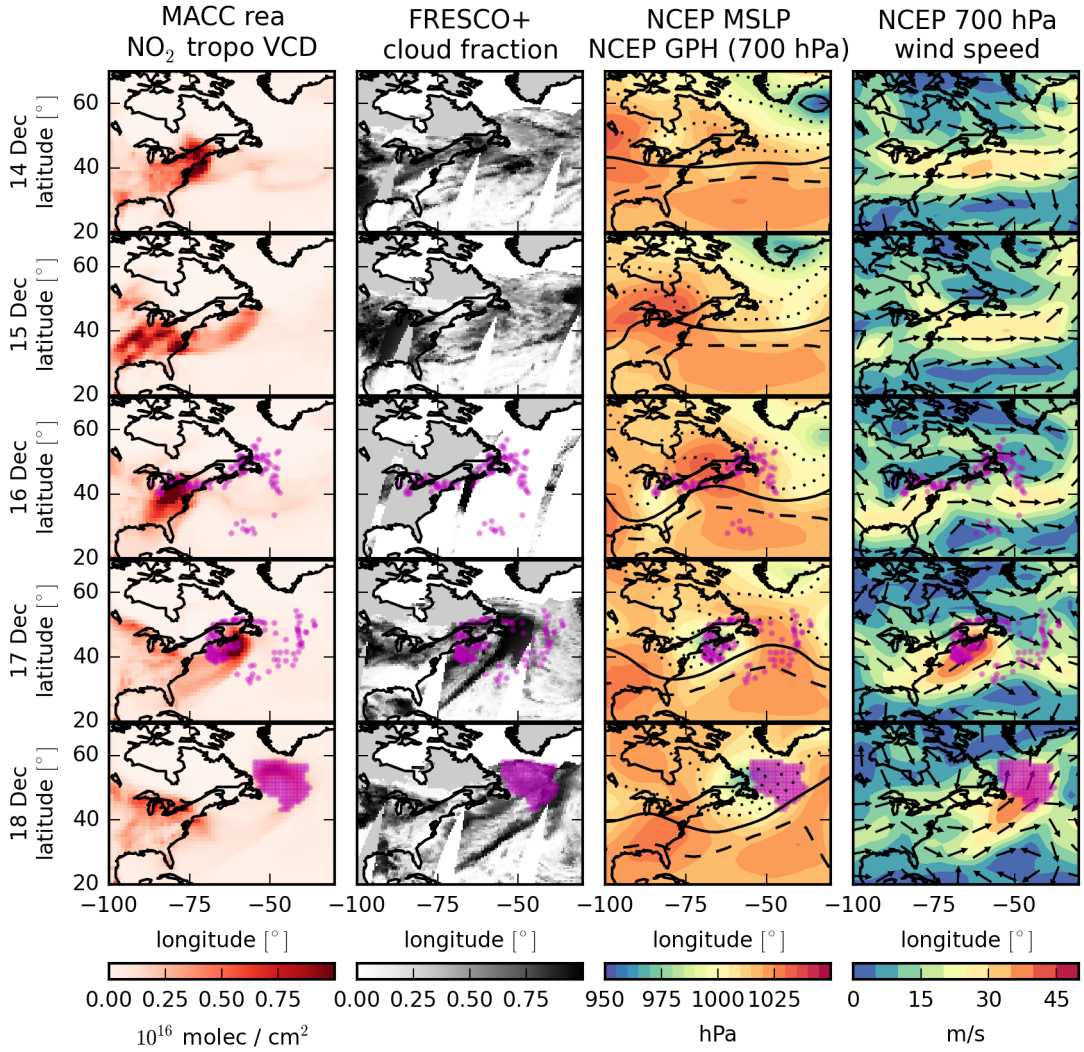

Figure 8.2: Illustration of the backtrajectory of the penultimate observation of this long-range transport event (18 December 2007) in MACC-II reanalysis data. Data as in Figure 8.1, but purple circles indicate the locations of the backtrajectories of the plume from 19 December 2007 at the respective dates. Only parts of the plume follow the backtrajectory to the estimated source region in the Chicago area. Many of the detected cells stray off the plume backtrajectory, showing implications of the coarse horizontal and vertical resolution of the plume detection algorithm. Also, MACC-II reanalysis model data and HYSPLIT_v4 backtrajectories are based on different meteorological data sets.

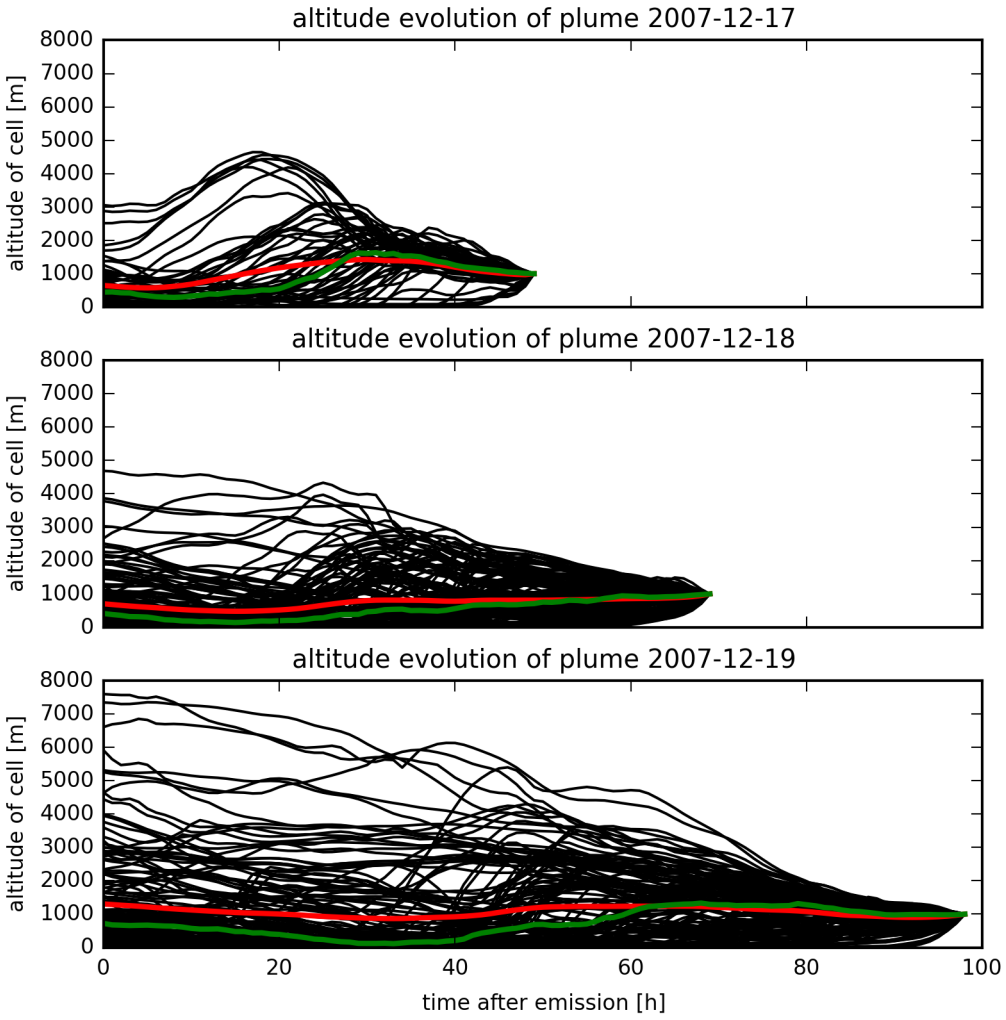

Figure 8.3: Altitudes of the backtrajectories for the long-range transport event over the North Atlantic on 16 to 19 December 2007, based on MACC-II reanalysis data. As in Figure 7.2. The observations on the first day show a prominent uplift about 24 hours after emission, while later observations do no longer indicate this so strongly.

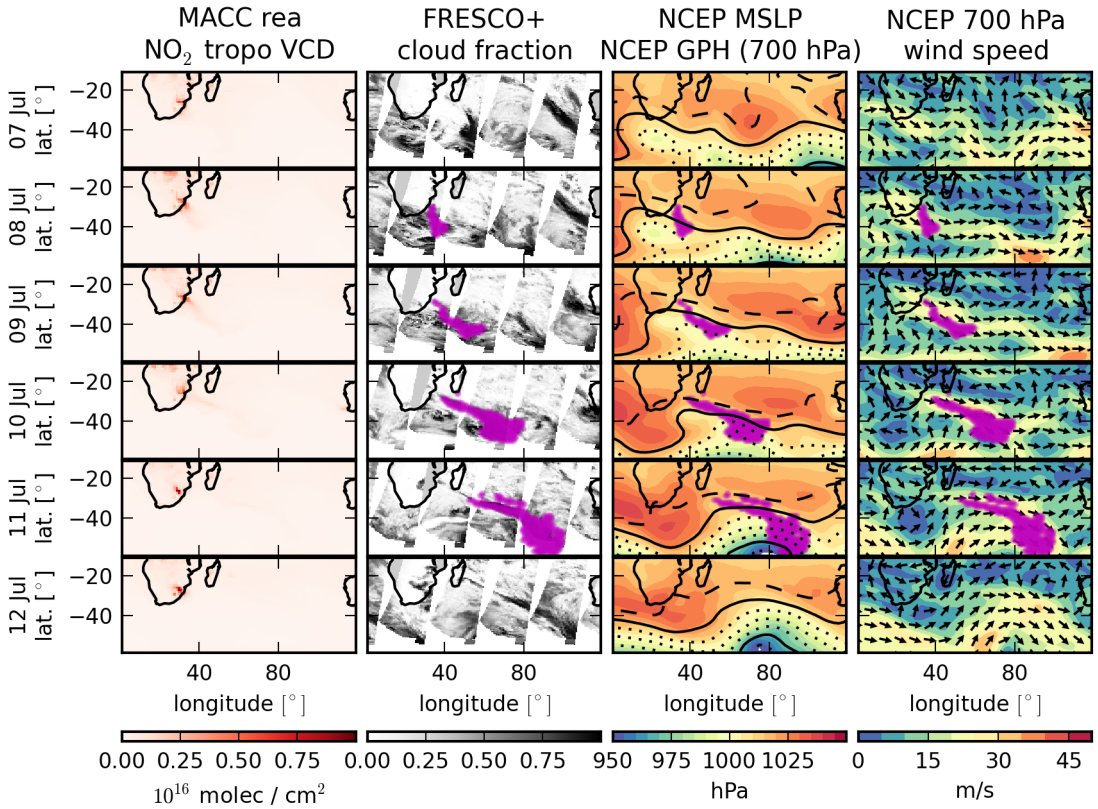

Figure 8.4: As for Figure 7.5, but showing the long-range transport event as found in MACC-II reanalysis data. Only four observations of the plume are made. It appears to leave a trail of NO_2 behind, which might indicate replenishing of the plume from the Highveld plateau until 09 July 2008. The trajectory of the plume is significantly further south than in GOME-2 / MetOp-A data.

The plume can already be observed on 08 July 2008 – one day earlier than in GOME-2 / MetOp-A observations, where regular outflow leads to a diminished sensitivity of the algorithm near the coast of South Africa. It moves towards the east-southeast, steadily increasing in size.

The plume is last detected on 11 July 2008. On this date, the plume was located around 20° or about 1,000 km west of the Australian west coast – heading east – in GOME-2 / MetOp-A data, whereas MACC-II reanalysis data show the plume significantly displaced to the south and show no indications of the plume impacting Australian air quality. This might be an effect of different emission times – bearing the chaotic nature of meteorology in mind – or of the meteorological data set used for MACC-II reanalysis. On 12 July 2008, the plume is so strongly diluted that it is no longer detected in MACC-II reanalysis data by the algorithm, while it can still be seen in GOME-2 / MetOp-A data.

The plume in this long-range transport event does not show a distinct arc-like structure or a compact shape as seen in Figure 7.5. It appears that this plume might not have been emitted due to a violent event such as a passing cold front, but rather through much more subtle processes that suffice for long-range transport in this exposed emission region. Instead, this plume consists of a compact bulk head (slowly increasing in horizontal extent) and an elongated tail, which only slowly moves away from the emission region. It appears likely that this plume's NO_2 content was still replenished from the emission region on the first two observations, which leads to an increasing NO_2 content. This also hints at a less violent emission mechanism.

As with the analsys in GOME-2 / MetOp-A data, age estimation of this plume is not consistent over consecutive days. This may be an effect of the more subtle weather conditions, the unusual shape of the plume and the elevated geography of the Highveld plateau. A joint analysis of all the estimated ages yields 43 hours as the best fitting age at the first time of observations. This is reasonable as the slow traveling speeds indicate a slow separation process from the source region.

It is difficult to look at the evolution of the NO_2 content in the plume. As the plume is continuously replenished, its NO_2 content increases. This leaves only the last two observations to determine the actual decay time of the NO_2. This analysis leads an initial mass $m_0 = 0.71\,\mathrm{Gg\,N}$ with a NO_2 lifetime of $\tau = 67\,\mathrm{h}$, which – surprisingly – is consistent with the previous case study.

Looking at the altitudes of the backtrajectories for all four observations of the plume shows strong inconsistencies. In particular, the initial height of the bulk of the plume steadily increases with every observation. This may be caused by the selection algorithm that selects the backtrajectory with the most plume cells in the continental boundary layer. If the dispersion rate of plume pixels is roughly constant at all altitudes, this will lead to a preference of high altitudes for the estimation of the plume altitude at observation, where wind speeds are higher and the remote continent is reached faster.

8.1.3 Europe, 1–3 October 2010

The third plume from GOME-2 / MetOp-A data that is also visible in MACC-II reanalysis data is part of the multi-part long-range transport event emitted from Central Europe on 01 to 03 October 2010 (Figure 8.5).

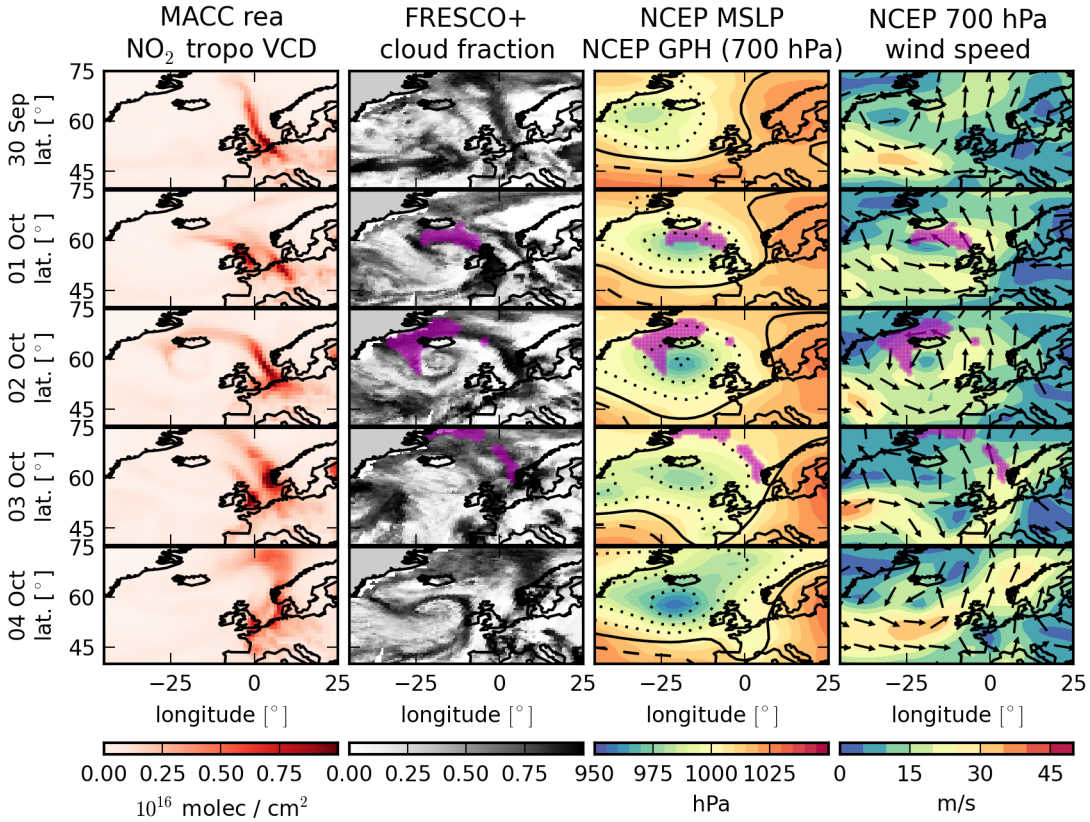

Figure 8.5: The event shown in Figure 7.9, but showing the event as obtained from MACC-II reanalysis data. The event is observed on three consecutive days (instead of two for GOME-2 / MetOp-A data). The plume is filamented around a cyclone near Iceland after emission from Central Europe before it drifts off towards the north-east.

Just as in GOME-2 / MetOp-A data, MACC-II reanalysis data show a fragmentation of this outflow into multiple plumes. The first fragment is transported towards north-northeast while the second fragment – which is studied in this chapter – enters the domain of a passing cyclone. Shear winds lead to a strong distortion of the plume's shape. The shape and location of the plume on 1 and 2 October 2010 are very similar in MACC-II reanalysis and GOME-2 / MetOp-A data. This confirms the detection of this plume and shows that the MACC-II reanalysis model adequately represents this type of long-range transport from a qualitative perspective.

Unlike GOME-2 / MetOp-A, the plume is detected for a third time on 3 October 2010 in MACC-II reanalysis data. At this time, the plume is already heavily fragmented and has traveled into the Arctic Ocean between Greenland and Svalbard. This confirms the deductions from Subsection 7.1.4.

Backtrajectories estimate the plumes to be 15, 37 and 65 hours old on consecutive observations. This is very consistent and indicates that the backtrajectories are reliable. This is also consistent with the observations from GOME-2 / MetOp-A data (21 and 36 hours for the first to observations). The plume is estimated to travel at the lowest possible altitude of 1,000 m a.m.s.l. on the first two days of observation (identical to GOME-2 / MetOp-A observations), rising to 1,500 m on the third day. Minimum ground travel speeds of the plumes are also consistent with 31 km/h from 1 to 2 October (identical to GOME-2 / MetOp-A derivations). Mean travel speed increases as the plume enters the part of the cyclone where travel direction and rotation constructively interfere.

As for the other cases, the plumes retrieved from MACC-II reanalysis data are much less massive than the plumes found in GOME-2 / MetOp-A data. However, there is an increase in plume mass from 1 to 2 October 2010 in both data sets. This is easily explained by looking at Figure 7.9 and Figure 8.5. In neither data set has the plume separated from the continent and it is likely that more NO_2 was emitted and replenished the plume over the ocean during the transport event, as in the previous case study. It is not possible to determine a reliable lifetime or initial mass from these observations.

However, the backtrajectories (Figure 8.6) of this event are pretty consistent, bearing in mind that the analysis assumes that all plume cells are emitted at the same time – which is not the case here. Most of the backtrajectories end up in central Europe on 01 October. The trajectories start as a compact bulk that is both sheared and translated in the influence of a stationary cyclone south of Iceland.

8.2 Statistical analysis

When performing the analysis described in Section 7.2 on MACC-II reanalysis data from 2007–2010, the algorithm obtains a total of 2773 long-range transport event candidates. Of these candidates, 2479 have been verified as long-range transport events and only 294 have been discarded during the verification process.

The small fraction of discarded plumes is representative of the lack of measurement errors and natural fluctuations in model data. Also, the stratospheric part of the NO_2 vertical column density is fully filtered from MACC-II reanalysis data before they are analyzed.

There are 20 % fewer verified long-range transport plumes in MACC-II reanalysis data

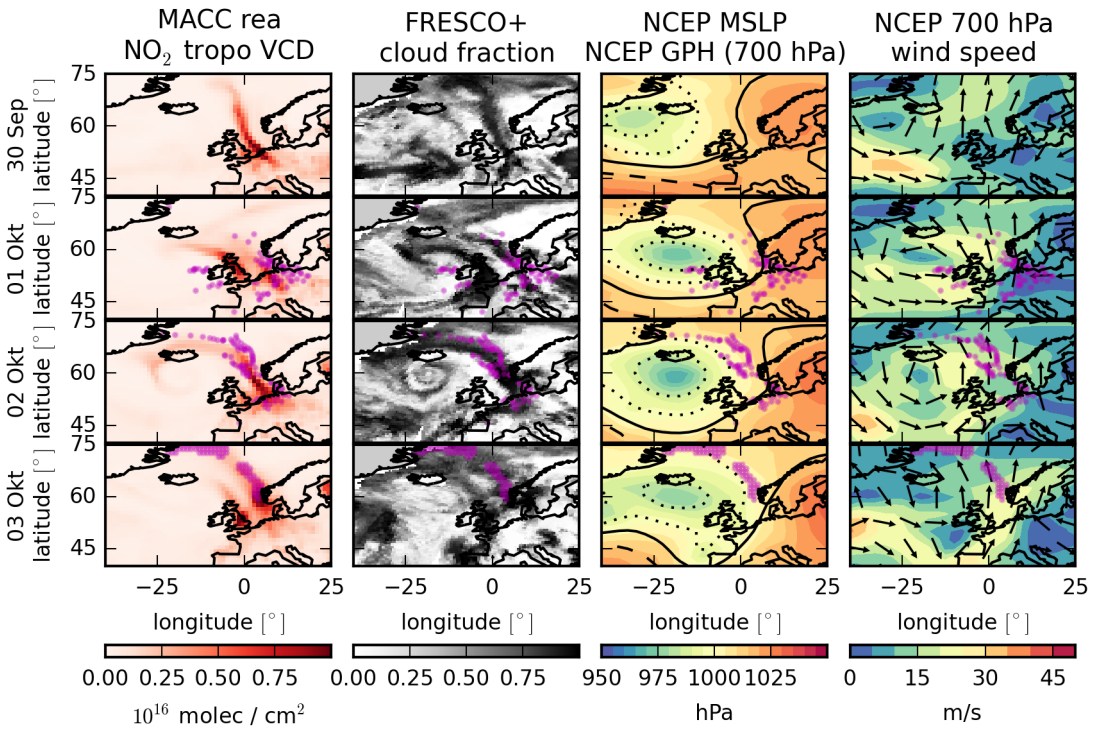

Figure 8.6: Illustration of the backtrajectory of the last observation of the long-range transport event seen on 01 October 2010 in MACC-II reanalysis data. Data as in Figure 8.2.

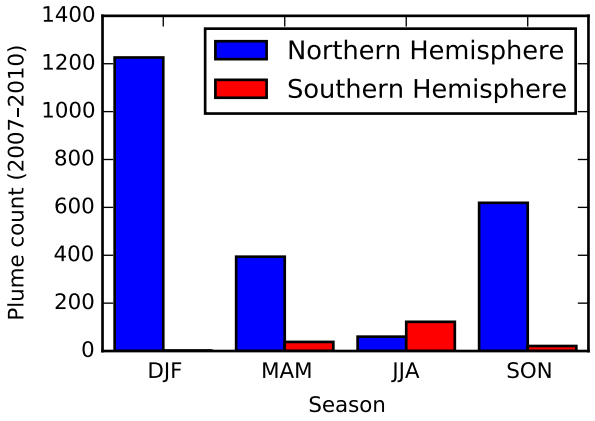

Figure 8.7: Number of verified long-range transport plumes found by the detection algorithm in 2007–2010 in MACC-II reanalysis data (as in Figure 7.10). There is a strong seasonality in both hemispheres, with a strong peak in local winter. Almost no long-range transport events were detected in the Southern Hemisphere.

than in GOME-2 / MetOp-A data, taking only the period of 2007–2010 into account. Several mechanisms contribute to a lower number of events in the model data:

- The model resolution is not as fine as the satellite data resolution. This may lead to small plumes not being detected and, occasionally, two or more large plumes being merged if they are in close vicinity.
- The model features a smooth NO_2 distribution with less small-scale fluctuations and less measurement noise. This will lead to a smaller fraction of small plumes in the data. Also, this will lead to less false positive detections compared to GOME-2 / MetOp-A.
- The model might not represent all mechanisms that lead to the emission of a plume in a long-range transport event. Convection on small scales, transport out of the planetary boundary layer or other forms of emission events may not be adequately represented and will lead to events missing in the data.
- Missed emissions from bush fires in MACC-II reanalysis.
- A possible overestimation of chemical loss of NO_2 in MACC-II reanalysis.

A counteracting mechanism is the smoothness of model data leading to a small overall sliding standard deviation of local tropospheric NO_2 vertical column densities. This makes the algorithm more sensitive to small deviations. However, these still have to exceed a total NO_2 content of 0.12 Gg N to be included in the data set. Model data are not limited by a finite signal-to-noise ratio.

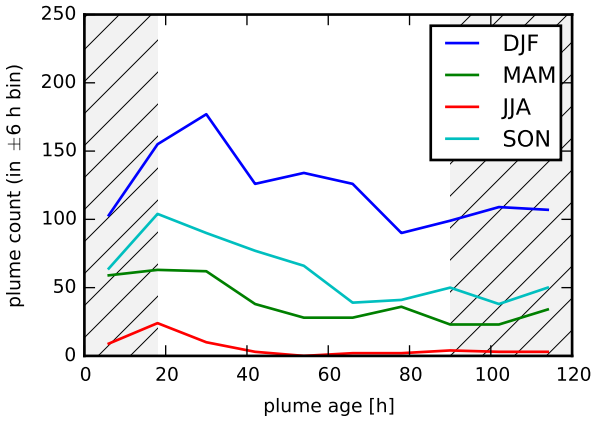

Figure 8.8: Plume age at the time of observation for long-range transport events observed in MACC-II reanalysis data in the Northern Hemisphere between 2007–2010, as in Figure 7.13. In contrast to GOME-2 / MetOp-A data, the distribution of numbers per age bin is relatively flat, probably owing to the enhanced signal-to-noise ratio in model data.

In Figure 8.7 you can see the absolute number of NO_2 long-range transport plumes detected in MACC-II reanalysis data in 2007–2010. There are almost no plumes detected in the Southern Hemisphere, in discordance with Figure 7.10. There is a strong seasonality in the plume counts, as in GOME-2 / MetOp-A data.

8.2.1 Plume properties

I perform an analogous analysis as in Subsection 7.2.2 to determine various properties of the plumes observed in MACC-II reanalysis data.

In Figure 8.8, the age distribution of NO_2 long-range transport plumes from the Northern Hemisphere as observed in MACC-II reanalysis data is shown, analogous to Figure 7.13. Again, absolute numbers are higher during winter. But the relative amount of old plumes (above 70 hours) in DJF is also larger than during MAM or SON, indicating that not only are more plumes emitted but they are also given greater longevity due to less sun light, less OH and less chemical conversion to HNO_3 during winter.

This is also apparent when fitting an exponential function to the data outside the hatched area. This yields a significantly higher value of 125 hours characteristic time scale for MACC-II reanalysis data as opposed to 97 hours in GOME-2 / MetOp-A data. This may be due to either chemical parameterizations in MACC-II reanalysis or due to its higher signal-to-noise ratio. Spring and autumn are more moderate with 76 hours, each, matching GOME-2 / MetOp-A observations.

Figure 8.9 shows the distribution of plume NO_2 content in the Northern Hemisphere. Barring the absolute numbers, this is almost exactly identical to the results from GOME-2 / MetOp-A data (Figure 7.11).

Looking at the altitude distribution (Figure 8.10), a significantly smaller proportion

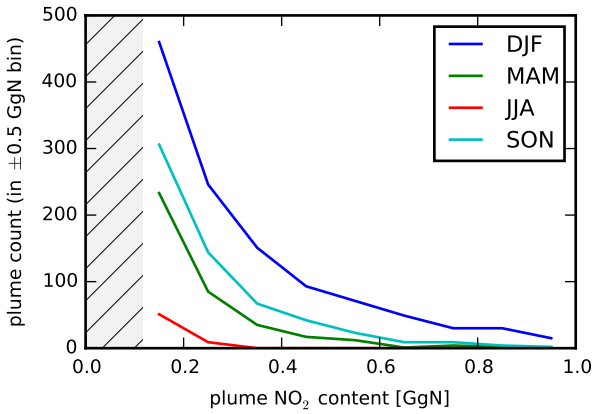

Figure 8.9: As per Figure 7.11. NO_2 content of long-range transport events observed in MACC-II reanalysis in the Northern Hemisphere, for different seasons. Note the lower mass limit of 5×10^{30}molecules (hatched area, corresponding to 0.12 Gg N).

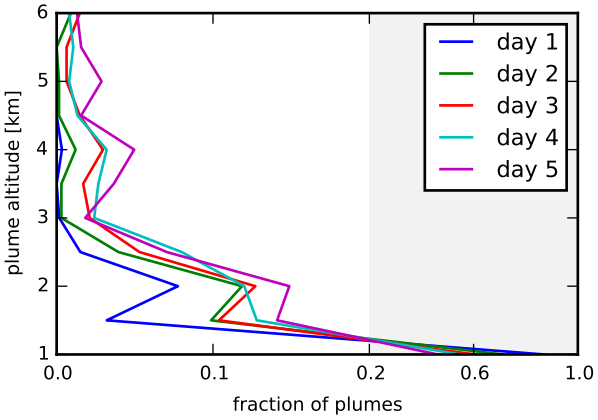

Figure 8.10: As per Figure 7.18. Altitude distribution of NO_2 long-range transport plumes found in MACC-II reanalysis data over the 11 altitude levels sampled in the HYSPLIT backtrajectories. Shown are the graphs for plumes younger than one day, between one and two days of age, etc. While most young plumes reside on the lowest level, they tend to distribute more equally in altitude over the following days. Note the compressed axis for fractions higher than 20 %.

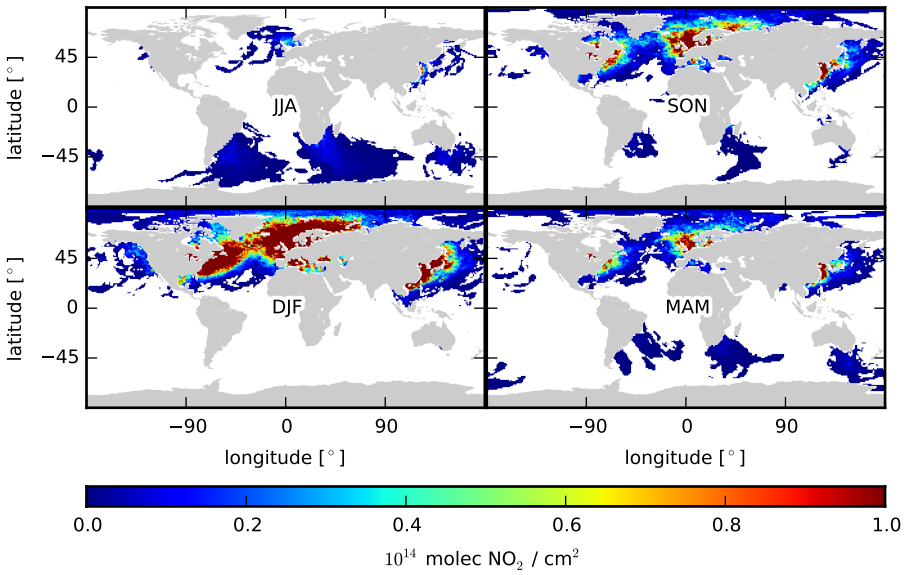

Figure 8.11: Seasonal maps of the mean vertical column density of NO_2 observed in plumes associated to long-range transport events, as in Figure 7.19. Emissions from South Africa, Australia and South America are barely visible while emissions from North America, Europe and China are very prominent. Seasonality is very distinctive in both hemispheres. The Northern Hemisphere shows elevated tropospheric NO_2 vertical column densities of transported NO_2 on the main storm tracks.

of plumes are found at elevated altitudes in MACC-II reanalysis data than in GOME-2 / MetOp-A data. There is a slight tendency towards higher altitudes (prolonging NO_2 lifetime) for older plumes but it is far less pronounced than in GOME-2 / MetOp-A data. Again, plumes that are estimated to be less than 1 day old travel almost entirely at an altitude of 1000 m.

8.2.2 Routes

I analyze the typical routes and sources of transports in MACC-II reanalysis data – in the same fashion as in Subsection 7.2.3. The seasonality of long-range transport routes in MACC-II reanalysis data is shown in Figure 8.11, corresponding to Figure 7.19 for GOME-2 / MetOp-A.

Routes from North America eastwards, from Europe east-, north- and west-wards are clearly visible. They are a lot clearer than in GOME-2 / MetOp-A data. In shape and amplitude, these routes are very similar in both data sets. While GOME-2 / MetOp-A data are cut off at about 60°N, MACC-II reanalysis data allows for observation up into Arctic regions. From this plot, it appears that most long-range transport events from Europe, although traveling towards the Arctic do not reach it with large amounts of

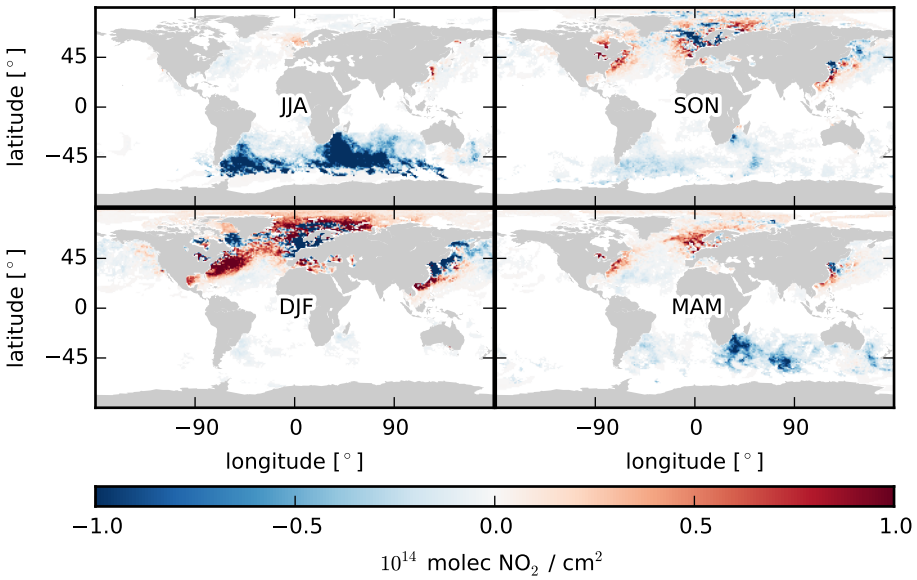

Figure 8.12: Difference map of routes from MACC-II reanalysis and GOME-2 / MetOp-A data (red indicates higher values in MACC-II reanalysis data). Created from Figure 7.19, which was regridded to MACC-II reanalysis 1.125° resolution, and Figure 8.11. There is a strong lack of observed long-range transport NO_2 in the Southern Hemisphere. Contrasting that, MACC-II reanalysis finds higher exports near North America and broader exports from Europe, extending more into the fringes. In China, MACC-II reanalysis appears to locate the exports significantly further south than observed in GOME-2 / MetOp-A.

NO_2. However, there is still some fraction of NO_2 that is relocated there, mostly from Europe. As the Arctic environment is very sensitive, this may lead to strong impacts on its atmospheric chemistry and may contribute to Arctic Haze.

On the Southern Hemisphere, there is significantly less transport detected in MACC-II reanalysis data. This result shows itself systematically for all comparisons. While transport is clearly present in the same regions as in GOME-2 / MetOp-A data (Argentina / Uruguay, South Africa, Australia) they are almost non-existent in comparison to transports on the Northern Hemisphere. This may be due to a problem of the representation of NO_2 concentrations on the Southern Hemisphere, which appear to be significantly lower throughout the entire MACC-II reanalysis data set.

Again, there is no transport observed in the tropics – as is expected.

Figure 8.12 shows the difference between routes from MACC-II reanalysis and GOME-2 / MetOp-A data. This, again, clearly shows the lack of long-range transports in the Southern Hemisphere in MACC-II reanalysis data. There are other interesting features, however. The tropospheric NO_2 vertical column densities in exports east of North America are significantly higher in MACC-II reanalysis data, which contrasts its tendency

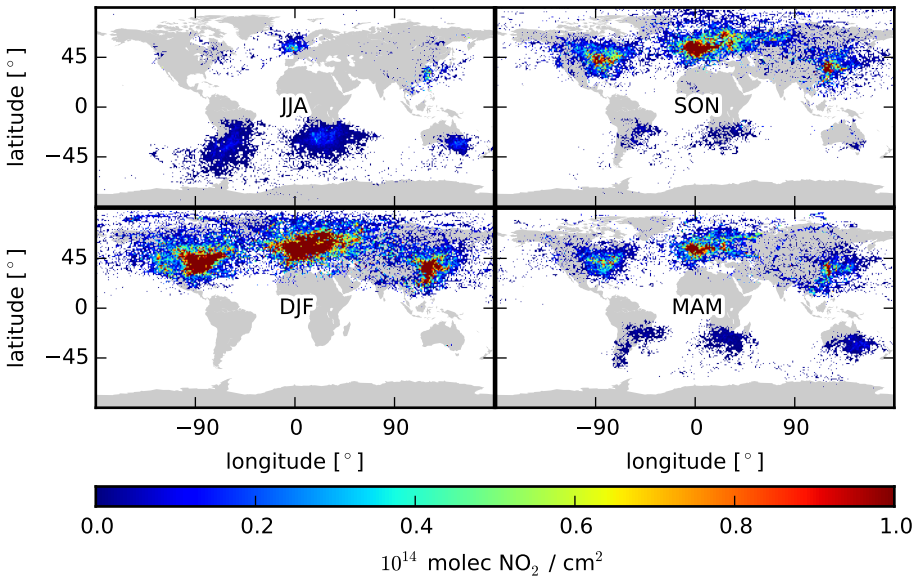

Figure 8.13: Seasonal maps of the mean tropospheric NO_2 vertical column density observed in plumes associated to long-range transport events, projected back to their sources as retrieved from the most likely backtrajectory. As in Figure 7.21 with GOME-2 / MetOp-A data. Typical sources are the same as for GOME-2 / MetOp-A data.

towards lower values on the Southern Hemisphere. Near Europe, the region of observed plumes is significantly broader, leading to a large area of emissions – including the polar circle where GOME-2 / MetOp-A cannot observe NO_2 reliably. There also appears to be a corridor, roughly on the direct route between Europe and North America, where MACC-II reanalysis sees significantly less NO_2 in transports. Near China, emissions appear to be located further south than in GOME-2 / MetOp-A data, probably owing to a difference in meteorological data.

8.2.3 Sources

When looking at the sources of NO_2 long-range transports in MACC-II reanalysis data (Figure 8.13), the same source regions as identified in GOME-2 / MetOp-A data can also be seen here. However, all sources appear to be weaker compared to results from GOME-2 / MetOp-A. These systematic discrepancies may either result from the uncertainty with which tropospheric NO_2 vertical column densities are determined from GOME-2 / MetOp-A (Section 4.8) or with the chemical parameterization or meteorological input data of the MACC-II reanalysis model.

Figure 8.14 shows the difference of the source maps from GOME-2 / MetOp-A and MACC-II reanalysis data. The weaker sources throughout all seasons and on both hemispheres are evident. Only in some scattered areas, source vertical column densities

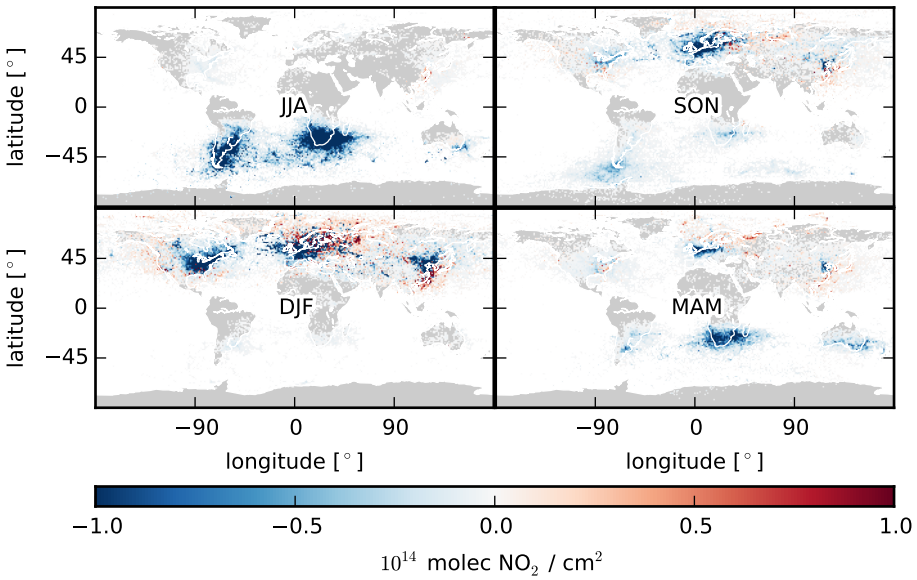

Figure 8.14: Difference map of routes from MACC-II reanalysis and GOME-2 / MetOp-A data (red indicates higher values in MACC-II reanalysis data). Created from Figure 7.21, which was regridded to MACC-II reanalysis 1.125° resolution, and Figure 8.13. All major source regions are weaker in MACC-II reanalysis data in all seasons.

are larger in MACC-II reanalysis data. This is probably mostly attributable to the random scatter of backtrajectories.

8.2.4 Regions

When comparing the regional results of long-range transports observed in GOME-2 / MetOp-A and MACC-II reanalysis data, I add two additional regions: South America and Australia. MACC-II reanalysis data has confirmed (although only vaguely due to its low NO_2 levels on the Southern Hemisphere) that these do in fact emit long-range transport events and are not mere observational artifacts from GOME-2 / MetOp-A tropospheric NO_2 vertical column density retrieval. All six regions with their associated areas of emission and observation are illustrated in Figure 8.15.

Figure 8.16 shows the number of plumes observed in both datasets for each region and season. While on the Northern Hemisphere, yearly totals are very similar, again, the lack of plumes in MACC-II reanalysis data on the Southern Hemisphere is evident. Surprisingly, Australia is exempt from this. Also, GOME-2 / MetOp-A detects a significantly higher fraction of plumes in the main season (winter), while MACC-II reanalysis detects a larger proportion in the off season (spring and autumn). This is quite surprising as the noise in GOME-2 / MetOp-A data is larger in winter, which should lead to less detections (as is requires a higher anomaly in the algorithm). Potentially, MACC-II

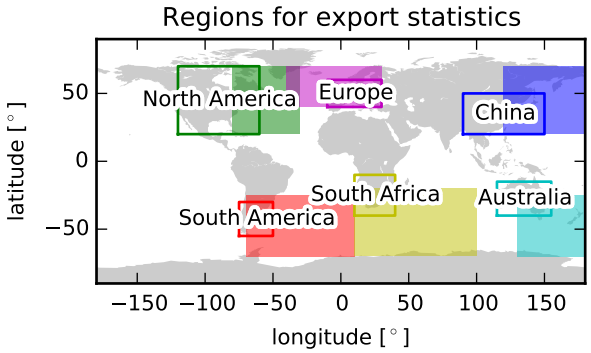

Figure 8.15: The regions used for the statistical comparison of MACC-II reanalysis and GOME-2 / MetOp-A data. Only plumes are considered that were observed over the ocean in the filled rectangle and were found over land-masses in the open rectangle 24 hours earlier. In comparison to Figure 7.22, South America and Australia have been added.

reanalysis simply detects too many plumes in the off season due to too low decay rates or parametrizatin of convection.

If we look at the NO_2 content exported in long-range transport from these regions per year (Figure 8.17), we find that the discrepancy between both data sets on the Southern Hemisphere becomes even larger. While South Africa emits around $3\,\mathrm{Gg\,N}/a$ in long-range transport events in GOME-2 / MetOp-A, it is reduced to less than $0.5\,\mathrm{Gg\,N}/a$ in MACC-II reanalysis data. For South America, the situation is similar. MACC-II reanalysis sees less emissions from Europe and China, while North America is attributed almost double emissions (inside the region defined in Figure 8.15).

Note that these numbers only represent the observed NO_2, not the NO_2 at emission, as both the time of emission and the lifetime of NO_2 inside plumes is uncertain; this would lead to very large uncertainties in these numbers. However, the shown numbers can be taken as a lower boundary of the actual export rate, which may well be higher by a factor of two or three.

A comparison of NO_2 content distribution for both data sets can be found in Figure 8.18. MACC-II reanalysis detects the largest proportion of massive plumes in North America, while it is only third in GOME-2 / MetOp-A data. Instead, Europe emits the largest plumes, there. Again, plumes on the Southern Hemisphere are significantly less massive in MACC-II reanalysis, where no observed plume holds more than $0.4\,\mathrm{Gg\,N}$ while South African plumes reach up to $3\,\mathrm{Gg\,N}$ in GOME-2 / MetOp-A data.

Finally, Figure 8.19 shows the average rate at which plumes are emitted from a region during its main season. Main season emission rates are quite similar between the two data sets. For Europe, MACC-II reanalysis finds slightly smaller emisison rates, for South Africa it almost goes down to a third. In GOME-2 / MetOp-A data, a region will emit a long-range transport event (of more than $0.12\,\mathrm{Gg\,N}$ upon observation) roughly every 3 days in its main season. For South Africa, GOME-2 / MetOp-A still finds about

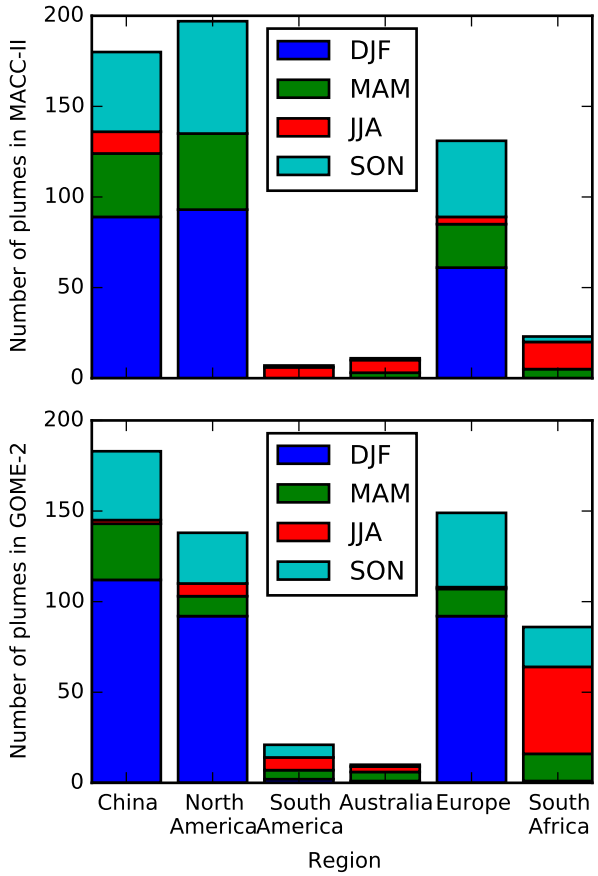

Figure 8.16: Number of long-range transport events observed in different regions in MACC-II reanalysis (top) and GOME-2 / MetOp-A (bottom) data, separated by season, in the period 2007–2010.

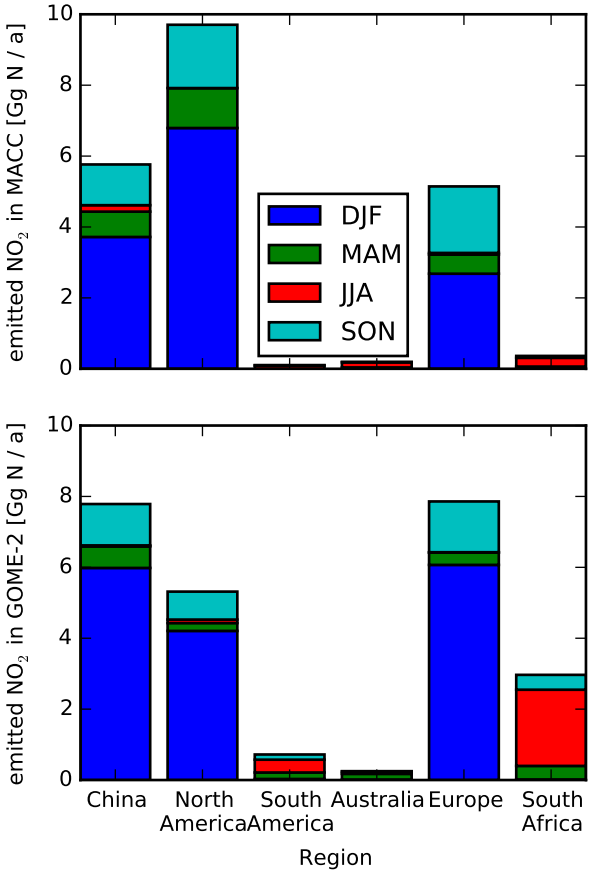

Figure 8.17: Stacked Histogram of yearly export of NO_2 in long-range transport events observed in different regions in MACC-II reanalysis (top) and GOME-2 / MetOp-A (bottom) data, separated by season. Note, that these numbers refer only to the NO_2 *observed* in these events, not the NO_2 content of the events when they were emitted in their source region.

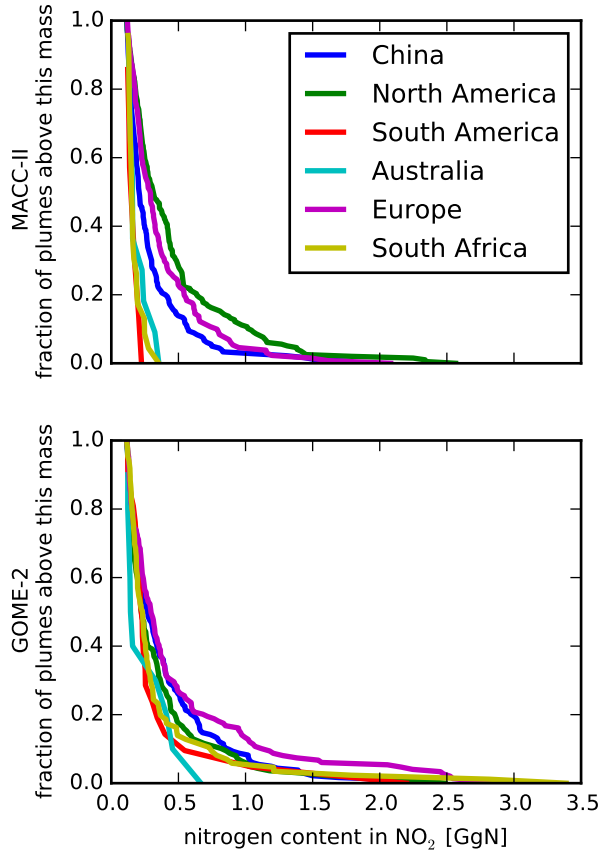

Figure 8.18: NO_2 content distribution of long-range transport events observed in different regions in MACC-II reanalysis (top) and GOME-2 / MetOp-A (bottom) data. The diagram shows, what fraction of a region's long-range transport population has an NO_2 content above the given value.

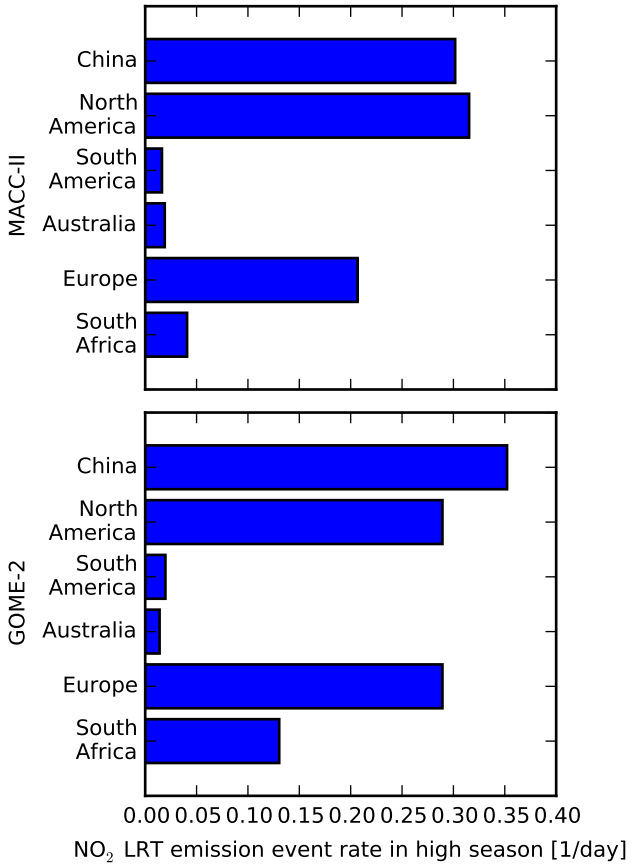

Figure 8.19: Frequency at which different regions emit long-range transport events during their main season – DJF for the Northern and JJA for the Southern Hemisphere – in MACC-II reanalysis (top) and GOME-2 / MetOp-A (bottom) data.

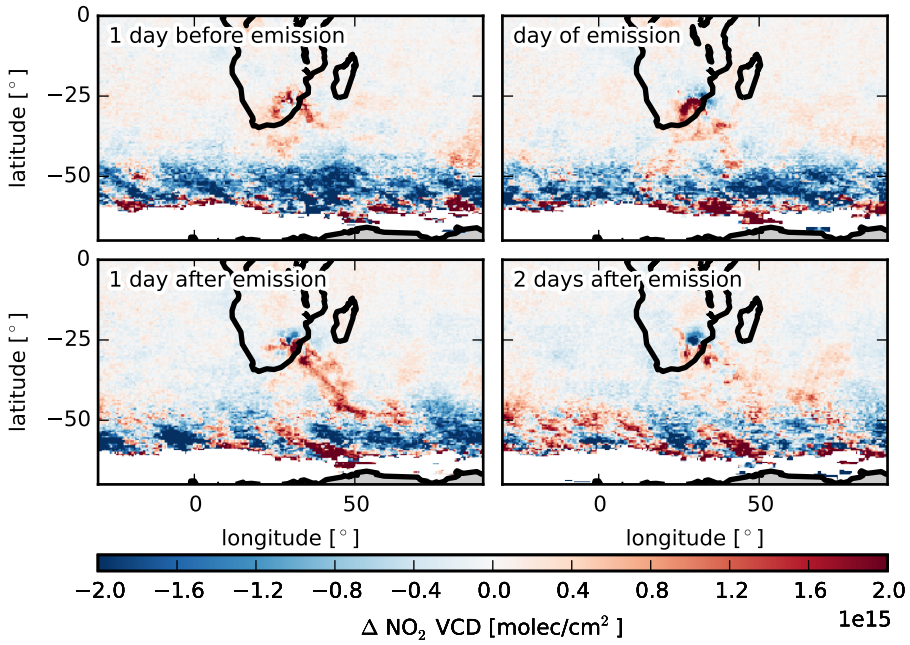

Figure 8.20: GOME-2 tropospheric NO_2 vertical column density for the days of plume emission in the South African region during summer (JJA) in 2007–2010. As in Figure 7.25 but for MACC-II reanalysis. There is an anomaly towards high values over the Highveld region before plume emission, although it is not as sharp as for plumes observed in GOME-2 / MetOp-A data. After emission, the NO_2 vertical column densities over the Highveld region are on average lower, while an upwards anomaly can be seen southeast of South Africa. Again, high fluctuations in the GOME-2 data and few observations result in visible noise in the anomalies near polar night.

one event per week, while it goes down to less than once a month for South America and Australia.

8.2.5 Meteorological conditions

I performed the same analysis as in Subsection 7.2.6 for the results from MACC-II reanalysis.

Composites of tropospheric NO_2 vertical column densities in South Africa before, during and after the day of emission (Figure 8.20) are very similar for emissions observed in MACC-II reanalysis as in emissions form GOME-2 / MetOp-A data. They are more broad and not as focussed on the Highveld plateau region. The build-up of NO_2 before emission is evident, however.

For Europe (Figure 8.21), the situation is a bit different. For MACC-II reanalysis emissions, there is a strong depletion of NO_2 in the Arctic and no anomaly over the

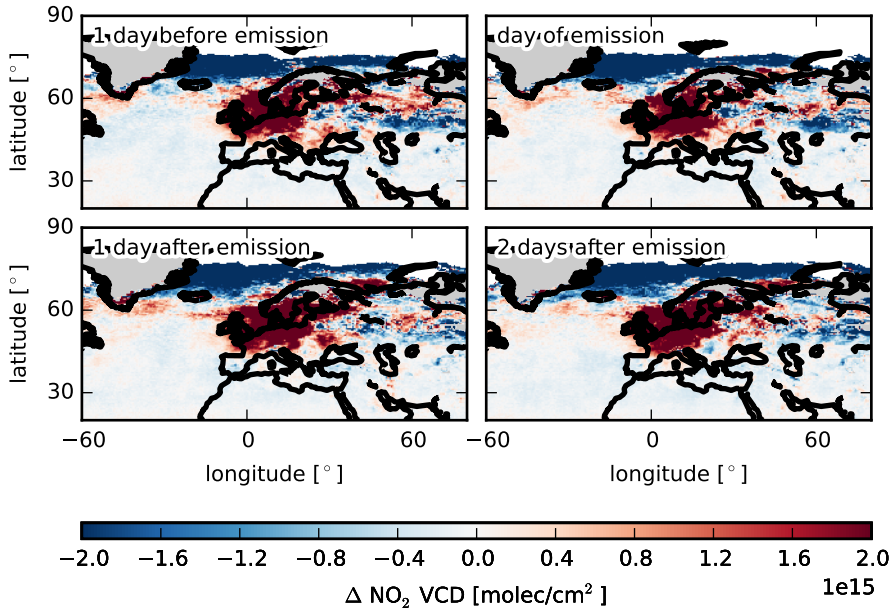

Figure 8.21: As in Figure 8.20, but for plumes emitted from Europe during winter (DJF) in 2007–2010. NO_2 depletion over the Arctic can be seen.

Atlantic. This might hint at false positive observations in GOME-2 / MetOp-A data near Europe's convoluted coast line. It is unlikely that this is an artifact of MACC-II reanalysis as this dataset has no information about GOME-2 / MetOp-A tropospheric NO_2 vertical column densities.

Figure 8.22 shows the same for North America. In MACC-II reanalysis data, a build-up of NO_2 in the Great Lake area can be seen on the day before emission that is depleted two days after emission. This was not as clearly evident in composite tropospheric NO_2 vertical column densities for GOME-2 / MetOp-A plumes. A build-up of NO_2 over Europe after an emission from North America is most likely not due to transport to Europe (which would typically take three to four days), but much rather coincidental.

Looking at the composite mean sea-level pressure for South African plumes in MACC-II reanalysis (Figure 8.23), we find a similar pattern as in GOME-2 / MetOp-A (Figure 7.27). There are alternating high and low anomalies with a low anomaly building up and slightly moving towards the southern tip of South Africa.

Over Europe (Figure 8.24), we find the identical pattern as for the GOME-2 / MetOp-A dataset, only amplified with a stronger low pressure anomaly over south-western Europe and a stronger high-pressure anomaly over Scandinavia and the Arctic. This confirms the theory of a channel for NO_2 emissions to leave the emission region.

For North America, again, there are no significant m.s.l.p. anomalies to be found (not shown). There is only a faint low-pressure anomaly over the Mid-East and a high-pressure anomaly off the East Coast visible *after* the emission. Unfortunately, MACC-II reanalysis data cannot show what GOME-2 / MetOp-A data did not see, in this case.

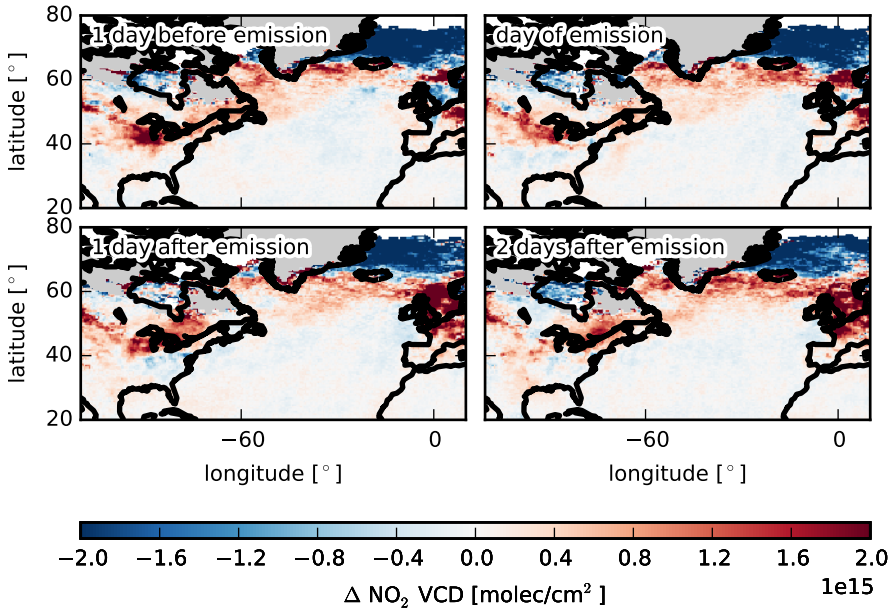

Figure 8.22: As in Figure 8.21, but for plumes emitted from North America. NO_2 build-up near the Great Lakes before plume emission can be seen as well as build-up over Europe *after* plume emission.

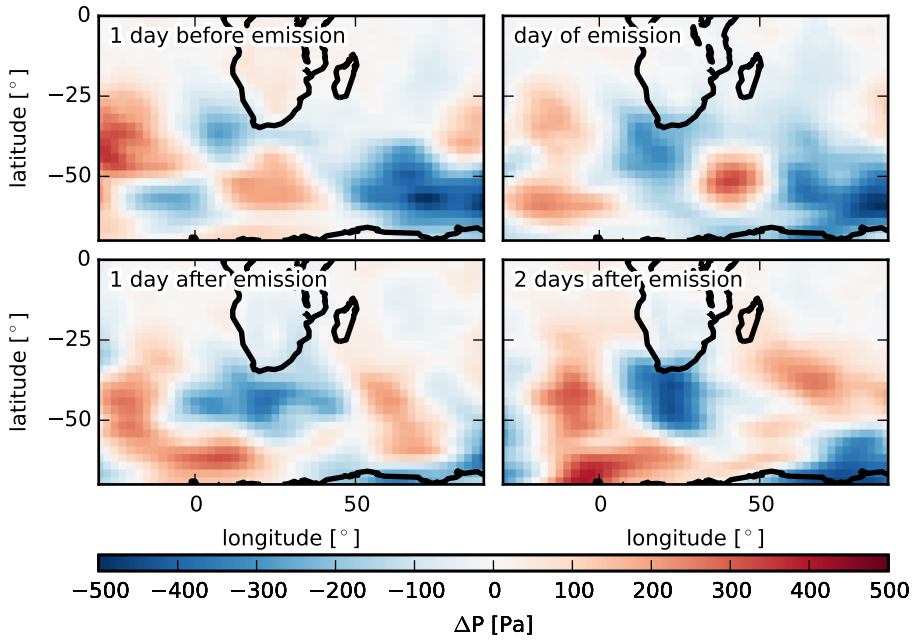

Figure 8.23: As in Figure 7.27 but for MACC-II reanalysis and showing NCEP DOE AMIP-II Reanalysis mean sea-level pressure for the days of plume emission in the South African region. Similar patterns are visible, although a bit less pronounced than for GOME-2 / MetOp-A emissions. This hints at the observed trend that South African long-range transport events are transported towards the South-East.

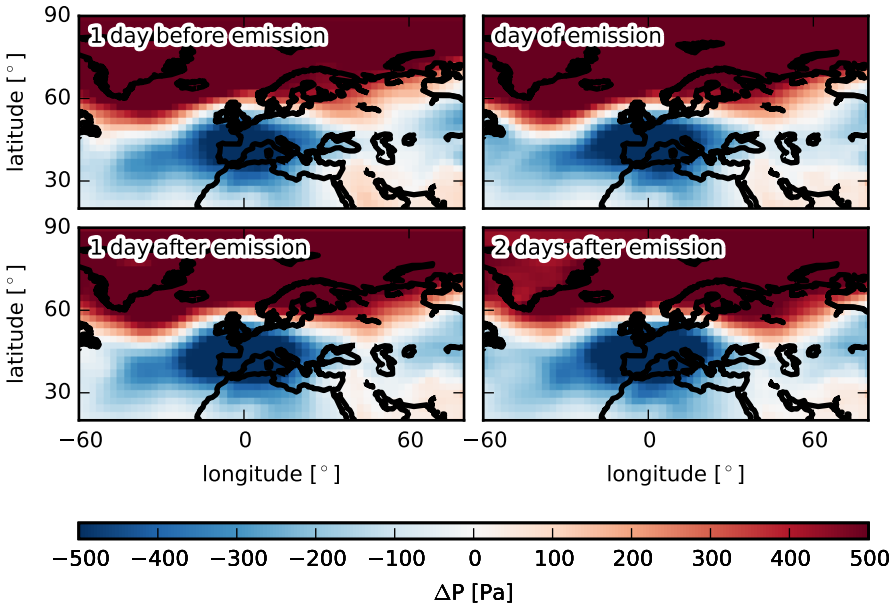

Figure 8.24: As in Figure 8.23, but for plumes emitted from Europe during winter (DJF) in 2007–2010. The low-pressure anomaly over Europe and the high-pressure anomaly in the Arctic correspond to the findings from GOME-2 / MetOp-A data and are even more pronounced, forming a strong channel over Central Europe. This hints at the observed trend that European long-range transport events are transported towards the North-West.

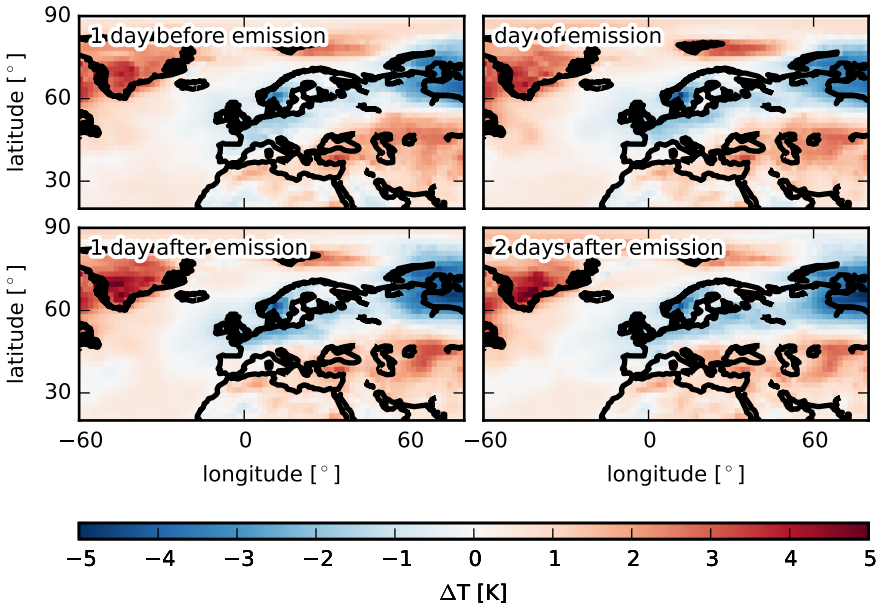

Figure 8.25: NCEP DOE AMIP-II Reanalysis surface air temperature for the days of plume emission in the South African region. Low and high temperature anomalies can be seen, corresponding to low and high pressure anomalies in Figure 8.24.

The air temperature anomalies for European plumes can be seen in Figure 8.25. As for GOME-2 / MetOp-A data, there is a temperature anomaly of about −3 K over Europe as well as a high temperature anomaly in the Arctic, both following their pressure anomalies.

8.2.6 Colocated plume observations

Lastly, after obtaining these two datasets, we can also look for colocations between long-range transport events observed in MACC-II reanalysis and GOME-2 / MetOp-A data in 2007–2010.

As criteria for a colocation, I require that the two plumes in question have to be observed on the same date and that their center of mass is separated less than a great-circle distance of $\Delta\theta < 4°$, corresponding to a maximum separation of roughly $s < 450\,\mathrm{km}$.

Using these criteria, we obtain a total of 579 colocations between both datasets. 2523 plumes are left unmatched from GOME-2 / MetOp-A data as well as 1912 plumes from MACC-II reanalysis data. These unmatched plumes might still have a corresponding plume in the other dataset, although at a greater separation or at a later time. If we allowed for separations of up to $s < 1000\,\mathrm{km}$ the number of colocations would increase to 991.

Note, that there are double matches in this dataset, meaning that a single plume in GOME-2 / MetOp-A could be matched to several MACC-II reanalysis plumes. All of these matches were included. There are significantly more MACC-II reanalysis plumes that could be matched to multiple GOME-2 / MetOp-A plumes than vice versa. This can probably be attributed to the high signal-to-noise ratio in GOME-2 / MetOp-A data, which will lead to large plumes being broken down into several smaller plumes in short distance. This will lead to multiple colocations.

The histogram of angular separations of the center of mass of plumes for colocations with a separation $s < 1000\,\mathrm{km}$ is shown in Figure 8.26. This shows a build-up scale of about 1° which is consistent with MACC-II reanalysis horizontal resolution of 1.125°. These plumes are perfect matches within the model resolutions. Above that separation, colocations steadily decrease even though the searched area increases nearly quadratically. There is a small local minimum of colocation separations around $\Delta\theta = 4°$ which I used as a cut-off for colocation for further study. From now on, all colocations are limited to a separation of $\Delta\theta = 4°$.

The difference between the estimated NO_2 content of colocated plumes is illustrated in Figure 8.27. This almost follows a gaussian distribution with a mean value of GOME-2 / MetOp-A NO_2 content being larger by about $\Delta m = 0.08\,\mathrm{Gg\,N}$. However, the standard deviation of this distribution equates to $\sigma = 0.6\,\mathrm{Gg\,N}$. Thus, this diagram is consistent with colocated plumes in GOME-2 / MetOp-A and MACC-II reanalysis data on average exhibiting the same NO_2 content. However, as earlier results have shown (Subsection 7.2.2), MACC-II reanalysis data simulates less NO_2 long-range transport; this means that there most likely are small plumes in MACC-II reanalysis data that are not reproduced by GOME-2 / MetOp-A.

In extreme cases, there may be NO_2 content differences of up to $\Delta m = \pm 2\,\mathrm{Gg\,N}$ between colocated plumes. It is likely that these colocations are false detections or

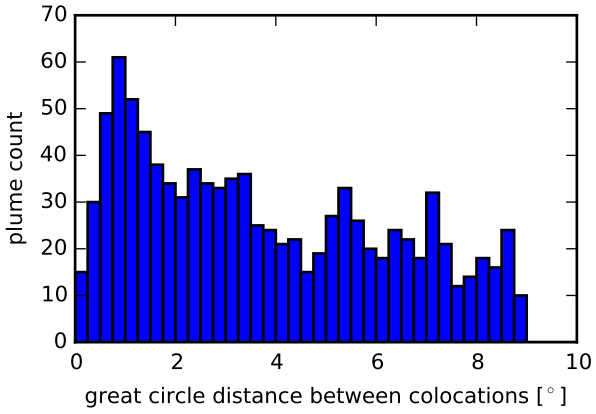

Figure 8.26: Histogram of great circle separations between the centers of colocated plumes from the GOME-2 / MetOp-A and MACC-II reanalysis dataset, limited to a maximum separation of $\Delta\theta < 9°$. The build-up for separations below 1° is most likely systematic and caused by the data resolutions (0.5° and 1.125° for GOME-2 / MetOp-A and MACC-II reanalysis, respectively).

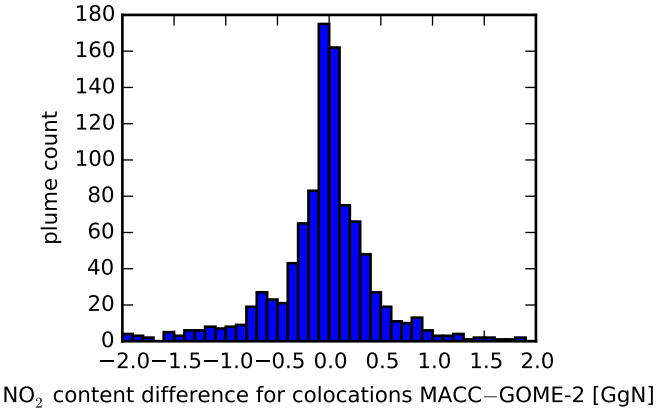

Figure 8.27: Histogram of the difference in NO_2 content between colocated plumes from the GOME-2 / MetOp-A and MACC-II reanalysis dataset, positive numbers indicating higher content in the MACC-II reanalysis plume.

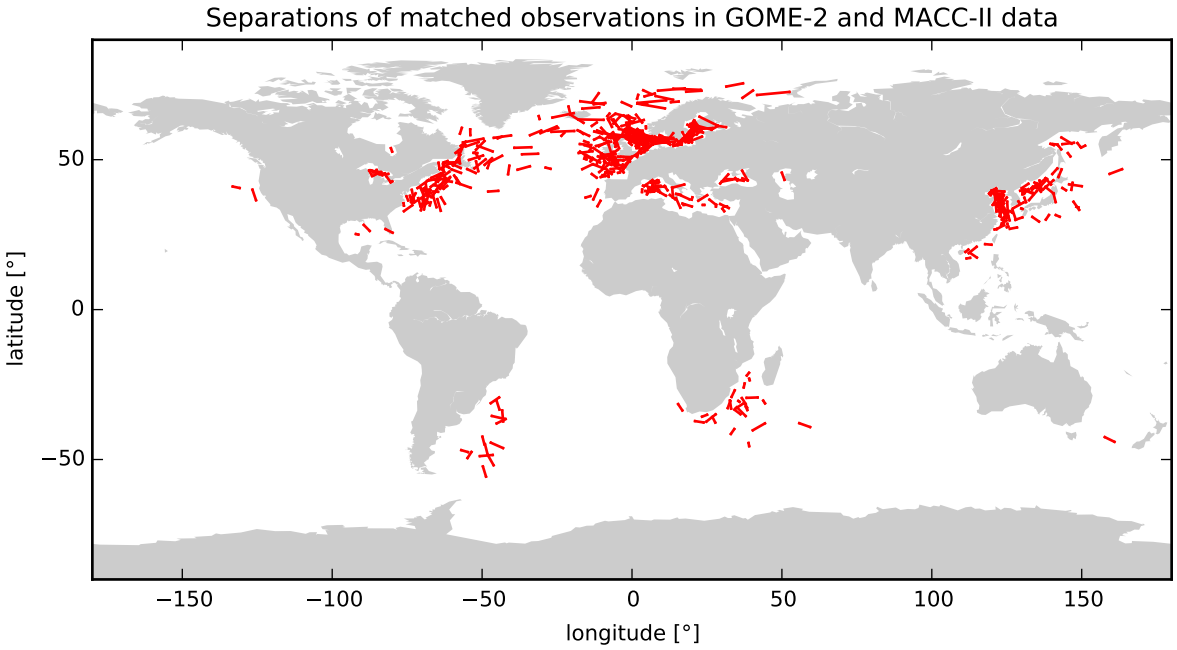

Figure 8.28: Map of colocated plumes. Red lines indicate the connection between the center of mass of the plume in both datasets. A lack of colocations in the Southern Hemisphere is evident while the Northern Hemisphere features a lot of colocations, especially near the shore.

colocate a whole plume in one dataset with a plume in the other dataset, that caputures only a fraction of the actual plume.

Looking at the age difference for colocated plumes (not shown) reveals that there is no systematic shift between datasets. However, the standard deviation here is $\sigma = 28\,\mathrm{h}$, meaning that backtrajectories of colocated plumes regularly differ by more than a day in age. This indicates that estimated ages of individual plumes have to be taken with a grain of salt in this current version, which will add further uncertainty to the estimated lifetimes of NO_2 for individual events.

In Figure 8.28 the connections between colocated plumes are shown on a world map. Most colocations can be seen in the Northern Hemisphere, especially near Europe. There is only a single colocation near Australia.

In contrast to this, Figure 8.29 shows the centers of mass of unmatched plumes in both datasets. There is a plethora of unmatched GOME-2 / MetOp-A plumes in the Southern Hemisphere, where there are almost no unmatched MACC-II reanalysis plumes. There appears to be a significant fraction of MACC-II reanalysis plumes very close to shores on the Northern Hemisphere that could not be reproduced in GOME-2 / MetOp-A data. This is exactly in the areas where a lot of regular and irregular outflow of NO_2 from emission region takes place. This leads to a very high sliding standard deviation for GOME-2 / MetOp-A data, which in turn leads to more strict criteria for the detection of

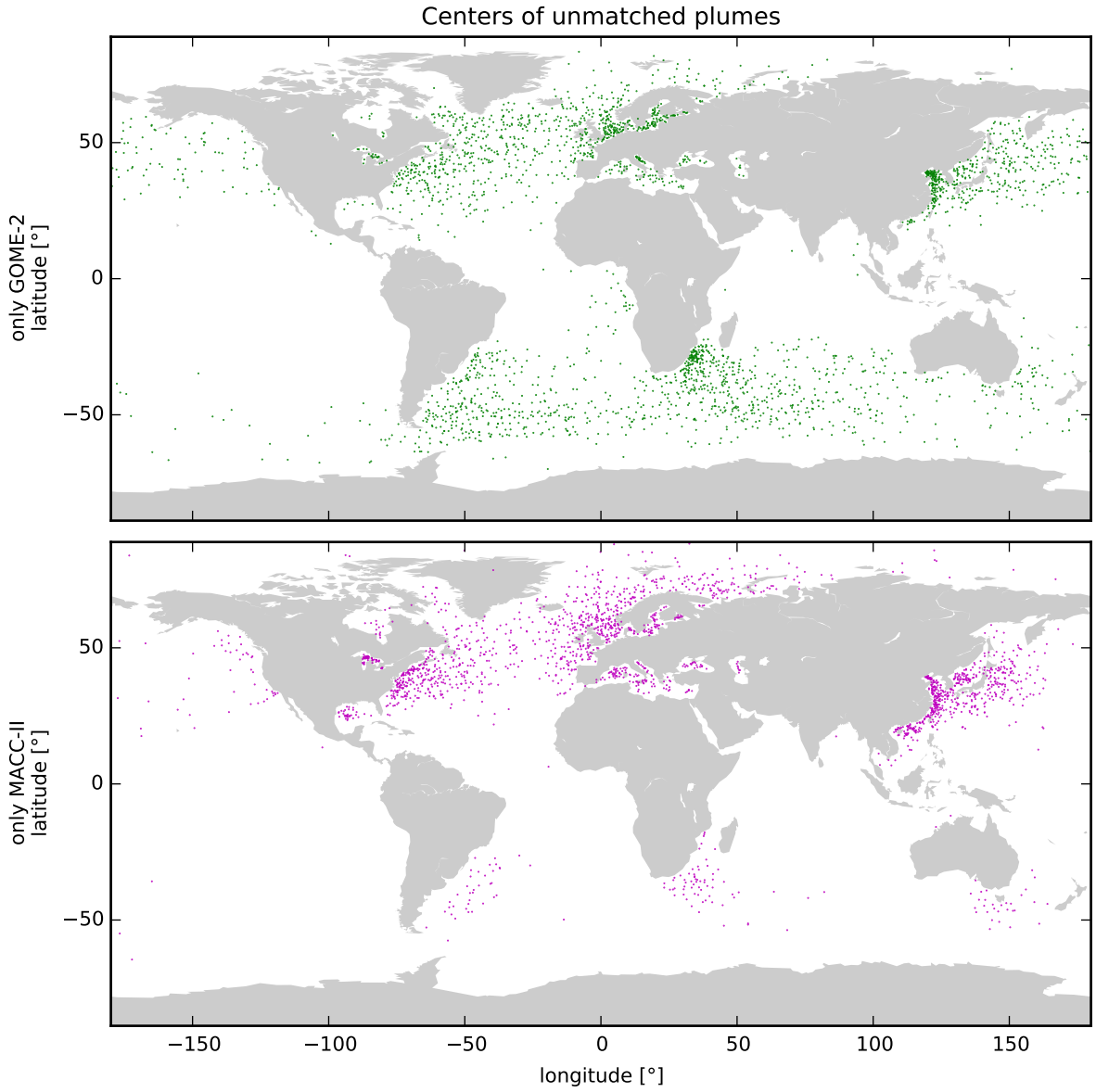

Figure 8.29: Map of unmatched plumes in GOME-2 / MetOp-A (top) and MACC-II reanalysis (bottom) data. There are a lot of unmatched plumes in GOME-2 / MetOp-A in the Southern Hemisphere and a concentration of unmatched plumes in MACC-II reanalysis near shores on the Northern Hemisphere.

a plume. If NO_2 concentrations in MACC-II reanalysis data exhibit smoother temporal variance – this will be the case especially for emissions – a lot more plumes near the shore can be detected there, even if the overall number of plumes were lower.

This concludes the analysis of NO_2 long-range transport from the MACC-II reanalysis dataset and its comparison to the results from GOME-2 / MetOp-A.

9 Discussion and conclusions

This chapter will take a brief review and discussion of the results presented in Chapter 6, Chapter 7 and Chapter 8.

9.1 Detection of long-range transport events

Using the algorithm presented in Chapter 6, I have succesfully detected NO_2 long-range transport events in both GOME-2 / MetOp-A and MACC-II reanalysis data in an automated analysis. The combined method of anomaly detection in the input data and a backtrajectory model successfully suppressed a large amount of false positives in the data set and lead to a reliable and stable inventory of global NO_2 long-range transport events in 2007-2011 for GOME-2 / MetOp-A and 2007-2010 for MACC-II reanalysis.

This algorithm can easily be applied to different data sets, both from satellite observations and model runs. Its operation is tailored to the specifics of detecting NO_2 long-range transport events, but can easily be modified to detect long-range transport of other unstable trace gases that have concentrated sources.

I have not implemented an algorithm to automatically link two instances of the same long-range transport plume on consecutive days. This has to be done by hand, currently, but might be feasible to automatize in future studies.

The quality of the backtrajectories for individual events is not very reliable and depends on the plume size. Currently, a strong limitation lies in the assumption that the plume is distributed in a single layer. Backtrajectory sets that are longer than 72 hours will have many stray trajectories due to the chaotic nature of meteorology. However, for the statistical analysis, these rough estimations of altitude and route appear to be sufficient.

In its current state, the algorithm is not fit to analyze long-range transport over continents. There, tropospheric NO_2 vertical column density fluctuations are too large and will lead to a high signal-to-noise ratio that will produce false positives (emission fluctuations detected as plume) and false negatives (high standard deviation will hinder plume detection). These problems are also visible, where long-range transport events are detected on the shore near an emission region, where the algorithm's sensitivity automatically becomes low.

9.2 Favorable conditions

In this study, it has become apparent that cyclones are a major driving force behind NO_2 long-range transport events. Plumes from long-range transport events follow major storm tracks. It is likely that one of the major causes of long-range transport is the passing of a cold front through a major emission region. There, NO_2 is lifted up when

the cold air moves under the warm, stable, NO_2-laden air and is transported into the free troposphere following the warm conveyor belt.

In South Africa, the elevated location of major industry and power plants may lower the requirements for long-range transport, as emissions are emitted at relatively high altitudes, with a thinner planetary boundary layer. The industrial area around the Highveld plateau (including Johannesburg and Pretoria) is relatively isolated, with very few NO_2 sources in its sourroundings, and is situated near the ocean. For this reason, NO_2 long-range transport from the Highveld plateau can be easily observed and South Africa appears as one of the major emitters of NO_2 long-range transport plumes.

Long-range transport of NO_2 takes place only at mid-latitudes. This is mainly due to two reasons. First, the lifetime of NO_2 is relatively short in the tropics, where solar irradiation is high. Second, both the northern and southern mid-latitudes feature prominent storm tracks along which cyclones travel regularly. Also, long-range transport events have to be emitted from high-pollution regions which are typically densely populated areas which are not located at polar latitudes.

From the statistical analysis, it is evident that most long-range transport events take place during local autumn and especially winter (the main season). In these seasons, cyclones are much more frequent than in spring and summer. In winter, the lifetime of NO_2 is higher due to the low irradiation, which makes it more likely that NO_2 will be transported from the planetary boundary layer into the free troposphere before decaying and allows the NO_2 to follow the cyclone for a longer time. Anthropogenic emissions are also highest in winter, when buildings are heated and use of motorized transport increases. All of these factors lead to the strong seasonality seen in both the 5-year GOME-2 / MetOp-A and 4-year MACC-II reanalysis data sets.

Besides long-range transport of anthropogenic emissions, there are also cases of long-range transport from natural biomass burning, as seen in the case study for an Australian transport event. These may contribute a significant amount of long-range transported NO_2 in the Southern Hemisphere.

From the data presented here, there is some indication that phases of atmospheric large-scale oscillations play a role in triggering NO_2 long-range transport. There appears to be a link between plume emission from Europe and the North Atlantic Oscillation index during winter, when NO_2 lifetime is high. There are also correlations to typical pressure and temperature anomalies for transports emitted from South Africa, China and Europe. However, this evidence can only hint at influences of global oscillations onto long-range transport emission. Further studies will be required in this regard.

Looking at the mean sea-level pressure, there is an average low pressure anomaly over southern Europe and a high pressure anomaly over Scandinavia associated to long-range transport events emitted from Europe. This leads to an effective pressure gradient towards the North-East, which in turn leads to high wind speeds in north-westward direction. This explains the atypical routes of European NO_2 long-range transport events in this direction, while most plumes associated to long-range transport events travel towards the East.

While the European pressure pattern is fairly stationary, there is a dynamic pattern associated to South African long-range transport events. Here, alternating high- and low-pressure anomalies move from the West towards the East over the course of a long-range transport event, hitting the Highveld plateau around the estimated time of plume

emission. This indicates moving cyclones that lift the NO_2 up from the industrial region and then transport the plume along their center towards the south-east.

In China, there is significant cloud formation visible, following the movement of the NO_2 after the emission out towards the Pacific Ocean. This, again, indicates the passage of a cold front through the Beijing metropolitan area, although this is only hinted at in the pressure anomalies.

$LiNO_x$, NO_x emitted by lightning, does not appear to play a major role in the process of NO_2 long-range transport. A few events are connected to thunderstorms that produce lightning, but this is only a minor fraction. $LiNO_x$ is hardly visible in satellite observations, due to unfavorable viewing conditions in thick thunderstorm clouds, with most NO_x being produced below or deep inside the cloud. This was confirmed by a sensitivity study. It is however possible, that $LiNO_x$ enhances the lifetime of individual NO_2 long-range transport events, replenishing the NO_x and allowing them to travel over longer distances before dissipating or decaying.

9.3 Characteristic properties

The 5-year statistical analysis of NO_2 long-range transport has revealed typical properties of these events. It showed that these transports occur in a variety of sizes, up to 4 Gg N in a single plume upon emission. The probability distribution function of plume NO_2 content roughly follows an exponentially decreasing function, leading to no characteristic size. This is expected as the NO_2 content is only subject to transport and does not cause the transport itself. The scale mass of this function – on the mass range analyzed – is on the order of 0.25 Gg N upon observation. The mean NO_2 content in this study is higher due to the exclusion of low-NO_2-content plumes.

This study did not analyze plumes of less than $5 \cdot 10^{30}$ molecules NO_2 (corresponding to 0.12 Gg N), due to computational feasibility and the dominance of statistical fluctuations in observational data on these scales. But as the NO_2 is not causal to the long-range transport, I expect the distribution to continue to smaller sizes. These smaller events may not be detected by observations of the GOME-2 / MetOp-A instrument. This implies that NO_2 long-range transport takes place abundantly, but only few of these events are observable and have an impact on remote atmospheric chemistry. Integrating the exponential mass distributions of SON, DJF and MAM in the Northern Hemisphere results in a total long-range transported NO_2 content of 61 Gg N/a upon observation (with 36 Gg N/a for the Southern Hemisphere), yielding even higher estimates when taking decay into account. This corresponds to a lower boundary of 0.23 % of yearly NO_2 emissions being subject to long-range transport over the ocean.

From the analysis it is evident that NO_2 long-range transport events start at low altitudes and then rapidly rise to an altitude of about 4,000 m before they spread out over the entire troposphere at older ages. The observed altitude distribution is in accordance with expectations, theoretical considerations and in-situ observations from the TRACE-P aircraft campaign (Crawford et al., 2003). Due to the employed method, there were no observations of NO_2 plumes reaching remote continental areas, but falling winds over the shore may lead to a descent of the polluted air masses, which will invariably impact local ozone chemistry. Further, PAN contained in the plume – which cannot be detected

by UV/vis satellite observations – may reconvert to NO_x, amplifying the impact over that estimated from NO_2 observations.

The observed ages of detected NO_2 long-range transport plumes are compatible with an exponential decay of the plumes themselves – by diffusion, meteorological shear and decay of the contained NO_2 itself. This shear and diffusion can be observed directly in the shape of the plumes in satellite and model data. The NO_2 lifetime was determined to be on the order of 100 h in individual long-range transport events that were observed over multiple days, except for bush fire emissions from Australia which decayed much more rapidly – maybe due to reactive species emitted in the bush fires. A view on the age distribution of all observed plumes also hints at lifetimes on the order of 80 h for the off-season and 100 h for the main season. This is in accordance with reported lifetimes from model analyses and theoretical lifetimes for the free troposphere.

NO_2 long-range transports can only be found in parts of the globe and follow typical routes from their emission regions out to the remote ocean or other continents. The strongest sources of NO_2 plumes over the ocean are the Beijing area in China, Central Europe, the East Coast of North America, and the Highveld plateau in South Africa. Argentina and Australia are only minor emission sources and there are no source regions in the tropics.

Except for Central Europe, all of the emission regions are situated near the east coast. This is not surprising as the dominant wind patterns in the mid-latitudes blow towards the East, driven by the Coriolis force in the second Hadley cell. The typical routes start in a polewards direction and then either vanish into polar night or follow zonal winds around the pole.

Central Europe is an exception. Here, long-range transport events are frequently emitted onto the North Sea, towards Iceland and Greenland. Note, that the algorithm cannot make any statement on *other* NO_2 long-range transport events going out towards Russia, as it is limited to observations over the ocean. However, other metropolitan areas near the west coast of their respective continent do not exhibit any long-range transport towards the ocean; this is limited to the European region. For oceanic European long-range transport events, the emissions are linked to a low pressure anomaly over Southern Europe and a high pressure anomaly over Scandinavia and the Baltic. This synoptic weather leads to strong winds towards the North Sea, facilitating the transport.

During their main season, major emission regions emit a long-range transport event more than once per week. For South America and Australia – which probably exhibit long-range transport of NO_2 from biomass burning – this rate goes down to roughly once per month.

In total, the analysis shows, more than a permil of yearly NO_x emissions are subject to long-range transport. This is a lower limit, as I did not correct for the decay of NO_2 during the first hours of the transport. Insufficient knowledge about the circumstances of the emission prevents any reliable analysis. In total, 97 Gg N/a can be estimated to be transported in these events. This is a significant fraction, considering the short lifetime in the boundary layer and that – in stationary conditions – NO_x emissions are bound to the planetary boundary layer (except for occasions of heavy biomass burning, when plumes can penetrate into the free troposphere or even the stratosphere).

9.4 Model data

The comparison of results from the GOME-2 / MetOp-A and MACC-II reanalysis datasets yields a lot of common results, but also some discrepancies.

In both datasets, the regular occurence of long-range transport is evident. On the Northern Hemisphere, both find similar numbers of events and quantities of exported NO_2. On the Southern Hemisphere, however, MACC-II reanalysis finds significantly less NO_2 long-range transport in both numbers and amount of NO_2. It appears likely that this is an effect of parameterizations, emission inventories or meteorology used in MACC-II reanalysis, as GOME-2 / MetOp-A observations face the same challenges on the Northern and Southern Hemisphere.

MACC-II reanalysis data did also not exhibit the transport event in the Australian case study, where bush fire emissions were transported. These individual pollution events cannot be attributed to emissions from a static inventory which may have lead to MACC-II reanalysis missing this event – as well as probably other biomass burning long-range transports. This may also explain parts of the discrepancy to GOME-2 / MetOp-A results on the Southern Hemisphere.

With the MACC-II reanalysis dataset, it is possible to observe transport at high latitudes, which reveals that long-range transport events from Europe reach the Arctic atmosphere. Even small amounts may have a strong impact on its sensitive atmospheric chemistry.

With model data, it is easier to detect long-range transports near the emission region, as the signal-to-noise ratio is significantly better than for satellite observations. This will also lead to less fragmented plumes; in satellite observations, two parts of a plume may be observed as separated due to the high background noise.

About a sixth to a third of plumes can be matched between both datasets. The NO_2 contained in matched plumes can easily vary by 1 Gg N, which can partially be explained by differences in the emissions, but partially hints at false positive matches. MACC-II reanalysis data has a lot of unmatched plumes near emission regions, where precise plume retrievals are difficult in GOME-2 / MetOp-A data. Many of the plumes seen in GOME-2 / MetOp-A on the Southern Hemisphere find no matching plume in MACC-II reanalysis data.

9.5 Impact

The preceding study hints at the impact that NO_2 long-range transport might have on pristine ecosystems. Cyclones are capable of relocating a significant fraction of accumulated NO_x emissions from metropolitan or industrial polluted regions to remote and possibly pristine regions.

Especially the Arctic Ocean appears to be affected by NO_2 long-range transport, with major routes from the Northern Hemisphere leading there. Trajectories indicate that NO_2 from both the East Coast of the USA and Central Europe is relocated to Greenland and the Arctic. The Arctic is an especially sensitive ecosystem that is usually devoid of short-lived anthropogenic pollution. Still, effects of anthropogenic pollution on the Arctic can be seen in the decreasing albedo of sea-ice and the sudden formation of Arctic

Haze.

In other emission regions, long-range transport events follow trajectories towards other land masses. In China, some long-range transports reach Taiwan and Japan before dissipating over the Pacific, while some follow a circular motion back to the Asian continent on the northern shore of Russia. South African long-range transport events follow a trajectory towards Australia and at least a few plumes have been observed near Australia's West Coast, heading towards the shore.

The abundance of long-range transport events in both observational and model data indicates that this is not an exceptional phenomenon, but rather a common effect that affects the major emission regions and thus their downind regions on a weekly basis during winter and autumn. While relocation from one populated and polluted area to another one may be mainly an issue of environmental politics, relocation of pollution to otherwise pristine regions may drastically affect sensitive atmospheric and surface chemistry and thus alter sensitive ecosystems.

9.6 Validation

This study has analyzed NO_2 long-range transport on both GOME-2 / MetOp-A observational satellite data and data from MACC-II reanalysis model runs. By comparing the results, it is evident that abundant NO_2 long-range transport is not just an artifact of satellite data or an artifact of parametrisations in the model. Many major events can be obseved in both data sets with similar properties and routes.

While there are only a few events in the model data that were not detected in satellite data, there are many events in the satellite data that could not be observed in the model data. While some of these may be false positive detections in the satellite data, it is likely that many of these events are actually real. The reason why they are not found in MACC-II reanalysis data most likely lies in the highly non-linear meteorology that initiates transport. It is still a strongly debated field how convection in the planetary boundary layer should be parameterized and what injection heights should be assumed in models and emission inventories.

Models with different parameterizations may yield very different results for NO_2 long-range transport, especially concerning small plumes. While the largest transport events are initiated by prominent, large-scale cyclones that should initiate effective vertical transport in any model, small events can be caused by weather systems on much smaller scales that may not neccessarily lead to an uplift of NO_2 from the planetary boundary layer.

Also, for the smaller long-range transport plumes, the used meteorological hind-cast data impacts the results. Especially in South Africa – which is almost a point-like source on the relevant scale – shifting the location of a cyclone by 100 km in the meteorological data may make the difference between modeling the emission of a plume or not.

It is striking that the results from both data sets are comparable in the Northern Hemisphere while they completely deviate in the Southern Hemisphere. This may partially be due to artifcats in the satellite data that characteristically appear in the Southern Hemisphere. While the algorithm is designed to filter these out by tracing them back to their origin, this method still leaves room for artifact NO_2 anomalies that can be traced

back to emission regions from some altitude. Still, the results hint at the possibility that there is some problem with parameterizing convection or modeling frontal systems in the Southern Hemisphere. Missing biomass burning emissions or unrepresentative emission inventories could also lead to a lack of long-range transport events in MACC-II reanalysis data.

10 Summary and Outlook

This final chapter summarizes the main results of this study and hints at possible further studies with regards to the topic of NO_2 long-range transport.

10.1 Outlook

Despite trying to be comprehensive, there are a lot of questions unanswered in this work.

First of all, it would be nice to circumvent the limit of only detecting long-range transport above the ocean. This will probably need some refinement of the detection algorithm and more precise observational data, requiring a more differentiated radiative transfer simulation. It would be neccessary to differentiate between local emissions and transported NO_2.

It would also be nice to directly link consecutive observations of the same plume to one another. This would allow to study the evolution of a plume not only for a few hand-picked case studies but for a more comprehensive and representative set of long-range transports. This is currently not possible due to the coarse nature of the used backtrajectories.

With the knowledge gained in this study, the approximations, assumptions and algorithmic decisions could be refined to enhance the data set, concerning travel altitudes, plume ages and sizes and also emission regions.

In-situ measurements of NO_2 profiles in downwind regions might also enable the verification of long-range transports in satellite and model data in the most precise of measurement data.

Finally, geostationary satellite observations of NO_2 will allow a detailed study of the intra-day evolution and the process of emission of long-range transport events.

Besides this, there are probably many more ideas to improve and expand on this study.

10.2 Summary

For this study, I have developed an algorithm that can detect, assess and verify NO_2 long-range transport events over the ocean in tropospheric NO_2 vertical column density maps of both GOME-2 / MetOp-A satellite and MACC-II reanalysis model data. It allows to generate a comprehensive dataset of such events which forms the basis for further analysis.

To this end, I had to adapt the GOME-2 / MetOp-A NO_2 retrieval to deal with the problems of non-stationary, elevated NO_2, obfuscation by clouds and and the intricate light-path under these observational conditions. Sensitivity studies show that the neccessary approximations in radiative transfer do not strongly impact the resulting tropospheric NO_2 vertical column densities for this particular purpose. Additionally,

a short study shows that clouds over bright surfaces do not hamper detection of NO_2 mixed into or residing beow them.

The algorithm finds anomalies in daily 2-D tropospheric NO_2 vertical column density maps. It will then select pixels with highly significant anomalies and aggregate them into anomalous plumes. These plumes are then backtraced starting on multiple altitudes using HYSPLIT_v4. A most likely trajectory is selected and plume properties like plume area, NO_2 content, age and altitude are determined. Finally, from the selected trajectory a verification process decides if this anomalous NO_2 plume is actually likely to be the result of long-range transport. Several thousand long-range transport events were identified in this manner. This method is also applicable to other kinds of datasets and not limited to this particular instrument or trace gases.

This study has shown that NO_2 long-range transport not only exists (despite the short lifetime) but is able to relocate significant amounts of NO_2 out of emission regions, potentially impacting regions on other continents or the atmospheric chemistry in otherwise pristine regions like the Arctic. The frequency of these events is higher than previous case studies suggested and the amount of NO_2 that is affected is estimated to be a few permil of the entire NO_2 emission budget. This is unexpectedly high as NO_2 is a short-lived species that is usually assumed to stay local to its emission region.

NO_2 long-range transport is visible in both satellite observations (in this case by GOME-2 / MetOp-A) and model data (MACC-II reanalysis). This confirms that this form of transport takes place regularly and current models are able to reproduce at least some of this NO_2 export.

This study also employed sensitivity studies to demonstrate that, with some assumptions, a resonable estimate of NO_2 retrieval parameters for satellite observations can be made for the difficult scenario of long-range transport, using radiative transfer simulations with SCIATRAN 3.1. There are some discrepancies between the results of data from satellite and model. Better emission inventories and parameterizations could make model data better suited for this kind of study while satellite instruments with less noise and more detailed radiative transfer modeling will help on the observational side.

Long-range transport events follow typical routes along storm tracks and usually head in an eastwards and polewards direction. Some amounts of long-range transported NO_2 are relocated to the sensitive Arctic atmosphere. It appears that plume emission can be triggered by passing cyclones, providing the neccessary uplift, and is correlated to the North Atlantic Oscillation. Most events are observed during local winter when the lifetime of NO_2 is long and the storm frequency and anthropogenic emissions are high. No events can be seen in the tropics and the Northern Hemisphere dominates the total inventory due to its strong emission sources.

Typical lifetimes of NO_2 within long-range transport events are on the order of 100 hours, which is significantly longer than inside the planetary boundary layer. In this time, a plume can traverse the distance between North America or Europe and the Arctic or between South Africa and Australia.

The main sources of NO_2 long-range transport events are the East Coast of North America (mostly the Great Lakes region), Central Europe, the Beijing Area and the Highveld plateau in South Africa which – due to its isolated location surrounded by ocean – allows for the clearest observations of long-range transports.

The results from this study imply that even concerning the chemistry of such a short-

lived species as NO_2, local regulations alone might not suffice and global agreements and collaboration will be neccessary to ensure good air quality – at least outside the tropics.

Publications

The following is a comprehensive list of the publications that I made connected to my PhD.

Papers

- Zien, A. W., Richter, A., Hilboll, A., Blechschmidt, A.-M., and Burrows, J. P.: Systematic analysis of tropospheric NO2 long-range transport events detected in GOME-2 satellite data, Atmos. Chem. Phys., 14, 7367–7396, doi: 10.5194/acp-14-7367-2014, URL `http://www.atmos-chem-phys.net/14/7367/2014/`, 2014

Oral presentations

- Zien, A., Richter, A., Hilboll, A., and Burrows, J.: Comparison of NO2 long-range transport events in GOME-2 observations and CTM simulations, European Geosciences Union General Assembly, Vienna, Austria, URL `http://www.doas-bremen.de/posters/egu_2012_zien.pdf`, 2012

- Zien, A., Richter, A., Hilboll, A., and Burrows, J.: A Statistical Evaluation of NO2 Long-Range Transport Events Using GOME-2 Observations, European Geosciences Union General Assembly, Vienna, Austria, URL `http://www.iup.uni-bremen.de/~azien/downloads/azien-egu2011-NO2LRTstatistics.pdf`, 2011b

Posters

- Zien, A., Richter, A., Hilboll, A., and Burrows, J.: Comparison of NO2 long-range transport events in GOME-2 observations and CTM simulations, European Geosciences Union General Assembly, Vienna, Austria, URL `http://www.doas-bremen.de/posters/egu_2012_zien.pdf`, 2012

- Zien, A., Richter, A., Hilboll, A., and Burrows, J.: Remote sensing trace gas observations by satellite instruments over bright surfaces, DPG Frühjahrstagung, Dresden, Germany, URL `http://www.doas-bremen.de/posters/dpg_2011_zien.pdf`, 2011a

- Zien, A., Richter, A., Hilboll, A., and Burrows, J.: Sensitivity of satellite observations over bright and cloudy scenes, COSPAR, Bremen, Germany, URL `http://www.doas-bremen.de/posters/cospar_2010_zien.pdf`, 2010b

- Zien, A., Richter, A., Hilboll, A., and Burrows, J.: Cloud effects on tropospheric NO2 measurements from satellite, DPG Frühjahrstagung, Hannover, Germany, URL http://www.doas-bremen.de/posters/dpg_2010_zien.pdf, 2010a

Acknowledgements

This work is part of the INTAS project.

It was inspired by work of Andreas Heckel, see http://www.doas-bremen.de/posters/egu_2005_heckel.p

I gratefully acknowledge the funding by the Deutsche Forschungsgemeinschaft[1] (DFG) and Universität Bremen through the INTAS project.

GOME-2 radiances have been provided by EUMETSAT.

NCEP Reanalysis data provided by the NOAA/OAR/ESRL PSD, Boulder, Colorado, USA, from their web site at http://www.esrl.noaa.gov/psd/.

NCEP EDAS and GDAS (FNL) Model Data (DSI-6141) provided by the NOAA/NCDC, Asheville, NC, USA, from their web site at http://www.ncdc.noaa.gov.

I wish to thank the World Wide Lightning Location Network (http://wwlln.net), a collaboration among over 50 universities and institutions, for providing the lightning location data used in this study.

The HYSPLIT_v4[2] model was provided by the NOAA/ARL.

The interactive shell IPython[3] (Perez and Granger, 2007) was used to analyze the data in this study. For plotting of data, I used the versatile Matplotlib[4] package (Hunter, 2007). Python[5] is awesome for science.

I would like to thank Professor John P. Burrows for supervising my work.

I would like to thank all members of the DOAS group at the Institute for Environmental Physics at the University of Bremen; especially Andreas Richter for being there for all kinds of questions and data requests and his patience with my work; Andreas Hilboll, Anja Schönhardt and Enno Peters for their questions and answers and for sharing and enduring PhD highs and lows with me.

I would like to thank my family for being so patient and awesome and allowing me to complete this study.

[1] http://dfg.de/
[2] http://ready.arl.noaa.gov/HYSPLIT.php
[3] https://ipython.org/
[4] http://matplotlib.org/
[5] https://www.python.org/

List of Figures

List of Tables

Bibliography

Abiodun, B. J., Ojumu, A. M., Jenner, S., and Ojumu, T. V.: The transport of atmospheric NOx and HNO3 over Cape Town, Atmos. Chem. Phys., 14, 559–575, doi:10.5194/acp-14-559-2014, URL http://www.atmos-chem-phys.net/14/559/2014/, 2014.

Arya, P. S.: Introduction to micrometeorology, vol. 79, Access Online via Elsevier, URL https://books.google.de/books?id=riWkURgS_I8C, 2001.

Ascher, D., Dubois, P. F., Hinsen, K., Hugunin, J., Oliphant, T., and others: Numerical python, Package to speed-up arithmetic operations on arrays of numbers. http://sourceforge. net/projects/numpy, URL http://www.cs.mcgill.ca/~hv/articles/Numerical/numpy.pdf, 2001.

Aschmann, J., Sinnhuber, B.-M., Atlas, E. L., and Schauffler, S. M.: Modeling the transport of very short-lived substances into the tropical upper troposphere and lower stratosphere, Atmos. Chem. Phys., 9, 9237–9247, doi:10.5194/acp-9-9237-2009, URL http://www.atmos-chem-phys.net/9/9237/2009/, 2009.

Barros, S. R. M., Dent, D., Isaksen, L., Robinson, G., Mozdzynski, G., and Wollenweber, F.: The IFS model: A parallel production weather code, Parallel Computing, 21, 1621–1638, doi:10.1016/0167-8191(96)80002-0, URL http://www.sciencedirect.com/science/article/pii/0167819196800020, 1995.

Barth, M. C., Kim, S.-W., Wang, C., Pickering, K. E., Ott, L. E., Stenchikov, G., Leriche, M., Cautenet, S., Pinty, J.-P., Barthe, C., and others: Cloud-scale model intercomparison of chemical constituent transport in deep convection, Atmospheric Chemistry and Physics, 7, 4709–4731, URL http://www.atmos-chem-phys.net/7/4709/2007/acp-7-4709-2007.pdf, 2007.

Beirle, S., Platt, U., Wenig, M., and Wagner, T.: Weekly cycle of NO2 by GOME measurements: a signature of anthropogenic sources, Atmos. Chem. Phys., 3, 2225–2232, doi:10.5194/acp-3-2225-2003, URL http://www.atmos-chem-phys.net/3/2225/2003/, 2003.

Beirle, S., Platt, U., Wenig, M., and Wagner, T.: NOx production by lightning estimated with GOME, Advances in Space Research, 34, 793–797, doi:10.1016/j.asr.2003.07.069, URL http://www.sciencedirect.com/science/article/pii/S0273117704003576, 2004.

Beirle, S., Salzmann, M., Lawrence, M. G., and Wagner, T.: Sensitivity of satellite observations for freshly produced lightning NOx, Atmos. Chem. Phys., 9, 1077–1094, doi:10.5194/acp-9-1077-2009, URL http://www.atmos-chem-phys.net/9/1077/2009/, 00000, 2009.

Beirle, S., Boersma, K. F., Platt, U., Lawrence, M. G., and Wagner, T.: Megacity Emissions and Lifetimes of Nitrogen Oxides Probed from Space, Science, 333, 1737–1739, doi:10.1126/science.1207824, URL http://www.sciencemag.org/content/333/6050/1737, 2011.

Blechschmidt, A.-M., Bakan, S., and Graßl, H.: Large-scale atmospheric circulation patterns during polar low events over the Nordic seas, Journal of Geophysical Research: Atmospheres, 114, n/a–n/a, doi:10.1029/2008JD010865, URL http://onlinelibrary.wiley.com/doi/10.1029/2008JD010865/abstract, 2009.

Bovensmann, H., Burrows, J. P., Buchwitz, M., Frerick, J., Noël, S., Rozanov, V. V., Chance, K. V., and Goede, A. P. H.: SCIAMACHY: Mission Objectives and Measurement Modes, Journal of the Atmospheric Sciences, 56, 127–150, doi:10.1175/1520-0469(1999)056<0127:SMOAMM>2.0.CO;2, URL http://journals.ametsoc.org/doi/abs/10.1175/1520-0469(1999)056%3C0127:SMOAMM%3E2.0.CO;2, 1999.

Bradshaw, J., Davis, D., Grodzinsky, G., Smyth, S., Newell, R., Sandholm, S., and Liu, S.: Observed distributions of nitrogen oxides in the remote free troposphere from the NASA Global Tropospheric Experiment programs, Reviews of Geophysics, 38, 61–116, doi:10.1029/1999RG900015, URL http://adsabs.harvard.edu/abs/2000RvGeo..38...61B, 2000.

Brasseur, G., Orlando, J. J., Tyndall, G. S., and others: Atmospheric chemistry and global change, Oxford University Press, URL http://agris.fao.org/agris-search/search.do?recordID=US201300030251, 1999.

Bredk: Layers of the atmosphere, URL http://commons.wikimedia.org/wiki/File:Atmospheric_Layers.svg, 2007.

Browning, K. A.: The dry intrusion perspective of extra-tropical cyclone development, Meteorological Applications, 4, 317–324, 1997.

Browning, K. A.: Mesoscale aspects of extratropical cyclones: An observational perspective, The life cycles of extratropical cyclones, pp. 265–283, 1999.

Burrows, J. P., Dehn, A., Deters, B., Himmelmann, S., Richter, A., Voigt, S., and Orphal, J.: Atmospheric Remote-Sensing Reference Data from GOME: Part 1. Temperature-Dependent Absorption Cross-Sections of NO2 in the 231–794 nm Range, Journal of Quantitative Spectroscopy and Radiative Transfer, 60, 1025–1031, doi:10.1016/S0022-4073(97)00197-0, URL http://www.sciencedirect.com/science/article/pii/S0022407397001970, 1998.

Burrows, J. P., Weber, M., Buchwitz, M., Rozanov, V., Ladstätter-Weißenmayer, A., Richter, A., DeBeek, R., Hoogen, R., Bramstedt, K., Eichmann, K.-U., Eisinger, M., and Perner, D.: The Global Ozone Monitoring Experiment (GOME): Mission Concept and First Scientific Results, Journal of the Atmospheric Sciences, 56, 151–175, doi:10.1175/1520-0469(1999)056<0151:TGOMEG>2.0.CO;2, URL http://journals.ametsoc.org/doi/abs/10.1175/1520-0469(1999)056%3C0151:TGOMEG%3E2.0.CO%3B2, 1999.

Byun, D. W., Ching, J. K. S., and others: Science algorithms of the EPA Models-3 community multiscale air quality (CMAQ) modeling system, US Environmental Protection Agency, Office of Research and Development Washington, DC, USA, URL http://www.epa.gov/asmdnerl/CMAQ/Documents/000_cover_exec.pdf, 1999.

Callies, J., Corpaccioli, E., Eisinger, M., Hahne, A., and Lefebvre, A.: GOME-2 - Metop's Second Generation sensor for Operational Ozone Monitoring, ESA Bulletin, 102, 2000.

Casiday, R. and Frey, R.: Improving Air Quality, URL http://www.chemistry.wustl.edu/~edudev/LabTutorials/CourseTutorials/bb/AirQuality/AirQuality.htm, 2001.

Chang, E. K. M. and Fu, Y.: Interdecadal Variations in Northern Hemisphere Winter Storm Track Intensity, Journal of Climate, 15, 642–658, doi:10.1175/1520-0442(2002)015<0642:IVINHW>2.0.CO;2, URL http://journals.ametsoc.org/doi/abs/10.1175/1520-0442(2002)015%3C0642:IVINHW%3E2.0.CO%3B2, 2002.

Christian, H. J.: Optical Detection of Lightning from Space, in: Proceedings of the 11th International Conference on Atmospheric Electricity, 715-718, Guntersville, Alabama, URL http://thunder.nsstc.nasa.gov/lis/, 1999.

Christian, H. J., R. J. Blakeslee, S. J. Goodman, D. A. Mach, M. F. Stewart, D. E. Buechler, W. J. Koshak, J. M. Hall, W. L. Boeck, K. T. Driscoll, and D. J. Bocippio: The Lightning Imaging Sensor, in: Proceedings of the 11th International Conference on Atmospheric Electricity, pp. 746–749, Guntersville, Alabama, URL http://thunder.nsstc.nasa.gov/bookshelf/pubs/LIS_ICAE99_Print.pdf, 1999.

Christoudias, T., Pozzer, A., and Lelieveld, J.: Influence of the North Atlantic Oscillation on air pollution transport, Atmos. Chem. Phys., 12, 869–877, doi:10.5194/acp-12-869-2012, URL http://www.atmos-chem-phys.net/12/869/2012/, 2012.

Crawford, J., Olson, J., Davis, D., Chen, G., Barrick, J., Shetter, R., Lefer, B., Jordan, C., Anderson, B., Clarke, A., Sachse, G., Blake, D., Singh, H., Sandolm, S., Tan, D., Kondo, Y., Avery, M., Flocke, F., Eisele, F., Mauldin, L., Zondlo, M., Brune, W., Harder, H., Martinez, M., Talbot, R., Bandy, A., and Thornton, D.: Clouds and trace gas distributions during TRACE-P, Journal of Geophysical Research, 108, 13 PP., doi:200310.1029/2002JD003177, URL http://www.agu.org/pubs/crossref/2003/2002JD003177.shtml, 2003.

Dikty, S. and Richter, A.: GOME-2 on MetOp-A Support for Analysis of GOME-2 In-Orbit Degradation and Impacts on Level 2 Data Products, Tech. Rep. Final Report, University of Bremen, Institute of Remote Sensing, Bremen, URL http://www.iup.uni-bremen.de/doas/reports/Final_Report_Level-2_Data_GOME-2_Degradation.pdf, 2012.

Draxler, R.: HYSPLIT4 user's guide, 1999.

Draxler, R. and Hess, G.: Description of the HYSPLIT_4 modeling system, NOAA Tech. Memo. ERL ARL-224, NOAA Air Resources Laboratory, Silver Spring, MD, 1997.

Draxler, R. and Hess, G.: An overview of the HYSPLIT_4 modeling system of trajectories, dispersion, and deposition, Aust. Meteor. Mag., 47, 295–308, 1998.

Eckhardt, S., Stohl, A., Beirle, S., Spichtinger, N., James, P., Forster, C., Junker, C., Wagner, T., Platt, U., and Jennings, S. G.: The North Atlantic Oscillation controls air pollution transport to the Arctic, Atmospheric Chemistry & Physics Discussions, 3, 3222–3240, URL http://adsabs.harvard.edu/abs/2003ACPD....3.3222E, 2003.

Ehhalt, D. H., Rohrer, F., and Wahner, A.: Sources and Distribution of NOx in the Upper Troposphere at Northern Mid-Latitudes, Journal of Geophysical Research, 97, PAGES 3725–3738, URL http://www.agu.org/journals/jd/v097/iD04/91JD03081/, 1992.

Ekman, V. W.: Om jordrotationens inverkan på vindströmmar i hafvet..., 1902.

Emmons, L. K., Walters, S., Hess, P. G., Lamarque, J.-F., Pfister, G. G., Fillmore, D., Granier, C., Guenther, A., Kinnison, D., Laepple, T., Orlando, J., Tie, X., Tyndall, G., Wiedinmyer, C., Baughcum, S. L., and Kloster, S.: Description and evaluation of the Model for Ozone and Related chemical Tracers, version 4 (MOZART-4), Geosci. Model Dev., 3, 43–67, doi:10.5194/gmd-3-43-2010, URL http://www.geosci-model-dev.net/3/43/2010/, 2010.

Engelen, R.: MACC-II Product and Service Specification, Tech. rep., Copernicus, URL https://www.gmes-atmosphere.eu/documents/maccii/general/, 2014.

Etling, D.: Die atmosphärische Grenzschicht, in: Theoretische Meteorologie, vol. Theoretische Meteorologie - Eine Einführung, pp. 297–340, Springer Berlin Heidelberg, URL http://link.springer.com/chapter/10.1007/978-3-540-75979-9_21, 2008.

Finlayson-Pitts, B. J. and Pitts Jr, J. N.: Chemistry of the upper and lower atmosphere: theory, experiments, and applications, Academic press, URL http://books.google.com/books?hl=de&lr=&id=mRoJUB5fxRwC&oi=fnd&pg=PP2&dq=finnlayson+pitts+pitts&ots=tO8qDvyM11&sig=43lJh4j6BkKT9toTCbvOLEeNvPs, 1999.

Fraunhofer, J.: Bestimmung des Brechungs-und des Farbenzerstreungs-Vermögens verschiedener Glasarten, in Bezug auf die Vervollkommnung achromatischer Fernröhre, Annalen der Physik, 56, 264–313, URL http://onlinelibrary.wiley.com/doi/10.1002/andp.18170560706/abstract, 1817.

Galloway, J. N. and Likens, G. E.: Acid precipitation: The importance of nitric acid, Atmospheric Environment, 15, 1081–1085, doi:10.1016/0004-6981(81)90109-8, URL http://adsabs.harvard.edu/abs/1981AtmEn..15.1081G, 1981.

Giles, D. M., Holben, B. N., Eck, T. F., Sinyuk, A., Smirnov, A., Slutsker, I., Dickerson, R. R., Thompson, A. M., and Schafer, J. S.: An analysis of AERONET aerosol absorption properties and classifications representative of aerosol source regions, Journal of Geophysical Research: Atmospheres, 117, doi:10.1029/2012JD018127, URL http://onlinelibrary.wiley.com/doi/10.1029/2012JD018127/abstract, 2012.

Grainger, J. F. and Ring, J.: Anomalous Fraunhofer Line Profiles, Nature, 193, 762–762, doi:10.1038/193762a0, URL http://adsabs.harvard.edu/abs/1962Natur.193..762G, 1962.

Heckel, A., Richter, A., Nüß, H., and Burrows, J.: Long-range transport of tropospheric NO2 as seen by GOME and SCIAMACHY, 2005.

Hilboll, A.: Tropospheric nitrogen dioxide from satellite measurements: SCHIAMACHY limb/nadir matching and multi-instrument trend analysis, Dissertation, Universität Bremen, Bremen, Germany, URL http://nbn-resolving.de/urn:nbn:de:gbv:46-00103664-15, 2013.

Hilboll, A., Richter, A., and Burrows, J. P.: Long-term changes of tropospheric NO2 over megacities derived from multiple satellite instruments, Atmos. Chem. Phys., 13, 4145–4169, doi:10.5194/acp-13-4145-2013, URL http://www.atmos-chem-phys.net/13/4145/2013/, 2013.

Hilboll, A., Richter, A., and Burrows, J.: Vertical information content of nadir measurements of tropospheric NO2 from satellite, URL http://www.iup.uni-bremen.de/doas/posters/egu_2014_hilboll.pdf, 2014.

Hunter, J. D.: Matplotlib: A 2D graphics environment, Computing in Science & Engineering, 9, 0090–95, URL http://doi.ieeecomputersociety.org/10.1109/mcse.2007.55, 2007.

Inness, A., Baier, F., Benedetti, A., Bouarar, I., Chabrillat, S., Clark, H., Clerbaux, C., Coheur, P., Engelen, R. J., Errera, Q., Flemming, J., George, M., Granier, C., Hadji-Lazaro, J., Huijnen, V., Hurtmans, D., Jones, L., Kaiser, J. W., Kapsomenakis, J., Lefever, K., Leitão, J., Razinger, M., Richter, A., Schultz, M. G., Simmons, A. J., Suttie, M., Stein, O., Thépaut, J.-N., Thouret, V., Vrekoussis, M., Zerefos, C., and the MACC team: The MACC reanalysis: an 8 yr data set of atmospheric composition, Atmos. Chem. Phys., 13, 4073–4109, doi:10.5194/acp-13-4073-2013, URL http://www.atmos-chem-phys.net/13/4073/2013/, 2013.

Janssens-Maenhout, G., Dentener, F., van Aardenne, J., Monni, S., Pagliari, V., Orlandini, L., Klimont, Z., Kurokawa, J., Akimoto, H., Ohara, T., and others: EDGAR-HTAP: a harmonized gridded air pollution emission dataset based on national inventories, European Commission, Joint Research Centre, Institute for Environment and Sustainability, Luxemburg, 2012.

Jones, E., Oliphant, T., and Peterson, P.: SciPy: Open source scientific tools for Python, http://www. scipy. org/, URL http://www.citeulike.org/group/2018/article/2644428, 2001.

Kokhanovsky, A. A. and Nauss, T.: Reflection and transmission of solar light by clouds: asymptotic theory, Atmospheric Chemistry & Physics, 6, 5537–5545, URL http://adsabs.harvard.edu/abs/2006ACP.....6.5537K, 2006.

Kokhanovsky, A. A., Rozanov, V. V., Burrows, J. P., Eichmann, K.-U., Lotz, W., and Vountas, M.: The SCIAMACHY cloud products: Algorithms and examples from ENVISAT, Advances in Space Research, 36, 789–799, URL http://www.sciencedirect.com/science/article/pii/S0273117705002899, 2005.

Konovalov, I. B., Beekmann, M., Burrows, J. P., and Richter, A.: Satellite measurement based estimates of decadal changes in European nitrogen oxides emissions, Atmospheric Chemistry and Physics, 8, 2623–2641, URL http://www.atmos-chem-phys.net/8/2623/2008/, 2008.

Kuenen, J. J. P., Visschedijk, A. J. H., Jozwicka, M., and Denier van der Gon, H. A. C.: TNO-MACC_II emission inventory; a multi-year (2003–2009) consistent high-resolution European emission inventory for air quality modelling, Atmos. Chem. Phys., 14, 10 963–10 976, doi:10.5194/acp-14-10963-2014, URL http://www.atmos-chem-phys.net/14/10963/2014/, 2014.

Labonne, M., Bréon, F.-M., and Chevallier, F.: Injection height of biomass burning aerosols as seen from a spaceborne lidar, Geophysical Research Letters, 34, doi:10.1029/2007GL029311, URL http://onlinelibrary.wiley.com/doi/10.1029/2007GL029311/abstract, 2007.

Leitão, J., Richter, A., Vrekoussis, M., Kokhanovsky, A., Zhang, Q. J., Beekmann, M., and Burrows, J. P.: On the improvement of NO2 satellite retrievals – aerosol impact on the airmass factors, Atmospheric Measurement Techniques, 3, 475–493, doi:10.5194/amt-3-475-2010, URL http://www.atmos-meas-tech.net/3/475/2010/amt-3-475-2010.html, 2010.

Lelieveld, J., Beirle, S., Hörmann, C., Stenchikov, G., and Wagner, T.: Abrupt recent trend changes in atmospheric nitrogen dioxide over the Middle East, Science Advances, 1, e1500 498, URL http://advances.sciencemag.org/content/1/7/e1500498.short, 2015.

Leue, C., Wenig, M., Wagner, T., Klimm, O., Platt, U., and Jähne, B.: Quantitative analysis of NOx emissions from Global Ozone Monitoring Experiment satellite image sequences, Journal of Geophysical Research: Atmospheres, 106, 5493–5505, doi:10.1029/2000JD900572, URL http://onlinelibrary.wiley.com/doi/10.1029/2000JD900572/abstract, 2001.

Lin, M., Holloway, T., Carmichael, G. R., and Fiore, A. M.: Quantifying pollution inflow and outflow over East Asia in spring with regional and global models, Atmos. Chem. Phys., 10, 4221–4239, URL http://www.atmos-chem-phys.net/10/4221/2010/, 2010.

Lin, X., Trainer, M., and Liu, S. C.: On the nonlinearity of the tropospheric ozone production, Journal of Geophysical Research: Atmospheres, 93, 15 879–15 888, doi:

10.1029/JD093iD12p15879, URL http://onlinelibrary.wiley.com/doi/10.1029/JD093iD12p15879/abstract, 1988.

Lyapunov, A. M.: The general problem of the stability of motion, International Journal of Control, 55, 531–534, doi:10.1080/00207179208934253, URL http://dx.doi.org/10.1080/00207179208934253, 1992.

Mann, H. B. and Whitney, D. R.: On a Test of Whether one of Two Random Variables is Stochastically Larger than the Other, The Annals of Mathematical Statistics, 18, 50–60, doi:10.1214/aoms/1177730491, URL http://projecteuclid.org/euclid.aoms/1177730491, 1947.

Martin, R. V., Chance, K., Jacob, D. J., Kurosu, T. P., Spurr, R. J. D., Bucsela, E., Gleason, J. F., Palmer, P. I., Bey, I., Fiore, A. M., Li, Q., Yantosca, R. M., and Koelemeijer, R. B. A.: An improved retrieval of tropospheric nitrogen dioxide from GOME, Journal of Geophysical Research (Atmospheres), 107, 4437, URL http://adsabs.harvard.edu/abs/2002JGRD..107.4437M, 2002.

Martin, R. V., Jacob, D. J., Chance, K., Kurosu, T. P., Palmer, P. I., and Evans, M. J.: Global inventory of nitrogen oxide emissions constrained by space-based observations of NO2 columns, Journal of Geophysical Research: Atmospheres, 108, doi:10.1029/2003JD003453, URL http://onlinelibrary.wiley.com/doi/10.1029/2003JD003453/abstract, 2003.

McCalla, C.: Objective Determination of the Tropopause Using WMO Operational Definitions, US Department of Commerce, National Oceanic and Atmospheric Administration, National Weather Service, National Meteorological Center, URL http://www.lib.ncep.noaa.gov/ncepofficenotes/files/014082BA.pdf, 1981.

McInnes, G.: Atmospheric Emission Inventory Guidebook: A Joint EMEP/CORINAIR Production, EC, 1996.

McLinden, C. A., Fioletov, V., Boersma, K. F., Kharol, S. K., Krotkov, N., Lamsal, L., Makar, P. A., Martin, R. V., Veefkind, J. P., and Yang, K.: Improved satellite retrievals of NO2 and SO2 over the Canadian oil sands and comparisons with surface measurements, Atmos. Chem. Phys, 14, 3637–3656, URL http://www.researchgate.net/profile/Chris_Mclinden/publication/262993432_Improved_satellite_retrievals_of_NO2_and_SO2_over_the_Canadian_oil_sands_and_comparisons_with_surface_measurements/links/0deec53b473608ec22000000.pdf, 2014.

Michalakes, J., Chen, S., Dudhia, J., Hart, L., Klemp, J., Middlecoff, J., and Skamarock, W.: Development of a next generation regional weather research and forecast model, in: Developments in Teracomputing: Proceedings of the Ninth ECMWF Workshop on the use of high performance computing in meteorology, vol. 1, pp. 269–276, World Scientific, 2001.

Mie, G.: Beiträge zur Optik trüber Medien, speziell kolloidaler Metallösungen, Annalen der Physik, 330, 377–445, doi:10.1002/andp.19083300302, URL http://onlinelibrary.wiley.com/doi/10.1002/andp.19083300302/abstract, 1908.

National Climatic Data Center, NESDIS, NOAA, U.S. Department of Commerce: NCEP EDAS and GDAS (FNL) Model Data (DSI-6141), URL http://www.ncdc.noaa.gov.

National Oceanic and Atmospheric Administration, National Aeronautics and Space Administration, and United States Air Force: U.S. Standard Atmosphere, 1976, Tech. rep., U.S. Government Printing Office, Washington, D.C., 1976.

Olivier, J. G. J., Bouwman, A. F., Mass, C. W. M. v. d., Berdowski, J. J. M., Veldt, C., Bloos, J. P. J., Visschedijk, A. J. H., Zandveld, P. Y. J., and Haverlag, J. L.: Description of EDGAR version 2.0: a set of global emission inventories of greenhouse gases and ozone-depleting substances for all anthropogenic and most natural sources on a per country basis and on 1 degree x 1 degree grid, Tech. rep., Rijksinstituut voor Volksgezondheid en Milieuhygiene, URL http://inis.iaea.org/Search/search.aspx?orig_q=RN:29006635, 1996.

Ott, L. E., Pickering, K. E., Stenchikov, G. L., Allen, D. J., DeCaria, A. J., Ridley, B., Lin, R.-F., Lang, S., and Tao, W.-K.: Production of lightning NOx and its vertical distribution calculated from three-dimensional cloud-scale chemical transport model simulations, Journal of Geophysical Research: Atmospheres, 115, doi:10.1029/2009JD011880, URL http://onlinelibrary.wiley.com/doi/10.1029/2009JD011880/abstract, 2010.

Perez, F. and Granger, B. E.: IPython: a system for interactive scientific computing, Computing in Science & Engineering, 9, 21–29, URL http://scitation.aip.org/content/aip/journal/cise/9/3/10.1109/MCSE.2007.53, 2007.

Platt, U. and Stutz, J.: Differential Optical Absorption Spectroscopy: Principles and Applications, Springer, Berlin, 1 edn., 2007.

Popp, C., Wang, P., Brunner, D., Stammes, P., Zhou, Y., and Grzegorski, M.: MERIS albedo climatology for FRESCO+ O2 A-band cloud retrieval, Atmospheric Measurement Techniques, 4, 463–483, doi:10.5194/amt-4-463-2011, URL http://www.atmos-meas-tech.net/4/463/2011/amt-4-463-2011.html, 2011.

Quinn, P. K., Shaw, G., Andrews, E., Dutton, E. G., Ruoho-Airola, T., and Gong, S. L.: Arctic haze: current trends and knowledge gaps, Tellus B, 59, 99–114, doi:10.1111/j.1600-0889.2006.00238.x, URL http://onlinelibrary.wiley.com/doi/10.1111/j.1600-0889.2006.00238.x/abstract, 2007.

Richter, A. and Burrows, J. P.: Tropospheric NO2 from GOME measurements, Advances in Space Research, 29, 1673–1683, URL http://www.sciencedirect.com/science/article/pii/S027311770200100X, 2002.

Richter, A., Burrows, J. P., Nüß, H., Granier, C., and Niemeier, U.: Increase in tropospheric nitrogen dioxide over China observed from space, Nature, 437, 129–132, doi:10.1038/nature04092, URL http://www.nature.com/nature/journal/v437/n7055/abs/nature04092.html, 2005.

Richter, A., Begoin, M., Hilboll, A., and Burrows, J. P.: An improved NO2 retrieval for the GOME-2 satellite instrument, Atmospheric Measurement Techniques, 4, 1147–1159, doi:10.5194/amt-4-1147-2011, URL http://www.atmos-meas-tech.net/4/1147/2011/amt-4-1147-2011.html, 2011.

Richter, A., Hilboll, A., and Burrows, J.: Improving satellite retrievals of large tropospheric NO columns, URL http://www.iup.uni-bremen.de/doas/posters/egu_2014_richter.pdf, 2014.

Riuttanen, L., Dal Maso, M., de Leeuw, G., Riipinen, I., Sogacheva, L., Vakkari, V., Laakso, L., and Kulmala, M.: Long-range transport of biomass burning smoke to Finland in 2006, Atmospheric Chemistry and Physics Discussions, 13, 4289–4330, doi:10.5194/acpd-13-4289-2013, URL http://www.atmos-chem-phys-discuss.net/13/4289/2013/acpd-13-4289-2013.html, 2013.

Rozanov, V., Rozanov, A., Kokhanovsky, A., and Burrows, J.: Radiative transfer through terrestrial atmosphere and ocean: Software package SCIATRAN, Journal of Quantitative Spectroscopy and Radiative Transfer, doi:10.1016/j.jqsrt.2013.07.004, URL http://www.sciencedirect.com/science/article/pii/S0022407313002872, 2014.

Sauvage, B., Cammas, J., Defer, E., Volz-Thomas, A., Thomas, K., and Holle, R. L.: Lightning NOx influence on large scale NOy and O3 plumes observed over the northern mid-latitudes, AGU Fall Meeting Abstracts, p. 0187, URL http://adsabs.harvard.edu/abs/2011AGUFM.A51A0187S, 2011.

Schaub, D., Weiss, A. K., Kaiser, J. W., Petritoli, A., Richter, A., Buchmann, B., and Burrows, J. P.: A transboundary transport episode of nitrogen dioxide as observed from GOME and its impact in the Alpine region, Atmos. Chem. Phys., 5, 23–37, doi:10.5194/acp-5-23-2005, URL http://www.atmos-chem-phys.net/5/23/2005/, 2005.

Schultz, M., Schmitt, R., Thomas, K., and Volz-Thomas, A.: Photochemical box modeling of long-range transport from North America to Tenerife during the North Atlantic Regional Experiment (NARE) 1993, Journal of Geophysical Research, 103, 13 477–13,488, doi:10.1029/97JD01481, URL http://www.agu.org/pubs/crossref/1998/97JD01481.shtml, 1998.

Schumann, U. and Huntrieser, H.: The global lightning-induced nitrogen oxides source, Atmos. Chem. Phys., 7, 3823–3907, doi:10.5194/acp-7-3823-2007, URL http://www.atmos-chem-phys.net/7/3823/2007/, 2007.

Seinfeld, J. H. and Pandis, S. N.: Atmospheric chemistry and physics: from air pollution to climate change, John Wiley & Sons, URL http://books.google.com/books?hl=de&lr=&id=YH2K9eWsZOcC&oi=fnd&pg=PA1991&dq=Seinfeld+and+Pandis,+Atmospheric+Chemistry+and+Physics&ots=hK3vPl9QHy&sig=jhMZ_6MmYgD7ewglhip5JtosPbs, 2012.

Shaw, G. E.: The Arctic Haze Phenomenon, Bulletin of the American Meteorological Society, 76, 2403–2413, doi:10.1175/1520-0477(1995)076<2403:TAHP>2.0.CO;2, URL http://journals.ametsoc.org/doi/abs/10.1175/1520-0477(1995)076%3C2403:TAHP%3E2.0.CO;2, 1995.

Sihler, H., Platt, U., Beirle, S., Marbach, T., Kühl, S., Dörner, S., Verschaeve, J., Frie\s s, U., Pöhler, D., Vogel, L., and others: Tropospheric BrO column densities in the Arctic derived from satellite: retrieval and comparison to ground-based measurements, Atmospheric Measurement Techniques, 5, 2779–2807, URL http://www.researchgate.net/profile/Thierry_Marbach/publication/258591576_Tropospheric_BrO_column_densities_in_the_Arctic_derived_from_satellite_retrieval_and_comparison_to_ground-based_measurements/links/544100420cf2e6f0c0f45e4e.pdf, 2012.

Singh, H. B. and Hanst, P. L.: Peroxyacetyl nitrate (PAN) in the unpolluted atmosphere: An important reservoir for nitrogen oxides, Geophysical Research Letters, 8, 941–944, doi:10.1029/GL008i008p00941, URL http://onlinelibrary.wiley.com/doi/10.1029/GL008i008p00941/abstract, 1981a.

Singh, H. B. and Hanst, P. L.: Peroxyacetyl nitrate (PAN) in the unpolluted atmosphere: An important reservoir for nitrogen oxides, Geophysical Research Letters, 8, 941–944, doi:10.1029/GL008i008p00941, URL http://onlinelibrary.wiley.com/doi/10.1029/GL008i008p00941/abstract, 1981b.

Solomon, S., Schmeltekopf, A. L., and Sanders, R. W.: On the interpretation of zenith sky absorption measurements, Journal of Geophysical Research, 92, 8311–8319, URL http://adsabs.harvard.edu/abs/1987JGR....92.8311S, 1987.

Spichtinger, N., Wenig, M., James, P., Wagner, T., Platt, U., and Stohl, A.: Satellite detection of a continental-scale plume of nitrogen oxides from boreal forest fires, Geophysical Research Letters, 28, 4579–4582, URL http://www.agu.org/pubs/crossref/2001/2001GL013484.shtml, 2001.

Stein, O., Flemming, J., Inness, A., Kaiser, J. W., and Schultz, M. G.: Global reactive gases forecasts and reanalysis in the MACC project, Journal of Integrative Environmental Sciences, 9, 57–70, doi:10.1080/1943815X.2012.696545, URL http://dx.doi.org/10.1080/1943815X.2012.696545, 2012.

Stohl, A., Huntrieser, H., Richter, A., Beirle, S., Cooper, O. R., Eckhardt, S., Forster, C., James, P., Spichtinger, N., and Wenig, M.: Rapid intercontinental air pollution transport associated with a meteorological bomb, Atmospheric Chemistry and Physics, 3, 969–985, URL http://www.atmos-chem-phys.net/3/969/2003/acp-3-969-2003.pdf, 2003.

Stohl, A., Forster, C., Frank, A., Seibert, P., and Wotawa, G.: Technical note: The Lagrangian particle dispersion model FLEXPART version 6.2, Atmos. Chem. Phys., 5, 2461–2474, doi:10.5194/acp-5-2461-2005, URL http://www.atmos-chem-phys.net/5/2461/2005/, 00523, 2005.

van der Werf, G. R., Randerson, J. T., Giglio, L., Collatz, G. J., Mu, M., Kasibhatla, P. S., Morton, D. C., DeFries, R. S., Jin, Y. v., and van Leeuwen, T. T.: Global fire emissions and the contribution of deforestation, savanna, forest, agricultural, and peat fires (1997–2009), Atmospheric Chemistry and Physics, 10, 11 707–11 735, URL http://www.atmos-chem-phys.net/10/11707/2010/, 2010.

Van Rossum, G. and Drake, F. L.: Python language reference manual, Network Theory, URL http://homepages.ipact.nl/~wichizaya/work/ref.pdf, 2003.

Vasilkov, A. P., Joiner, J., Haffner, D., Bhartia, P. K., and Spurr, R. J. D.: What do satellite backscatter ultraviolet and visible spectrometers see over snow and ice? A study of clouds and ozone using the A-train, Atmospheric Measurement Techniques, 3, 619–629, URL http://www.atmos-meas-tech.net/3/619/2010/amt-3-619-2010.html, 2010.

Vrekoussis, M., Richter, A., Hilboll, A., Burrows, J. P., Gerasopoulos, E., Lelieveld, J., Barrie, L., Zerefos, C., and Mihalopoulos, N.: Economic crisis detected from space: air quality observations over Athens/Greece, Geophysical Research Letters, 40, 458–463, URL http://onlinelibrary.wiley.com/doi/10.1002/grl.50118/full, 2013.

Wagner, T., Erle, F., Marquard, L., Otten, C., Pfeilsticker, K., Senne, T., Stutz, J., and Platt, U.: Cloudy sky optical paths as derived from differential optical absorption spectroscopy observations, Journal of Geophysical Research: Atmospheres, 103, 25 307–25 321, doi:10.1029/98JD01021, URL http://onlinelibrary.wiley.com/doi/10.1029/98JD01021/abstract, 1998.

Walker, T. W., Martin, R. V., van Donkelaar, A., Leaitch, W. R., MacDonald, A. M., Anlauf, K. G., Cohen, R. C., Bertram, T. H., Huey, L. G., Avery, M. A., Weinheimer, A. J., Flocke, F. M., Tarasick, D. W., Thompson, A. M., Streets, D. G., and Liu, X.: Trans-Pacific transport of reactive nitrogen and ozone to Canada during spring, Atmos. Chem. Phys., 10, 8353–8372, doi:10.5194/acp-10-8353-2010, URL http://www.atmos-chem-phys.net/10/8353/2010/, 2010.

Wang, P., Stammes, P., van der A, R., Pinardi, G., and van Roozendael, M.: FRESCO+: an improved O2 A-band cloud retrieval algorithm for tropospheric trace gas retrievals, Atmos. Chem. Phys., 8, 6565–6576, doi:10.5194/acp-8-6565-2008, URL http://www.atmos-chem-phys.net/8/6565/2008/, 2008.

Wenig, M., Spichtinger, N., Stohl, A., Held, G., Beirle, S., Wagner, T., Jähne, B., and Platt, U.: Intercontinental transport of nitrogen oxide pollution plumes, Atmospheric Chemistry and Physics, 3, 387–393, URL http://hal.archives-ouvertes.fr/hal-00295247, 2003.

Whittaker, L. M. and Horn, L. H.: Northern Hemisphere extratropical cyclone activity for four mid-season months, Journal of Climatology, 4, 297–310, doi:10.1002/joc.3370040307, URL http://onlinelibrary.wiley.com/doi/10.1002/joc.3370040307/abstract, 1984.

World Health Organization: Health aspects of air pollution with particulate matter, ozone and nitrogen dioxide: Report on a WHO Working Group, World Health Organization, WHO, Regional Office for Europe, 2003.

Zhang, Q., Streets, D. G., He, K., Wang, Y., Richter, A., Burrows, J. P., Uno, I., Jang, C. J., Chen, D., Yao, Z., and others: NOx emission trends for China, 1995–2004: The view from the ground and the view from space, Journal of Geophysical Research: Atmospheres (1984–2012), 112, URL http://onlinelibrary.wiley.com/doi/10.1029/2007JD008684/pdf, 2007.

Zien, A., Richter, A., Hilboll, A., and Burrows, J.: Cloud effects on tropospheric NO2 measurements from satellite, DPG Frühjahrstagung, Hannover, Germany, URL http://www.doas-bremen.de/posters/dpg_2010_zien.pdf, 2010a.

Zien, A., Richter, A., Hilboll, A., and Burrows, J.: Sensitivity of satellite observations over bright and cloudy scenes, COSPAR, Bremen, Germany, URL http://www.doas-bremen.de/posters/cospar_2010_zien.pdf, 2010b.

Zien, A., Richter, A., Hilboll, A., and Burrows, J.: Remote sensing trace gas observations by satellite instruments over bright surfaces, DPG Frühjahrstagung, Dresden, Germany, URL http://www.doas-bremen.de/posters/dpg_2011_zien.pdf, 2011a.

Zien, A., Richter, A., Hilboll, A., and Burrows, J.: A Statistical Evaluation of NO2 Long-Range Transport Events Using GOME-2 Observations, European Geosciences Union General Assembly, Vienna, Austria, URL http://www.iup.uni-bremen.de/~azien/downloads/azien-egu2011-NO2LRTstatistics.pdf, 2011b.

Zien, A., Richter, A., Hilboll, A., and Burrows, J.: Comparison of NO2 long-range transport events in GOME-2 observations and CTM simulations, European Geosciences Union General Assembly, Vienna, Austria, URL http://www.doas-bremen.de/posters/egu_2012_zien.pdf, 2012a.

Zien, A., Richter, A., Hilboll, A., and Burrows, J. P.: Automated identification and verification of long-range transport events of NO2 in GOME-2 observations, DPG Frühjahrstagung, Berlin, Germany, URL http://www.iup.uni-bremen.de/~azien/downloads/azien-dpg2012-NO2LRTidentification.pdf, 2012b.

Zien, A. W., Richter, A., Hilboll, A., Blechschmidt, A.-M., and Burrows, J. P.: Systematic analysis of tropospheric NO2 long-range transport events detected in GOME-2 satellite data, Atmos. Chem. Phys., 14, 7367–7396, doi:10.5194/acp-14-7367-2014, URL http://www.atmos-chem-phys.net/14/7367/2014/, 2014.